

ARO

The Scientific Journal of Koya University

Determination of Multi-performance Characteristics in Electric Discharge Machining of DIN 1.2767 Steel Using Grey Relational Analysis. Assessment of the Upstream Slope Stability of Darbandikhan Rockfill Dam during Draw-down. Effect of Sand Percentage on the Compaction Properties and Undrained Shear Strength of Low Plasticity Clay. Corrosion in Crude Oil Distillation Unit Overhead: A recent Case Study. Feasibility Study of Concrete Louvers for High-rise Residential Buildings in Terms of Cooling Energy Requirements. Structural Behavior of Reinforced Concrete Beams Incorporating Foamed Glass as Aggregates. Assessment of Acoustical Characteristics for Recent Mosque Buildings in Erbil City of Iraq. Design and Construction of Zana Robot for Modeling Human Player in Rock-paper-scissors Game using Multilayer Perceptron, Radial basis Functions and Markov Algorithms. Evaluation of Flying Ad Hoc Network Topologies, Mobility Models, and IEEE Standards for Different Video Applications. A Comparative Study of Electrical Characterization of P-Doped Distributed Bragg Reflectors Mirrors for 1300 nm Vertical Cavity Semiconductor Optical Amplifiers. Assessment the Natural Radioactivity of Radionuclides (^{226}Ra , ^{232}Th , ^{40}K , and ^{137}Cs) in Wheat Grain. Design and Fabrication of a Novel Ultra Compact Microstrip Diplexer Using Interdigital and Spiral Cells. Chemical Characterization and Antidiabetic Activity of Essential Oils from *Pelargonium graveolens* Leaves. A Study on the Prevalence and Source of Staphylococci and Methicillin-resistant *Staphylococcus aureus* Causing Superficial Incisional Surgical Site Infection.



ARO-The Scientific Journal of Koya University

The ARO (“Today” in Hewramí Kurdish), is an international scientific journal published by the Koya University with p-ISSN: 2410-9355, e-ISSN: 2307-549X and DOI: 10.14500/2307-549X. ARO is a journal of original scientific research, global news, and commentary. The ARO Scientific Journal is a peer-reviewed, open access journal that publishes original research articles as well as review articles in areas of Science, Engineering and Technology.



ARO Executive Publisher

Dr. Wali M. Hamad; President of Koya University and the Executive Publisher of ARO.

ARO Editorial Board

The Editorial Board of ARO includes an eight-member Senior Executive Editorial Board and a seven-member Associate Editorial Board that help in setting journal policy; a Board of Reviewing Editors consisting of more than 250 leading scientists.

ARO Editorial Group

Senior Executive Editors: Dilan M. Rostam, Salah I. Yahya, Basim M. Fadhil, Fahmi F. Muhammad, Mohammed H. Zangana, Jorge Correia, Fouad Mohammed, Jacek Binda Nadhir Al-Ansari, Howri Mansurbeg, Tara F. Tahir and Yazan A. Khaleel

Associate Editors: Hamed M. Jassim, Ikbal M.G. Tahir, Saddon T. Ahmad, Sahar B. Mahmood and Layth I. Abd Ali.

This issue reviewers: Abbas Rezaei, Abdulqader Abdullah, Asaad M. Jassim, Azad Mohammed, Bestun Shwan, Bushra H. Marouf, Chro A. Hamaradha, Fahmi F. Muhammadsharif, Faris R. Ahmed, Farzin Shama, Ganesh B. Loganathan, Govand S. Kadir, Halgurd S. Maghdid, Hamed M. Jassim, Hastyar Najmuldenn, Hiwa H. Azeez, Hoshyar Q. Rasul, Husein A. Husein, Ibrahim N. Qader, Kamran J. Naquvi, Karwan W. Qadir, Laith A. Najam, Ribwar K. Abdulrahman, Safia Blbas, Salah I. Yahya, Sudad H. Al-Obaidi, Zahraa N. Rashied

ARO Editorial Web and New Media: Dilan M. Rostam and Salah I. Yahya

Secretarial Office of the Journal: Haneen H. Falah

Journal Proofreader: Salah I. Yahya

ARO, the International journal of original scientific research and commentary is an online and published twice a year, as well, by Koya University. The published articles are free and online open access distributed under the Creative Commons Attribution License (CC BY-NC-SA 4.0: <https://creativecommons.org/licenses/by-nc-sa/4.0/>). Responsibility of the content rests upon the authors and not upon ARO or Koya University.

ARO the Scientific Journal Office

Koya University, University Park
Danielle Mitterrand Boulevard, Koya KOY45
Kurdistan Region - F.R. Iraq

Tel.: +964 (0) 748 012 7423

Mobile: +964 (0) 750 187 5489

E-mail: aro.journal@koyauniversity.org

url: aro.koyauniversity.org

June 2021

ARO

The Scientific Journal of Koya University

Vol IX, No 1(2021)

Contents

Aro Editorial Words	iii
Abubaker Y. Fatatit, Ali Kalyon	01
Determination of Multi-performance Characteristics in Electric Discharge Machining of DIN 1.2767 Steel Using Grey Relational Analysis	
Sirwan Gh. Salim, Krikar M. G. Noori	08
Assessment of the Upstream Slope Stability of Darbandikhan Rockfill Dam during Drawdown	
Iyad Alkroosh, Ali Al-Robay, Prabir Sarker, Saif Alzabeebee	16
Effect of Sand Percentage on the Compaction Properties and Undrained Shear Strength of Low Plasticity Clay	
Ari A. Ahmed	21
Corrosion in Crude Oil Distillation Unit Overhead: A recent Case Study	
Sara Dh. Bahaadin, Binaee Y. Raof, Hendren Abdulrahman	28
Feasibility Study of Concrete Louvers for High-rise Residential Buildings in Terms of Cooling Energy Requirements	
Dawood S. Atrushi	40
Structural Behavior of Reinforced Concrete Beams Incorporating Foamed Glass as Aggregates	
Dawa A. A. Masih, Nawzad K. Jalal, Manar N. A. Mohammed, Sulaiman A. Mustafa	51
The Assessment of Acoustical Characteristics for Recent Mosque Buildings in Erbil City of Iraq	
Maryam Ghasemi, Abdolreza Roshani, Peshawa J. Muhammad Ali, Farhad F. Nia, Ehsan Nazemi, Gholam H. Roshani	67
Design and Construction of Zana Robot for Modeling Human Player in Rock-paper-scissors Game using Multilayer Perceptron, Radial basis Functions and Markov Algorithms	
Ghassan QasMarrogy	77
Evaluation of Flying Ad Hoc Network Topologies, Mobility Models, and IEEE Standards for Different Video Applications	
Faten A. Chaqmaqchee	89
A Comparative Study of Electrical Characterization of P-Doped Distributed Bragg Reflectors Mirrors for 1300 nm Vertical Cavity Semiconductor Optical Amplifiers	

Zakariya A. Hussein, Najeba F. Salih, Shalaw Z. Sedeeq	95
Assessment the Natural Radioactivity of Radionuclides (^{226}Ra , ^{232}Th , ^{40}K , and ^{137}Cs) in Wheat Grain	
Salah I. Yahya, Abbas Rezaei	103
Design and Fabrication of a Novel Ultra Compact Microstrip Diplexer Using Interdigital and Spiral Cells	
Javed Ahamad, Subasini Uthirapathy	109
Chemical Characterization and Antidiabetic Activity of Essential Oils from <i>Pelargonium graveolens</i> Leaves	
Kameran M. Ali, Bahrouz M. A. Al-Jaff	114
A Study on the Prevalence and Source of Staphylococci and Methicillin-resistant <i>Staphylococcus aureus</i> Causing Superficial Incisional Surgical Site Infection	
General Information	122
Guide to Author	123
Aro Reviewer/Associate Editor Application Form	125

ARO Editorial Words

Dear readers,

Aro, the Scientific Journal of Koya University, is closing its sixteenth issue (Vol IX, No 1, 2021). It has been an exciting and yet dynamic season for our journal. Aro is publishing its 16th issue as an internationally listed Scientific Journal in Kurdistan Region of Iraq. Notably, Aro has been accepted for indexing in the Emerging Sources Citation Index (ESCI), a new edition of Web of Science™ as of Feb 2016. Content in this index is under consideration by WoS (Clarivate Analytics) to be accepted in the Science Citation Index Expanded™ (SCIE). Aro's individual articles are currently listed by WoS (Clarivate Analytics) using articles unique DOI numbers which is a historical achievement for our academic community. Aro is starting its ninth-year journey in leading the quality of regional scientific publications with global impact. The editorial team have been working tirelessly to keep the novel mission and sustain Aro's future publications with greater impacts and citations. It is exciting that Aro has been awarded to DOAJ Seal listing which is an indication of a trusted high standard open access scientific work. The upcoming new season will be an even more exciting period in Aro's life as WoS (Clarivate Analytics) will examine our journal for a full permanent listing.

Aro continues its mission to provide resources, support and advice for researchers in the process of publishing their scientific papers, while at the same time offering free public access to scientific research by open online access. This is a daunting task which we hope to advance in the years to come. Thus, in the sections to follow, we would like to share and elaborate on the core elements that constitute Aro. However, finding reliable and skilled reviewers remain a big challenge for us.

Aro was created with a long-term vision of becoming accessible to all researchers in Kurdistan and beyond, and covering a wide range of scholarly disciplines in sciences. Aro is a peer-reviewed, open access journal that publishes original scientific research, global news, letters and commentary as well as review articles in areas of natural sciences and technology. In this issue, you will have access to original research papers in a variety of areas, such as Physics, Chemistry, Biology, Civil Engineering, Software Engineering, Electrical and Electronics Engineering, Chemical Engineering, Wireless networks and Geology.

The great responses from researchers, academics and professionals in the last eight years have made us create a wider Editorial Board which serves the wider submitted scientific manuscripts. However, it is clear that having a dedicated and well-organised editorial board for the journal is only one side of the coin. The other is the ability to attract submissions of quality research and scholarly work. We are thankful to all of those who put their trust in Aro and presented their original research work for publication in Vol. IX, No. 1 (2021) of the journal, as well as, our thanks are extended to the 27 peer-reviewers from the Universities worldwide for their efforts in reviewing and enabling this issue of Aro.

Your support and feedback are invited and appreciated.

Dilan M. Rostam
Editor-in-Chief

Wali M Hamad
Executive Publisher

Dilan M. Rostam, Salah I. Yahya, Basim M. Fadhil, Fahmi F. Muhammad, Mohammed H. Zangana, Jorge Correia, Fouad Mohammed, Jacek Binda Nadhir Al-Ansari, Howri Mansurbeg, Tara F. Tahir and Yazen A. Khaleel
Executive Editorial Board

Determination of Multi-performance Characteristics in Electric Discharge Machining of DIN 1.2767 Steel Using Grey Relational Analysis

Abubaker Y. Fatatit¹ and Ali Kalyon²

¹Department of Manufacturing Engineering, Natural and Applied Sciences, Karabük University, Karabük 078050, Turkey

²Department of Mechanical Engineering, Faculty of Engineering, Yalova University, Yalova 077200, Turkey

Abstract—Electric discharge machining (EDM) is one of the most important unconventional machining processes, which can cut hard materials and complex shapes that are difficult to machine by conventional machining processes easily and with high accuracy. In this study, L18 orthogonal array combined with gray relational analysis (GRA) is implemented to investigate the multiple performances characteristics in EDM of DIN 1.2767 Tool Steel. Machining process parameters selected were discharge current (I_p), pulse-on time (T_{on}), pulse-off time (T_{off}), and electrode material (copper alloys [NSS and B2]). The investigated performances characteristics were tool wear rate (TWR) and material removal rate (MRR). Analysis of variance (ANOVA) and Taguchi's signal-to-noise ratio with the help of Minitab-17 software were used to analysis the effect of the process parameters on TWR and MRR. The experimental results and data analysis reveal that TWR and MRR are more affected by I_p and T_{on} . The minimum TWR was obtained at parametric combination I_p (6A), T_{on} (800 μ s), and T_{off} (800 μ s) and the maximum MRR attained at I_p (25A), T_{on} (800 μ s), T_{off} (200 μ s), and NSS electrode. After applying GRA, the optimal parametric combination for MRR and TWR was determined as I_p (25A), T_{on} (800 μ s), T_{off} (200 μ s), and NSS electrode. The study also exhibited the occurrence of an interaction between the variables on the responses. In addition, scanning electron microscopy images showed that the metal surface was affected with the increase in T_{on} and T_{off} .

Index Terms—Electrical discharge machining, Gray relation, Optimization, Taguchi, DIN 1.2767 Tool steel.

I. INTRODUCTION

The greatly improved properties of new engineering materials made it difficult to machine using the conventional machining processes. Non-conventional

machining processes can easily machine hard and brittle materials, complex geometries, and delicate components with tight tolerance, extreme surface finish, and free of burrs. Electric discharge machining (EDM) is one of the non-conventional machining processes that based on the conversion of electric energy into extremely high temperature (plasma channel) in localized region impinge on the work material surface caused melting or evaporating (Amorim and Weingaertner, 2007; Ho and Newman, 2003; Muthuramalingam and Mohan, 2015). The width and intensity of the plasma channel depend on many parameters which have complex relationships between each other in addition to other factors that affect the process's mechanism, making it difficult to achieve optimal performance for the EDM process. High temperature causes melt and wear of the electrode. The most used electrodes, with high conductivity of electricity and a high melting point such as copper, are tungsten, copper tungsten, silver tungsten aluminum, graphite and other, and metals and alloys. The selection of electrode material relies on the type of the EDM machine power supply circuit, the surface quality, and the type of workpiece material that is to be machined (Daniel, 2019; Shyha and Rudd, 2016).

Several experimental tests, which have been conducted to increase efficiency and improve EDM process performance, were related to EDM and mentioned that substantial researches have been conducted for improving EDM performance measures such as material removal rate (MRR), tool wear rate (TWR), surface roughness (Ra), and wear ratio. The most widely used material are steel materials, EN series, Ti-6AL-4V, SiC, B₄C, WC-Co, Al₂O₃+Ti S45C, and Inconel 718. The main electric input parameters have been used are T_{on} , T_{off} , I_p , and V and non-electric parameters including dielectric medium, flashing pressure, and electrode rotation. There are many optimization techniques and result analysis tools used such as Taguchi, response surface methodology, gray relationships analysis, ANOVA, and multiple regression analysis (Ramabalan and S, 2015; Patil and Jadhav, 2016).

Yerui et al., 2016, conducted experiments on TiC/Ni using EDM. The experimental results revealed that as the I_p

ARO-The Scientific Journal of Koya University
Vol. IX, No.1 (2021), Article ID: ARO.10718, 7 pages
DOI:10.14500/aro.10718

Received: 23 August 2020; Accepted: 16 January 2021

Regular research paper: Published 01 March 2021

Corresponding author's e-mail: ali.kalyon@yalova.edu.tr

Copyright © 2021 Abubaker Y. Fatatit and Ali Kalyon. This is an open-access article distributed under the Creative Commons Attribution License.



increased, the discharge energy increased, which results in an increase in the MRR. MRR increases with the increase of T_{on} , but when T_{on} was longer than 30 μs MRR decreased slowly. This was as a result of the expansion of the plasma channel and the effect of debris on it. Dastagiri and Kumar, 2014, reported that the higher the I_p , the more discharging energy. Then, the metal temperature rises in a very localized region, thus more MRR can be achieved. T_{on} increases, MRR increases and then decreases. Kalyon, 2020, applied Taguchi method and gray relational analysis (GRA) for optimization of EDM of Caldie cold work tool steel, considering process parameters such as I_p , T_{on} , and electrode materials (graphite and copper). The results revealed that with increasing I_p and T_{on} , the MRR and Ra increased. The optimal parameter setting for maximum MRR and minimum Ra obtained by GRA is graphite electrode, 6 A and 50 μs . Habib, 2009, performed experiments using copper as a tool electrode on an EDM with selected input parameters on conductive metal matrix composite Al/SiC. Results of the study showed that the higher I_p offered higher MRR. An increase of T_{on} caused an increase in MRR until it reached 200 μs and then MRR began to decrease. TWR was found to be directly proportional to I_p and T_{on} . Gopalakannan et al., 2013, investigated EDM performance and optimizing the process parameters of AL7075-B₄C MMC using response surface methodology. The process parameters were I_p , T_{on} , T_{off} , and gap voltage. It was concluded that the two main significant process parameters that affect the MRR were I_p and T_{on} . The MRR increased with the increase in T_{on} and then decreased with longer T_{on} . Furthermore, TWR decreased with the increase of T_{on} . I_p and T_{on} have statistically significant effect on TWR. Venkatesh et al., 2015, studied the EDM performance of EN 31, EN 8, and HCHCr, and they used three electrodes, copper, brass, and chromium copper. They mentioned that the optimal MRR and TWR were at chromium copper electrode followed by copper then brass. The brass electrode achieved minimal surface roughness, but TWR was high and MRR was low. Besides, performance measures were influenced by workpiece material. Kumar, 2012, conducted EDM experiments on OHNS Die Steel using three different electrodes (copper-chromium, brass, and copper). Their results showed that the copper-chromium electrode produced higher MRR, better surface finish, and lower TWR compared to other electrodes. Lin and Lin, 2002, adopted the orthogonal array (OA) with GRA for multiperformance characteristics optimization of KD11 alloy steel. It was concluded that the performance characteristics such as MRR, TWR, and surface roughness were improved. Doniavi et al., 2008; Singh et al., 2004, concluded that OA and GRA can be successfully applied to obtain optimal level of EDM process parameters for multiperformance characteristics.

The electrode performance used in EDM is an important problem affecting machinability. TWR and MRR are important performance measures when evaluating the electrode performance. The low rate of wear of the electrode will ensure the dimensional integrity of the workpiece. High MRR will result in shorter machining times and reduced machining costs. This study aims to determine the optimal

parametric setting for minimizing TWR and maximizing MRR on DIN 1.2767 steels by applying GRA. In addition to determine the effect of the process parameters on TWR and MRR Taguchi optimization method was used. As a result, machinability of DIN 2767 Tool Steel was improved by using application of EDM method.

II. EXPERIMENTAL SETUP

The experiments were designed according to L_{18} Taguchi OA and performed on the FURKAN M25A sinker EDM machine. The experimental setup of EDM machine is shown in Fig. 1. Two electrodes, B2 and NSS, with a diameter of 16 mm were used. The physical properties and chemical compositions of electrodes are presented in Tables I-III. Before conducting each experiment, the electrode was polished on silicon carbide paper with grit sizes in this sequence, 150, 240, 320, 400, 600, and 800. The work material was DIN 1.2767 tool steel. This type of steel has crucial application in industry such as cutting and bending tools, drawing jaws, plastic molds, gears requiring shock resistance, heavy-duty shafts, and axles. Its chemical composition is listed in Table IV.

The size of each workpiece is 50 mm × 25 mm × 12 mm. The work materials' surface was machined by milling and grinding machines before conducting the EDM experiments. The electrode materials, I_p , T_{on} , and T_{off} , were selected as process parameters. Table V illustrates the process parameters and their levels. The polarity of the workpieces was positive and the electrode was negative. The kerosene was chosen as a dielectric fluid with lateral flushing pressure of 0.25 bar. The EDM time of each experiment was 1 h. The workpieces and the electrode were weighed before and after conducting the experiments. MRR and TWR can be calculated as below:

$$MRR(mm^3/min) = \frac{W_i - W_f}{t * \rho} \quad (1)$$

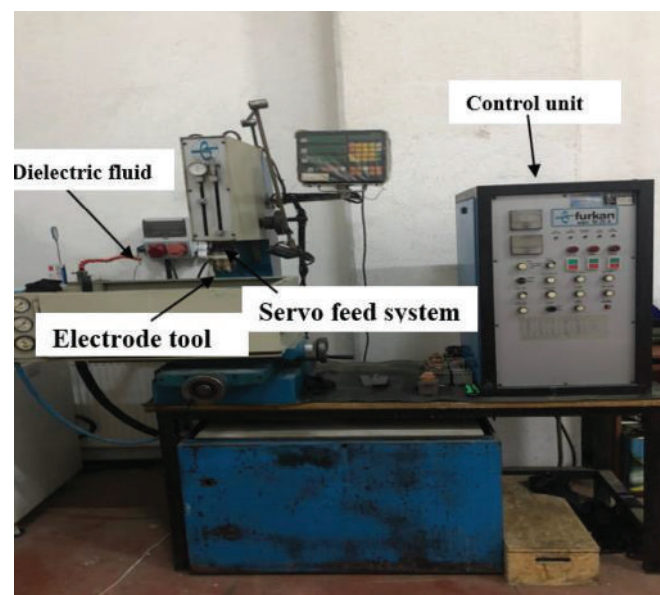


Fig. 1. Electric discharge machining (FURKAN M25A).

TABLE I
PHYSICAL PROPERTIES OF THE ELECTRODES

Material	Density (g/cm ³)	Electrical conductivity (MS/m)	Thermal conductivity (W/m K)	Melting temperature range (°C)
B2	8,3	≥16	120–170	870–980
NSS	8,81	≥23	190–240	1020–1040

TABLE II
CHEMICAL COMPOSITION OF NSS (CuNi2SiCr)

Element	Si	Mn	Cr	Ni	Fe	Pb	Cu
Weight (%)	0,65	0,10	0,35	2,5	0,15	0,02	Balance

TABLE III
CHEMICAL COMPOSITION OF B2 (CuBe2)

Element	Ni	Be	Co	Fe	Cu
Weight (%)	0,30	1,95	0,30	0,20	Balance

TABLE IV
CHEMICAL COMPOSITION OF DIN 1.2767

Element	C	Si	Mn	Cr	Mo	Ni	Fe
Weight (%)	0,45	0,25	0,35	1,35	0,25	4,05	Balance

TABLE V
CONTROL FACTORS AND LEVELS

Factor notation	Factor	Unit	Level 1	Level 2	Level 3
E	Tool material		NSS	B2	
A	Ip	A	6	12	25
B	Ton	μs	50	200	800
C	Toff	μs	50	200	800

$$TWR (mm^3 / min) = \frac{T_i - T_f}{t * \rho} \quad (2)$$

Where, W_i is the initial weight of the workpiece, W_f is the final weight, T_i is the initial weight of the electrode, T_f is the final weight of the electrode, ρ is the density, and t is the machining time in minutes.

Table VI shows the values of TWR and MRR after performing experiments according to L_{18} Taguchi OA and performing the calculations of MRR and TWR by applying Equations 1 and 2.

III. TAGUCHI'S SIGNAL-TO-NOISE RATIO (S/N)

Taguchi's S/N is a statistic that combines the mean and variance. The goal of robust experimentation is to determine an optimal combination of process parameters (control factor) settings that achieve robustness against factors that cause variability in the performance (noise factors). Selecting type of S/N depending on the goal of the experiments. In the case of the "smaller the better," S/N is calculated according to Equation 3, which is used when calculating TWR. When calculating MRR, larger the better, and the S/N ratio is given by Equation 4. Higher values of the S/N indicate process parameter settings that optimize the performance characteristics (Krishnaiah and Shahabudeen, 2012).

$$S / N = -10 \log \left[\frac{1}{n} \sum_{i=1}^n y_i^2 \right] \quad (3)$$

$$S / N = -10 \log \left[\frac{1}{n} \sum_{i=1}^n \frac{1}{y_i^2} \right] \quad (4)$$

Where, y_i is the performance response, i is the observation value, and n is the number of tests in an experiment.

IV. GRA

In many experiments and studies, process parameters cannot be set only for one response. Because of many reasons, one of them is that the objective is to maximize some responses and to minimize some responses together. GRA is among methods that can be employed to solve/optimize multiresponse problems. In GRA, the multiresponses are converted into a single response and then attain the levels of the optimal factors (Kalyon et al., 2018; Singh, 2018). Optimization in GRA is performed as the following steps:

1. Data pre-processing: Translation of responses values Y_{ij} into normalized values Z_{ij} ($0 \leq Z_{ij} \leq 1$). In case of normalized data processing for the response larger the better, Equation (5) is used, if the response smaller the better, the Equation (6) is applied and if the response is nominal the best, then the normalized values can be expressed by Equation (7).

$$Z_{ij} = \frac{Y_{ij} - \min(Y_{ij}, i = 1, 2, \dots, n)}{\max(Y_{ij}, i = 1, 2, \dots, n) - \min(Y_{ij}, i = 1, 2, \dots, n)} \quad (5)$$

$$Z_{ij} = \frac{\max(Y_{ij}, i = 1, 2, \dots, n) - Y_{ij}}{\max(Y_{ij}, i = 1, 2, \dots, n) - \min(Y_{ij}, i = 1, 2, \dots, n)} \quad (6)$$

$$Z_{ij} = \frac{(|Y_{ij} - T|) - \min(|Y_{ij} - T|, i = 1, 2, \dots, n)}{\max(|Y_{ij} - T|, i = 1, 2, \dots, n) - \min(|Y_{ij} - T|, i = 1, 2, \dots, n)} \quad (7)$$

where: $i=1, 2, \dots, n$ experiments. Y_{ij} = the i^{th} normalized value of the j^{th} response variable.

2. Gray relational coefficient: Gray relational coefficient is implemented for obtaining how close ideal and normalized response Z_{ij} are. The gray relational coefficient can be expressed by Equation (8).

$$GC_{ij} = \frac{\Delta_{min} + \lambda \Delta_{max}}{\Delta_{ij} + \lambda \Delta_{max}} \quad (8)$$

where: $\Delta = |Y_{oj} - Y_{ij}|$, Δ_{min} = minimum value of Δ , Δ_{max} = maximum value of Δ , Y_{oj} = the ideal normalized value of j^{th} response, λ = distinguish coefficient in between zero and one. It dominates the range of the gray relational coefficient.

3. Gray relational grade (G_j): The G_j computes the average sum of the GC_{ij} , and it is calculated as in Equation (9). The highest value of G_j is referred to optimal multiple response. Where m is number of responses.

TABLE VI
EXPERIMENTAL RESULTS

Exp. No.	Control factors	Tool	Ip (A)	Ton (μ s)	Toff (μ s)	Tool wear rate (mm^3/min)	Material removal rate (mm^3/min)
1	E ₁ A ₁ B ₁ C ₁	NSS	6	50	50	0,25	3,59
2	E ₁ A ₁ B ₂ C ₂	NSS	6	200	200	0,19	2,16
3	E ₁ A ₁ B ₃ C ₃	NSS	6	800	800	0,02	0,06
4	E ₁ A ₂ B ₁ C ₂	NSS	12	50	200	1,63	4,65
5	E ₁ A ₂ B ₂ C ₃	NSS	12	200	800	0,19	7,2
6	E ₁ A ₂ B ₃ C ₁	NSS	12	800	50	0,02	4,01
7	E ₁ A ₃ B ₁ C ₃	NSS	25	50	800	1,68	2,86
8	E ₁ A ₃ B ₂ C ₁	NSS	25	200	50	2,19	22,72
9	E ₁ A ₃ B ₃ C ₂	NSS	25	800	200	0,15	25,24
10	E ₂ A ₁ B ₁ C ₁	B2	6	50	50	0,63	2,01
11	E ₂ A ₁ B ₂ C ₂	B2	6	200	200	0,02	1,97
12	E ₂ A ₁ B ₃ C ₃	B2	6	800	800	0,02	0,65
13	E ₂ A ₂ B ₁ C ₂	B2	12	50	200	0,66	0,8
14	E ₂ A ₂ B ₂ C ₃	B2	12	200	800	0,4	4,08
15	E ₂ A ₂ B ₃ C ₁	B2	12	800	50	0,04	4,35
16	E ₂ A ₃ B ₁ C ₃	B2	25	50	800	1,14	0,65
17	E ₂ A ₃ B ₂ C ₁	B2	25	200	50	2,42	18,14
18	E ₂ A ₃ B ₃ C ₂	B2	25	800	200	0,36	20,5

$$G_j = \frac{1}{m} \sum GC_{ij} \quad (9)$$

Where: m is number of responses.

V. RESULTS AND DISCUSSION

A. Effect of the Process Parameters on TWR and MRR

Taguchi's S/N is used in the analysis of experiments results to indicate the effect of the process parameters and the process parameter settings that optimize the performance characteristics. Fig. 2 shows the main effects plot for S/N of MRR and TWR, where smaller is better is used in the case of TWR and larger is better in the case of MRR. It is clear that the optimum value of MRR gained by NSS electrode, Ip (25A), T_{on} 200 μ s, and T_{off} 50 μ s and optimum value of TWR gained at parameters Ip 6 A, T_{on} 800 μ s, and T_{off} 800 μ s while the effect of both electrodes on TWR response is close. MRR is directly proportional to Ip and inversely proportional to T_{off}. Similar observation has been reported by Lee and Li, 2001. As Ip increases, discharge energy increases, the highest temperature reached on the workpiece is also increases, hence, more MRR achieved (Dastagiri and Kumar, 2014). Furthermore, as it shown, MRR is directly proportional to Ip and inversely proportional to T_{off}. The increase of the T_{on}, TWR decreases gradually while MRR increases. However, a long T_{on}, MRR decreased. This decrease is due to the expansion of the electric plasma channel (Dastagiri and Kumar, 2014; Kalyon, 2020; Kumar, 2012). On the other hand, Lee and Li (2001) explained that a long Ton causes the arcing and decreases MRR. Furthermore, as it is shown, the NSS electrode achieves the best MRR while the effect of both electrodes on TWR response is close.

Interaction exists when the influence of one process parameters depends on the level of the other process

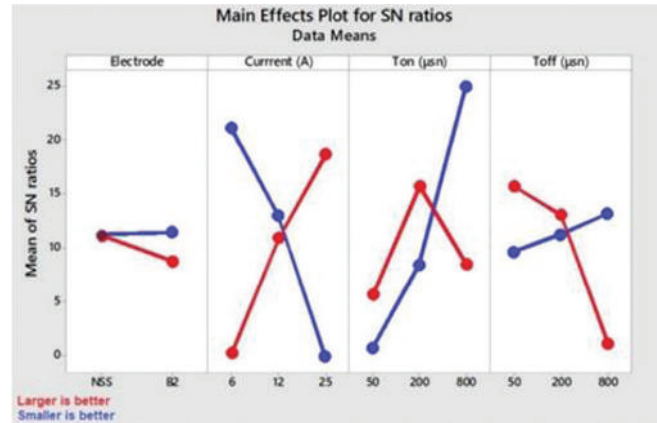


Fig. 2. Signal-to-noise ratio for tool wear rate and material removal rate.

parameter (Antony, 2003). Fig. 3-5 represent the combined effect (interaction) of process parameters on TWR. It is clear that the change in TWR from level to level of any process parameter depends on the level of the other parameter. While, the fluctuating effect of these parameters on the TWR was observed, but a lower TWR could be achieved when treated with the parameters Ip (6A), Ton (800 μ s), and Toff (800 μ s). Hence, minimum TWR can be achieved at low Ip and high values of Ton and Toff.

The interaction effects of parameters for MRR are illustrated in Fig. 6-8. It is seen the strong combined effect of process parameters on MRR. As can be seen from figure, MRR is positively affected by increase of Ip. For achieving maximum MRR, the optimum process parameter settings are Ip = 25A, T_{on} = 800 μ s and T_{off} = 200 μ s or Ip =25A, T_{on} = 200 μ s and T_{off} = 50 μ s.

It is important to study the contribution of the process parameters because not all parameters affect the performance in the same manner. Fig. 9 shows the results of the ANOVA analysis in determining the contribution of process parameters to TWR and MRR. Ip has the most significant effect on the

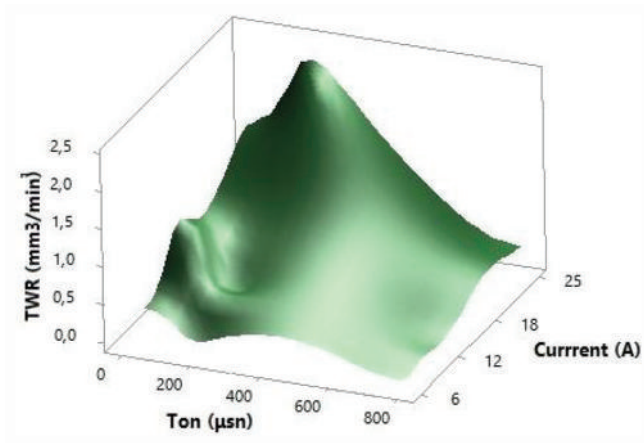


Fig. 3. Effect of T_{on} and current on tool wear rate.

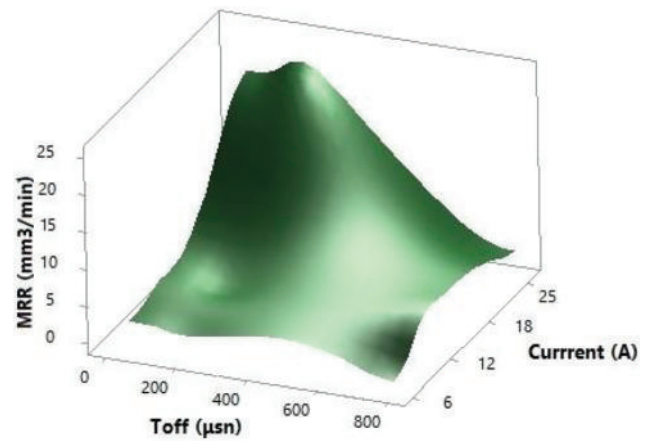


Fig. 6. Effect of T_{off} and current on material removal rate.

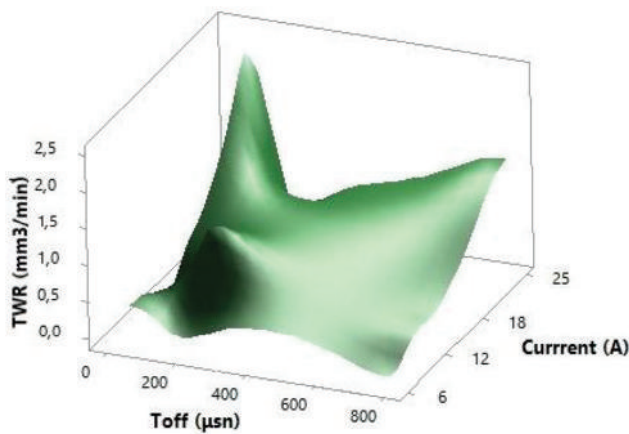


Fig. 4. Effect of T_{off} and current on tool wear rate.

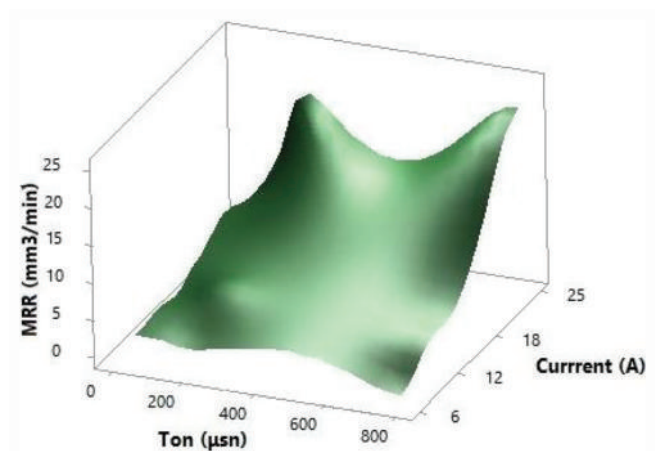


Fig. 7. Effect of T_{on} and current on material removal rate.

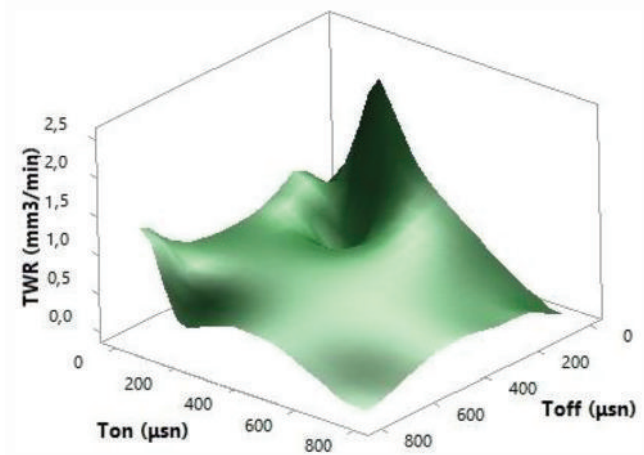


Fig. 5. Effect of T_{on} and T_{off} on tool wear rate.

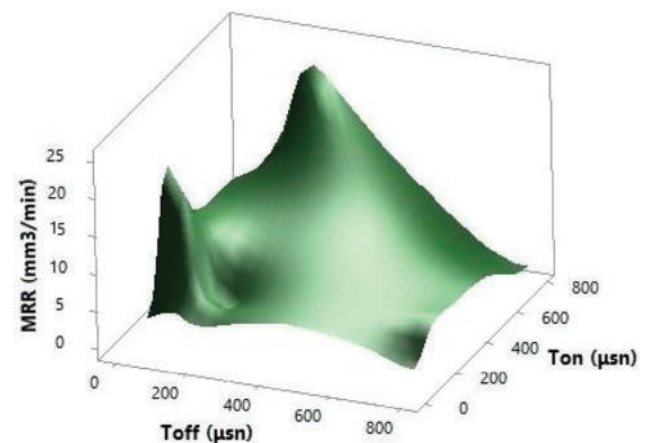


Fig. 8. Effect of T_{off} and T_{on} on material removal rate.

MRR and EWR followed by T_{on} and T_{off} while electrode material has the least effect on MRR and TWR. By focusing on the most influencing factors, a higher performance improvement ratio can be obtained. It is also clear that I_p and T_{off} have higher impact ratios in the case of MRR compared to the TWR. In the case of T_{on} , the rate of impact on the TWR is higher. In T_{on} , the TWR effect is higher. Electrode material has a negligible effect for both responses.

B. Multiresponse Optimization with GRA

From Fig. 2, we note that the values of the process parameters that achieve optimal MRR differ from the values of the process parameters that achieve optimal TWR. While, the study aims to obtain the optimal set of process parameters to achieve the minimum TWR and maximum MRR. To achieve this, GRA provides statistical and mathematical

equations which enables it to optimize multiobjective problems (Harpreet and Amandeep, 2012; Krishnaiah and Shahabudeen, 2012; Singh, 2018). After implementing the GRA steps as in Equations 5–9 which were previously mentioned, the results are shown in Table VII. It is clear from the last column in the table that Experiment 9 was

ranked 1 and this means that it achieved the best parametric combination ($E_1A_3B_3C_2$), that is, NSS electrode, I_p (25 A), T_{on} (800 μ s), and T_{off} (200 μ s) for optimal TWR and MRR of DIN 2767 Tool Steel.

C. Effect of Process Parameters on Surface Quality

In EDM, the workpiece surface is subjected to very high temperature and rapid cooling, which causes cracks and changes in surface properties. Fig. 6 exhibits scanning electron microscopy (SEM) images of EDMed surfaces. In Fig. 10a, when the process parameters I_p (6 A), T_{on} (50 μ s), and T_{off} (50 μ s), SEM image is examined, it is seen that there are globules of debris, pockmarks, microcracks, and crater formations on the surface. Fig. 10b shows surface EDMed with I_p (6A), T_{on} (200 μ s), and T_{off} (200 μ s). It is seen that microcracks are more on the surfaces processed with 6 A, T_{on} (200 μ s), and T_{off} (200 μ s). The surface crack density (SCD), microholes, and pits on the workpiece surface are intensively dependent on pulse energy (I_p and T_{on}) variations (Jabbaripour et al., 2012). When T_{on} excessive (i.e., 23 μ s), the severity of the crack width increases (Lee and Li, 2001).

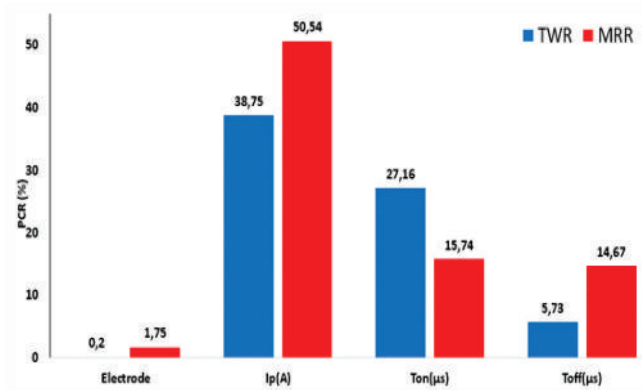


Fig. 9. Effect of parameters on tool wear rate and material removal rate as a result of ANOVA.

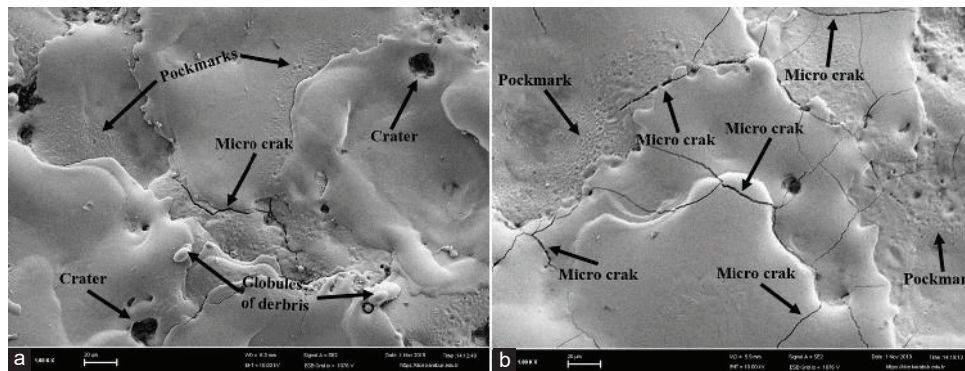


Fig. 10. Scanning electron microscopy surface images: (a) Process parameters I_p (6 A), T_{on} (50 μ s), and T_{off} (50 μ s), (b) process parameters I_p (6 A), T_{on} (200 μ s), and T_{off} (200 μ s).

TABLE VII
NORMALIZATION AND COEFFICIENT MATRIX VALUES

Exp. No.	Normalized tool wear rate	Normalized material removal rate	Gray relation coefficient tool wear rate	Gray relation coefficient material removal rate	Gray relation grade	Rank
1	0,904	0,140	0,839	0,368	0,603	10
2	0,929	0,083	0,876	0,353	0,614	9
3	1,000	0,000	1,000	0,333	0,667	7
4	0,329	0,182	0,427	0,379	0,403	17
5	0,929	0,284	0,876	0,411	0,643	8
6	1,000	0,157	1,000	0,372	0,686	3
7	0,308	0,111	0,420	0,360	0,390	18
8	0,096	0,900	0,356	0,833	0,595	11
9	0,946	1,000	0,902	1,000	0,951	1
10	0,746	0,077	0,663	0,351	0,507	13
11	1,000	0,076	1,000	0,351	0,676	5
12	1,000	0,023	1,000	0,339	0,669	6
13	0,733	0,029	0,652	0,340	0,496	14
14	0,842	0,160	0,759	0,373	0,566	12
15	0,992	0,170	0,984	0,376	0,680	4
16	0,533	0,023	0,517	0,339	0,428	16
17	0,000	0,718	0,333	0,639	0,486	15
18	0,858	0,812	0,779	0,726	0,753	2

The values of SCD reported by Bhattacharyya et al., 2007, were minimum at I_p and T_{on} in range 18–22 A and 20–100 μ s, respectively. Guu, 2005, concluded that low discharge energy should be used to avoid surface damage.

VI. CONCLUSIONS

This paper presented the use of OA with GRA for the optimization for the EDM process with the multiple performance characteristics. Taguchi method and ANOVA were applied to determine the contribution of parameters which affecting MRR and TWR. The main conclusions of this paper are summarized as follows:

- I_p was the most significant process parameter followed by T_{on} , T_{off} , and electrode material, respectively
- When I_p increased, MRR increases gradually. With the increase of T_{on} , MRR increased first and then decreases. MRR decreases with increase of T_{off}
- TWR is inversely proportional to I_p and directly proportional to T_{on} and T_{off}
- NSS electrode has higher effect on MRR than B2, while the effect of both electrodes for TWR was close to each other
- The minimum TWR was achieved at I_p (6A), T_{on} (800 μ s), and T_{off} (800 μ s) and the maximum MRR achieved at I_p (25A), T_{on} (800 μ s), and T_{off} (200 μ s). After applying GRA, the optimal parameters combination for MRR and TWR was determined as I_p (25A), T_{on} (800 μ s), T_{off} (200 μ s), and NSS electrode.

REFERENCES

- Amorim, F.L. and Weingaertner, W.L., 2007. The behavior of graphite and copper electrodes on the finish die-sinking electrical discharge machining (EDM) of AISI P20 tool steel. *Journal of the Brazilian Society of Mechanical Sciences and Engineering*, 29(4), pp.366-371.
- Antony, J., 2003. *Design of Experiments for Engineers and Scientists*. Elsevier Science and Technology Book, Amsterdam, Netherlands, pp.189-198.
- Bhattacharyya, B., Gangopadhyay, S. and Sarkar, B.R., 2007. Modelling and analysis of EDMED job surface integrity. *Journal of Materials Processing Technology*, 189(1-3), pp.169-177.
- Daniel, T., Liu, C., Mou, J. and Jahan, M.P., 2019. Micro-Wire-EDM. In: *Micro-electrical Discharge Machining Processes*. Springer, Singapore, pp.67-92.
- Dastagiri, M. and Kumar, A.H., 2014. Experimental investigation of EDM parameters on stainless steel and En41b. *Procedia Engineering*, 97(1), pp.1551-1564.
- Doniavi, A., Eskandarza, M., Abdi, A. and Totonchi, A., 2008. Empirical modeling of EDM parameters using GRA. *Asian Journal of Scientific Research*, 1(5), pp.502-509.
- Gopalakannan, S., Senthilvelan, T. and Ranganathan, S., 2013. Statistical optimization of EDM parameters on machining of aluminum Hybrid Metal Matrix composite by applying Taguchi based Grey analysis. *Journal of Scientific and Industrial Research*, 72(6), pp.358-365.
- Guu, Y.H., 2005. AFM surface imaging of AISI D2 tool steel machined by the EDM process. *Applied Surface Science*, 242(3-4), pp.245-250.
- Habib, S.S., 2009. Study of the parameters in electrical discharge machining through response surface methodology approach. *Applied Mathematical Modelling*, 33(12), pp.4397-4407.
- Harpreet, S. and Amandeep, S., 2012. Effect of pulse on/pulse off time on machining of AISI D3 die steel using copper and brass electrode in EDM. *International Journal of Engineering and Science*, 1(9), pp.19-22.
- Ho, K.H. and Newman, S.T., 2003. State of the art electrical discharge machining (EDM). *International Journal of Machine Tools and Manufacture*, 43(13), pp.1287-1300.
- Jabbaripour, B., Sadeghi, M.H., Faridvand, S. and Shabgard, M.R., 2012. Investigating the effects of Edm parameters on surface integrity, MRR And TWR in machining of Ti-6al-4v. *Machining Science and Technology*, 16(3), pp.419-444.
- Kalyon, A., Günay, M., Özyürek, D., 2018. Application of grey relational analysis based on Taguchi method for optimizing machining parameters in hard turning of high chrome cast iron. *Advances in Manufacturing*, 6(4), pp.419-429.
- Kalyon, A., 2020. Optimization of machining parameters in sinking electrical discharge machine of caldie plastic mold tool steel. *Sādhanā*, 45(1), pp.1-13.
- Krishnaiah, K. and Shahabudeen, P., 2012. *Applied Design of Experiments and Taguchi Methods*. PHI Learning Pvt. Ltd., New Delhi, pp.211-231.
- Kumar, S., 2012. Copper-chromium alloy as a superior electrode material for electrical discharge machining of die steels. *International Journal of Materials Engineering Innovation*, 3, pp.316-329.
- Lee, S.H. and Li, X.P., 2001. Study of the effect of machining parameters on the machining characteristics in electrical discharge machining of tungsten carbide. *Journal of Materials Processing Technology*, 115(3), pp.344-358.
- Lin, J.L. and Lin, C.L., 2002. The use of the orthogonal array with grey relational analysis to optimize the electrical discharge machining process with multiple performance characteristics. *International Journal of Machine Tools and Manufacture*, 42(2), pp.237-244.
- Muthuramalingam, T. and Mohan, B., 2015. A review on influence of electrical process parameters in EDM process. *Archives of Civil and Mechanical Engineering*, 15(1), pp.87-94.
- Patil, K.K. and Jadhav, V.D., 2016. Study of machining parameters in EDM. *International Journal for Research in Applied Science and Engineering Technology*, 4(1), pp.72-78.
- Ramabalan, J.J. and S., 2015. Die sinking edm process parameters: A review. *International Journal of Engineering and Robotics Research*, 4(1), pp.315-326.
- Shyha, I. and Rudd, M., 2016. Electro-discharge machining of metal matrix composite materials. *Advances in Materials and Processing Technologies*, 2(2), pp.235-244.
- Singh, K., 2018. Optimization of process parameters of powder mixed EDM for high carbon high chromium alloy steel (D2 steel) through GRA approach. *Grey Systems: Theory and Application*, 8(4), pp.388-398.
- Singh, P.N., Raghukandan, K. and Pai, B., 2004. Optimization by grey relational analysis of EDM parameters on machining Al-10%SiCp composites. *Journal of Materials Processing Technology*, 155, pp.1658-1661.
- Venkatesh, B., Naveen, P., Maurya, B. and Priya, D.S., 2015. Experimental investigation of Edm using electrode materials copper, brass and chromium copper for alloy steels. *International Journal of Advance Engineering and Research Development*, 2(4), 1-12.
- Yerui, F., Yongfeng, G. and Zongfeng, L., 2016. Experimental investigation of EDM parameters for TiC/Ni cermet machining. *Procedia Cirp*, 42, pp.18-22.

Assessment of the Upstream Slope Stability of Darbandikhan Rockfill Dam during Drawdown

Sirwan Gh. Salim¹ and Krikar M. G. Noori²

¹Department of City Planning, Technical College of Engineering, Sulaimani Polytechnic University, Sulaymaniyah, Kurdistan Region – F.R. Iraq

²Koya Technical Institute, Erbil Polytechnic University, Koya, Kurdistan Region – F.R. Iraq

Abstract—Earth and rockfill dams face a variety of loading conditions during lifetime. One of the most critical loading conditions is the rapid drawdown of water level after steady state conditions. Rapid drawdown may cause instability of upstream slope of the dam. The present work examines the stability of a rockfill dam under different drawdown rates in terms of factor of safety for the upstream slope of the dam. For this purpose, a computer software named GeoStudio 2012 SEEP/W and SLOPE/W has been used for the numerical analysis. The results showed that the drawdown rate has a significant effect on stability of rockfill dam in which increasing the drawdown rate from 1 m/day to 10 m/day decreases the stability of the dam by 33%. Based on the outcomes, for the studied case the drawdown rate (1 m/day) can be recommended.

Index Terms—Drawdown rate, Earth/Rockfill dam, Factor of safety, GeoStudio 2012, Pore water pressure

I. INTRODUCTION

Many partial or total failures of earth/rockfill dams have been recorded around the globe as a result of prompt lowering of reservoir level; the most famous case was San Luis Dam in California. The dam was among the largest earth dams in the world (height = 100 m, length = 5500 m). The dam was safe for several years during normal steady state operation. Upstream slide happened in 1981 due to fast drawdown of water to nearly mid-height of the dam (Sica, Pagano and Rotili, 2019; Alonso and Pinyol, 2009). During steady state, the water in the reservoir is at normal level, this condition helps the stabilization of upstream slope. When, it is necessary to drawdown the water quickly for emergency case or any operation reason, the upstream slope subjects one of the critical conditions that need a comprehensive study on

stability of the dam (Alonso and Pinyol, 2009; Siacara, Beck and Futai, 2020).

Rapid drawdown of water has two impacts; changing the pore water pressure of the dam materials and reducing the external hydrostatic pressure (Siacara, Beck and Futai, 2020). Reduction of water level may cause instability of the dam since the water inside the soil cannot escape from the soil as the water drawdown from the reservoir (Siacara, Beck and Futai, 2020; Pinyol, Alonso and Olivella, 2008). There are some factors which affect the stability of upstream slope under drawdown conditions such as hydraulic conductivity and mechanical properties of soil, side slope ratio, and the rate of reducing water level (Siacara, Beck and Futai, 2020; Souliyavong, et al., 2012; Fattah, Omran and Hassan, 2015; Tatewar and Pawade, 2012).

Gao, et al. (2013) prepared stability charts to find factor of safety more precisely for 3D slopes during four rapid drawdown scenarios based on the kinematic approach of limit analysis. Sica, Pagano and Rotili (2019) pointed out that specifying the maximum drawdown rate which a dam can be experienced during its life safely is very important particularly for those dams located near to the earthquake prone areas.

In this paper, two-dimensional numerical analysis to study the behavior of a high rockfill dam in Kurdistan was adopted using GeoStudio 2012 software, which has a great importance for electricity generation, water supply, irrigation, and flood control. The embankment is one of the largest dams in Kurdistan named Darbandikhan rockfill dam. One of the incentives of adopting this study is that the dam authority may be obligated to evacuate the reservoir for inspection and maintenance of the dam especially after the earthquake. Therefore, this paper presents the safe drawdown rate for Darbandikhan dam that the dam's authority can apply.

II. METHODOLOGY AND MODELING

The research is carried out to study the stability of the upstream dam slope during drawdown and analysis of transient seepage condition to determine the pore water pressure.

ARO-The Scientific Journal of Koya University
Vol. IX, No.1 (2021), Article ID: ARO.10678, 8 pages
DOI: 10.14500/aro.10678

Received 16 May 2020; Accepted: 25 January 2021

Regular research paper: Published: 01 March 2021

Corresponding author's e-mail: krikar.noori@epu.edu.iq

Copyright © 2021 Sirwan Gh. Salim and Krikar M.G. Noori.

This is an open-access article distributed under the Creative Commons Attribution License.



A. Seepage Analysis Theory

The fundamental flow laws for steady state and transient condition based on Darcy’s law, in this regard, SEEP/W is formulated on the basis that the flow of water through both saturated and unsaturated soil follows Darcy’s equation (SEEP/W, 2012; Rulon and Freeze, 1985). The general governing differential equation for two-dimensional seepage can be expressed as:

$$\frac{\partial}{\partial x} \left(k_x \frac{\partial H}{\partial x} \right) + \frac{\partial}{\partial y} \left(k_y \frac{\partial H}{\partial y} \right) + Q = \frac{\partial \theta}{\partial t} \quad (1)$$

Where H = total head, k_x = hydraulic conductivity in the x direction; k_y = hydraulic conductivity in y -direction; Q = applied boundary flux; θ = volumetric water content; and t = time.

B. Slope Stability Analysis Theory

Limit equilibrium analysis methods have been applied in solving geotechnical engineering problems for many years to evaluate the stability of embankment slopes. In this regard, applying SLOPE/W uses the theory of limit equilibrium of forces and moments, stability analysis of embankment dam can be accomplished to determine the critical failure surface and compute the values of factor of safety against failure (SLOPE/W, 2012).

The slope stability is governed by upward resisting forces and downward mobilized forces. The relative stability of slope is characterized by the term factor of safety (FOS). The factor of safety is expressed as that factor by which the shear strength of the soil must be reduced to bring the mass of soil into a state of limiting equilibrium along a selected slip surface, and defined as:

$$FoS = \frac{\sum S_{resisting}}{\sum S_{mobilised}} \quad (2)$$

Shear strength (resistance):

$$S_{resisting} = c' + (N - u) \tan \phi' \quad (3)$$

Shear mobilized:

$$S_{mobilised} = W \sin \alpha \quad (4)$$

where: c' = effective cohesion, ϕ' = effective angle of internal friction, $N = W \cos \alpha$ total normal stress, and u = pore-water pressure. W = the slice weight, α = base inclination.

In this study, various limit equilibrium methods such as the methods of Bishop (Bishop, 1955) (Bishop and Morgenstern, 1960), Morgenstern-Price (Morgenstern and Price, 1965), (Janbu, 1954) (Janbu, 1968), and Swedish Ordinary (or Fellenius method) (Fellenius, 1936) have been used to analyze the slope of the embankment dam during drawdown conditions. Fig. 1 illustrates all the forces acting on a circular slip surface.

Reference can be made to Fig. 1, the factor of safety with respect to moment equilibrium and horizontal force equilibrium, respectively, is:

$$FoS_m = \frac{\sum (c' \beta R + (N - u \beta) R \tan \phi')}{\sum W_x - \sum N_f + \sum kW_e \pm \sum D_d \pm \sum A_a} \quad (5)$$

$$FoS_f = \frac{\sum (c' \beta \cos \alpha + (N - u \beta) \cos \alpha \tan \phi')}{\sum N \sin \alpha + \sum kW - \sum D \cos \omega \pm \sum A} \quad (6)$$

C. Case study: Darbandikhan Rockfill Dam

Darbandikhan dam is a multi-applications embankment dam, located on the Diyala-Sirwan River approximately 65 km southeast of Sulaimani City in Kurdistan (coordinates at 35°06'46"N , 45°42'23"E) (Tourism of Kurdistan, 2020). The Darbandikhan dam is a rock-fill embankment type with a central clay core on a foundation of sedimentary rocks. The dam height is 128 m, its crest width is 17 m, and the width of the base is 513 m, whereas the crest length is 445 m (535 m if the spillway section is included) (Davis and ASCE, 1958). The material properties of the rockfill dam components are summarized in Table I, whereas the dam cross-section shown in Fig. 2.

D. Numerical Modeling

To investigate the stability of dam upstream slope during drawdown and analysis of transient seepage condition to determine the pore water pressure, the dam was simulated. Using the numerical analysis of SEEP/W and SLOPE/W in GeoStudio 2012 software and having the geometrical and mechanical characteristics of the dam, two-dimensional modeling of Darbandikhan rockfill dam was performed. The study was carried out to examine the effects of the reservoir water level drawdown in different time periods (5 days, 10 days, 25 days, and 51 days) (drawdown rate DDR 10.2 m/day, 5.1 m/day, 2 m/day, and 1 m/day), respectively,

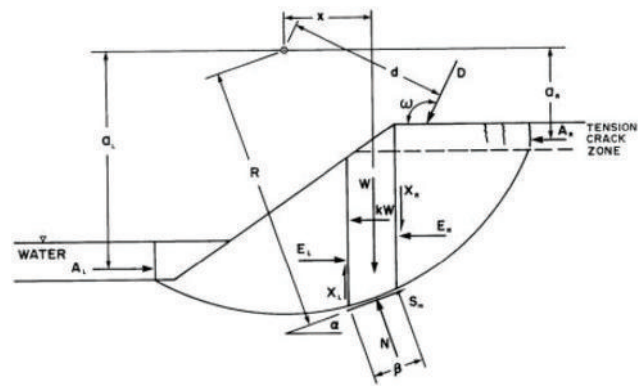


Fig. 1. Forces acting on a slice through a sliding mass with a circular slip surface (SLOPE/W, 2012).

TABLE I
MATERIAL PROPERTIES OF DARBANDIKHAN ROCKFILL DAM
(DAVIS AND ASCE, 1958).

Materials	Permeability (m/s)	Density (KN/m ³)	Cohesion (Kpa)	Friction angle (degrees)
Core	1×10 ⁻⁹	18.7	108	13
Shell	1×10 ⁻⁵ *	20*	10	38
Filter	1×10 ⁻⁴ *	20*	0	38*

*Means data were assumed

and to determine the factor of safety and pore water pressure on the dam upstream slope using various limit equilibrium methods such as Bishop's method, Morgenstern-Price, Janbu, and Swedish Ordinary method. It should be mentioned that the maximum water level drawdown is almost 51 m, from normal operating level (elevation 485m) drawdown to maximum drawdown level (elevation 434 m) (Davis and ASCE, 1958).

The finite element mesh of the rockfill dam in SEEP/W was used to replicate the structure of the dam. The program generates a well behaved of unstructured pattern of quadrilateral and triangular elements with 4 and 3 nodes, respectively, Fig. 3. The reservoir level at the dam 10 m below the crest was defined as constant total head boundaries with the values of 118 m. In the analysis of transient seepage condition, results from steady-state seepage were applied as parent to define the initial pore-water pressure distribution in SLOPE/W. The upstream boundary condition was defined by a total head function to numerically simulate the reservoir drawdown. In this type of boundary, the total head is defined as a function of time and was decreased linearly from 118 m to 67 m at different rates of the reservoir

drawdown. Furthermore, to examine the stability of the dam upstream slope during drawdown, the general limit equilibrium method presented in SLOPE/W was used. In the present study, the entry and exit slip surface method was employed to define trial failure surfaces for each modeling case. To obtain a minimum factor of safety in a critical surface for each drawdown scenario, the program analyzed all the trial surfaces.

III. RESULTS AND DISCUSSION

In the present study, to examine the effects of the reservoir drawdown with different time periods and drawdown rates on the stability of the upstream slope of Darbandikhan rockfill dam, the factor of safety and pore water pressure were calculated by Morgenstern-Price, Bishop, Janbu, and Ordinary method. Fig. 4 displays the critical slip surface and factor of safety after drawdown (DDR 5.1 m/day).

Overall, the factor of safety of the upstream slope decreased under the effect of drawdown over the period given, whereas for the last step at the end of the period, there is a little

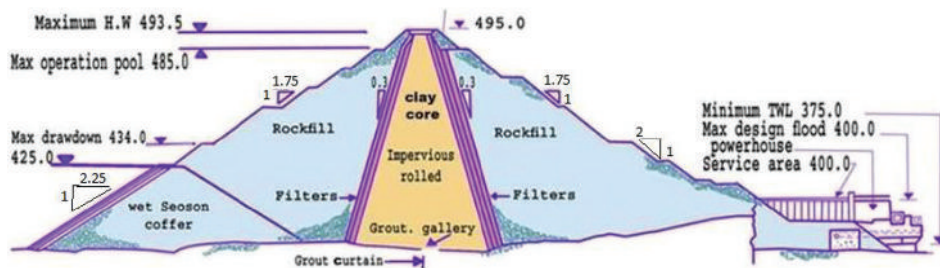


Fig. 2. Cross section of Darbandikhan rockfill dam (Davis, and ASCE, 1958).

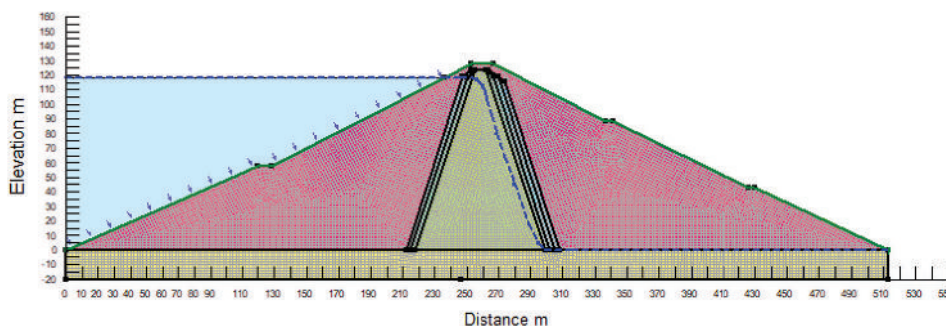


Fig. 3. SEEP/W finite element mesh of Darbandikhan rockfill dam.

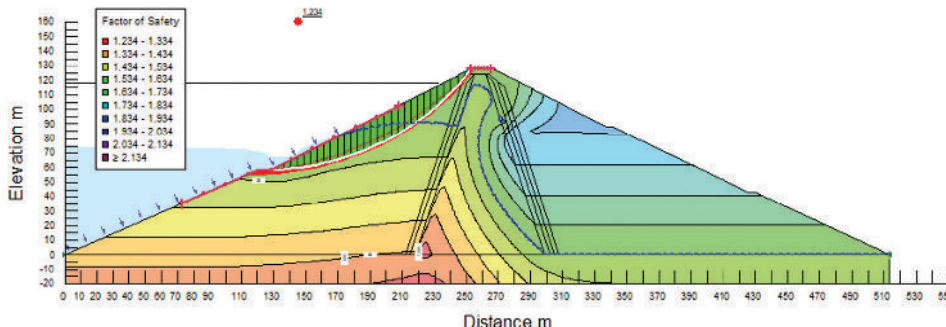


Fig. 4. Critical slip surface and factor of safety after drawdown (DDR 5.1m/day) using Morgenstern-price method.

increasing almost in all methods, this is due to the dissipation of the pore-water pressure in the embankment with time. The achieved outcomes considerably show that drawdowning the 51 m of the reservoir level rapidly in a short period, for example, 5 days provided a lower factor of safety of the dam slope stability compared to the slowly drawdowning the upstream reservoir

over a long period 51 days for all analysis methods. According to the results, the Morgenstern-Price method provides the higher factor of safety in comparison with the other methods and Janbu method affords the lowest factor of safety, Fig. 5.

As shown in Fig. 6, the results for the Morgenstern-Price and Bishop methods are quite similar, the initial factor of

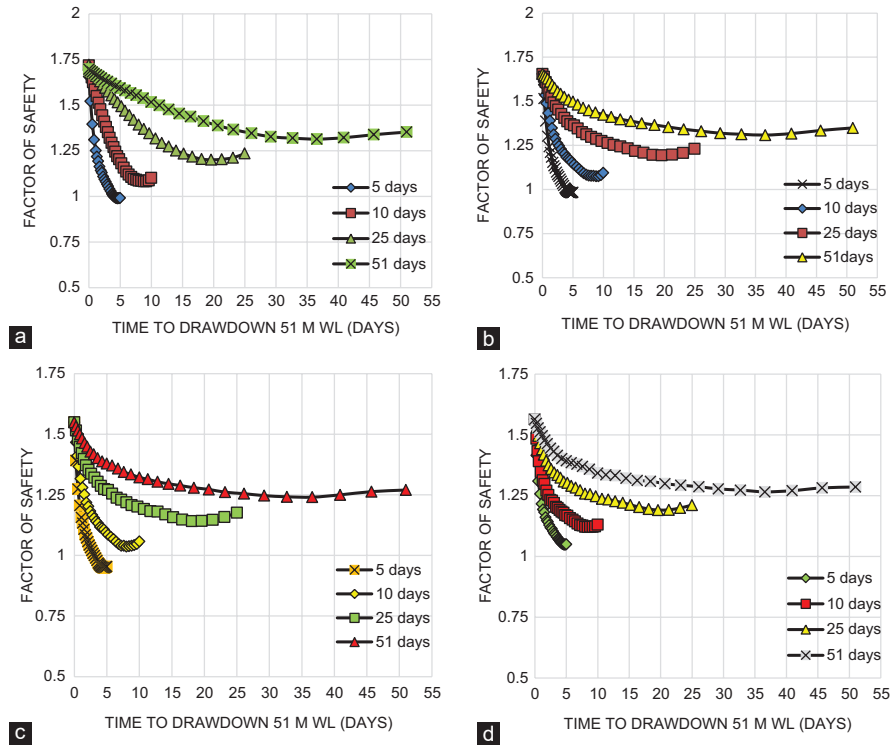


Fig. 5. Factor of safety for the reservoir drawdown with different times, analyzed by (a) Morgenstern-price (b) Bishop, (c) Janbu, and (d) Ordinary method.

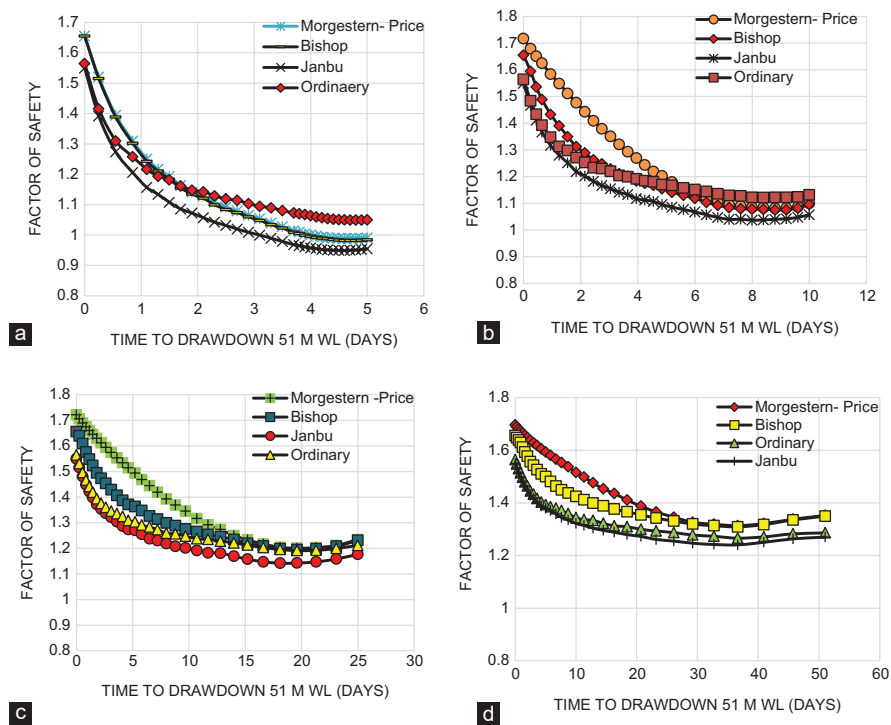


Fig. 6. Comparison of the factor of safety for the reservoir drawdown with time (a) DDR 10.2m/day (b) 5.1 m/day (c) 2m/day, and (d) 1m/day

safety began at around 1.7 in average and then gradually reduced after rapidly drawdowning 51 m of the water level in 5 days, reaching nearly 0.98 at the end of the period for both methods. Likewise, approximately 1.55 was the initial factor of safety for the rest of methods (Janbu and Ordinary), and then decreased steadily until reached slightly above 1 for Ordinary and somewhat below 1 for Janbu method at the last time of the period. In comparison, the slower drawdowning of the reservoir level, the higher the factor of safety of the dam upstream slope will be observed.

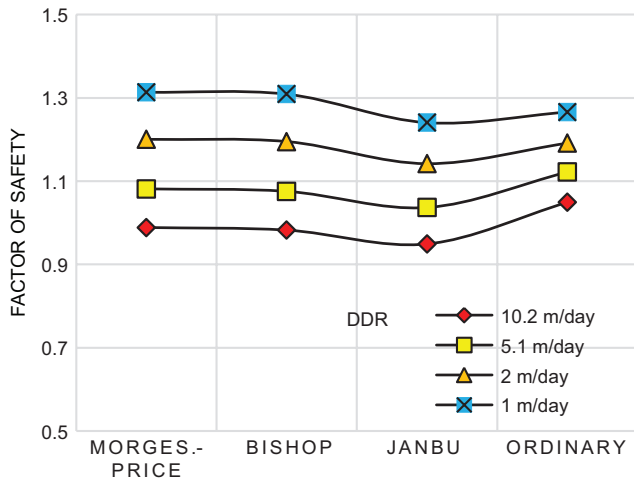


Fig. 7. Minimum value factor of safety within the critical slip surface for upstream slope with various drawdown rates for all methods.

The minimum value factor of safety within the critical slip surface for the embankment upstream slope with various drawdown rates shown in Fig. 7. Based on the obtained results, the DDR 10.2 m/day gave a factor of safety of upstream slope lower than 1 for all analysis methods except Ordinary method provided a value of factor of safety slightly above 1. This is unacceptable outcome compared to the guide line of the minimum required factor of safety for the upstream slope during drawdown, Table II. The calculated values of the 1 m/day and 2 m/day of drawdown rate presented the stability of the upstream slope with a factor of safety ranging from 1.2 to 1.3, whereas the result for the drawdown rate of 5.1 m/day was questionable which was on average 1.1.

During rapid drawdown, the influence of the steady water on the upstream side disappeared, whereas the pore water pressure within the dam may stay high, Fig. 8. Accordingly,

TABLE II
GUIDELINE OF MINIMUM REQUIRED FACTOR OF SAFETY
(NOVAK, ET AL. 2001)

Design loading condition	Minimum factor of safety	
	Downstream slope	Upstream slope
1. During and at end of construction	1.25	1.25
2. Long-term operational, reservoir full	1.5	1.5
3. Rapid drawdown	-	1.2
4. Seismic loading with 1, 2, or 3 above	1.1	1.1

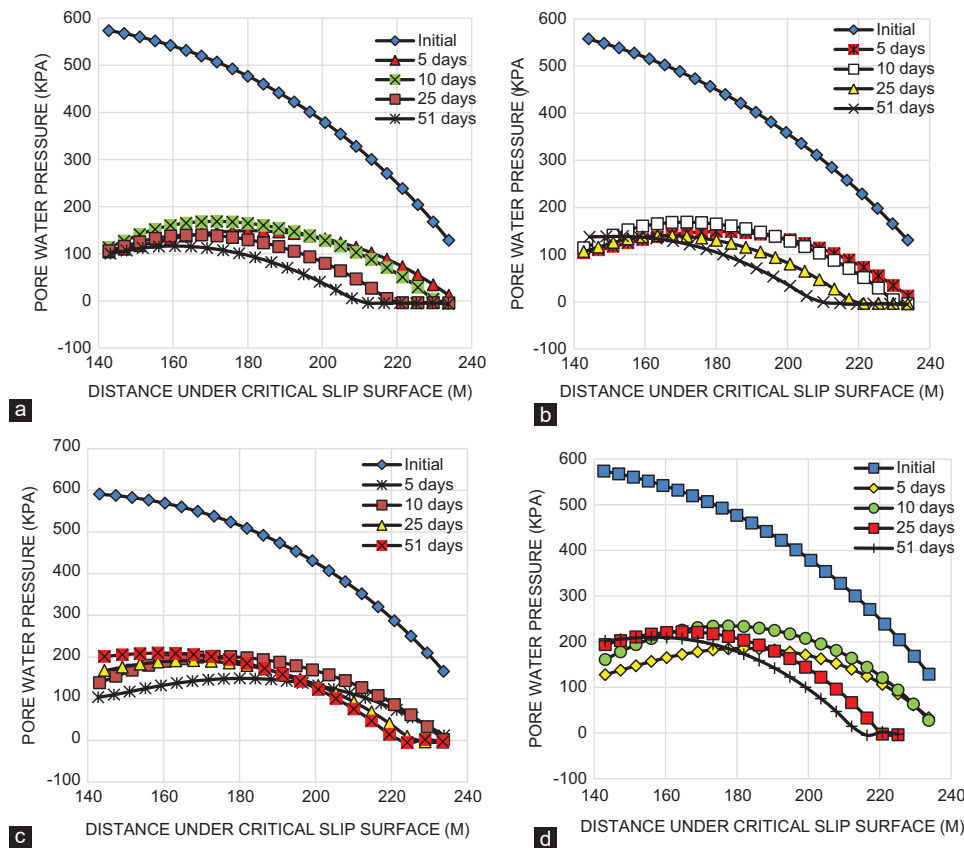


Fig. 8. Difference of pore water pressure within the drawdown period by (a) Morgenstern-price, (b) Bishop, (c) Janbu, (d) Ordinary method.

the stability of the upstream slope of the embankment can be greatly declined, because the hydrodynamic pressure generates the tensile downward forces, resulting in a reduction of the shear strength (resistance) of the upstream face. In addition, shear mobilizing of the upstream face

increased because there is not enough resisting force against it. Therefore, based on Eq. (3), the dissipation of pore water pressure increases the shear resistance of the dam materials. The pore water pressure within the materials can reduce to a negative value and creates suction force during the dissipation process, and thus the slope stability increases. Figs. 9 and 10 display difference between shear mobilized and shear resistance of the critical slip surface of upstream slope after drawdown for initial condition, DDR 10.2 m/day, and DDR 1 m/day, respectively (Souliyavong, et al., 2012; Fattah, Omran and Hassan, 2015; Duncan, Wright and Wong, 1990; Abbas, Aljanabi and Mutiny, 2017).

Consequently, to increase the safety and stability of the upstream slope of the dam, the dissipation of pore water pressure from the saturated zone within the materials should have adequate time, hence, the low drawdown rate tolerates more time because the shear resistance of the dam materials subjected to a lower drawdown rate is more than that of the dam at a higher drawdown rate.

So that to determine the effect of drawdown rate on the pore water pressure in different locations, three critical points in the upstream slope of the dam have been set almost on the critical slip surface, Fig. 11. The Morgenstern-Price method was used to model and analyze the problem. The variation of pore water pressure with time throughout drawdown in the reservoir at points 1, 2, and 3 is shown in Fig. 12. It can be seen that the pore water pressure at all points decreases almost linearly with time. The dissipation of pore water pressure in the embankment is thus crucial and approximately affected by the permeability of the embankment materials.

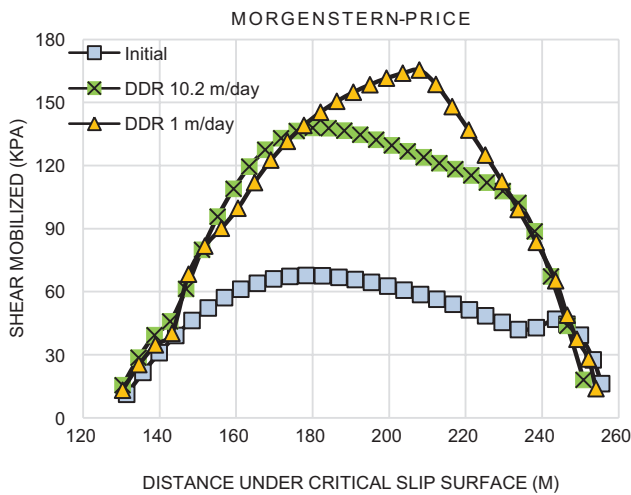


Fig. 9. Variation of shear mobilized of the critical slip surface of upstream slope after drawdown.

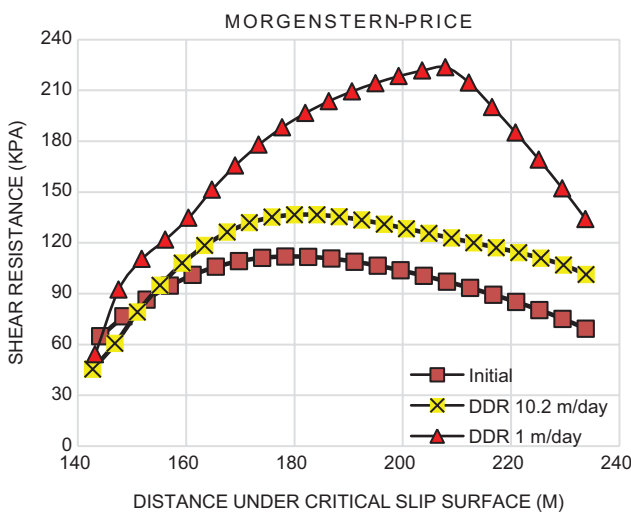


Fig. 10. Variation of shear resistance of the critical slip surface of upstream slope after drawdown.

IV. CONCLUSION

In this study, the geometrical and geotechnical properties of Darbandikhan rockfill dam as a case study, using GeoStudio 2012 software, SEEP/W, and SLOPE/W, were investigated. To examine the stability of the dam upstream slope, the effects of different drawdown rates (DDR 10.2 m/day, 5.1 m/day, 2 m/day, and 1 m/day), using various analysis methods, were studied.

In conclusion, the factor of safety of the upstream slope decreased under the effect of drawdown over the periods

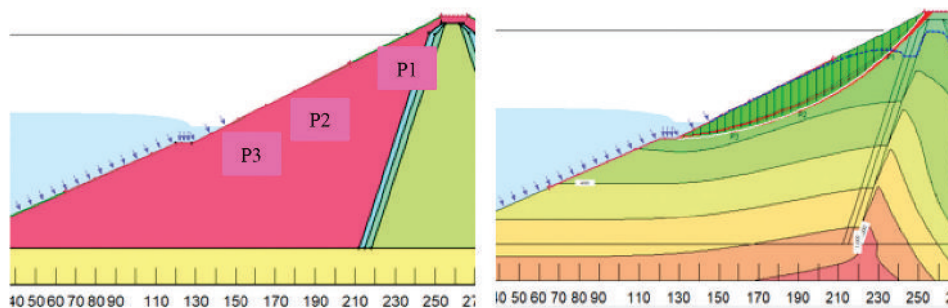


Fig. 11. Location of critical points in the upstream slope of the dam almost on the critical slip surface.

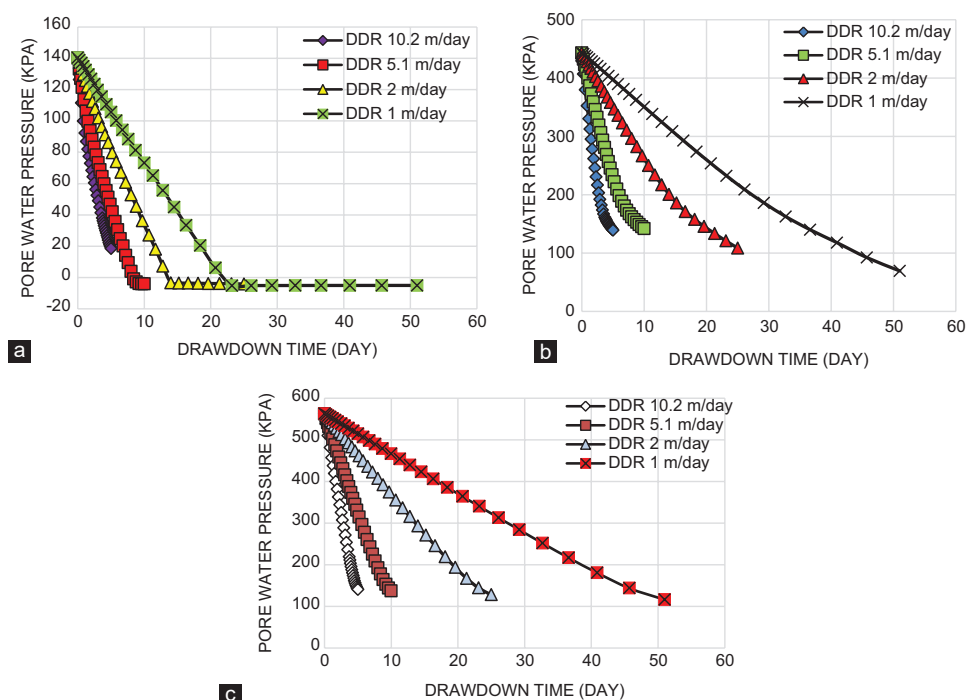


Fig. 12. Pore water pressure variation with time during drawdown in the reservoir at (a) point 1, (b) point 2, and (c) point 3, Morgenstern-Price method.

given. Respect to the Morgenstern-Price method, higher factor of safety in comparison with the other methods were observed, whereas the lowest factor of safety was based on Janbu method. The stability of the upstream slope increases with decreasing the rate of drawdowning water level in the reservoir. Whereas the rapid drawdown gave a lower factor of safety of the dam slope stability, and this is due to that the pore water pressure remaining high in the soil and taking time to dissipate which leads to increasing in shear mobilizing and decreasing the soil shear resistance. Consequently, the low drawdown rate allows more time to squeeze water and then increases the stability of the slope.

The results of this study reveal that the rapid drop of water in the reservoir is most dangerous case for upstream slope because the pore water pressure cannot dissipate quickly and leads to instability of the dam upstream face. Therefore, for the examined case, the drawdown rate 1 m/day would be suggested.

REFERENCES

- Abbas, J.M., Aljanabi, Q.A. and Mutiny, Z.A., 2017. Slope stability analysis of an earth dam. *Diyala Journal of Engineering and Science*, 10(1), pp.106-117.
- Alonso, E. and Pinyol, N., 2009. *Slope Stability Under Rapid Drawdown Conditions*, Barcelona.
- Bishop, A.W. and Morgenstern, N., 1960. Stability coefficients for earth slopes. *Geotechniques*, 4(10), pp.164-169.
- Bishop, A.W., 1955. The use of slip circle in the stability analysis of slopes. *Geotechniques*, 1(5), pp.7-17.
- Davis, C.V. and Asce, M., 1958. *Rockfill Dam, the Derbandi Khan Dam, Portland, Oregon*.
- Duncan, J.M., Wright, S.G. and Wong, K.S., 1990. *Slope Stability during Rapid Drawdown*.
- Fattah, M.Y., Omran, H.A. and Hassan, M.A., 2015. Behavior of an earth dam during rapid drawdown of water in reservoir-case study. *International Journal of Advanced Research*, 3(10), pp.110-122.
- Fellenius, W., 1936. *Calculation of Stability of Earth Dams*, pp.445-463.
- Gao, Y.F., Zhang, F., Lei, G.H. and Li, D.Y., 2013. An extended limit analysis of three-dimensional slope stability. *Geotechnique*, 6(63), pp.518-524.
- Janbu, N., 1954. *Applications of Composite Slip Surfaces for Stability Analyses*, *Stockhol*, pp.39-43.
- Janbu, N., 1968. *Slope Stability computations*. Technical University of Norway, Trondheim.
- Morgenstern, N.R. and Price, V.E., 1965. The analysis of the stability of general slip surfaces. *Geotechnique*, 1(15), pp.79-93.
- Novak, P., Moffat, A., Nalluri, C. and Narayanan, R., 2001. *Hydraulic Structures*. Spon Press, London.
- Pinyol, N.M., Alonso, E.E. and Olivella, S., 2008. Rapid drawdown in slopes and embankments. *Water Resources Research*, 44, pp.1-22.
- Rulon, J.J. and Freeze, R.A., 1985. Multiple seepage faces on layered slopes and their implications for slope stability analysis. *Canadian Geotechnical Journal*, 22, pp.347-356.
- SEEP/W, 2012. *GEO-SLOPE International Ltd., Seepage Modeling with SEEP/W 2012: An Engineering Methodology*. 6th ed. GEO-SLOPE International Ltd., Alberta.
- Siacara, A.T., Beck, A.T. and Futai, M.M., 2020. Reliability analysis of rapid drawdown of an earth dam using direct coupling. *Computers and Geotechnics*, 118, pp.1-16.
- Sica, S., Pagano, L. and Rotili, F., 2019. Rapid drawdown on earth dam stability after a strong earthquake. *Computers and Geotechnics*, 116, p.103187.

SLOPE/W, 2012. *GEO-SLOPE International Ltd., Stability Modelling with SLOPE/W 2012: An Engineering Methodology*. 6th ed. GEO-SLOPE International Ltd., Alberta.

Souliyavong, T., Gallage, C., Egodawatta, P. and Maher, B., 2012. *Factors Affecting the Stability Analysis of Earth Dam Slopes Subjected to Reservoir Drawdown, Kuala Lumpur*, pp.507-512.

Tatewar, S.P. and Pawade, L.N., 2012. Stability analysis of earth dam by geostudio software. *International Journal of Civil Engineering and Technology*, 3(1), pp.437-446.

Tourism of Kurdistan, 2020. *Official Site of General Board of Tourism of Kurdistan-Iraq*. Available from: <http://www.bot.gov.krd/sulaimaniya-province/darbandikhan>. [Last accessed on 2020 Apr 01]

Effect of Sand Percentage on the Compaction Properties and Undrained Shear Strength of Low Plasticity Clay

Iyad Alkroosh¹, Ali Al-Robay¹, Prabir Sarker² and Saif Alzabeebee³

¹Department of Civil Engineering, College of Engineering,
University of Al-Qadisiyah, Al-Qadisiyah, Iraq

²School of Civil and Mechanical Engineering,
Curtin University, WA, Australia

³Department of Roads and Transport Engineering, College of Engineering,
University of Al-Qadisiyah, Al-Qadisiyah, Iraq

Abstract—This paper investigates the influence of sand content on the mechanical behavior of a low plasticity clay that collected from south of Iraq (Sumer town). Samples have been prepared with sand contents of 0%, 10%, 20%, 30%, and 40% of the clay weight. Standard Proctor and unconfined compression tests have been carried out and the optimum moisture content, maximum dry density, and undrained shear strength have been determined. The results show a gradual increasing trend of the maximum dry density with the increase of the sand content up to 30%. The highest dry density reaches 1.90 g/cm³ corresponding to an optimum moisture content of 12%. In addition, this paper shows that the undrained shear strength is inversely proportional to the increase of the percentage of sand. The results of this work provide a useful addition to the literature regarding the behaviour of low plasticity clay-sand mixture.

Index Terms—clay sand mixture, low plasticity, optimum moisture content, undrained shear strength.

I. INTRODUCTION

Soil beneath building foundations are often made up of layers of clay or sand or both. The clay occasionally exists in a form described as low or high plasticity clay which is often characterized by low strength and high compressibility (Das, 2010; Cabalar et al., 2018; Ghanizadeh et al., 2020). Due to these undesirable properties, clayey soils may be considered unsuitable for supporting foundations. Building on clayey soil usually needs dredging and replacement of the clay by stronger soils. Alternately, soil improvement techniques need

to be adopted when it is difficult and costly to conduct soil replacement.

Improvement of clay properties can be achieved by compaction or with the addition of other suitable materials. Compaction is a commonly used method to improve the mechanical properties of soil supporting foundations. It is also considered as a favorite method extensively used to improve subgrade for highway embankments, earth dams, and many other engineering structures (Das, 2010). The compaction involves soil densification by removing air with application of mechanical energy. The main advantage of this process is the increase of bearing capacity and reduction of the undesirable settlements of structures (Bowles, 1996).

Dynamic compaction was found to be useful for improving the engineering properties of soft to medium clays and silts (Narendranathan and Lee, 2013). However, compaction does not always bring satisfactory results, particularly when the compacted soil is soft clay. For instance, compacted soils of quarries were often rejected because they failed to meet the minimum limit of dry density specified by the Iraqi general specifications for roads and bridges (Ministry of housing and construction, 2003). Consequently, huge earth quarries of such soil were abandoned making the contractor bear additional cost and efforts. Therefore, addition of suitable materials is considered when compaction of clays does not yield satisfactory results.

Addition of materials to improve the physical properties of clayey soils has received the attention of many researchers. Khemissa and Mahamedi (2014) proved significant increase in strength and durability of expansive over-consolidated clay when 8% of cement and 4% of lime were added to the clay. Garzón et al. (2015) concluded that the composites of phyllite clay and cement improved the engineering properties including plasticity index, maximum dry density, unconfined shear strength, and coefficient of permeability. Mixing of clay with a percentage of sand usually improves the density and strength characteristics of clay. Several researchers attempted studies investigating into the behavior of clay-sand mixtures

ARO-The Scientific Journal of Koya University
Vol. IX, No.1 (2021), Article ID: ARO.10748, 5 pages
DOI:10.14500/aro.10748

Received: 14 November 2020; Accepted: 01 February 2021
Regular research paper: Published: 01 March 2021

Corresponding author's e-mail: saif.alzabeebee@qu.edu.iq
Copyright © 2021 Iyad Alkroosh, Ali Al-Robay, Prabir Sarker, Saif Alzabeebee. This is an open-access article distributed under the Creative Commons Attribution License.



and reported improved properties. Shafiee et al. (2008) investigated the undrained behavior of compacted sand-clay mixtures under monotonic load and found that the addition of sand improved the undrained shear strength. Khan et al. (2014) studied the influence of adding 20–40% of sand to natural clay of high plasticity and reported an increase in clay density and compressive strength. Kim et al. (2016) reported that for mixtures of sand and high plasticity clay, the cyclic shear strength of low-density mixtures increased and that of high-density mixtures decreased with the increase of fines content. Deng et al. (2017) studied the effect of sand fraction on the hydro-mechanical behavior of sand-clay mixture utilizing oedometer compression test. They found that the compression response was remarkably different for the from that of common clays, where the compression behavior of the clay-sand mixture deviated from that of normal clay for the cases with vertical compression stress equal to or more than 400 kPa.

Procter test and unconfined compression strength test are commonly carried out to evaluate the quality of the improved soil. The Procter test is usually undertaken to determine the maximum dry density of compacted soil specimens. The ratio of field to laboratory densities indicates whether or not the field compaction achieved an acceptable level. The unconfined compression test is useful for estimating the undrained bearing capacity of fine-grained soil for foundations, stability of slopes, and determining the stress-strain characteristics under undrained conditions (Budhu, 2010, Benmebarek et al., 2017, Khitas et al., 2020). It is also used for design of road embankments, shallow foundations, and retaining walls (Holtz et al., 2011).

This study investigated the effect of the percentage of sand on the density of compacted clay to improve understanding of the influence of adding the sand on the mechanical response of the clay. In addition, the undrained shear strength of the compacted clay was also investigated for samples prepared at the optimum moisture content and maximum dry density for each mixing sand percent to aid understanding of the influence of the sand percentage on the undrain response of the low plasticity clay and also provide parameters that are useful for future numerical studies on the topic (Alzabeebe, 2014).

II. METHODOLOGY

A. Site and Sample Collection

A sampling site was selected which has the same soil properties as those of the rejected quarries. To determine a suitable site for sample collection, technical advice was sought from professional consultants who are experts in soil investigations business in the region of the middle provinces of Iraq. Sumer town, which is located at 30 km north east of Al-Diwaniyah city, was determined as an ideal site for sample collection. A review of the reports of past site investigations in the area found that the type of clay in demand usually exists at a depth of 1.0 m below the ground surface. This study adopted the American Society for Testing and Materials (ASTM) practice for soil investigation and

sampling (ASTM D1452/D1452M-16, 2016). A hand auger, shovel, and manual digging accessories were used to dig the ground to reach the sampling depth. A soil of clayey nature began to appear from a depth of 0.7 m. Initial evaluation was made to the excavated soil in the field by visual inspection and a simple field test. The soil showed sticky behavior when water was added to it and thus it was concluded that the soil is clay (Budhu, 2011). The excavated soil sample was grey in color, had a homogeneous structure, and could be easily molded by fingers. The samples were transported to the Soil Mechanics Laboratory of College of Engineering, University of Al-Qadisiyah as per standard practice for preserving and transporting soil samples (ASTM D4220/D4220M-14, 2014).

B. Laboratory Work

Soil sample classification

After the initial evaluation of the extracted sample by field test, it was evaluated further in the laboratory to ensure that the sample was clay of low plasticity. The plasticity test was carried out to determine the type of soil sample. In this test, a relationship between liquid limit and plasticity index was defined. The liquid limit and plastic limit tests were performed as per the ASTM D4318-17e1 (2017) and the unified soil classification system (USCS) was adopted to classify the soil sample (ASTM D2487-17, 2017).

Removing coarse particles from the sample

Although the collected soil sample is evaluated as clayey soil, a percentage of coarse particles were expected to exist in the sample. To obtain a purely fine-grained soil, the sample was sieved and then washed on the sieve # 200. The passing solution was collected in a bowl and then placed in an oven with a temperature of 100°C for 24 h to remove the water. It was found that the percentage of the soil passing sieve # 200 is more than 95%.

Preparing sand fraction

The sand used in this study was available locally. It was brought from Al-Najaf Province which usually supplies sand as a construction material to most regions in Iraq. Based on the ASTM D2487-17 (2017), USCS defines sand as a portion of soil particles that pass sieve #4 (4.75 mm) and retained on sieve # 200 (75 µm). Usually, sand contains a percentage of coarse particles of size larger than 4.75 mm and fine particles of size smaller than 0.075 mm. To collect the sand grains only, an amount of soil was sieved as per the standard test method for sieve analysis of soils (ASTM D6913/D6913M-17, 2017). The particles passing through sieve # 4 and retaining on sieve # 200 were used in the subsequent tests.

Compaction test

The soil sample was compacted using standard Proctor's compaction tests in accordance with the ASTM D698-12e2 (2012), Method A to determine its maximum dry density and optimum moisture content. The test was carried out on the sample that contains zero percentage of sand and then on samples with 10%–40% of sand. The sand fraction was added as a percentage by weight varying in 10% increment. Before the test, measurements of the mold dimensions and

its weight with the baseplate were recorded. The soil sample was prepared by adding an amount of water to the dry sample and then mixing it thoroughly to get a consistent distribution of the moisture. The sample was then compacted in Proctor’s mold of 100 mm diameter and 117 mm height. The sample was placed in the mold in three layers and each layer was knocked by 25 blows distributed evenly on its surface using a standard rammer which weighs 2.5 kg and falls off from a height of 300 mm. Then, the mold and the compacted soil with the base plate were weighed. A sample was taken from the core of the compacted specimen for determination of the moisture content in accordance with the ASTM standard (ASTM D2216-19, 2019). This process was continued until the weight of the compacted soil began to drop.

Unconfined compression test

This test is usually used to determine the undrained shear strength of the soil. It was also used by previous studies to investigate the shear strength of the soil (for example, Javdanian, 2017; Toufigh and Rahmanned, 2018; Manimaran et al., 2019). Therefore, this test is used in this study to determine the influence of adding the sand on the undrained shear strength of the clayey soil. The test was conducted, according to the ASTM D2166/D216 6M- 16 (2016). The samples used in the test were extracted from the compacted soil specimen in Proctor’s mold at the optimum moisture content. A steel tube of dimensions 35 mm in diameter and 76 mm in height, which is specified for the test sample, was pushed into the compacted soil sample, and pulled off with unconfined compression test sample. The sample was then extracted from the tube using the sample extruder and placed in the test frame based on the standard test method (ASTM D2166/D2166M-16, 2016). After that, a vertical stress was applied on the sample and the produced settlement was measured. The peak stress was considered as the undrained shear strength of the soil.

III. RESULTS AND DISCUSSION

As the percentage of the soil passing sieve # 200 was found to be more than 95%, this means that the classification of the soil is based on the liquid and plastic limits using the USCS (ASTM D2487-17, 2017). The plasticity test results showed that the liquid limit and plastic limit of the soil were 39% and 22%, respectively. Using the plasticity chart of the USCS, the soil was classified as CL as shown in Fig. 1. This means that the soil was clay of low plasticity.

A. Variation of the OMC and Maximum Dry Density with the Sand Content

The results of the Proctor’s test for the clay-sand samples which contained different fractions of sand are presented in Fig. 2. It is clear from Fig. 2 that the clay with no added sand and the clay-sand mixture soils show the similar trend for the dry density-moisture content relationship, where increasing the moisture content increases the dry density up to a certain moisture content (OMC). Beyond this optimum moisture content, the dry density declined.

To provide better insight into the effect of the sand percentage on the maximum dry density and the optimum moisture content are obtained from Fig. 2 for each case and are presented in Table I and Fig. 3. It is evident from Fig. 3 that the range of the OMC variations was between 11% and 20%, where largest OMC was obtained in the sample of pure clay (20%) and this OMC declines as the sand percentage increases. This is because the clay particles have more capability to absorb water than sand particle; hence, as the sand percentage increases the capability of the soil (clay-sand mixture) to absorb water decreases. On the other hand, Fig. 3 also shows that the maximum dry density varied in increasing rate from 1.65 g/cm³ to reach the maximum value of 1.90 g/cm³ when the sand fraction was 30%. The maximum dry density then dropped to 1.78 g/cm³ when the sand fraction was increased to 40%.

It is also clear from Fig. 3 that, there is a fast increase in dry density with increase of sand content between 10% and 30%, beyond which the density declined rapidly. This is because when the sand was added to the samples, the coarse particles were arranged by compaction in a way that increased the volume of solids per unit of total volume. Hence, the void ratio decreased whereas dry density increased with the increase of sand fraction. This continued until the fraction of fine particles became less than that required for optimum arrangement of solid particles per unit volume. Therefore, the void ratio began to rise again, whereas dry density started to fall. The inverse variations in the optimum moisture content with increasing sand percentage is due to the decrease in the surface area of soil particles with the presence of sand. This led to reducing the amount of water required to facilitate the arrangement of soil particles by compaction to reach the maximum dry density (Holtz et al., 2011).

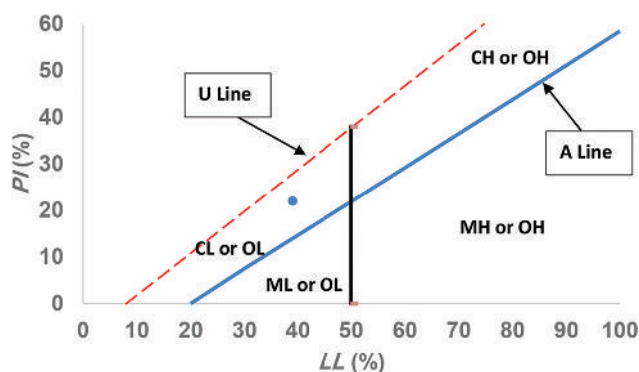


Fig. 1. Plasticity chart for classifying the soil.

TABLE I
SUMMARY OF THE OBTAINED MAXIMUM DRY DENSITY AND OPTIMUM MOISTURE CONTENT

Soil	Maximum dry density (kg/cm ³)	Optimum moisture content (%)
Clay with not added sand	1.65	20
Clay with 10% of sand	1.80	15
Clay with 20% of sand	1.84	13
Clay with 30% of sand	1.90	12
Clay with 40% of sand	1.78	11

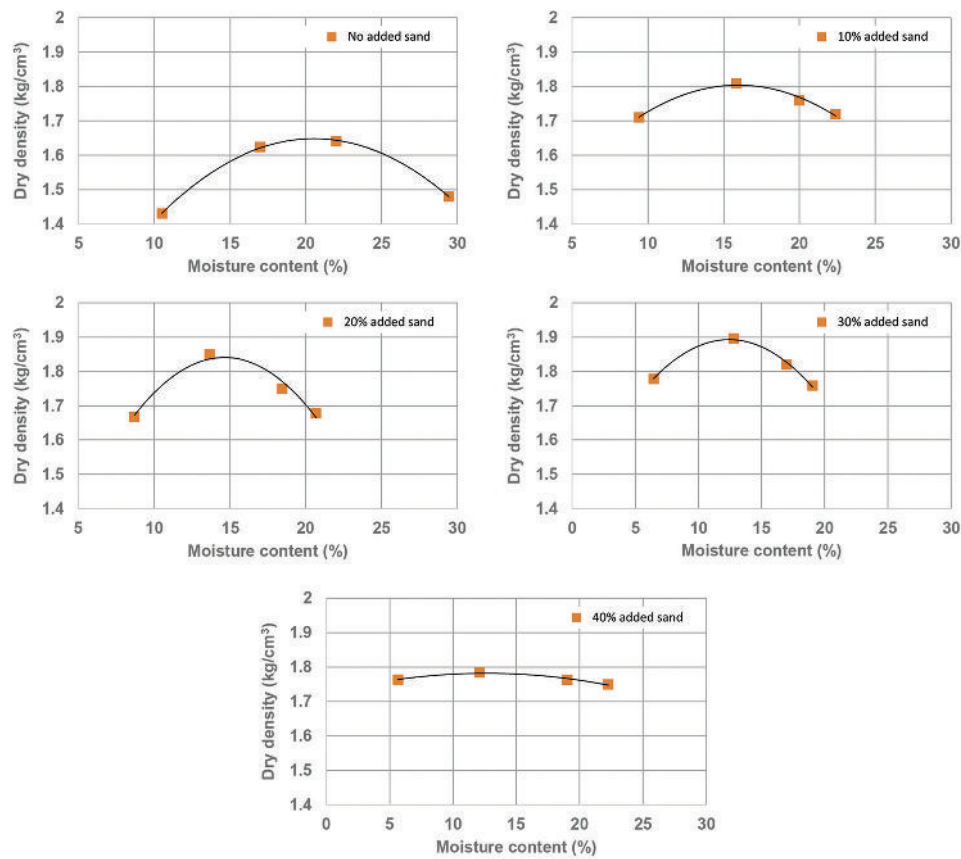


Fig. 2. Relationship of moisture content versus dry density for clay containing various sand percentages.

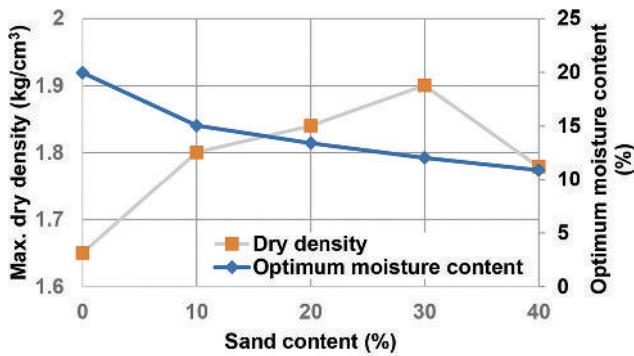


Fig. 3. Effect of sand percentage on the dry density and optimum moisture content of compacted clay.

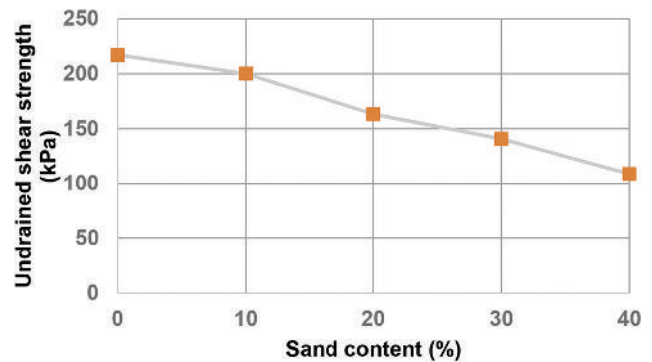


Fig. 4. Effect of sand percentage on the undrained shear strength of compacted clay.

B. Variation of Undrained Shear Strength with the Sand Content

The influence of sand fraction on the values of undrained shear strength of the compacted clay is provided in Fig. 4. It is clear from the figure that the undrained shear strength dropped from 220 kPa for 0% sand to 111 kPa for 40% sand. The rate of drop in the undrained shear strength continued with the increase of sand percentage. The decline in undrained shear strength with increasing sand percentage in the sample is due to the reduction in cohesion. When sand was added to the sample, the attraction between the clay particles was reduced due to the separation of clay particles by sand particles. Thus, the undrained shear strength continued to drop with

the increasing sand fraction. Moreover, the reduction in shear strength could be attributed to the path of failure plane which passes through a weaker zone in a case of clay-sand mixes (Mullins and Panayiotopoulos, 2013). In addition, the cross-sectional area of the sample may reduce when the sample contains sand particles which fell out from the sides in the test samples. As a result, stress concentration increases making the sample fail under smaller applied load (Khan et al., 2014).

IV. CONCLUSIONS

This study investigated the characteristics of compacted clay of low plasticity mixed with sand at different percentages.

The results have shown that dry density increased with increase of sand fraction up to 30% of the sample by weight. The maximum increase in dry density was reached when the added sand fraction was 30%. The optimum moisture content decreased with the increasing percentage of added sand. The undrained shear strength varied inversely with increasing percentage of sand. A significant decrease in the undrained shear strength was observed initially with a steady decrease thereafter with the increase of sand fraction.

REFERENCES

- Alzabeebee, S.I.A., 2014. *Dynamic Response of Shallow Foundation on Elastic-plastic Clayey Soil Subjected to Impact Load*. In: The Proceeding of the 1st International Conference on Engineering, Al-Mustansiriya University, Iraq, pp.155-165.
- ASTM D1452/D1452M-16., 2016. *Standard Practice for Soil Exploration and Sampling by Auger Borings*. ASTM International, West Conshohocken.
- ASTM D2166/D2166M-16., 2016. *Standard Test Method for Unconfined Compressive Strength of Cohesive Soil*. ASTM International, West Conshohocken.
- ASTM D2216-19., 2019. *Standard Test Methods for Laboratory Determination of Water (Moisture) Content of Soil and Rock by Mass*. ASTM International, West Conshohocken.
- ASTM D2487-17., 2017. *Standard Practice for Classification of Soils for Engineering Purposes (Unified Soil Classification System)*. ASTM International, West Conshohocken.
- ASTM D4220/D4220M-14., 2014. *Standard Practices for Preserving and Transporting Soil Samples*. ASTM International, West Conshohocken.
- ASTM D4318-17e1., 2017. *Standard Test Methods for Liquid Limit, Plastic Limit, and Plasticity Index of Soils*. ASTM International, West Conshohocken.
- ASTM D6913/D6913M-17., 2017. *Standard Test Methods for Particle-Size Distribution (Gradation) of Soils Using Sieve Analysis*. ASTM International, West Conshohocken.
- ASTM D698-12e2., 2012. *Standard Test Methods for Laboratory Compaction Characteristics of Soil Using Standard Effort (12 400 ft-lbf/ft³ 600 kN-m/m³)*. ASTM International, West Conshohocken.
- Benmebarek, S., Saifi, I. and Benmebarek, N., 2017. Depth factors for undrained bearing capacity of circular footing by numerical approach. *Journal of Rock Mechanics and Geotechnical Engineering*, 9, pp.761-766.
- Bowles, J.E., 1996. *Foundation Analysis and Design*. 5th ed. McGraw-Hill, New York.
- Budhu, M., 2011. *Soil Mechanics and Foundations*. John Wiley and Sons, Hoboken.
- Cabalar, A.F., Awraheem, M.H. and Khalaf, M.M., 2018. Geotechnical properties of a low-plasticity clay with biopolymer. *Journal of Materials in Civil Engineering*, 30(8), p.04018170.
- Das, B.M., 2010. *Principles of Geotechnical Engineering*. 7th ed. Cengage Learning, Stamford.
- Deng, Y., Wu, Z.Y., Cui S. and Wang, Q., 2017. Sand fraction effect on hydro-mechanical behavior of sand-clay mixture. *Applied Clay Science*, 135, pp.355-361.
- Garzón, E., Cano, M., O'Kelly, B.C. and Sánchez-Soto, P.J., 2015. Phyllite clay-cement composites having improved engineering properties and material applications. *Applied Clay Science*, 114, pp.229-233.
- Ghanizadeh, A.R., Yarmahmoudi, A. and Abbaslou, H., 2020. Mechanical properties of low plasticity clay soil stabilized with iron ore mine tailing and Portland cement. *Journal of Mining and Environment*, 11(3), pp.837-853.
- Holtz, R.D., Kovacs, W.D. and Sheahan, T.C., 2011. *An Introduction to Geotechnical Engineering*. Prentice Hall, New Jersey.
- Javdanian, H., 2017. The effect of geopolymerization on the unconfined compressive strength of stabilized fine-grained soils. *International Journal of Engineering-Transactions B: Applications*, 30, pp.1673-1680.
- Khan, F.S., Raghunandan, M.E. and Clark, R., 2014. Compressive strength of clay-sand mixes. *Advances in Material Science and Engineering*, 2014, p.921815.
- Khemissa, M. and Mahamedi, A., 2014. Cement and lime mixture stabilization of an expansive overconsolidated clay. *Applied Clay Science*, 95, pp.104-110.
- Khitas, N.E.H., Benmeddour, D., Mellas, M. and Mabrouki, A., 2020. The undrained bearing capacity of strip footings under eccentric loading: effect of soil-footing interface tensile strength. *International Journal of Geotechnical Engineering*, 4(2), pp.169-175.
- Kim, U., Kim, D. and Zhuang, L., 2016. Influence of fines content on the undrained cyclic shear strength of sand-clay mixtures. *Soil Dynamics and Earthquake Engineering*, 83, pp.124-134.
- Manimaran, A., Seenu, S. and Ravichandran, P.T., 2019. Stimulation behaviour study on clay treated with ground granulated blast slag and groundnut shell ash. *International Journal of Engineering B: Application*, 32, pp.673-678.
- Ministry of Housing and Construction., 2003. *State commission of Road and Bridge, Revised edition of the General Specification for Road and Bridge*. Department of Planning and Studies, Baghdad.
- Mullins, E.C. and Panayiotopoulos, K.P., 2013. The strength of unsaturated mixtures of sand and kaolin and the concept of effective stress. *Journal of Soil Science*, 35, pp.459-468.
- Narendranathan, N. and Lee, E.C., 2015. Dynamic compaction and dynamic consolidation of soils. *Ground Improvement Case Histories*, 21, pp.365-398.
- Shafiee, A., Tavakoli, H.R. and Jafari, M.K., 2008. Undrained behaviour of compacted sand-clay mixtures under monotonic loading paths. *Journal of Applied Sciences*, 8, pp.3108-3118.
- Toufigh, V. and Rahmamejad, M., 2018. Influence of curing time and water content on unconfined compressive strength of sand stabilized using epoxy resin. *International Journal of Engineering B: Application*, 31, pp.1187-1195.

Corrosion in Crude Oil Distillation Unit Overhead: A recent Case Study

Ari A. Ahmed

Department of Chemical Engineering, Firat University,
Elazığ, Turkey

Abstract—Despite all the technological advances and the control mechanisms that exist today to achieve the control of corrosion in overhead systems in atmospheric crude oil distillation units, there is still a high level of difficulty in predicting the phenomenon due to the complexity of the chemical compounds involved in the entire process. The study of this practical case aims to determine what control mechanisms should be optimized in a refinery located in the Autonomous Region of Iraqi Kurdistan to prevent corrosion phenomena's in this specific system and how it should be done to achieve these improvements. It has been suggested that the corrosion mechanisms by hydrochloric acid and by ammonium chloride have been those that have acted in the operational context of the mentioned facility. To test this hypothesis, a study of the unit's operational conditions and analytical tests were carried out on the construction material of various components and the products (sediments) found inside the tower. The results show that a lack of control in the salts and sediments content of the feed crude have caused an increase in the hydrolysis process of certain components upstream of the tower and thus the generation of acids and salts was promoted. On this basis, it is necessary to optimize the primary treatment of crude oil and update the chemical treatments and washing water systems to adapt to the new conditions of the feed of the refinery.

Index Terms—Ammonium chloride, Crude overhead, Dew point, HCl, Salt formation, Salt hydrolysis.

I. INTRODUCTION

The crude distillation unit (CDU) in question is going through a forced maintenance stage, due to operational and processes upsetting that do not allow obtaining the products with the required quality and quantity.

Since the beginning of 2020, the main problems in the process were thought to be associated with the efficiency and performance of the crude heater, assuming that it was plugged due to coke deposition phenomena. Due to this, the unit was put out-of-service to check for damage and perform deep cleaning on the heater tubes. This problem was fixed

and now it has moved to the atmospheric tower, where it has been observed that there is no outlet for Kerosene and Diesel products. In addition, there were problems in maintaining the profile of the tower, which is why it was decided to put the unit out-of-service to verify, now in greater depth, the problems in the aforementioned tower.

II. BACKGROUND

A. Corrosion in Crude Distillation Overhead Systems

Corrosion in crude distillation overhead systems is a common problem in refineries. According to The National Association for Corrosion Engineers International Publication 34109, the primary mechanism of concern in the overhead system is the acidic attack of unit metallurgy due to the presence of high concentrations of HCl in condensing water. Under-deposit corrosion and fouling usually resulting from unintended consequences of acid neutralization and/or inefficient desalter operations are also a big problem (Chambers et al., 2011, Duggan and Rechten, 1998, Eaton et al., 2009).

Crude oils contain varying amounts of chloride salts (NaCl, MgCl₂, and CaCl₂), and these salts generally account for the bulk of the HCl formation and corrosion in CDUs, specifically in the overhead system.

The HCl is evolved from the hydrolysis of MgCl₂ and CaCl₂ to form HCl during heating in the crude oil preheat train and associated heaters. NaCl does not hydrolyze to a great extent under normal CDU furnace conditions. Therefore, NaCl generally is not considered a significant contributor to CDU distillation tower overhead system corrosion. Table I shows the hydrolysis reactions involved in this context.

Studies made by Schempp et al., Thornthwaite, et al., and Braden et al., confirm that HCl does not cause corrosion problems at temperatures above the aqueous dew point. However, at temperatures equal to or below the aqueous dew point, HCl readily dissolves in water to form corrosive hydrochloric acid. At temperatures above the aqueous dew point, HCl can react with some alkaline species to form corrosive salts.

HCl, formed in the process as previously described, often combines with NH₃ to form solid NH₄Cl salt in CDU distillation tower overhead systems (Saab et al., 2005). The temperature at which NH₄Cl forms is dependent on the partial pressures of HCl and NH₃. These partial pressures can be estimated from the chloride and NH₃ contents measured in



the water phase of the associated overhead drum, accounting for the presence of water and hydrocarbon vapors in the system. Fig. 1 (Fan et al., 2001) shows the graphs normally used for this purpose.

According to Lordo (2006), NH₃ may be carried into the CDU from multiple sources including the presence of NH₃ in desalter wash water or from the use of NH₃ as a neutralizer. Fig. 2 presents a diagram of NH₄Cl salt formation at various temperatures and concentrations of NH₃ and HCl in an overhead system. The knowledge of the salt formation

TABLE I
HYDROLYSIS REACTIONS

Reaction	Approximate starting temperature, °C(°F)	Approximate degree of hydrolysis at 340°C(650°F)
MgCl ₂ +2H ₂ O→Mg(OH) ₂ +2HCl	120(248)	90%
CaCl ₂ +H ₂ O→Ca(OH) ₂ +2HCl	210(410)	10%
NaCl+H ₂ O→NaOH+HCl	>500(>930)	2%

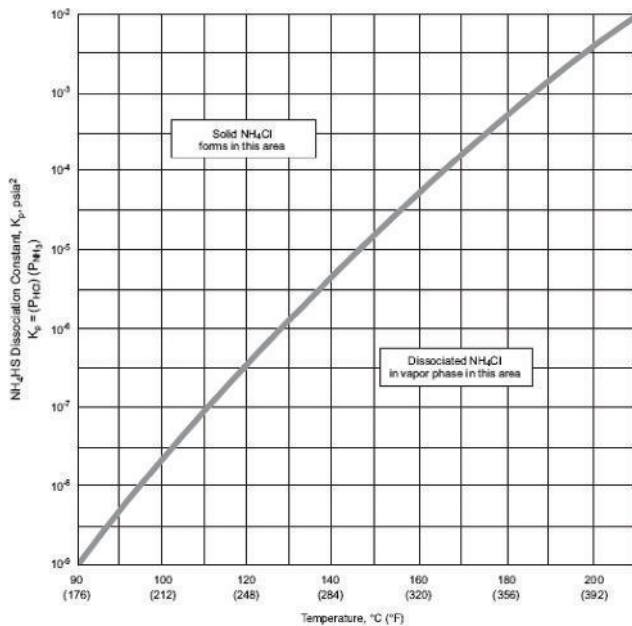


Fig. 1. NH₄Cl deposition temperature estimation (Turner et al., 1998).

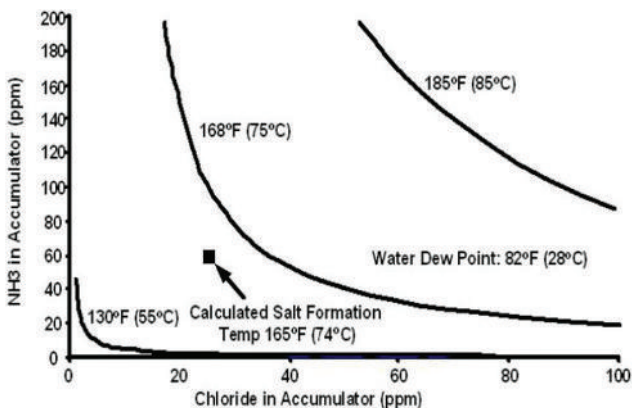


Fig. 2. NH₄Cl salt formation at various overhead temperatures (Lordo et al., 2006).

thermodynamics, as stated by Duggan et al., (1998) allows the construction of a figure for injection rates of neutralizer to avoid salt formation, as shown in Fig. 3.

The partial pressure of each component, that is, can be calculated by taking the moles of the component in the vapor phase divided by the total moles in the vapor phase multiplied by the absolute pressure (P) in the process.

$$P_{pi} = (n_i \text{ vapor phase}) / (n_{\text{total vapor phase}}) \times P$$

Where n_i is the mole fraction (in the vapor) of the component.

The same procedure can be used to estimate the NH₄Cl deposition temperature from Fig. 1.

The net NH₃ yield can be calculated from the nitrogen level in the feed and the percent denitrification.

Giesbrecht, et al., and Gutzeit, in their studies, established that the control of NH₄Cl corrosion is generally approached in one of three ways. The first is lowering the formation temperature of the salt by reducing the HCl and NH₃ contents in the overhead system. These reductions are often achieved by improving desalter operation to reduce chloride and NH₃ carry-over or by eliminating external sources of NH₃. Once NH₄Cl is formed, corrosion is commonly controlled using continuous or intermittent water wash that is adequately distributed. Excess water is normally added to ensure that all the water is not evaporated. A common range of excess water is between 10 and 25 vol%. This is the amount of water that is required to saturate the overhead vapor. Second, changing operations to maintain equipment temperatures above the salt formation temperature are sometimes feasible. Finally, for systems using NH₃ as a neutralizer, limiting the amount of NH₃ added to that required for pH control of the accumulated water in the overhead drum is commonly practiced.

B. Process Description of the Unit Under Study

The distillation unit has a standard configuration without facilities for crude desalination. Fig. 4 shows a simplified schematic of the unit. The crude desalter is the main defense against the presence of excessive amounts of inorganic chloride salts. The limitation of inorganic chloride salts entering the CDU substantially reduces the presence of HCl in the CDU overhead circuit. Experience shows that chloride content of the desalted crude feed to the CDU that exceeds 20 ppm have the potential of leading to significant corrosion and fouling problems in the overhead circuit.

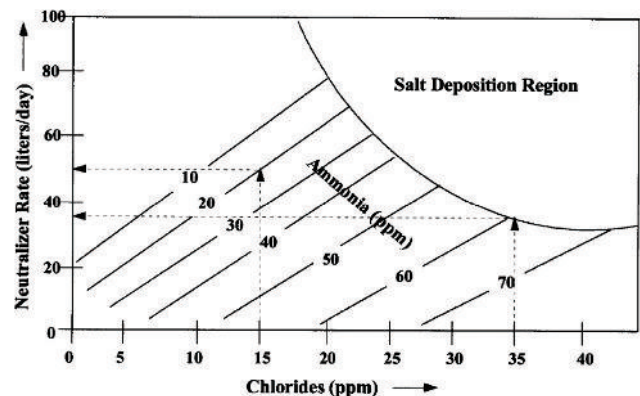


Fig. 3. Neutralizer monographs (Duggan et al., 1998).

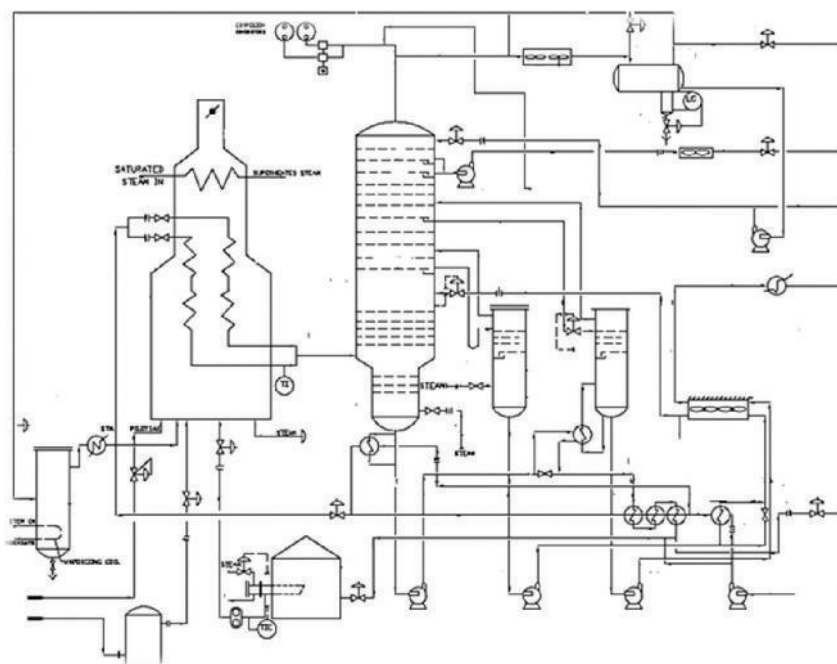


Fig. 4. Simplified scheme of the distillation unit under study (modified figure).

Crude oil feed is received from the crude feed pump and sent through a series of heat exchangers to a temperature around 162°C. The crude oil is heated at 370°C in crude heater and enters atmospheric tower where it is fractionated into the following products:

- Off gas
- Light naphtha
- Heavy naphtha
- Kerosene
- Diesel
- Atmospheric residue or tower bottoms (ATB or residual fuel oil).

The overhead vapor is condensed by an air cooler and the off gas is either routed to the heater as fuel gas or to the flare depending on pressure in the overhead accumulator drum. Naphtha collects in the drum and part is pumped back to the tower as reflux and the other part pumped normally to further processing or alternately to storage.

Unstripped kerosene and diesel products are drawn from the crude tower and fed to the top of the side steam stripper. Steam stripped vapors are returned to the crude tower above the draw tray. The stripped kerosene and diesel are pumped through rundown coolers to the kerosene treater unit provided by others and storage.

Below the flash zone the residue is steam stripped inside the crude column to reduce the volatiles. The atmospheric tower bottoms product is fuel oil and is cooled by heat exchange with the crude rundown to storage.

III. CASE STUDY

Fig. 5 shows a simple schematic of the tower. It is an equipment manufactured basically in Monel (alloy 400),

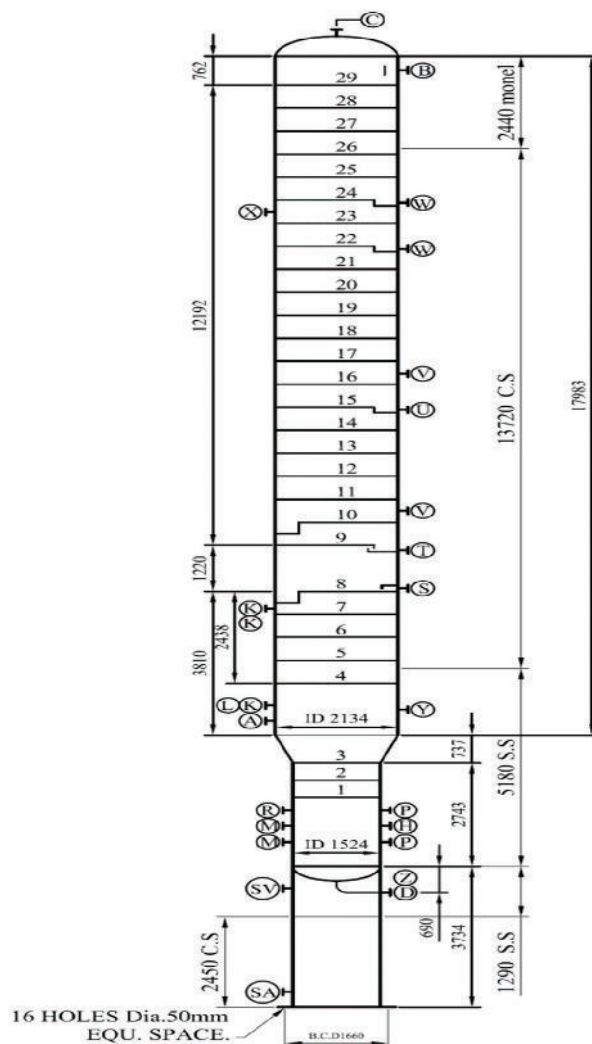


Fig. 5. V-111 simplified scheme.

carbon steel and martensitic stainless steel. The solid Monel is above the tray 25, between tray 5 and 25 is carbon steel and below tray 5 there is SS410.

The tower has a 20-inch manhole for the entry and removal of trays; these are attached to the tower with support rings. Its diameter is 21634 mm, except for the three first trays, which have 1524 mm in diameter. The flow control mechanism is through Glitsch V-1 type valves.

After all the cleaning and security protocols were followed, an inspection was carried out on the inside of the atmospheric tower. The entrance to the tower was made at the height of plate 23, and then went up to the top of the tower and went down tray by tray. The most relevant findings of this activity are shown in Fig. 6.




Picture	Comments
	TRAY 28–Monel The tray is in an advanced state of corrosion. It can be seen total perforation of the tray. The valve holes have lost dimension, which compromises the operation of the valves. The presence of salts adhered to the tower walls and tray can be observed. The presence of yellowish and whitish products stands out. The former is associated with sulfur products and the latter with ammonia salts
	Tray 24–SS410 Note the areas with large holes caused by corrosion phenomena. This tray is not completely plugged but does not have associated valves. The valve ports have completely lost their dimensions
	Kerosene Nozzle This nozzle is partially plugged. The withdrawal tray has a large number of products and is deflected. There is no way this nozzle would allow kerosene removal. The red circle shows the uniqueness of the nozzle

Fig. 6. Some of the inspection findings inside the atmospheric tower.

The inspection allowed verifying that there is a serious phenomenon of plugging and corrosion in the tower. The main problem is in the quality of the feed supply to the unit; it is obvious that the water and sediment content and the concentration of salts are higher than the design of the unit has the capacity to process. For this reason, it was defined at this point that the main characteristic to study in this phenomenon is the content of salts in the feed crude.

Throughout 2020, the content of salts in feed crude oil is above 119 PTB, the month of March being the most critical with values as high as 355 PTB. These values are high if we consider that unit two does not have desalters, which are considered the first barrier to protect against corrosion and plugging.

Fig. 7 shows a graph with this year's trend. It is known that in previous years the salt content was much lower, even in other units of the refinery, which processes the same crude oil, work has been carried out even without a desalter, which is an indicator that the content of salts has varied greatly through time.

Apart from the precipitation temperature estimation exercises described above, there are other mechanisms to establish a relationship between salt content and corrosion and plugging in the internal part of the tower. One of them is the chemical analysis of the products found on the trays. Fig. 8 shows the results obtained in a sample extracted from the top section of the tower between trays 23 and 29. It can be seen that only 9% of the sample evaporated at 500°C. The rest of the sample is soluble in water and in a solution acidified with HCl, which is indicative that its composition is possibly salts and sediments, in addition to some corrosion products.

After the inspection was completed and the condition of the trays was verified, the question was raised as to whether the metallurgy of these components was correct. The tower has metallurgies set forth in the most recognized standards and recommended practices in the refining industry. Fig. 9 shows a simplified schematization of the overhead systems of the unit.

Three samples of Monel internals were analyzed using optical emission spectrometry technique. Sample number 1 corresponds to the valves, number 2 to the trays, and number

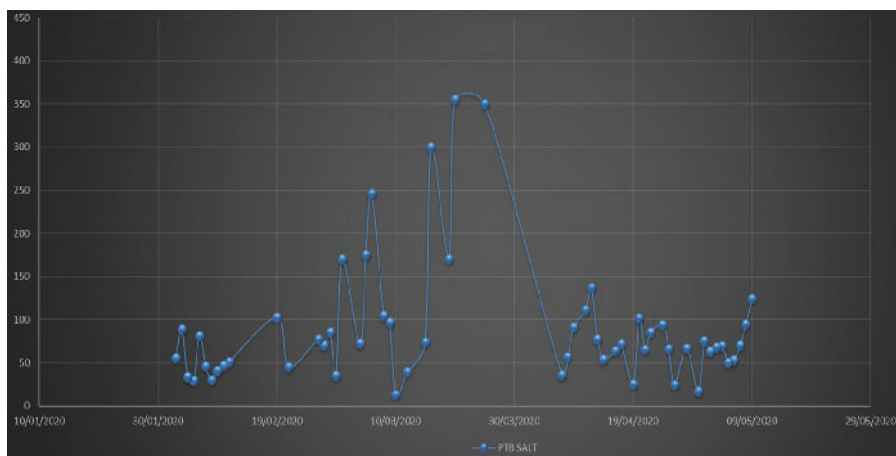


Fig. 7. Salts PTB trend in crude feed – 2020.

3 to the hardware. Taking into account the limitations of the test method, the results appear to be OK for valves and plates. The hardware turned out to be stainless steel. This represents a deviation generated during the installation of the internals.

The same procedure was repeated for the stainless-steel trays. The results area is presented in Tables II and III.

Nickel based alloys have been widely used in different applications in petroleum refining, due to its high corrosion resistant in different conditions (Groysman and Hiram, 1997). Alloy 400, Monel, is a precipitation alloy of nickel containing considerable amount of copper (approximately 30–33 wt% copper) as a substantial element to provide solid solution strengthening. Furthermore, small amount of iron is added to improve the resistance of the alloy to cavitation and erosion in condenser tube application. It was reported by Groysman that, Monel 400, is susceptible to sulfide stress cracking when the surrounding environment contains sulfurous compounds such as hydrogen sulfide (H₂S), mercury salts, and hydrofluoric acid. The presence of oxidizing agents (oxygen, ferric, and cupric ions) will increase the corrosion rate, particularly for Alloy 400 and Alloy B-2.

Having evaluated all the morphological characteristics of the components degraded by corrosion, the chemical composition of the products found in the internal part of the

tower, as well as the metallurgy of the internal components, it can be concluded that there are combined corrosion mechanisms that affected the integrity of the atmospheric distillation tower and internals. Those mechanisms can be described as NH₄Cl corrosion and HCl corrosion. These mechanisms are described in the literature as very aggressive and depend on the combination of a series of variables, which are observed in Fig. 10.

TABLE II
CHEMICAL COMPOSITION OF THE TOWER INTERNALS IN THE MONEL SECTION.
1-VALVES, 2-TRAYS, 3-HARDWARE

Element	Weight %-1	Weight %-2	Weight %-3
C	0.22	0.26	0.03
Si	0.95	1.56	0.45
P	0.01	0.01	0.03
S	0.03	0.04	0.01
Cr	0.2	0.13	13.4
Mo	0.18	0.23	0.01
Ni	>52.2	>52.2	0.17
Al	0.39	0.4	0.01
Co	0.09	0.09	0.01
Cu	>9.72	>9.72	0.21
Nb	0.24	0.27	0.04
Ti	0.69	0.38	0.01
V	0.9	0.9	0.05
W	1.29	1.84	0.01
Pb	0.07	0.07	0.01
Sn	0.04	0.04	0.01
Mg	0.09	0.11	0.01
As	0.03	0.03	0
Zr	0.21	0.02	0
Bi	0.04	0.04	0
Ca	0.02	0.01	0
Ce	0.04	0.04	0
Sb	0.29	0.28	0
Te	0.06	0.06	0
B	0.01	0.01	0
Zn	0.05	0.05	0.01
La	0.03	0.03	0

Analysis steps	Description
1 →	5 g of sample in 500 ml of H ₂ O reduce the pH from 7 to 4.5
2 →	Ignition of 10 g at 500°C for 2 h and 30min. 9.6% wt. of organic compounds were lost
3 →	
4 →	After ignition, 1 g of sample was dissolved in HCl. 56.9% wt. was lost, indicating possible inorganic products
5 →	Additional analysis: Cl ⁻ =147 ppm, SO ₄ ⁻² =236 ppm, Ca ⁺² =6200 ppm. Na ⁺¹ =108 ppm

Fig. 8. Lab results – sample taken from atmospheric tower internal trays.

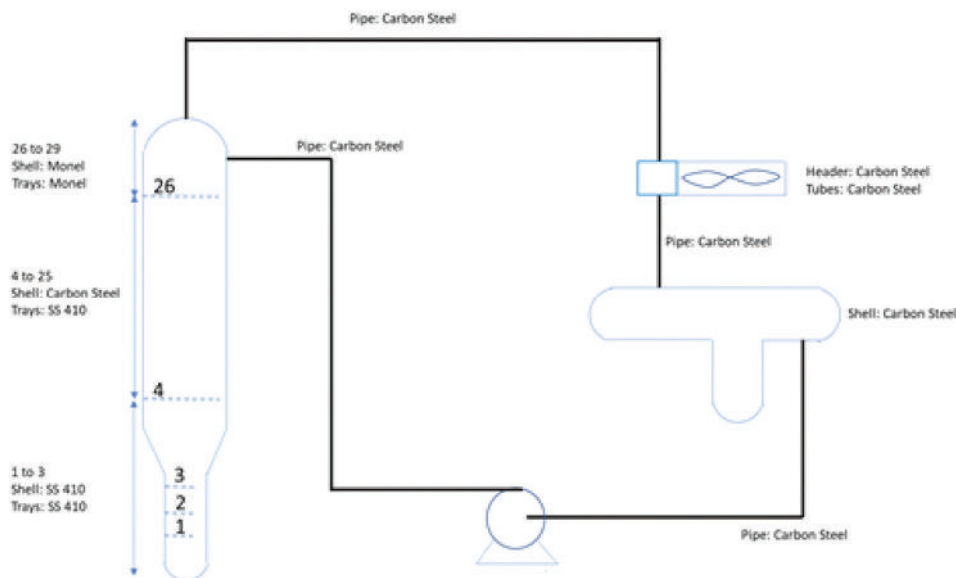


Fig. 9. Simplified schematization of the overheads systems in the units plus the entire tower metallurgy description.

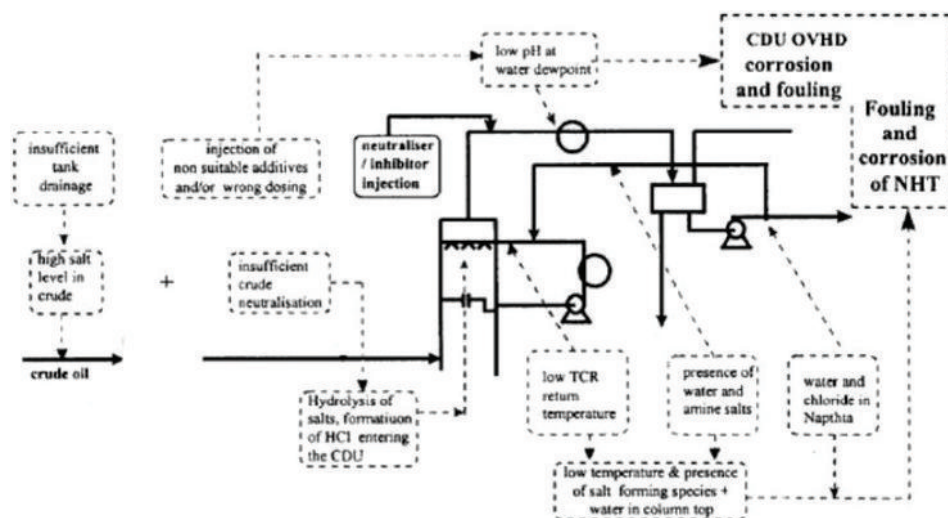


Fig. 10. Schematic of crude feed, desalter, atmospheric distillation unit, and overhead circuit along with common corrosion and fouling problems (Kapusta et al., 2001).

TABLE III
CHEMICAL COMPOSITION OF THE TOWER INTERNALS IN THE STAINLESS-STEEL
SECTION. 1-VALVES 2-TRAYS 3-HARDWARE

Element	Weight %-1	Weight %-2	Weight %-3
C	0.18	0.22	0.04
Mn	0.44	0.58	0.39
Si	0.39	0.48	0.49
S	0.01	0	0
P	0.04	0.04	0.05
Cr	12.46	13.91	13.19
Ni	0.17	0.07	0.15
Mo	0.02	0	0.01
Cu	0.04	0	0.18
V	0.05	0.03	0.05
Ti	0	0	0
Al	0	0	0
Co	0.01	0	0.01
Nb	0	0	0
W	0.01	0.01	0.01
Pb	0	0	0
Sn	0.01	0	0.02
As	0.05	0.03	0.03
Ca	0	0	0
B	0	0	0
Fe	86.1	84.6	85.3
Sb	0	0.01	0.01

IV. CONCLUSIONS

After having evaluated the operational context and the evidence of the inspections and analyzes carried out, it can be concluded that the degradation mechanism that has affected the internals of the atmospheric distillation tower under study was Corrosion by Ammonium Chloride (NH_4Cl) in Combination with Corrosion by Hydrochloric Acid (HCl). These mechanisms caused irremediable damage to the mechanical and metallurgical integrity of the tower's internals, making its operational performance impossible.

To remedy this problem and avoid a new occurrence, it is necessary to implement operational improvements,

such as optimizing the primary treatment of crude oil in production facilities, reducing the water and sediment content to a maximum of 1%, control the content of salts after desalters to a maximum of 30 ptb, define a new tankage strategy that improves dehydration, and, update the operating model of chemical treatments and washing water systems to adapt to the new conditions of the diets of the refinery.

REFERENCES

- Braden, V., Petersen, P., Malpiedi, M., Bowerbank, L. and Gorman, J., 1998. *Crude Unit Overhead Corrosion Control*. CORROSION Conference, NACE International, Houston, USA, Paper No. 98585.
- Chambers, B., Yap, K., Srinivasan, S. and Yunovich, M., 2011. *Corrosion in Crude Distillation Unit Overhead Operations: A Comprehensive Review*. CORROSION Conference, NACE International, Houston, USA, Paper No. 11360.
- Duggan, G. and Rechien, R., 1998. *Application of Ionic Equilibria Process Simulation for Atmospheric Distillation Overhead Systems*. Corrosion/98, NACE International, Houston, TX, Paper No. 98586.
- Eaton, P., Kaur, H. and Gray, M., 2009. *Factors Affecting Salt Hydrolysis in Heavy Crude*. Eurocorr/2009, Nice France, September, Paper No. 8295.
- Fan, D., Fort, W., Shargay, C., Turner, J. and Messer, B., 2001. *Design Considerations to Minimize Ammonium Chloride Corrosion in Hydrotreatment Reactions*. Paper Presented at the CORROSION 2001, Houston, Texas, 01543.
- Giesbrecht, V., Duggan, G. and Jackson, D., 2002. *Effective Corrosion Control Techniques for Crude Unit Overheads*. Corrosion/02, NACE International, Paper No. 02477.
- Groysman, A. and Hiram, A., 1997. *Corrosion Monitoring and Control in Refinery Process Units*, Corrosion/97. NACE International, Houston, TX, Paper No. 97512.
- Gutzeit, J., 2007. *Controlling Crude Unit Overhead Corrosion Rules of Thumb for Better Crude Desalting*. Corrosion/07, NACE International, Houston, TX, Paper No. 07567.
- Kapusta, S., Ooms, A., Buijss, J., Fan, D. and Fort, W. 3rd, 2001. *Systematic Approach to Controlling Fouling and Corrosion in Crude Unit Overheads and Hydrotreater Reactor Effluents*. Corrosion/01, NACE International, Houston,

TX, Paper No. 01535.

Lordo, S. and Eisenhower, A., 2006. Sensitivity analysis for modeling overhead chloride salt deposition and corrosion issues. *Journal of Physics: Conference Series*, 1378, p.022089.

N.N., 2007. *Corrosion Control in the Refining Industry Course Manual, Chapter 2: Crude Distillation and Desalting*. NACE International, Houston, USA.

N.N., 2009. *Crude Distillation Unit Distillation Tower Overhead System Corrosion, NACE International Publication 34109 (Task Group 342)*. NACE International, Houston, USA.

Rechtien, R. and Duggan, G., 2006. *Identifying the Impacts of Amine*

Contamination on Crude Units, CORROSION Conference. NACE International, Houston, USA, Paper No. 06851.

Saab, M., Dias, O.C. and Faqeer, F.M., 2005. *Damage Mechanisms and Corrosion Control in a Crude Unit Overhead Line*. Corrosion/05, NACE International, Houston, TX, Paper No. 05566.

Schempp, P., Preub, K. and Troeger, M., 2016. About the correlation between crude oil corrosiveness and results from corrosion monitoring in an oil refinery. *Corrosion*, 72, pp.843-855.

Thornthwaite, P. and Davies, J., 2016. Monitoring and simulation resolves overhead corrosion. *PTQ*, 1, pp.53-63.

Feasibility Study of Concrete Louvers for High-rise Residential Buildings in Terms of Cooling Energy Requirements

Sara Dh. Bahaadin¹, Binaee Y. Raof¹ and Hendren H. Abdulrahman²

¹Department of City Planning, Technical College of Engineering, Sulaimani Polytechnic University, Sulaimani, Kurdistan Region – F.R. Iraq

²Department of Architecture, College of Engineering, University of Sulaimani, Sulaimani, Kurdistan Region – F.R. Iraq

Abstract—High-rise residential buildings are increasing worldwide, including cities in the Kurdistan Region of Iraq. Therefore, creating sustainable environments in and around these residential buildings are becoming an important problem. Improving energy efficiency in buildings has received critical attention worldwide. Countries have developed national sustainability strategies that lead to the lower energy consumption while maintaining comfort, reducing energy consumption, and minimizing harmful emissions. In this paper, an analysis of the impact of external shading devices in high-rise residential buildings on energy consumption of a 13-storey building in Sulaimani city is studied. The study is focused on fixed shading elements, explaining the influence of the design of vertical and horizontal shading devices on the total energy consumption of this type of building. The results show that both a single fixed horizontal blind with a depth of 20 cm and a triple vertical shading with the same depth are considered useless. The reduction in cooling loads by two fixed horizontal louvers almost doubled compared to a single fixed horizontal shading with 20 cm. Moreover, triple fixed horizontal louvers with 40 cm have almost the same effect on reducing cooling loads as triple fixed louvers with 60 cm. On the other hand, a triple fixed horizontal shading device with 60 cm has twice the effect on reducing annual cooling loads as a triple fixed vertical shading device with 60 cm.

Index Terms—High-rise building; Shading devices; cooling loads; Energy consumption; Sulaimani city.

I. INTRODUCTION

Since scientific research on the subject of housing has shown that the experience of living in high-rise apartments varies greatly for different people, cultures, and environmental conditions. For example, a European's perception of living

in a high-rise is not desirable, whereas in many Asian cities, people prepared to live in high-rise blocks (Arsalan and Sev, 2014).

Some observers believe that high-rise residential buildings, especially sustainable housing, are a fundamental commitment to urban life that should be maintained and improved.

Tall buildings have many environmental benefits, for example, sufficient access to sunlight to install solar panels. On the other hand, a high-rise residential building requires a large amount of energy for its operation and utilities. Many high-rise buildings consume more energy per inhabitant than a well-built townhouse and not much less than a small, well-built detached house (Ali and Al-Kodmany, 2012).

Today, almost all countries have national sustainability strategies in place and energy efficiency is undeniably one of the main pillars of sustainability. Therefore, environmental impact assessment is a key priority when designing new high-rise residential projects (Ali and Al-Kodmany, 2012).

In most countries, buildings require large amounts of energy for both cooling and heating. Furthermore, in the last decade in the Kurdistan region about 50% of the total energy consumption was consumed in the residential sector (Morad and Ismail, 2017). Indeed, cooling loads due to solar gains represent about half of the global cooling loads for residential and non-residential buildings (Datta, 2001).

To control the effect of solar energy on the indoor climate, one usually focuses on the role of the building skin and fenestration, which act as filters between outside and inside of the building. Heat transfer can take place through radiation, ventilation, conduction, and convection. Here, the focus is on windows, which is the critical point for indoor heat gains. Glazing can account for up to 22% of energy consumption in residential buildings. Uncontrolled heat gain through windows leads to overheating and, thus, to poor thermal performance (Tariq and Jinia, 2012). The solar radiation that passes through windows has two effects on the thermal environment indoors: (1) Direct effects due to the incidence of direct and diffuse solar radiation on people, and (2) indirect effects due to the absorption of part of the

ARO-The Scientific Journal of Koya University
Vol. VIII, No.2 (2020), Article ID: ARO.10743, 12 pages
DOI:10.14500/aro.10743

Received: 26 October 2020; Accepted: 14 February 2021
Regular research paper: Published: 01 March 2021

Corresponding author's e-mail: sara.bahaadin@spu.edu.iq
Copyright © 2021 Sara Dh. Bahaadin, Binaee Y. Raof and
Hendren H. Abdulrahman. This is an open-access article distributed
under the Creative Commons Attribution License.



solar radiation by the interior surfaces of the room and the furnishings (Athienitis and Haghghat, 1992). Furthermore, the most excellent source of heat gain may be solar radiation entering through an opening (Tariq and Jinia, 2012). To reduce heat gain, the surfaces on which the sun rays fall must be protected, with emphasis on shading devices, since windows allow most of the incident heat to penetrate, thereby increasing the risk of overheating (Datta, 2001).

External shading devices on a building façade considered a passive design strategy as they reduce solar radiation, which is the most important factor affecting the architectural environment. Many studies have demonstrated the benefits of external shading devices, but some of them are designed for esthetic purposes only, without taking account of their high potential for reducing solar radiation (Shahdan, et al., 2018).

External shading devices are used to block solar radiation before reaching inside the building. They are therefore more effective than internal shading devices and offer better performance in terms of shading and visibility. A series of simulations and measurements have verified the differentiated advantages in illumination and building energy consumption using this system (Kim and Kim, 2010). However, other parameters can be influenced by external shading devices, such as daylight and natural ventilation performance of the building. Consequently, the design and construction of external shading devices must be carefully studied and correctly designed to ensure effective functioning (Tariq and Jinia, 2012).

II. PREVIOUS STUDIES

A wide number of parametric studies on sun oriented shading devices and energy uses have been made since the improvement of energy simulation computer programs.

The available literature examines what savings can be achieved by using external shading units. Different methods have been examined; the most common method is energy simulation software to determine energy savings using the external shading units.

In 2017, Idchabani, et al., 2017, investigated the influence of external shading overhangs and devices on the energy performance of buildings in a hot climate. Depending on the orientation of the window and the dimensions of the overhangs and slats in the city of Marrakech, different situations were simulated. In the analysis, it was criticized that the devices have less influence on the reduction of the cooling demand than the overhangs, and the most significant reduction was found for the directions NE and the NW area. However, the strongest reduction of the cooling load in SE and SW orientations was found for the overhang projection.

A study by Datta, 2001 examined the effect of fixed horizontal devices and their impact on the thermal performance of buildings using TRNSYS simulation. The shading devices were optimized in terms of annual energy loads and the optimal plan was designed according to the area's climate. It was found that the shading factor varies according to the time of day and is different for summer and winter (Datta, 2001).

Besides, as highlighted in the work of Alzoubi and Al-Zoubi, 2010 each side of a building requires a different shading treatment, as sunlight is incident from different angles on each side. Besides, there is an optimal orientation for shading devices that keep the internal light level within the acceptable range with a minimum amount of solar gain.

The study by Abdel Monteleb and Ali highlighted the effect of horizontal shading overhangs on the thermal performance of indoor spaces in residential buildings in New Assiut city, which has a hot, arid desert climate. The study shows that 100 cm wide horizontal overhangs had the lowest ambient temperature values for all tested orientations, with a strong recommendation to increase the use of overhangs in the south facade. In contrast, 12 cm horizontal overhangs had the highest ambient temperature values for all selected orientations. The wider the overhang, the lower the ambient temperature. Furthermore, the increase in the overhang width from 12 cm to 100 cm resulted in a decrease in room temperature by 2°C. This reduction in temperature applies to the east, west, and south façades, whereas it is insignificant for the north façade (AbdelMonteleb, 2013)

However, in another article by Abd El-Monteleb and Ali, the influence of vertical shading devices on the thermal performance of residential buildings for the same city (New Assiut) was clarified, the results showed that the 38 cm wide vertical slats lead to a reduction of the indoor temperature around 2°C in all the same three orientations as mentioned for horizontal shadow overhangs. However, for the northern façade, the result is similar to the research paper mentioned above (Abd El-Monteleb and Ahmed, 2012).

There is a lack of research to investigate the effects of fixed shading devices on cooling energy demand. In the meantime, study gap is there is no specific study on the impact of the width and number of fixed horizontal and vertical shading devices on the cooling loads for high-rise residential buildings with different orientations.

Therefore, this research attempts to answer the following question: To what extent the parametric variables (width, number, and orientation) of fixed horizontal and vertical shading elements are related to the annual cooling loads of residential high-rise buildings in the city of Sulaimani or another location with similar climatic characteristics.

There is a lack of research on the effects of fixed shading devices on energy demand for Sulaimani climate and condition. Meanwhile, there is no specific study on the impact of the width and number of fixed horizontal and vertical shading devices on the cooling loads for high-rise residential buildings with different orientations.

III. AIMS OF THE STUDY

The focus of this study is to review and to assess the impact of different orientations on the actual cooling energy consumption of a typical high-rise residential building. It is an investigation of the correlation between the reduction of cooling loads in these buildings and the construction and the design of fixed shading devices in various forms such as

vertical and horizontal. Furthermore, the setting of parameters for the required width and number of both vertical and horizontal fixed shading devices for frequently used opening sizes in typical high-rise residential buildings.

The research tries to find a suitable selection of shading elements that have a significant influence on the energy performance of such residential buildings.

IV. METHODOLOGY

To fill the knowledge gap identified above, a study will be conducted for a high-rise residential building in the city of Sulaimani through a computer simulation analysis using the DesignBuilder software (DesignBuilder, 2018) to determine the potential for annual savings of cooling energy through the use of fixed shading devices. Design Builder is exclusive software designed to model and to evaluate the environmental design and performance of buildings. This program uses climate data provided by the EnergyPlus simulation engine to calculate the energy consumption of buildings in terms of cooling, heating, and lighting loads (Shaeri, et al., 2019). It has been used consistently in many studies in this field. Furthermore, the reason for choosing this tool and method is the time and energy savings achieved by modeling the case in computer software instead of creating an actual model for testing and evaluation.

The study focuses on comparing and evaluating the effects of using different shading devices, namely, fixed horizontal and vertical shading elements, on all different window orientations in terms of annual cooling load requirements and total energy consumption. The main factors in this study are solar heat gain and direct normal solar radiation, as they have a direct influence on indoor air temperature and consequently on cooling loads.

The simulation process will be based on two main scenarios. A comparison will be made between these scenarios in terms of the effect of each type of proposed

shading element on the changes they have on the annual and monthly cooling loads.

V. SULAIMANI CLIMATE

The city of Sulaimani is located in Kurdistan Region in Iraq, at a latitude of 35°33'53.86" N and a longitude of 45°25'58.44" E (Date and Time .Info, 2020). And according to Koeppen's world map, it has a Mediterranean climate with dry summers and cool, wet winters (Csa) zone (Kottek , et al., 2006)

The climatic characteristics of Sulaimani are cold and rainy in winter, mild in spring and autumn. The city is characterized by long hot summer with high solar radiation, low humidity, and moderate rainfall. Fig. 1 shows the year-round temperatures for Sulaimani. The figure shows that the maximum temperature in January is 13°C, and the minimum is almost -14°C. Furthermore, the maximum temperature in July is 42°C.

In Sulaimani, direct solar radiation reaches its minimum in December and February, which is about 400 Wh/m², while the maximum radiation reaches almost 700Wh/m² in August, as shown in Fig. 2.

VI. THE CASE STUDY

One of the 23 high-rise residential buildings located at Darwaza city residential complex at the southern part of Sulaimani city in Kurdistan region of Iraq has been selected as the high-rise case study residential building because it has 13 floor and the building facades have windows in all orientations with no shading elements. The building is a point block (Neufert, et al., 2000) with a square-shaped layout. The total building gross floor area is 7696 m². The reason for choosing this building is that it is the most popular design type for high-rise residential buildings in Sulaimani and has the general configurations of this building type and also

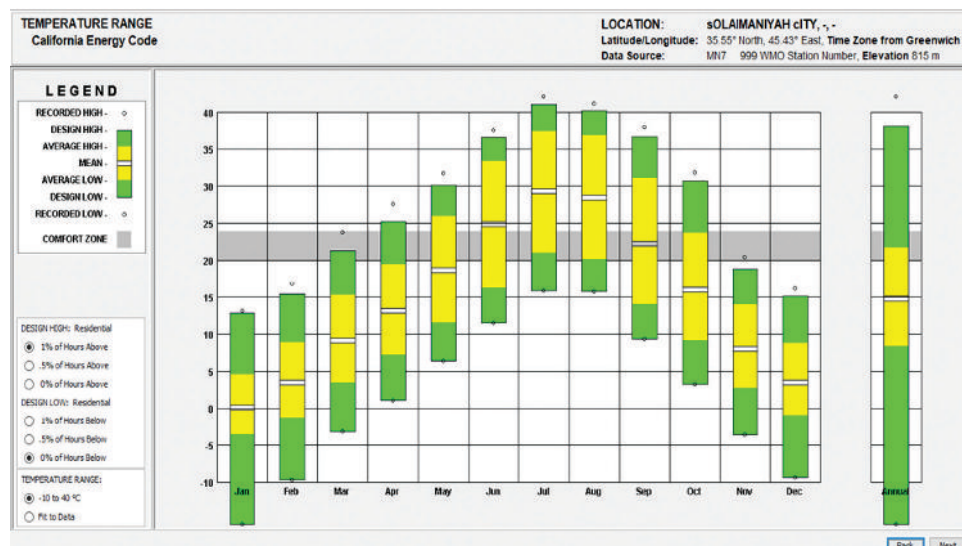


Fig. 1. Sulaimani air temperature data, based on the Sulaimani weather data file. Reproduced by climate consultant 6.0 software, 400 Wh/m², whereas the maximum radiation reaches almost 700 Wh/m² in August, see Fig. 2.

because it consumes a large amount of energy for cooling, which is about 377,000 kWh annually, Figs. 3 and 4.

The building is detached therefore it is facing all the four orientations (north, east, south, and west), However, on each floor, each apartment has two orientations, as shown in Table I. There are four apartments and a staircase on each floor, the total floor area is 592.6 m², the area of each apartment is approximately 148.2 m², with a ceiling height of 2.60 m. Furthermore, each apartment contains three bedrooms, two bathrooms in addition to the living room and a kitchen Figs. 5 and has two walls facing the outside. The sun enters each apartment through five windows, but the shading elements are installed and tested only on three windows of each apartment, as the other two windows already have a horizontal overhang of 1.0 m.

The standard building materials are listed in Table II. The glazing type is double glazing, clear glass, with 3mm

thickness of each pane, the air layer between the panes is 6 mm and no shading elements are attached. The total window/floor area is 85 m²; therefore, the window to wall ratio is 27%, this allows a high level of direct sunlight within the units. Besides, a split unit system is used for mechanical heating and cooling, which is powered by electricity from the grid and consumes a huge amount of energy annually.

A. Scenarios and Variables

Since thermal comfort and reduction of energy consumption for cooling, heating, lighting, or other purposes depend heavily on the orientation of the building and its opening (Ashmawy and Azmy, 2018) and also the amount of solar radiation strongly depends on the orientation of the building. Therefore, two scenarios were determined for the simulation based on the change in the orientation of the

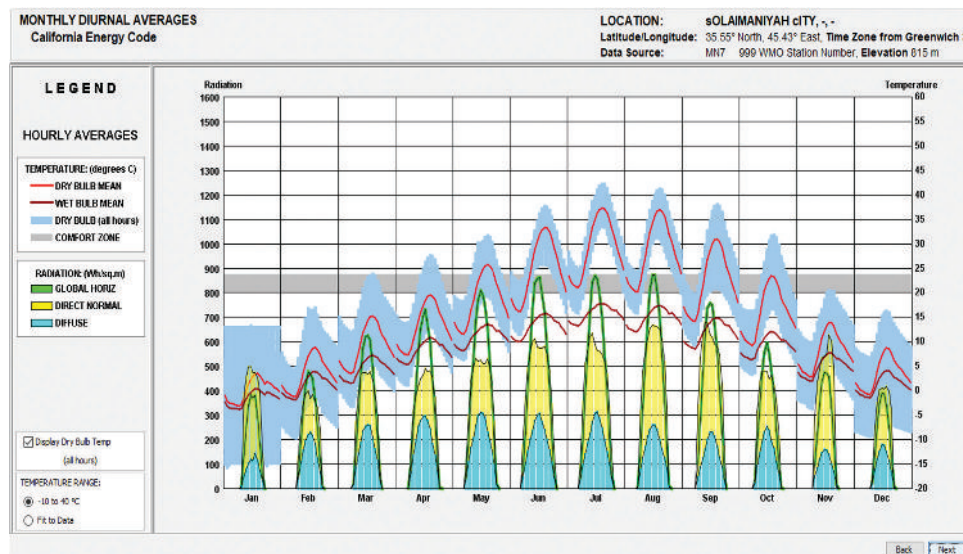


Fig. 2. Sulaimani monthly diurnal averages, based on the Sulaimani weather data file. Reproduced by Climate consultant were by electricity from the grid and consumes a huge amount of energy annually.

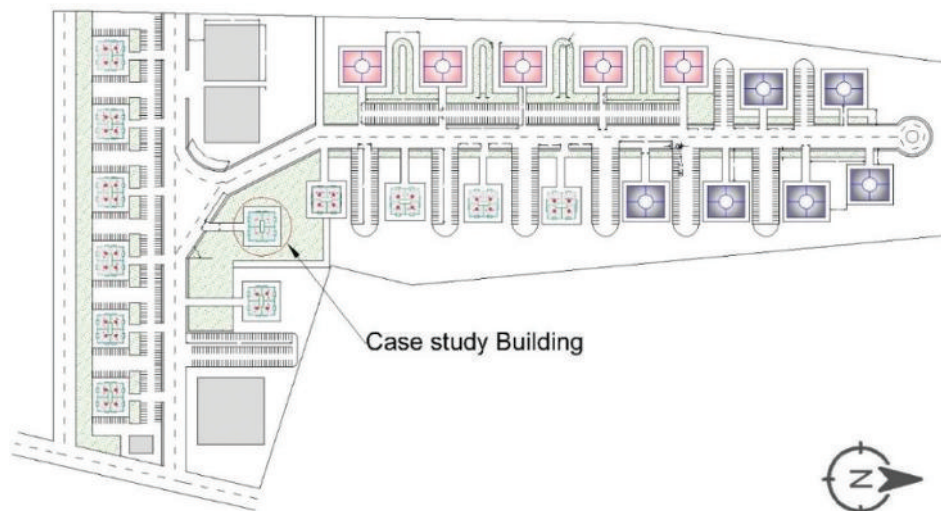


Fig. 3. Darwaza city site plan and the studied building located on it (Source: Author).

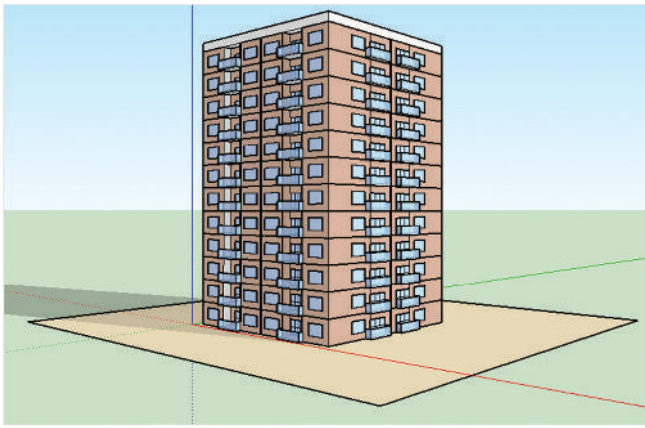


Fig. 4. Case study building model constructed in SketchUp (Source: Author).

case building. Scenario A is oriented in all four directions (north, east, south, and west), which it is the real building orientation, and scenario B is rotated 45° from the north, Figs. 6 and 7. Table I illustrates the setting of the two scenarios. However, the other variables in this study are the design and sizing of the shading elements and their effect on the annual cooling loads, which will be described in detail later.

B. The Shading Models, Configurations, and Details

The main objective in installing shading devices on a window is to prevent direct sunlight from entering the buildings and thus reduces overheating. According to the Sun shading table of the climate consultant software (Milne and



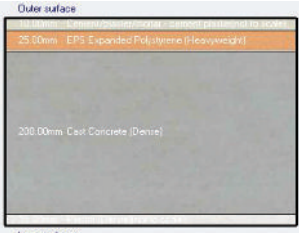


Fig. 5. Case study building typical floor layout (Source: Author).

TABLE I
THE ILLUSTRATIONS FOR THE SETTING OF THE TWO SIMULATION SCENARIOS AND THE ORIENTATION OF THE APARTMENTS IN THE PROTOTYPE BUILDING
(SOURCE: AUTHOR)

Apartment	Scenario A				Scenario B			
	Scenario -A-apartment code	Scenario -A-apartment orientation	Window code	Window orientation	Scenario -B-apartment code	Scenario -B-apartment orientation	Window code	Window orientation
1	1A	N, E	1A-W1	N	1B	NE, NW	1B-W1	NW
			1A-W2	N			1B-W2	NW
			1A-W3	E			1B-W3	NE
2	2A	N, W	2A-W1	N	2B	NW, SW	2B-W1	NW
			2A-W2	N			2B-W2	NW
			2A-W3	W			2B-W3	SW
3	3A	S, E	3A-W1	S	3B	NE, SE	3B-W1	SE
			3A-W2	S			3B-W2	SE
			3A-W3	E			3B-W3	NE
4	4A	S, W	4A-W1	S	4B	SE, SW	4B-W1	SE
			4A-W2	S			4B-W2	SE
			4A-W3	W			4B-W3	SW

TABLE II

REAL CASE BUILDING CONSTRUCTION MATERIALS (SOURCE: AUTHOR)

External walls	Materials (out to in)	Thickness mm
	Cement/plaster/mortar	30.00
	EPS expanded polystyrene	25.00
	Cast concrete	200.00
	Plaster (dense)	15.00
Slabs	Materials	Thickness mm
	Timber flooring	10.00
	Floor/roof screed	50.00
	Cast concrete (dense)	200.00
	Air gap (downwards)	100.00
	Gypsum plasterboard	20.00
Internal walls	Materials	Thickness mm
	Gypsum plasterboard	30.00
	Concrete block (light weight)	100.00
	Gypsum plasterboard	30.00

Liggett, 2019), Sulaimani climate has 1217 h of sunshine in the summer-autumn season from June 21 to December 21, when the temperature is higher than 27°C, which is perceived as unpleasant and requires shade, Fig. 8.

Therefore, a comparative analysis between horizontal and vertical shading elements (with different depth and number) was performed on the described building windows on all orientations in both scenarios to evaluate their impact on the annual cooling energy consumption. Furthermore, the proper depth, shape, and number of elements that would result in a higher reduction of cooling energy for Sulaimani climate were determined and tested with DesignBuilder. As the sixth floor is located in the middle of the building (12 floors + the ground floor), it was selected to study, assuming that the results are almost the same for all the apartments of the building.

According to the Sun shading table of the climate consultant software (Milne and Liggett, 2019), Sulaimani climate has 1217 h of sunshine in the summer-autumn season from June 21 to December 21

Table III shows the configuration of the shading elements tested in this study. The most suitable and reasonable shapes and widths are tested according to the altitude angle of the city of Sulaimani, which is about 80° maximum in June and 30° minimum in December (Milne and Liggett,

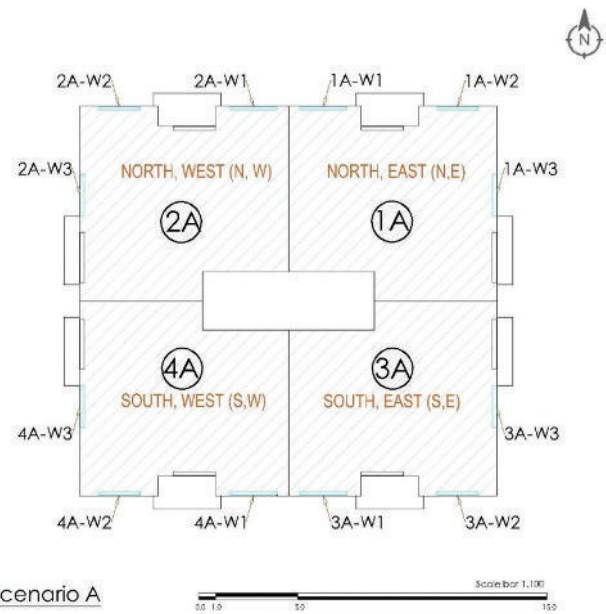


Fig. 6. Scenario (A) case study real orientations (North, East, South, and West) – Plan (Source: Author).

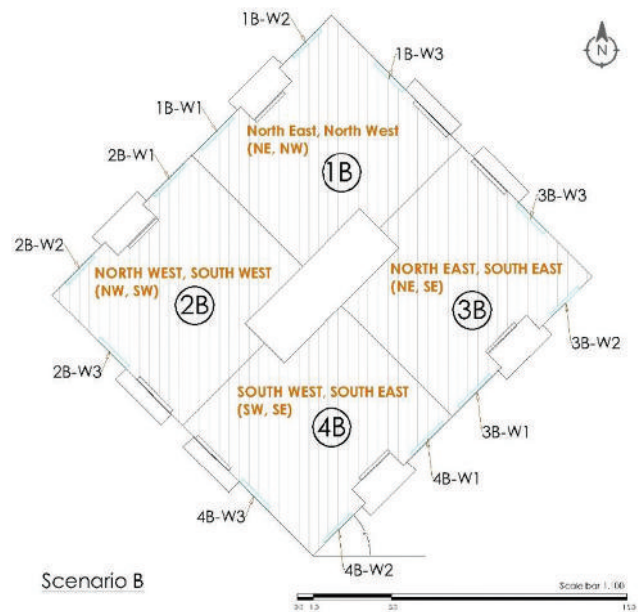


Fig. 7. Scenario (B) case study orientation rotated 45° from the North – Plan (Source: Author), when the temperature is higher than 27°C, which is perceived as unpleasant and requires shade, Fig. 8.

2019). Therefore, the effect of single, double, and triple fixed horizontal shading devices on the cooling energy performance of each apartment will be tested. The length of the horizontal blinds was determined according to the width of the windows, which is 250 cm. As with the vertical units, fixed shading devices are chosen and tested at three different depths along the length of the window, as shown in Table III and Fig. 9.

Depths greater than 60 cm are not considered, as this is not practical and negatively affects natural lighting and

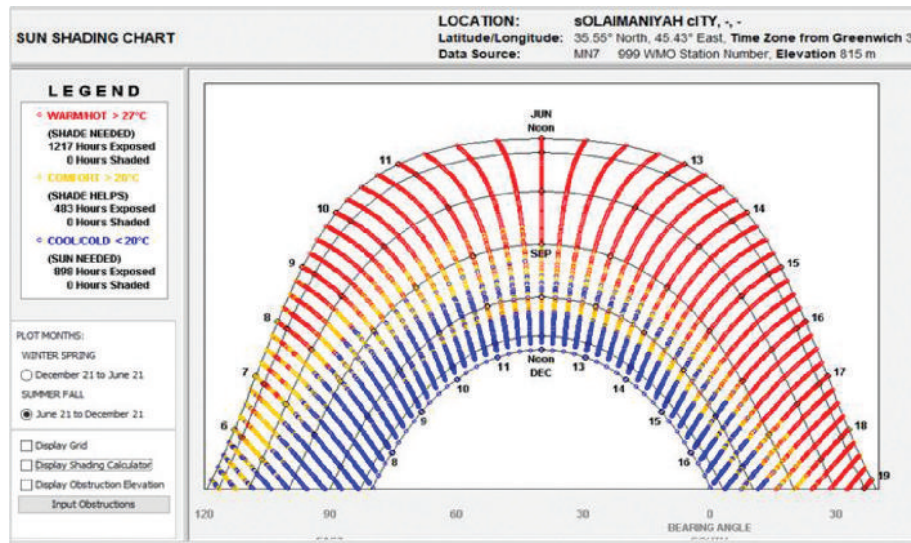


Fig. 8. Sun shading chart reproduced from climate consultant 6.0 software (Milne and Liggett, 2019).

TABLE III
 SHADING ELEMENTS ARRANGEMENT AND NUMBER (SOURCE: AUTHOR)

Horizontal shading elements			Vertical shading elements		
Number of louvers	Width(cm)		Number of fins	Width(cm)	
1	20		3	20	
	40			40	
	60			60	
Horizontal shading elements			Horizontal shading elements		
Number of louvers	Width (cm)		Number of louvers	Width (cm)	
2	20		3	20	
	40			40	
	60			60	

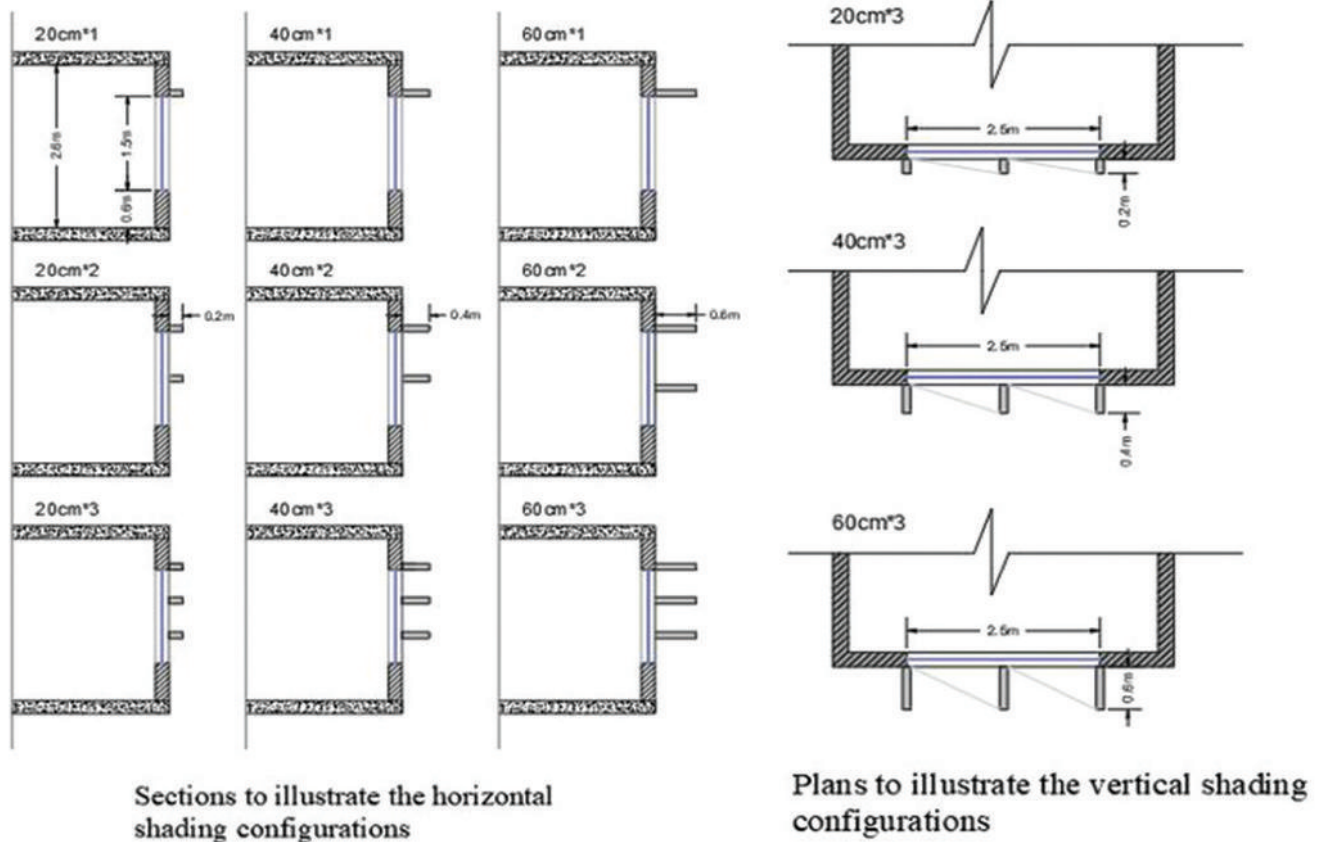


Fig. 9. Plans and sections of the shading elements arrangement and dimensions (Source: Author).

obstructs visibility according to previous studies. Besides, the thickness of all slats has been set at a fixed 10 cm and all are made of concrete.

VII. THE SIMULATION

The case study high-rise residential building has been modeled in the DesignBuilder software based on the actual building specifications and construction materials and entering the Sulaimani EnergyPlus weather data file into the software, the operating temperature was set for the operation of mechanical cooling with the split-unit system and natural ventilation was switched off, Table IV. The cooling period starts from April to the end of October. However, the annual cooling load consumption is also recorded from the simulation to evaluate the impact of the fixed shading devices on it. Therefore, a simulation of the annual energy consumption was performed for scenarios A and B, with 13 individual simulations for each scenario. The first simulation refers to the energy performance of each floor plan including four apartments without shading devices, nine simulations for the horizontal shading elements, and the last three simulations refer to the vertical shading elements Fig. 8. A total of 26 simulations were carried out for each floor plan to evaluate and to analyze the best shading device for each scenario and orientation.

TABLE IV
TEMPERATURE INDICATORS OF THE MECHANICAL SPLIT UNIT COOLING SYSTEM SET FOR THE CASE STUDY (CIBSE, 2006)

Room	Cooling air supply temperature °C	Cooling set back temperature °C
Living room	21	25
Kitchen	19	22
Bedrooms	21	25
Bathrooms	22	25
Circulation	21	25
Store	21	25

VIII. RESULTS AND DISCUSSION

The simulation analysis results show that the months April to October are considered hot months in which cooling systems are highly required. The results indicate that a change in orientation of the building and other variables such as the width and number of shading elements, influence the level of cooling loads inside the modeled residential building.

The total annual cooling load required for each floor is 29,494 kW/h without installation of shading for scenario A, whereas for scenario B the total is 30,204 kW/h. August shows the highest energy demand for cooling for all alignments before and after the installation of shading devices.

A. Horizontal Louvers

After simulating the model without shading devices, a single fixed horizontal louver was installed on the top of the windows. In general, the results showed that for both scenarios (A and B), a single fixed horizontal louver with a depth of 20 cm reduced the cooling loads by only 2% of the total annual cooling loads, Table V.

However, in some orientations, the extension of the louver width has improved the performance of the blades. Individual fixed louvers with a width of 40 cm and 60 cm do not show a significant reduction in cooling loads for apartments 1A, 1B and 2A, 2B, as shown in Table VI. Yet, the effect of the width expansion is noticeable with the 60 cm wide fixed individual louver and reaches about 5.0% for apartments 3 and 4 in both scenarios.

Nevertheless, the effect of adding another fixed louver to the 40 cm and 60 cm deep slats of the windows is more obvious and the reduction in energy consumption is almost twice as high as with the single fixed horizontal shading device. For a moment, the double fixed 60 cm louver led to a maximum 9.4% reduction of cooling loads in apartment 4B, whereas, the least reduction, however, is 3.4% for apartment 2A when using a 40 cm louver. Moreover, the role of changing the orientation of the building is evident.

The effect of using double fixed blades on the cooling load of the same flat with different orientation cannot be ignored. For example, the difference in cooling load reduction for apartments 2A oriented North West (N, W) and 2B oriented northwest-southwest (NW, SW) is around 2.5%, as shown in Table VII.

Meanwhile, the 40 cm triple fixed blinds have an almost similar effect of the 60 cm triple fixed blinds on the reduction of the cooling loads for both scenarios A and B. Therefore, the 40 cm triple fixed blinds are more efficient, as the results in Table VIII show. Compared with the study by (AbdelMonteleb, 2013) which is carried out for hot, and arid desert climate, the results are more dissimilar with increasing horizontal shading, the greater the overhang, the lower the ambient temperature.

B. Vertical Fins

After analyzing the data, as shown in Table IX, it can be concluded that the maximum reduction of cooling loads can reach almost 5% after installing triple fixed vertical shading elements. However, the 20 cm vertical fins have an insignificant influence on the cooling loads. Except for apartments 3B (NE, SE) and 4B (SW, SE), which reaches about 3.0%.

TABLE V
EFFECT OF SINGLE FIXED HORIZONTAL SHADING DEVICES (20 CM WIDTH) ON BOTH SCENARIOS A AND B (SOURCE: AUTHOR)

Apartment	Scenario A				Apartment	Scenario B			
	Annual cooling load		Reduction kW	Reduction percentage		Annual cooling load		Reduction kW	Reduction percentage
	Without shade (kW)	With shade (kW)				Without shade (kW)	With shade (kW)		
N, E	7327	7265	62	0.8%	NE, NW	7391	7324	67	0.9%
N, W	7076	7037	39	0.6%	NW, SW	7615	7491	124	1.6%
S, E	7671	7514	157	2%	NE, SE	7532	7447	85	1.1%
S, W	7420	7283	137	1.8%	SE, SW	7666	7532	134	1.7%

TABLE VI
EFFECTS OF SINGLE FIXED HORIZONTAL LOUVERS ON BOTH SCENARIOS A AND B (WIDTH OF 40 CM AND 60 CM) ON THE ANNUAL COOLING LOADS (SOURCE: AUTHOR)

Apartment	1 Horizontal louvre - 40 cm width						1 horizontal louver - 60 cm width					
	Scenario A		% Cooling loads Reduction	Scenario B		% Cooling loads Reduction	Scenario A		% Cooling loads Reduction	Scenario B		% Cooling loads Reduction
	Cooling load kWh			Cooling load kWh			Cooling load kWh			Cooling load kWh		
	No shade	With shade	No shade	With shade	No shade	With shade	No shade	With shade	No shade	With shade		
1	7327	7202	1.7%	7391	7243	2%	7327	7147	2.4%	7391	7177	2.9%
2	7076	6982	1.3%	7532	7346	2.5%	7076	6935	2.0%	7532	7263	3.6%
3	7671	7361	4.0%	7615	7353	3.4%	7671	7255	5.4%	7615	7245	4.9%
4	7420	7141	3.7%	7666	7380	3.7%	7420	7045	5.0%	7666	7302	4.7%

TABLE VII
EFFECTS OF DOUBLE FIXED HORIZONTAL LOUVERS, SCENARIOS A AND B (WIDTH OF 40 CM AND 60 CM) ON THE ANNUAL COOLING LOADS (SOURCE: AUTHOR)

Apartment	2 Horizontal louvers - 40 cm width						2 Horizontal louvers - 60 cm width					
	Scenario A		% Cooling loads Reduction	Scenario B		% Cooling loads Reduction	Scenario A		% Cooling loads Reduction	Scenario B		% Cooling loads Reduction
	Cooling load kWh			Cooling load kWh			Cooling load kWh			Cooling load kWh		
	No shade	With shade	No shade	With shade	No shade	With shade	No shade	With shade	No shade	With shade		
1	7327	7026	4.0%	7391	7025	5.0%	7327	6986	4.6%	7391	6977	5.6%
2	7076	6832	3.4%	7532	7098	5.8%	7076	6798	4%	7532	7035	6.6%
3	7671	7080	7.7%	7615	7049	7.4%	7671	7017	8.5%	7615	6963	8.5%
4	7420	6890	7.1%	7666	7046	8.0%	7420	6835	7.9%	7666	6945	9.4%

TABLE VIII

EFFECTS OF TRIPLE FIXED HORIZONTAL LOUVERS ON SCENARIOS A AND B (WIDTH OF 20 CM, 40 CM AND 60 CM) ON THE ANNUAL COOLING LOADS (SOURCE: AUTHOR)

Apartment	3 Horizontal louvers – 20 cm width					
	Scenario A Cooling load kWh		% Cooling loads Reduction	Scenario B Cooling load kWh		% Cooling loads Reduction
	No shade	With shade		No shade	With shade	
1	7327	7032	4%	7391	7034	4.8%
2	7076	6837	3.3%	7532	7123	5.4%
3	7671	7127	7%	7615	7092	6.8%
4	7420	6934	6.5%	7666	7105	7.3%

Apartment	3 Horizontal louvres – 40 cm width					
	Scenario A Cooling load kWh		% Cooling loads Reduction	Scenario B Cooling load kWh		% Cooling loads Reduction
	No shade	With shade		No shade	With shade	
1	7327	6912	5.6%	7391	6898	6.6%
2	7076	6742	4.7%	7532	6970	7.4%
3	7671	6961	9.3%	7615	6909	9.2%
4	7420	6793	8.4%	7666	6903	9.9%

Apartment	3 Horizontal louvers – 60 cm width					
	Scenario A Cooling load kWh		% Cooling loads Reduction	Scenario B Cooling load kWh		% Cooling loads Reduction
	No shade	With shade		No shade	With shade	
1	7327	6900	5.8%	7391	6884	6.8%
2	7076	6731	4.8%	7532	6945	7.7%
3	7671	6931	9.6%	7615	6867	9.8%
4	7420	6766	8.8%	7666	6839	10%

TABLE IX

EFFECTS OF TRIPLE FIXED VERTICAL SHADING ELEMENTS ON SCENARIOS A AND B (WIDTH OF 20 CM, 40 CM AND 60 CM) ON THE ANNUAL COOLING LOADS (SOURCE: AUTHOR)

Apartment	3 Vertical Shading Elements – 20 cm width					
	Scenario A Cooling load kWh		% Cooling loads reduction	Scenario B Cooling load kWh		% Cooling loads reduction
	No shade	With shade		No shade	With shade	
1	7327	7168	2.2%	7391	7189	2.7%
2	7076	6940	1.9%	7532	7321	2.8%
3	7671	7456	2.8%	7615	7371	3.2%
4	7420	7228	2.6%	7666	7429	3.0%

Apartment	3 Vertical Shading Elements – 40 cm width					
	Scenario A Cooling load kWh		% Cooling loads reduction	Scenario B Cooling load kWh		% Cooling loads reduction
	No shade	With shade		No shade	With shade	
1	7327	7103	3%	7391	7080	4.2%
2	7076	6878	2.8%	7532	7207	4.3%
3	7671	7375	3.8%	7615	7245	4.8%
4	7420	7149	3.6%	7666	7306	4.7%

Apartment	3 Vertical Shading Elements – 60 cm width					
	Scenario A Cooling load kWh		% Cooling loads reduction	Scenario B Cooling load kWh		% Cooling loads reduction
	No shade	With shade		No shade	With shade	
1	7327	7119	2.8%	7391	7065	4.4%
2	7076	6886	2.7%	7532	7205	4.3%
3	7671	7409	3.4%	7615	7251	4.7%
4	7420	7175	3.3%	7666	7319	4.5%

For the triple fixed 40 cm slats, as far as the scenarios are concerned, the percentages of reducing the cooling loads are higher in scenario B because of alignment. The highest reduction is 4.8% and can be seen in apartment

3B, orientation NE, SE. Yet, even if the depth of the slats is increased from 40 cm to 60 cm for both scenarios, still the 40 cm fixed slats are more effective in reducing solar radiation than the slats with 60 cm depth.

TABLE X
THE EFFECT OF TRIPLE FIXED VERTICAL AND HORIZONTAL SHADING DEVICES (40 CM WIDTH) ON SCENARIO A (SOURCE: AUTHOR)

Scenario (A)	Horizontal				Vertical			
	Annual cooling load		Reduction kW	Reduction percentage %	Annual cooling load		Reduction kW	Reduction percentage %
	Without shade (kW)	With shade (kW)			Without shade (kW)	With shade (kW)		
1 N, E	7327	6912	415	5.6%	7327	7103	224	3.0%
2 N, W	7076	6742	334	4.7%	7076	6875	201	2.8%
3 S, E	7671	6961	710	9.3%	7671	7375	296	3.8%
4 S, W	7420	6793	627	8.4%	7420	7149	271	3.6%

TABLE XI
THE EFFECT OF TRIPLE FIXED VERTICAL AND HORIZONTAL SHADING DEVICES (40 CM WIDTH) ON SCENARIO B (SOURCE: AUTHOR)

Scenario (B)	Horizontal				Vertical			
	Annual cooling load		Reduction kW	Reduction percentage %	Annual cooling load		Reduction kW	Reduction percentage %
	Without shade (kW)	With shade (kW)			Without shade (kW)	With shade (kW)		
1 NE, NW	7391	6898	493	6.6%	7391	7080	311	4.2%
2 NW, SW	7532	6970	562	7.4%	7532	7207	325	4.3%
3 NE, SE	7615	6909	706	9.2%	7615	7245	370	4.8%
4 SE, SW	7666	6903	763	9.9%	7666	7306	360	4.7%

There is a similarity between the above-mentioned result and the results of a research on the influence of vertical shading devices on thermal performance for hot, arid climate (Abd El-Monteleb and Ahmed, 2012) only for the north facade. Because the results showed that the lower the ambient temperature for other facades, the greater the projection, whereas an increase in the length of more than 38 cm is insignificant for the north facade.

C. Comparison between the Horizontal and Vertical 40 cm Wide Louvers

It is shown from Table X and Table XI that the fixed horizontal slats work better than the fixed vertical slats in both scenarios. In Scenario A, the vertical slats, the maximum percentage of annual cooling loads reduction is of the apartment 3A, by 3.8%. Whilst, the horizontal louvers performed better and the least reduction was 4.7% in apartment 2A and went up to 9.3% in apartment 3A. As of Scenario B, the positive effect of the fixed horizontal slats is noticeable for all apartments; the decrease is ranged between 6.6% and 9.9%. However, the highest effect of the fixed vertical shading elements can be observed in apartment 3B, where the reduction is only 4.8%.

IX. CONCLUSIONS

This research looked at the impact of modifying fixed horizontal and vertical concrete shading components through different orientations in Sulaimani weather conditions. To study aimed their effect on cooling energy consumption of a 13-storey residential building in the city. As far as the results are concerned, fixed shading devices can be used as an architectural element and as a climate-responsive strategy in the design of buildings in Sulaimani. Noticeably, a single horizontal louver with a depth of 20 cm installed on the top of any window, with any of the eight main orientations of a compass, is considered inefficient. Its effect can be almost

neglected, as leads to a maximum reduction of the annual cooling loads of an apartment by only 2%. Moreover, triple vertical shadings with a depth of 20 cm, installed in the middle and on both sides of each window with any of the tested orientation, are considered inefficient too. As in both Scenarios A and B, they only affect the energy consumption for cooling the apartments by a maximum of only 3.2%.

Conversely, the most effective fixed shading element is a triple horizontal with 60 cm width, for all the selected orientations of both scenarios. Its effectiveness results in a 7% reduction in the energy required for cooling the four apartments on one floor in scenario A, and 9% in scenario B. Besides, the analyzed data illustrate that a 60 cm double horizontal shading device has almost the same effect as a 40 cm triple horizontal ones. As of the 40 cm and 60 cm triple vertical slats, the reductions in annual cooling demands are very close for both widths. In Scenario A; lead to a reduction of the cooling load in all apartments by almost 2.7–3.8%. In Scenario B, however, the reduction of the cooling load is in the range of 4.2–4.8%. In fact, the 40 cm deep fins are more efficient and are considered more effective.

Eventually, the triple 60 cm horizontal shading device has twice the effect on the cooling load of all apartments in Scenarios A and B than a triple-fixed 60 cm vertical shading device, except for apartments 3A and 4A, where the fixed horizontal component has a triple effect.

In conclusion, these effective louvers according to the results are recommended to be used in high-rise residential buildings for hot climates from the early stages of design as a passive design strategy to contribute in lessening energy demand in high-rise residential buildings in particular and the residential sector in general.

REFERENCES

Abd El-Monteleb, A. and Ahmed, M.A., 2012. Using simulation for studying the influence of vertical shading devices on the thermal performance of residential

- buildings (Case study: New Assiut City). *Ain Shams Engineering Journal*, 3(2), pp.163-174.
- Idchabani, R., El Ganaoui, M. and Sick, F., 2017. Analysis of exterior shading by overhangs and fins in hot climate. *Energy Procedia*, 139, pp.379-384.
- AbdelMonteleb, A., 2013. Using simulation for studying the influence of horizontal shading device protrusion on the thermal performance of spaces in residential buildings. *Alexandria Engineering Journal*, 52(4), pp.787-796.
- Ali, M.M. and Al-Kodmany, K., 2012. Tall Buildings and Urban Habitat of the 21st Century: A Global Perspective. *Buildings*, 2(4), pp.384-423.
- Alzoubi, H.H. and Al-Zoubi, A., 2010. Assessment of building façade performance in terms of daylighting and the associated energy consumption in architectural spaces: Vertical and horizontal shading devices for southern exposure facades. *Energy Conversion and Management*, 8(51), pp.1592-1599.
- Arsalan, G. and Sev, A., 2014. *Significant Issues in and Around High-Rise Residential Environments*. Mimar Sinan Fine Arts University, Istanbul.
- Ashmawy, R.E. and Azmy, N.Y., 2018. Buildings orientation and its impact on the energy consumption. *The Academic Research Community Publication*, 2(3), pp.35-49.
- Athienitis, A. and Haghghat, F., 1992. *A Study of the Effect of Solar Radiation on the indoor Environment*. Amer Society of Heating, Anaheim, CA, pp.257-261.
- CIBSE, 2006. *CIBSE Guide A: Environmental Design*. The Chartered Institution of Building Services Engineers, London, Norwich.
- Date and Time Info., 2020. *Date and Time*. Available from: <https://www.dateandtime.info/citycoordinates.php?id=98463>. [Last accessed on 2020 Oct 16].
- Datta, G., 2001. Effect of fixed horizontal louver shading devices on thermal performance of building by TRNSYS simulation. *Renewable Energy*, 23(3-4), pp.497-507.
- DesignBuilder., 2018. *Designbuilder Software ltd.v.5.5.2.3*. Available from: <https://www.designbuilder.co.uk>. [Last accessed on 2018 Dec 01].
- Kim, J.T. and Kim, G., 2010. Advanced external shading device to maximize visual and view performance. *Indoor and Built Environment*, 19(1), pp.65-72.
- Kottek, M., Grieser, J., Beck, C., Rudolf, B. And Rubel, F., 2006. World Map of Köppen-Geiger Climate Classification. *Meteorologische Zeitschrift*, 15(3), pp.259-263.
- Milne, N. and Liggett, R., 2019. *Climate Consultant v.6 Build 15*. Available from: <http://www.energy-design-tools.aud.ucla.edu>. [Last accessed on 2020 Oct 01].
- Morad, D.H. and Ismail, S.K., 2017. A comparative study between the climate response strategies and thermal comfort of a traditional and contemporary houses in KRG: Erbil. *Kurdistan Journal of Applied Research*, 2(3), pp.1-11.
- Neufert, E., Neufert, P. and Baiche, B., 2000. *Neufert Architects' Data*. 3rd ed. Blackwell Publishing, Oxford.
- Shaeri, J., Habibi, A., Yaghoubi, M. and Chokhachian, A., 2019. The optimum window-to-wall ratio in office buildings for hot-humid, hot-dry, and cold climates in Iran. *Environments*, 6, pp.5-16.
- Shahdan, M., Ahmad, S. and Hussin, M.A., 2018. External Shading Devices for Energy Efficient Building. Vol. 117. *IOP Conference Series: Earth and Environmental Science*.
- Tariq, S.H. and Jinia, M.A., 2012. Effect of fixed horizontal shading devices in south facing residential buildings at Dhaka, Bangladesh. *Asian Journal of Applied Science and Engineering*, 1(2), pp.9-19.

Structural Behavior of Reinforced Concrete Beams Incorporating Foamed Glass as Aggregates

Dawood S. Atrushi

Department of Civil Engineering, College of Engineering, University of Duhok,
Duhok, Kurdistan Region – F.R. Iraq

Abstract—Natural resources that are utilized in civil engineering applications can be saved by replacing them with some recycled materials to produce sustainable concrete with required mechanical and durability properties. In recent years, recycled glass is being used as aggregates in concrete production in many countries across the world. In the present study, the structural properties of reinforced concrete beams containing foamed glass (FG) as a partial natural coarse aggregate replacement are investigated. Five concrete mixes were employed to conduct the present study. The coarse aggregate was replaced with 0%, 25%, 50%, 75%, and 100% (by volume) of FG. Four point-loading flexural tests on beams were conducted up to failure. The results showed that the compressive strength was decreasing linearly with the increasing amount of FG. It was also observed that the ductility of the reinforced concrete beams significantly improved. However, the load-carrying capacity of the beam and load at which the first crack occurs was reduced. It was concluded that the inclusion of FG in structural concrete applications is possible and the structural behavior of concrete beams proved to be similar to that of other types of lightweight aggregate concrete such as wood and plastic aggregates used in similar structural elements.

Index Terms—Aggregate, Concrete, Foamed glass, Reinforced concrete beam, Strength, Structural behavior.

I. INTRODUCTION

The environmental building design and construction have recently witnessed a surge in the consideration of the sustainability of structure and its effects. Natural materials that are utilized in the construction of a project can be saved by replacing them with recycled lightweight aggregate to produce lightweight aggregate concrete. The commercial demand for light yet strong concrete has been gaining popularity for the past few decades in the construction industry, such as in concrete cellular blocks (Rostam, Ali and Atrushi, 2016). The relatively heavy self-weight of normal concrete where the density is about 2400 kg/m³, poses risks of earthquake damage in a structure (Kilic, et al.,

2003); in most cases, high rise buildings are affected during earthquakes due to the higher unit weight of normal concrete (Wuest, Denarié and Bruhwiler, 2007). Lighter concrete offers design flexibility and considerable cost savings due to its inherent economies and advantages over normal concrete in a variety of structural applications by providing less dead load, longer spans such as long-span bridges and flyovers, and low heat conductivity (Shafigh, et al., 2011).

Glass is amongst the oldest man-made materials and as such has been used for many years in various applications. As a result, a large volume of post-consumer glass is being generated and discarded often which is likely to increase considerably in the future. Therefore, in recent years several studies have been conducted to evaluate and promote the potential use of waste glass in new concrete production. As a result, waste and recycled glass is now being used as aggregates in concrete production in many countries across the world. Foamed glass (FG) aggregates offer several advantages such as the design of lightweight concrete and its presence as an environmentally-friendly material by preserving the environment through means of reducing landfills and saving more natural resources. However, the use of FG aggregates in concrete production as a partial or full replacement to natural aggregates has generally indicated toward a decrease in the compressive strength in comparison to normal concrete. It was also observed that mixes containing FG aggregates tend to gain slightly higher early compressive strength compared to normal concrete; this could be due to the high alkali content in the FG aggregates (Adom-Asamoah and Afrifa, 2010). In general, with an increase in the replacement of natural aggregates with recycled materials a decrease in compressive strength has been reported (Herki and Khatib, 2016). Investigations on the full replacement of natural aggregates by FG aggregates have shown a substantial drop in the mechanical and durability properties of the concrete which does not even meet the required 28-days strength and durability performance (Shuab and Ray, 1991; Demirbog and Gu, 2003; Rossignolo, Agnesini and Morais, 2003; Hossain, 2004; Babu, Babu and Wee, 2005; Gennaro, et al., 2008; Subasi, 2009; Limbachiya, Meddah and Fotiadou, 2012). The authors express that there are still gaps in our knowledge of the properties and structural behavior of concrete containing FG; because concrete properties can vary considerably depending on

ARO-The Scientific Journal of Koya University
Vol. IX, No.1 (2021), Article ID: ARO.10746, 60 pages
DOI:10.14500/aro.10746

Received: 01 November 2020; Accepted: 01 February 2021

Regular research paper: Published: 01 March 2021

Corresponding author's e-mail: dawood.sulaiman@uod.ac

Copyright © 2021 Dawood S. Atrushi. This is an open-access article distributed under the Creative Commons Attribution License.



the type of FG and the technique of recycling used, and so any conclusions may only be valid for the specific project studied. There is not enough information in the literature on the structural behavior of concrete containing FG; therefore, in this study; an experimental program was conducted to investigate the structural behavior of reinforced concrete beams incorporating FG as natural aggregates replacement.

II. MATERIALS AND METHODS

The cement used was ordinary Portland cement. The fine aggregates used were river sand with particles ranging from 63 μm to 4 mm in size. The coarse aggregates were natural gravel and stones with particles ranging from 4 mm to 20 mm in size. The foam glass coarse particles, shown in Fig. 1, used as partial replacement of natural coarse aggregates were also similar in size ranging from 4 mm to 20 mm, where particle size distribution or grading is done according to BS EN 933-1:1997. Foam glass was originally manufactured from waste glass by generating a gas in glass at a temperature between 700°C and 900°C, where foaming agents such as calcium sulfate (CaSO_4) or calcium carbonate (CaCO_3) are also added (Hurley, 2003). The gas expands thus producing a structure of cells to form a porous body. The density of coarse aggregate and FG is 1200 kg/m^3 and 267 kg/m^3 , respectively.

For all concrete mixtures, the cement content and the W/C ratio were kept constant at 330 kg/m^3 and 0.5, respectively. The mixtures had proportions of 1 (cement): 2 (fine aggregates): 4 (coarse aggregates). For this experimental program, five mixtures were carried out consisting of three reinforced concrete beams for each mixture with rectangular cross-sections of 100 mm width \times 150 mm depth \times 700 mm length. The first mix, which was used as the reference mix, comprises of 100% natural aggregates. In the remaining mixes the natural aggregates have been partially replaced by different amounts of FG aggregates in terms of volume with replacement levels of 25%, 50%, 75%, and 100%.

The variation in the number of replacements was used to obtain more data which could be used to draw a better conclusion. Table I illustrates the mix combinations, and the given numbers 0–187.2 kg for the FG have the same volume of the 1316–0 kg of coarse aggregate. The grading curves complied with BS EN 933-1:1997 for the natural and FG aggregates and are presented in Fig. 2.

A total of 15 reinforced beams were made from five different mixtures as stated previously. The number of compression bars was two for all beams, but those in tension consisted of three for each concrete beam with 12 mm bar diameter. The compression reinforcement at the top was primarily for holding purposes and ease of holding stirrups upright. The shear links were 8 mm diameters and placed at 50 mm centers to the sides and 75 mm centers toward flexural zones as shown in Fig. 3b. Loading set-up for the reinforced concrete beams is shown in Fig. 3a. The yield stress of the steel bars is 415 MPa.

Three reinforced concrete beams along with three cubes (100 mm \times 100 mm \times 100 mm) were cast from each concrete



Fig. 1. Foam glass coarse particle.

TABLE I
FULL DETAILS OF CONCRETE MIXTURES (kg/M^3)

Mix No.	FG (%)	Cement	Water	FA	CA	FG	W/C
1	00	330	165	658	1316	0	0.5
2	25	330	165	658	987	47.1	0.5
3	50	330	165	658	658	94.3	0.5
4	75	330	165	658	329	140.1	0.5
5	100	330	165	658	0	187.2	0.5

mix. Plywood mold was used for the beams whereas steel molds conforming to BS EN 12390-2:2012 was used for the cubes. Before casting began, the molds were visually inspected and cleaned thoroughly. Thereafter, a thin layer of oil was applied to the inside surfaces of the molds for easy de-molding.

The concrete mixer was cleaned and slightly damped with water to avoid any absorption of water by the concrete mixer. The required material; fine aggregates, coarse aggregates, FG, and cement were then gently poured into the mixer. Once all the dry materials were inside, the mixer water was then poured little by a little while mixing. After almost 5 min of through mixture until the texture of the concrete was satisfied, the mixing process was stopped and a slump test was carried out in accordance to BS EN 12350-2:2009 to test the properties of fresh concrete such as concrete consistency and the workability.

In the meantime, an already prepared reinforcement cage was gently placed into the molds after applying the thin layer of oil on the inside surface, the appropriate cover was provided for top and bottom along with both sides. Concrete was poured into the molds up to about half level and then compacted using a vibrator table, and the second layer of concrete was then poured to the top level of the molds and compacted again. Along with the beams, three cubes of 100 mm \times 100 mm \times 100 mm from each mix combination to determine the mechanical properties were also prepared in a similar manner using a testing machine of 3000 kN capacity at the loading rate of 0.6 MPa/s complied with BS EN 12390-4:2000. Fresh concrete was poured into the steel molds in three equal layers, and then compacted to a smooth

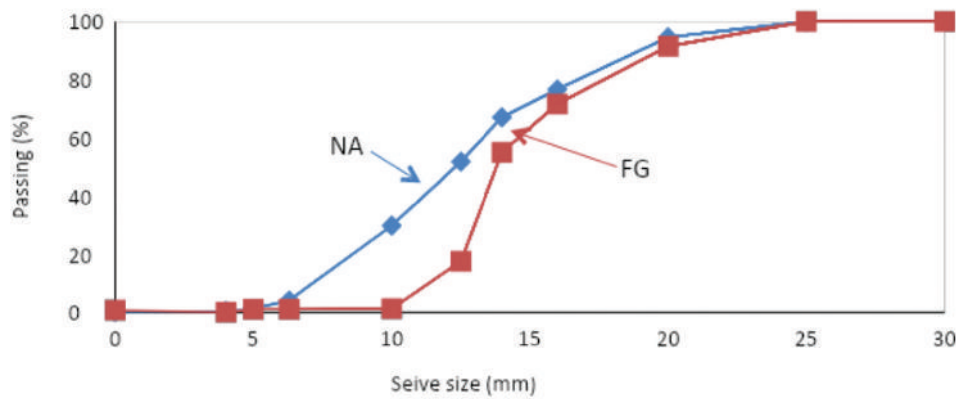


Fig. 2. Particle size distribution of aggregates.

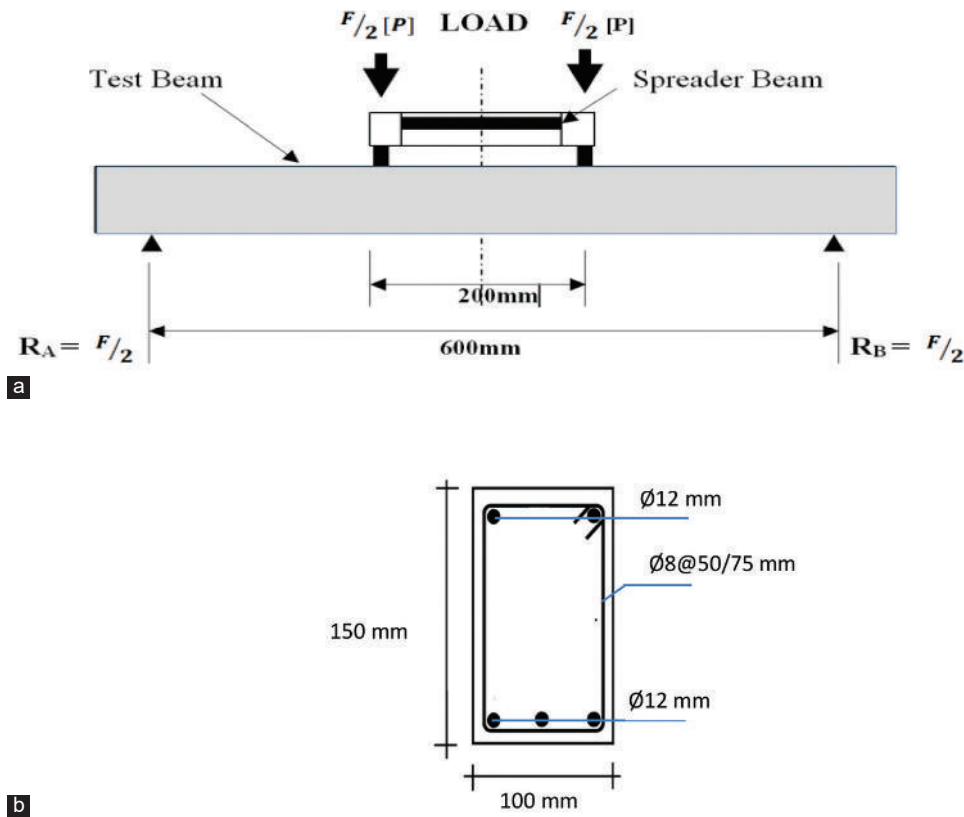


Fig. 3. (a) Loading set-up for the reinforced concrete beams, (b) typical cross-section with steel bars and stirrups.

finish and top surface. The completed beams and cubes were then left for settling down for approximately 24 h at room temperature. The following day they were de-molded and marked with the corresponding mix propositions. The beams and cubes were wrapped with plastic sheets then cured at room temperature (at about 20°C). They were in the curing process for 28 days (Fig. 4). The cubes were not placed inside the curing tank to maintain consistency with the beams which were left for curing at room temperature.

III. TEST RESULTS AND DISCUSSIONS

A. Workability

The results indicate that generally, partial or full replacement of FG with natural coarse aggregates has

small effect on the initial slump values and the workability of the concrete. Fig. 5 shows the comparison of slump test results against various mixes studied; it can be seen that for 25 and 50% replacement of FG aggregates in terms of volume, the slump values have remained almost the same and a slight decrease for 75 and 100% resulting in a small change in the workability. For higher percentage replacement of FG aggregates, the reduction in workability could be attributed to the more angular grain shape texture than natural coarse aggregate which could have resulted in less fluidity and loss of workability as the percentage replacement of FG increased. Another factor could be an important absorption of water by the porous FG aggregates under dry conditions.



Fig. 4. Specimen wrapped with plastic sheets.

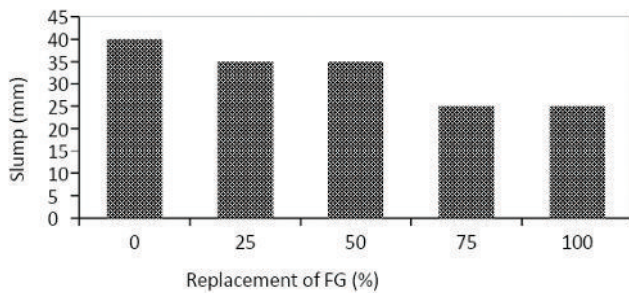


Fig. 5. Slump values.

B. Flexural Behavior

As described earlier, four-point loading flexural tests were conducted up to failure on all beams. The beams were tested as a simply supported beam under point loading test. The main focus of the present study was to observe the following characteristics for all the beams with the different percentage replacement of FG with NA, which are load-deflection behavior at mid-span for each load increment, load at which the first crack appears, mode of failure and crack pattern, and ductility behavior. Strain gauges are used to measure the deflection.

C. Control Mix (0% FG)

The observations from all three beams in a mixture show almost the same trend; the first crack was recorded 55 mm away from the center line, between the two-point loads, inside the flexural zone at a load of 28 kN, which is approximately 42% of the ultimate failure load. Immediately after the first crack at 30 kN load, a second crack 15 mm away from the centerline, which was also inside the flexural zone was observed. As the load increased, further hairline cracks started to appear. During the loading zone of 28 kN–48 kN, a total of six cracks appeared. These cracks started to form inside the flexural zone and with continuous load increments; they started to take a diagonal shape toward the compression zone of the beam without the width of the cracks changing significantly, suggesting that these were secondary flexural cracks, as secondary cracks appear under low loads and are widely spaced without influencing others to arise. They start to develop during the initial stages of

cracking as a result of internal expansion and contraction of concrete constituents, in addition to the low flexural stresses due to the self-weight of the beam and the applied loads. When the load was gradually applied, the tensile stresses developing at the bottom fibers exceeded the flexural tensile stress of the concrete at 28 kN which led to the development of these cracks. The main cracks started to form at a later stage than the secondary cracks. These were formed under the situation when a section was considered and there was a difference in strain between the steel and the concrete. Hassoun and Al-Manaseer (2008) stated that at low tensile stresses in steel bars, the number of cracks increases, whereas the widths of cracks remain small; as tensile stresses are increased, an equilibrium stage is reached. When stresses are further increased, the second stage of cracking develops, and crack widths increase without any significant increase in the number of cracks. Usually, one or two cracks start to widen more than the others, forming critical cracks. This was evident during the experiment. From 48 kN up to failure load, only one additional crack was observed and a single crack started to widen and spread toward the point load indicating the development of the second stage of the cracking, that is, the main cracks.

The beams failed in the shape of a diagonal crack (known as shear failure) which started in the tension side of the beam and with progressive loads propagated toward the compression side under the point load failing at an ultimate load of 66 kN with the mode of failure being a shear compression failure.

It was observed that the load-deflection curve is fairly linear before the first crack was formed at 28 kN where the deflection was recorded to be 0.47 mm, indicating that this was the elastic stage. After the occurrence of first crack, a slight change in the load-deflection behavior, as shown in Fig. 6, was observed, which was also linear up to the yield point where the deflection was recorded to be 1.38 mm. With further load increase beyond the yielding of the reinforcement, the curve entered the plastic region and was almost horizontal up to the ultimate/failure load where the deflection was recorded to be 6.93 mm.

D. Mix 2 (25% FG)

The first hairline flexural crack in this beam occurred at the load of 28 kN which is approximately 39% of its ultimate load. The position of this crack was roughly 135 mm away from the center line on the tension side of the beam. As the load increased to 36 kN, more secondary hairline flexural cracks were observed. At 56 kN two additional cracks suddenly emerged approximately 200 mm away from the centerline of the beam. These were tension cracks as they initiated from the middle section of the beam. In total, there were nine cracks in this beam. The width of the tension cracks started to extend rapidly as the load increased. The failure load for this beam was 72 kN, approximately 8% higher load carrying capacity in comparison to the control beam with the same tension reinforcement. The failure was due to crushing of concrete and it was in the form of a diagonal crack which

initiated from the middle of the beam suggesting that this was a shear compressive failure. The deflection when the first crack appeared at 28 kN was measured 0.68 mm which is slightly higher than the control beam. Fig. 7 shows the load-deflection behavior for this beam. Similar to the previous beams, the curve is linear during the un-cracked elastic stage, a slight change is then observed up to the yield point and a final turn leading to the ultimate strength. At the failure load of 72 kN, the deflection was 5.2 mm for this beam compared to 6.30 mm in the other suggesting that it is less ductile in comparison.

E. Mix 3 (50% FG)

The first hairline flexural crack appeared approximately 150 mm away from the centerline at 22 kN. The incorporation of FG content seems to have reduced the load at which the first crack appeared in this specimen. This could be due to the fact that foam glass concrete has a less tensile strength in comparison to concrete from normal aggregates. As the load increased, further secondary cracks were observed which were all in the mid-span region between the point loads. In total, this specimen had six cracks. With 50% replacement to normal aggregates by FG material, the load-carrying capacity

has decreased by 23% and 27% in comparison to control mix (0% FG) and mix containing 25% FG, respectively. The mode of failure was a combination of shear and flexural failure. Initially, the crack formed near the bottom fibers of the beam and with the increase in load the crack started to expand and extend towards the top fibers, in particular, toward the point load, by the crack taking a diagonal shape. Compared to the previous beams, the load-deflection curve for this specimen as shown in Fig. 8 is unusual and does not show the three distinct stages expected in a typical reinforced concrete member. At the first crack, the deflection was 0.66 mm which is high compared to the previous beams and the curve is almost linear up to the yield point. The deflection at failure was 1.50 mm and before failure, this specimen did not provide ample warning of impending failure suggesting that it was less ductile to the previous beams.

F. Mix 4 (75% FG)

Hairline flexural cracks started to appear at 20 kN which is roughly 41% of its ultimate load. As the load increased; further, secondary cracks were observed. A total of seven cracks were found on this specimen. The position of the cracks was at various distances from the centerline and with

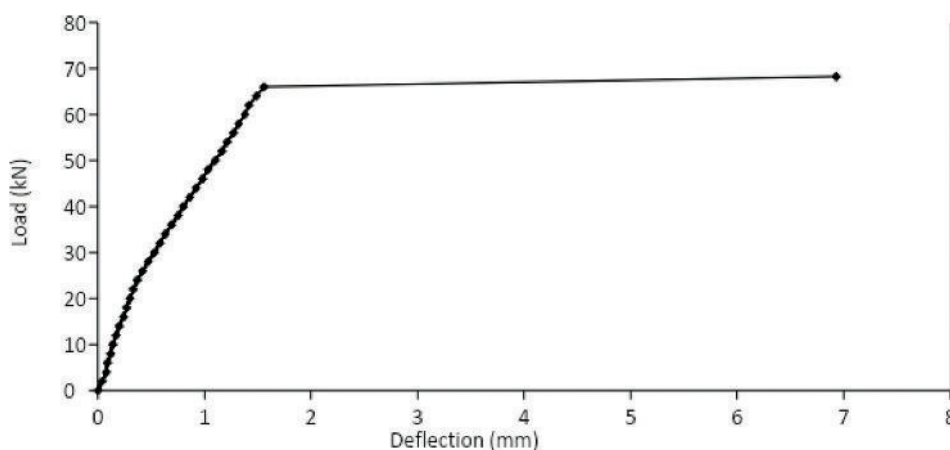


Fig. 6. Load-deflection behavior of the control mix (0% FG) beam.

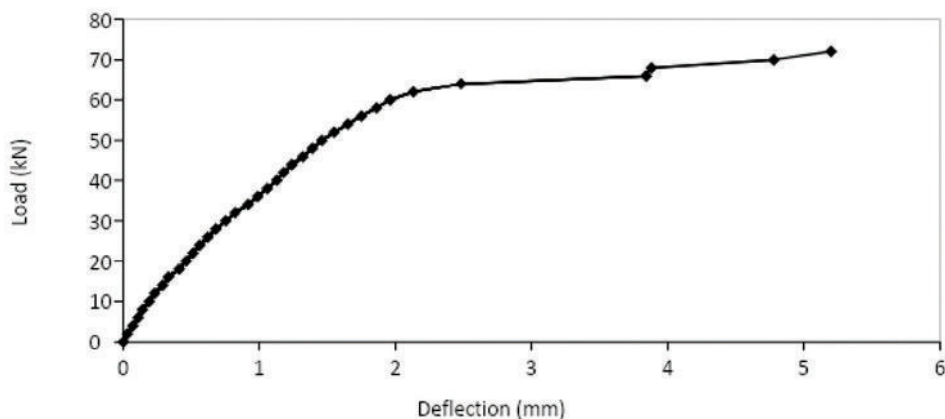


Fig. 7. Load-deflection behavior of 25% FG beam.

the exception of the third crack which appeared at 32 kN toward the middle depth of the beam, whereas all other cracks originated from the bottom propagating toward the top. Failure load for this beam was 48.09 kN. The cracks which originated from the middle depth of the beam and extended at a faster rate compared to all other cracks. The failure also occurred due to this crack. The sudden emergence and rapid change in the width indicated that the failure mode for this beam was a shear failure. At first cracking, the deflection was recorded 0.38 mm. As the load increased, it is shown in Fig. 9 that the deflection also increased, on failure the deflection was 2.75 mm.

G. Mix 5 (100% FG)

It was observed that the 100% replacement of FG dramatically reduced the load at which the first crack appeared. Hairline flexural cracks started to surface at 12 kN which is almost 60% reduction to the load at which the first crack appeared with the 0% FG replacement. With further increase in the load additional cracks developed at the bottom surface of the beam relatively close to the support and rapidly started widening and propagating toward the point load. The failure occurred at 36 kN by crushing with associated spalling of concrete cover in the compression

zone. There were eight cracks in total for this beam. The beam failed in a mode of shear failure. The typical events of a load-deflection curve to failure were observed. It is shown in Fig. 10 that the curve is fairly linear up to 12 kN identified as the first cracking of concrete. At yield point, the curve is still linear and the deflection was 0.83 mm. However, between the yielding of tensile reinforcement and the ultimate strength, the curve did not behave in the usual manner, that is, horizontally; this is because the failure was brittle and provided little or no warning before failure. Fig. 11 shows the typical experimental load-deflection curves for all beams reinforced with 3T8 tension reinforcement, where the average values of the three tests for each mixture are shown.

H. Load at First Crack and Ultimate Loads of Beams

The appearances of reinforced concrete elements may greatly be reduced if cracks develop and more so when cracks are prominent. Excessive cracks and deep cracks affect the durability of concrete. Although strength may not be directly affected, the corrosion within the concrete can eventually cause the structures to fail. As beams deflect during loading, cracks occur first in the tension zone. Further loading tends to increase the width of the crack which gradually lead to

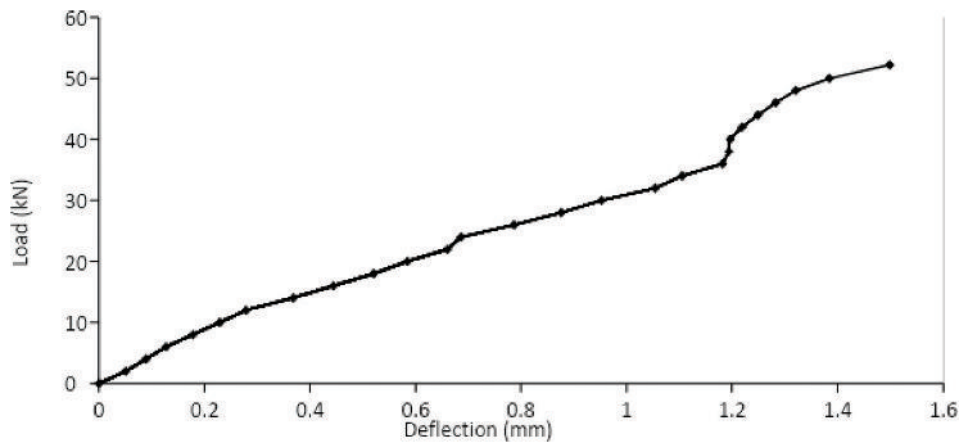


Fig. 8. Load-deflection behavior of 50% FG beam.

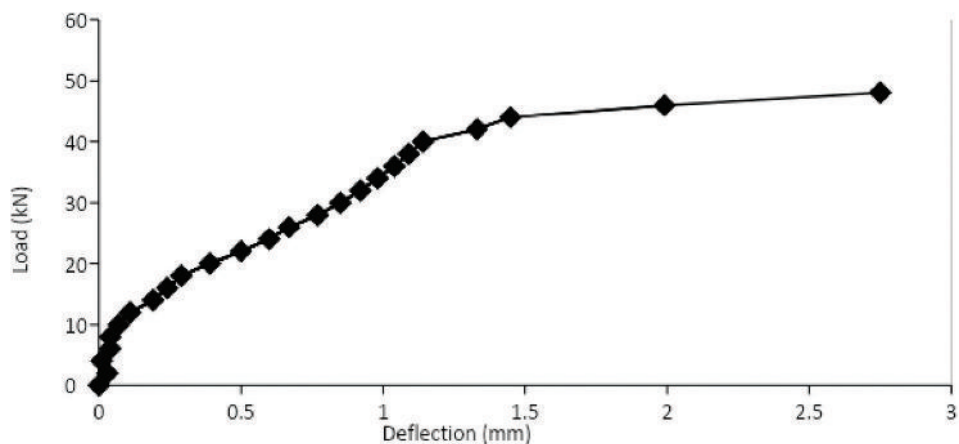


Fig. 9. Load-deflection behavior of 75% FG beam.

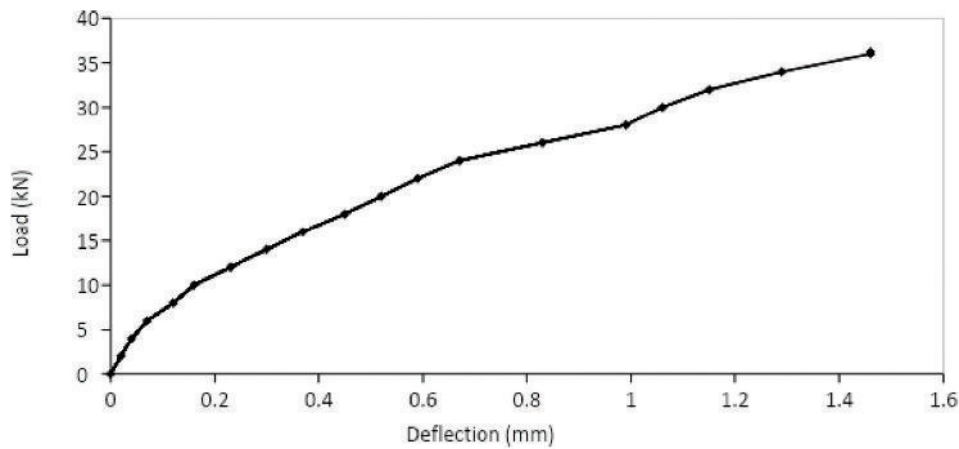


Fig. 10. Load-deflection behavior of 100% FG beam.

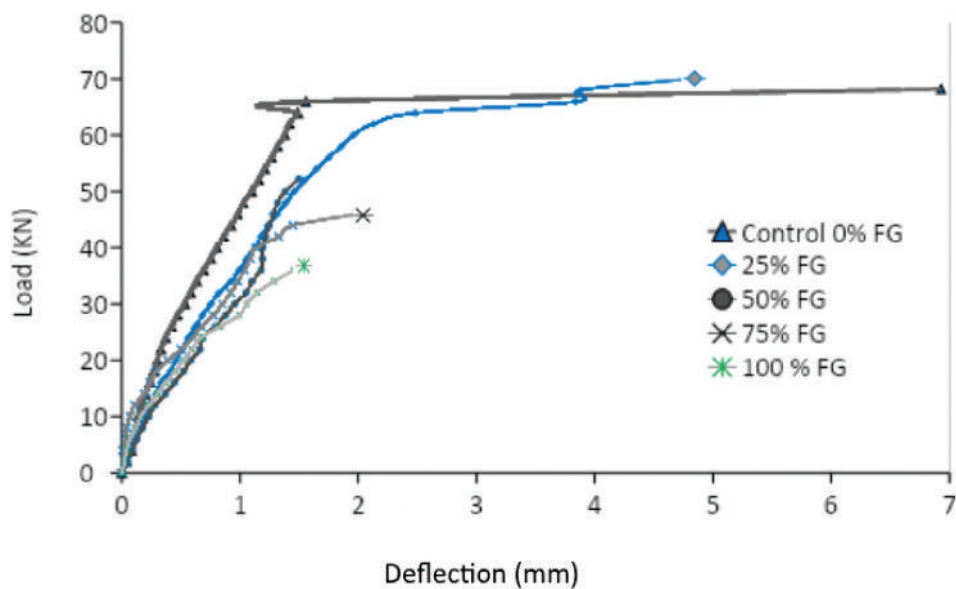


Fig. 11. Load-deflection curves for beams.

durability problems over time and may cause final failure (Adom-Asamoah and Afrifa, 2010).

During loading of beams, it was observed that the first crack in all the beams always started to form close to the mid-span of the beam. The cracks forming on the surface of the beam were mostly vertical cracks known as flexural cracks. For the beams, initial cracking occurred at about 38%–42% of its ultimate load. Lim, et al. (2006) reported that the parameter which provides distinct and conclusive evidence of slower growth of cracks is the amount of tension reinforcement, the higher amount is more effective at a given load level.

Fig. 12 shows the load at which the first crack appeared in the beams, it can be seen that as the percentage replacement of FG increases the first cracking load decreases, as in the first crack appears at a lower load. The reason for this could be due to reduction in the modulus of elasticity of FG concrete as Limbachya, et al. (2011) has reported that increasing the proportions of coarse FG aggregates in the concrete mix significantly reduces the

modulus of elasticity of concrete and that up to 30% partial replacement to normal aggregates might be considered as the maximum amount that could be added without a major negative effect on the modulus of elasticity of FG concrete.

Fig. 13 shows the comparison of load-carrying capacity for all beams. It can be seen that as the percentage replacement of FG increases the load-carrying capacity decreases. For 100% foam glass replacement, there is a reduction of almost 50% in the load-carrying capacity in comparison to the control beam. It seems that the compressive strength of FG holds key significance in this reduction as the percentage reduction in concrete compressive strength correlates to the percentage of reduction in the load-carrying capacity. For example, the compressive strength of control mix was 30.67 MPa and the load capacity of the beam from that mix was 68.23 kN whereas for 100% replacement the compressive strength and failure load for the beam was 14.97 MPa and 36.24 kN, respectively, indicating a reduction of almost 50% in strength and load-carrying capacity.

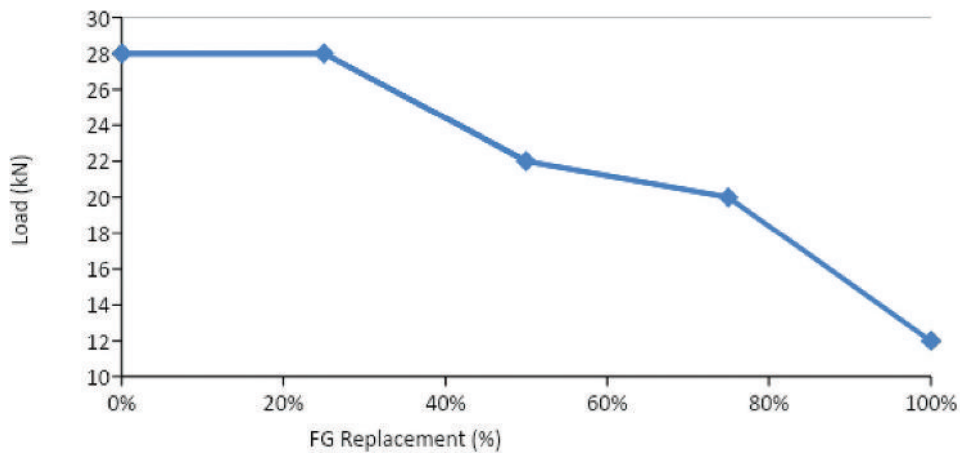


Fig. 12. Load at the first crack for all beams.

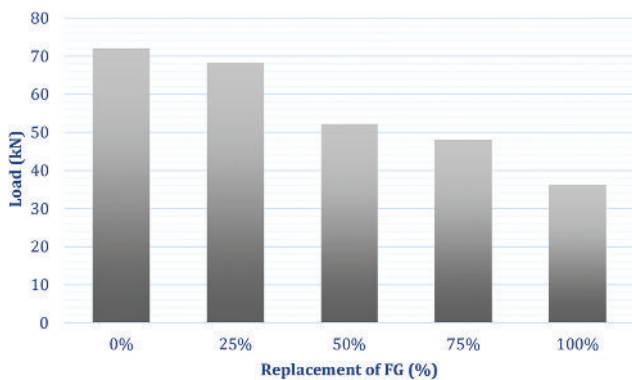


Fig. 13. Comparison of the load-carrying capacity of beams.

I. Cracking Behavior and Mode of Failure

Initially, vertical cracks known as flexural cracks started to form in the pure bending region. On further load increment, as shear stresses increased diagonal cracks were noticed which originated from the middle depth of the beam suggesting they were critical shear cracks and as load increased these cracks began widening at a faster rate and extending toward the point load, these cracks ultimately became the cause of failure, unlike the first secondary flexural cracks which appeared in the bending zone and remained almost the same until failure. The mode of failure in a structural reinforced concrete beam depends on a number of factors such as flexural tension reinforcement, flexural compression reinforcement, shear reinforcement, concrete compressive strength, and span to effective depth ratio. Although the beams in this study were designed to fail pure flexural mode, it can be concluded from analyzing Fig. 14 that failure for beams occurred mainly through combined diagonal tension and/or flexural-shear failure.

J. Displacement Ductility

Table II shows the ductility of the beams tested in the present study. In reinforced concrete structures ductility is significantly important as any member should be able to withstand large deflections at near maximum load-carrying

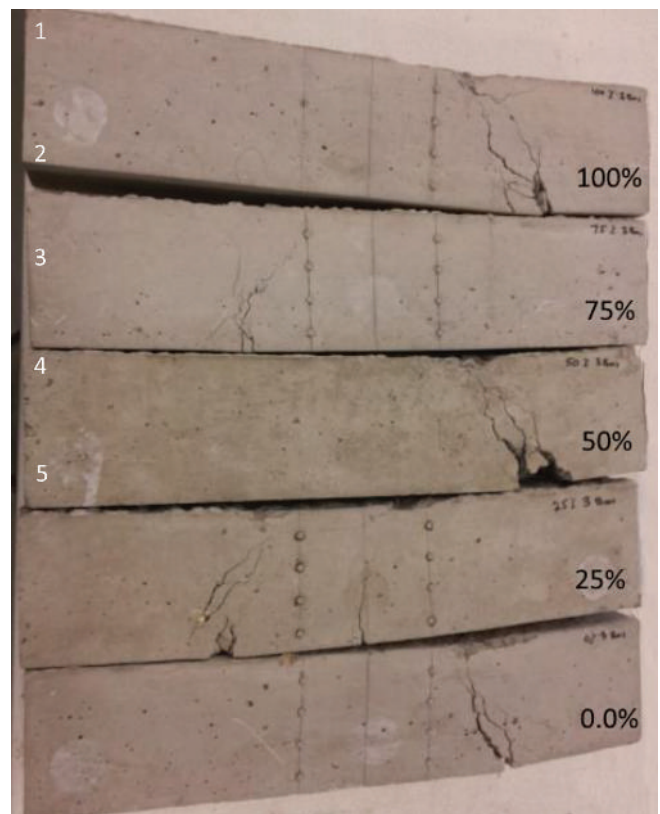


Fig. 14. Failure mode of the beams.

capacity, providing sufficient warning to the imminence of failure. Ductility allows stress redistribution and warning of impending failure. A structural member capable of withstanding large deformations before failure is a ductile material. In contrast; a material which fails at small strain without providing ample warning of impending failure is classified as brittle. Ashour (2000) has stated that members with a ductility ratio in the range of 3–5 have adequate ductility and can be considered for structural members subjected to large displacements such as sudden forces caused by earthquakes. The results presented in Table II show that displacement ductility ratio reduces by increasing FG.

K. Compressive Strength

Fig. 15 shows the compressive strength complied with BS EN 12390-3:2009 for concrete containing different percentage replacements of FG aggregates. The experimental results suggest that the partial or full replacement of natural aggregate has, generally, resulted in a decrease to the compressive strength compared to the control mix. It can be seen that 75% or full replacement of NA by the FG aggregates has resulted in a considerable drop in the compressive strength of concrete which does not meet the minimum requirements of 28-day design strength

of 17 MPa for lightweight aggregate concrete (Hedjazi, 2019), keeping in mind that the modulus of elasticity and the concrete strength is different in compression and tension (Atrushi, 2003). This is in agreement with the findings reported by Limbachya, et al. (2011).

The results also indicated that the higher the amount of the FG added, the larger the strength loss observed as shown in Fig. 16. For 25% replacement, the strength loss was around 20% whereas for 100% replacement the reduction is above 50%. It has been reported that the low density, high porosity, and high crushing value of FG particles have a significant contribution to the reduction of the compressive strength of FG concretes in comparison to concrete from normal aggregates (Limbachya, et al. 2010). Moreover, as previously stated the compressive strength has had a direct influence on the load-carrying capacity of the beams, the higher the compressive strength is, the higher the load-carrying capacity was found.

TABLE II
DISPLACEMENT DUCTILITY RATIO OF ALL BEAMS

Beams	Yield stage		Ultimate stage		Displacement ductility ratio D_u/D_y
	Load (kN)	Deflection D_y , (mm)	Load (kN)	Deflection D_u , (mm)	
0 % FG	62	1.42	68.23	6.93	4.88
25% FG	54	1.65	72.07	5.2	3.15
50 % FG	36	1.2	52.21	1.5	1.25
75 % FG	40	1.14	48.09	2.75	2.41
100% FG	28	0.99	36.24	1.46	1.47

L. Density

The densities of the cubes were measured on the same day as the structural tests were carried out complied with BS

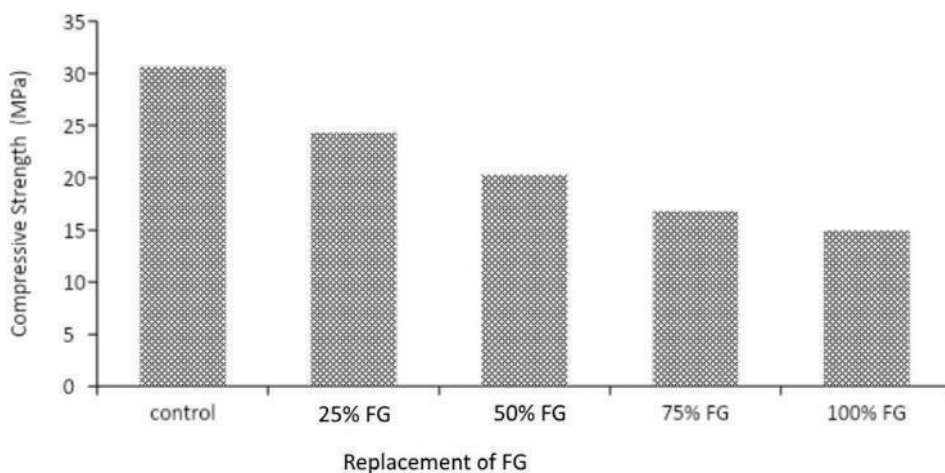


Fig. 15. Compressive strength of all mix proportions.

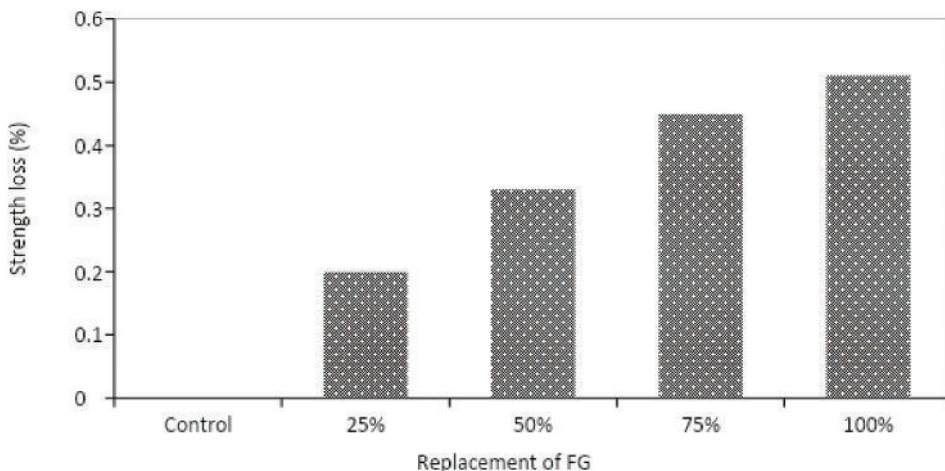


Fig. 16. Comparison of compressive strength loss.

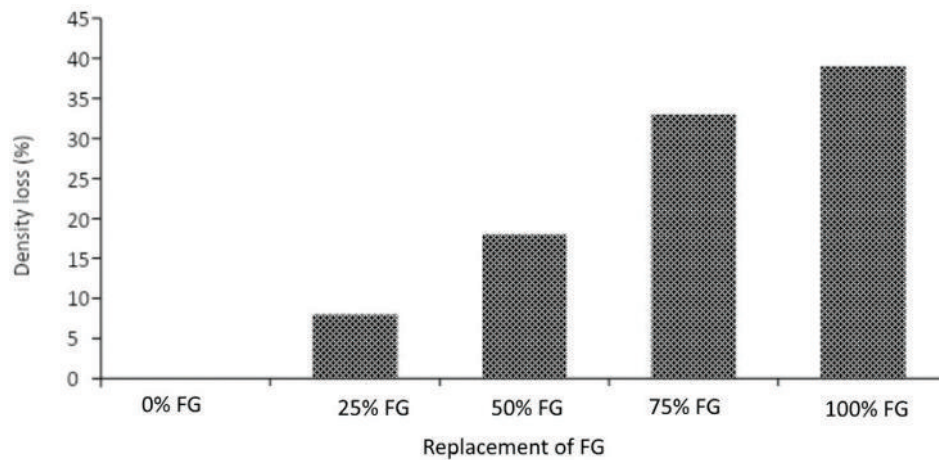


Fig. 17. Density reduction of all concrete cubes.

EN 12390-7:2009. Based on the results the density reduction graph as shown in Fig. 17 has been produced. It can be seen that incorporation of FG aggregates in concrete decreases the density. However, this reduction was predictable as FG is a lightweight material and its density is much lower than that of normal concrete.

It can be seen that by replacing 25% of normal aggregates with FG aggregates the decrease in density is about 8%, which shows no significant reduction. However, for 100% replacement, the reduction is 39% which is quite significant. It was observed that the density has a direct influence on the concrete compressive strength as the reduction in compressive strength correlates to the reduction in density. This indicates that higher FG content in concrete will result in a lower density and compressive strength. This is in agreement with the findings reported by Limbachiya, Meddah and Fotiadou (2012).

IV. CONCLUSIONS

According to the results obtained there is a great potential for the use of FG aggregates in concrete as a substitute to natural aggregates; because structural behavior of concrete containing FG is comparable to other types of lightweight aggregate concrete. Partial replacement of 25% FG aggregates showed no significant effects in all engineering properties studied such as flexural behavior, load-carrying capacity, first cracking load, ductility behavior, compressive strength, and density. According to the results obtained in the present study, the following conclusions can be drawn:

- Incorporation of FG aggregates showed little effect on the consistency of concrete but a decrease in the compressive strength and density of concrete. However, partial replacements of 25% and 50% have achieved the required 28-days strength.
- Reinforced concrete beams with FG had a higher deflection in comparison to beams prepared with normal aggregates. However, an increase in FG content slightly decreased the first cracking load but drastically reduced the load-carrying capacity.

V. ACKNOWLEDGMENT

I would like to thank Kingston University London for their hospitality, technical support, and valuable discussions during my Postdoctoral research work at the university. Thanks also to the University of Duhok for their support.

REFERENCES

- Adom-Asamoah, M. and Afrifa, R.O., 2010. A study of concrete properties using phyllite as coarse aggregates. *Materials and Design*, 31(9), pp.4561-4566.
- Ashour, S.A., 2000. Effect of compressive strength and tensile reinforcement ratio on flexural behaviour of high-strength concrete. *Engineering Structures*, 22(5), pp.413-423.
- Atrushi, D.S., 2003. *Tensile and Compressive Creep of Early Age Concrete: Testing and Modelling*, Doctoral Thesis. Norwegian University of Science and Technology, Norway. Available from: <https://www.ntnuopen.ntnu.no/ntnu-xmlui/handle/11250/231168>.
- Babu, D.S.T., Babu, K. and Wee, T.H., 2005. Properties of lightweight expanded polystyrene aggregate concrete containing fly ash. *Cement and Concrete Research*, 35, pp.1218-1223.
- British Standards Institution, BS EN 12350-2., 2009. *Testing Fresh Concrete Part 2: Slump-test*. British Standards Institution, United Kingdom.
- British Standards Institution, BS EN 12390-2., 2012. *Testing Hardened Concrete Part 2: Making and Curing Specimens for Strength Tests*. British Standards Institution, United Kingdom.
- British Standards Institution, BS EN 12390-3., 2009. *Testing Hardened Concrete Part 3: Compressive Strength of Test Specimens*. British Standards Institution, United Kingdom.
- British Standards Institution, BS EN 12390-4., 2000. *Testing Hardened Concrete Part 4: Compressive Strength, Specification for Testing Machines*. British Standards Institution, United Kingdom.
- British Standards Institution, BS EN 12390-7., 2009. *Testing Hardened Concrete Part 7: Density of Hardened Concrete*. British Standards Institution, United Kingdom.
- British Standards Institution, BS EN 933-1., 1997. *Tests for Geometrical Properties of Aggregates. Part 1: Determination of Particle Size Distribution Sieving Method*. British Standards Institution, United Kingdom.
- Demirboga, R. and Gu, R., 2003. The effects of expanded perlite aggregate, silica fume and fly ash on the thermal conductivity of lightweight concrete. *Cement*

and *Concrete Research*, 33(5), pp.723-727.

Gennaro, R., Langella, A., Amore, M.D., Dondi, M., Colella, A., Cappelletti, P. and Gennaro, M., 2008. Use of zeolite-rich rocks and waste materials for the production of structural lightweight concrete. *Applied Clay Science*, 41(1-2), pp.61-72.

Hassoun, M.N. and Al-Manaseer, A., 2008. *Structural Concrete: Theory and Design*. John Wiley and Sons, Hoboken, New Jersey.

Hedjazi, S., 2019. *Compressive Strength of Lightweight Concrete*. IntechOpen, London.

Herki, B.M.A. and Khatib, J.M., 2016. Structural behaviour of reinforced concrete beams containing a novel lightweight aggregate. *International Journal of Structural Engineering*, 7(1), pp.1-30.

Hossain, K.M.A., 2004. Properties of volcanic pumice-based cement and lightweight concrete. *Cement and Concrete Research*, 34(2), pp.283-291.

Hurley, J.A., 2003. *A UK Market Survey for Foam Glass. Glass: Research and Development, Final Report, the Waste and Resources Action Programme*. WRAP Report, No. GLA-0015.

Kilic, A., Atis, C.D., Yasar, E. and Ozcan, F., 2003. High-strength lightweight concrete made with scoria aggregate containing mineral admixtures. *Cement and Concrete Research*, 33(10), pp.1595-1599.

Lim, H.S., Wee, T.H., Mansour, M.A. and Kong, K.H., 2006). Flexural behaviour of reinforced lightweight aggregate concrete beams. *Journal of Advanced Concrete Technology*, 4(3), pp.1-10.

Limbachiya, M., Meddah, M.S. and Fotiadou, S., 2011. Performance of granulated foamed glass concrete. *Construction and Building Materials*, 28(1), pp.759-768.

Limbachiya, M., Meddah, S. and Fotiadou, S., 2012. Performance of granulated foam glass concrete. *Construction and Building Materials*, 28(1), pp.759-768.

Rossignolo, J.A., Agnesini, M.V.C. and Morais, J.A., 2003. Properties of high-performance LWAC for precast structures with Brazilian lightweight aggregates. *Cement and Concrete Composites*, 25(1), pp.77-82.

Rostam, D., Ali, T. and Atrushi, S.D., 2016. Economical and structural feasibility of concrete cellular and solid blocks in Kurdistan region. *The Scientific Journal of Koya University*, 4(1), pp.1-7.

Shafiqh, P., Hassanpour, M., Razavi, S.V. and Kobraei, M., 2011. An Investigation of the Flexural behaviour of reinforced lightweight concrete beams. *International Journal of the Physical Sciences*, 6(10), pp.2414-2421.

Shuab, H.A. and Ray, B., 1991. Flexural behaviour of high-strength lightweight concrete beams. *ACI Structure*, 88(1), pp.66-77.

Subasi, S., 2009. The effects of using fly ash on high strength lightweight concrete produced with expanded clay aggregate. *Scientific Research and Essays*, 4(4), pp.275-288.

Wuest, J., Denarié, E. and Bruhwiler, E., 2007. *Measurement and Modelling of Fibre Distribution and Orientation in UHPFRC*. In: Proceedings of the 5th International RILEM. pp.259-266.

Assessment of Acoustical Characteristics for Recent Mosque Buildings in Erbil City of Iraq

Dawa A. A. Masih, Nawzad K. Jalal, Manar N. A. Mohammed, Sulaiman A. Mustafa

Department of Architecture, Faculty of Engineering, Koya University,
Daniel Mitterrand Boulevard, Koya KOY45 AB64, Kurdistan Region – F.R. Iraq

Abstract—The study of mosque acoustics, concerning acoustical features, sound quality for speech intelligibility, and additional practical acoustic criteria, is commonly overlooked. Acoustic quality is vital to the fundamental use of mosques, in terms of contributing toward prayers and worshippers' appreciation. This paper undertakes a comparative analysis of the acoustic quality level and the acoustical characteristics for two modern mosque buildings constructed in Erbil city. This work investigates and examines the acoustical quality and performance of these two mosques and their prayer halls through room simulation using ODEON Room Acoustics Software, to assess the degree of speech intelligibility according to acoustic criteria relative to the spatial requirements and design guidelines. The sound pressure level and other room-acoustic indicators, such as reverberation time (T30), early decay time, and speech transmission index, are tested. The outcomes demonstrate the quality of acoustics in the investigated mosques during semi-occupied and fully-occupied circumstances. The results specify that the sound quality within the both mosques is displeasing as the loudspeakers were off.

Index Terms—Acoustic parameters; mosque acoustics; ODEON; reverberation time; Speech Transmission Index.

I. INTRODUCTION

The mosque is the most fundamental example of Islamic architecture that has evolved to be connected with needs of Muslim communities in diverse geographical and historical contexts. A number of various worship activities occur within these multifunctional public spaces, and such diverse functions have diverse acoustical demands and requirements. Three distinctive activities are practiced in mosques, either independently or in combination with one another, as shown in Fig. 1. The first one is carrying out prayers, individually or in congregation (led by the imam). The second is participating in preaching, particularly the Friday sermon. The third is listening as well as reciting verses from the

Holy Quran. Despite the fact that mosque construction gives high emphasis to architectural esthetic, good quality levels in terms of acoustics are sorely lacking, despite the fundamental importance of this dimension for users of such structures (Wasim, 2007). Indeed, given the mosque's core functions, the most effective determining factor of its architectural design ought to be its acoustical requirements (Hammad, 1990), but little if any precise guidelines have been developed for mosques in this regard (Waseem, 2007). The previous studies reveal that appropriate interior design and wisely detailed building envelope with extensive acoustical consideration are key elements for improving the acoustical performance of mosques. However, most mosques usually have hard and reflective interior finished surfaces, hampering speech intelligibility due to echoes, and/or reverberations, because of cavernous hall spaces within mosques, and their sheltering elements such as domes.

In new-generation mosques, sound reinforcement systems have been utilized to achieve acoustical comfort levels, but this is not an adequate solution without a proper architectural design of the space (Lewers and Anderson, 1984; Suárez, Sendra, Navarro and León, 2004). Clearly, it is a significant quality requirement for mosque structures to offer satisfaction with the intelligibility and ambience of oral communication and tranquility for worshippers. Beside the main function, which is delivering the religious message, other activities conducted in mosques which require speech intelligibility include prayer, speaking publicly, education, lectures, and Quran recitation. Hence, it is undeniable that the quality of acoustics has a significant role which is related to the function of a mosque as a worship center in addition to the spread of knowledge and propagation (*da'wa*). Computer simulation techniques are mostly used in mosque renovations or investigating the acoustical quality of mosques (Orfali, 2007). Evaluated acoustical metrics are generally speech transmission index (STI), sound pressure levels (SPL), and reverberation time (RT) (early decay time [EDT], T30). The aim of this paper is to study and to compare the sound performance two major modern mosque projects in Erbil, Dayk and Altun Mosques. Computer simulation techniques (ODEON 16 Basics edition) were utilized to measure the acoustical parameters of the mosques' main prayer halls. The results indicate that the sound quality of both mosques' main prayer halls was unsatisfactory whilst the loudspeakers were

ARO-The Scientific Journal of Koya University
Vol. IX, No.1 (2021), Article ID: ARO.10784, 16 pages
DOI: 10.14500/aro.10784

Received: 13 January 2021; Accepted: 20 February 2021
Regular research paper: Published: 01 March 2021

Corresponding author's e-mail: dawa.azad@koyauniversity.org
Copyright © 2021 Dawa A. A. Masih, Nawzad K. Jalal, Manar N. A. Mohammed, Sulaiman A. Mustafa. This is an open-access article distributed under the Creative Commons Attribution License.



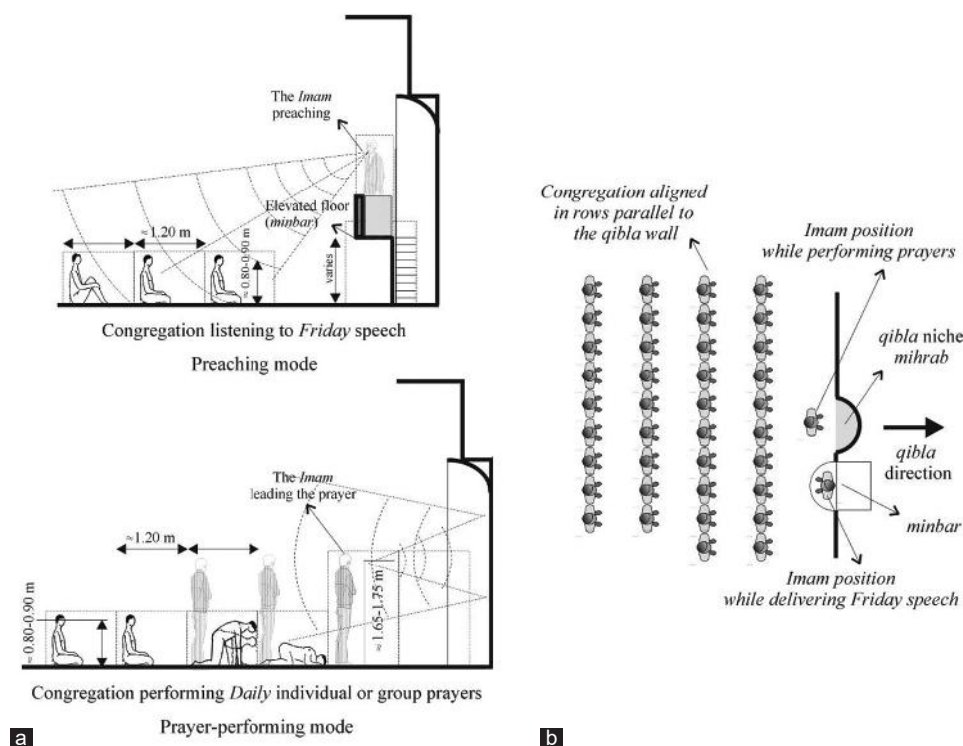


Fig. 1. Different postures and orientation of the worshippers concerning the imam in the two main religious modes. (a) Sections showing worshippers listening to the Friday sermon (that is, the preaching mode) and performing daily prayer (that is, the prayer-performing mode). (b) Plan view showing positions of the imam and worshippers in group prayer performance.

off. Moreover, in the daily prayer scenarios only worshippers in the initial rows close to the imam had a satisfactory STI score.

The essential aspects that influence sound quality inside mosques consist of physical and acoustic aspects. The former includes the form and scheme of the mosque, whereas the latter consists of user-related factors such as the occurrence of background noise and reverberation sound (Lamancusa, 2000). The most important acoustic quality level in the mosque is required during Friday sermons, when all worshippers should be able to hear the imam preaching; aside from this, it is necessary to be able to hear the imam during the five daily prayers. This requires acoustical measures to stifle unwanted noise whereas enhancing the desired sounds. A decent acoustic design can offer an enhanced and more convenient atmosphere within the mosque concerning the clarity and intelligibility of speech (Othman, Harith, Ibrahim and Ahmad, 2016). Marie (2009) conducted a number of quantity tests to develop some practical replicas to estimate the sound levels for prayers with different parameters, for instance, the room volume, the prayers number, the room background noise without occupants, as well as the RT. Acoustic parameters refer to speech comfort and clarity in terms of the echo time and background noise (Chiang and Lai, 2008), which with reverberation substantially contribute to the effective acoustic quality level of a room. To generate a beneficial sound level, testing must consider the noise criteria (NC) based on the background noise, RT, and STI should be considered.

As previously mentioned, in designing a mosque, an effective acoustic system is necessary for the worshippers. When delivering speeches or sermons in a mosque, worshippers further from the pulpit (*minbar*) would struggle to hear clearly, and the message would not be conveniently relayed to some people. Architects in recent times usually focus more on designing buildings in accordance with appearance or forms, and the primary operation of the space is actually neglected. Poor acoustic design impairs user use and aesthetic enjoyment of the structure – regardless of its visual attractiveness – due to frustrating the primary activities of users, such as the inability to clearly hear the voice of the imam during prayers. Therefore, early consideration of acoustic design is necessary while designing mosques, including in terms of material choices, geometrical forms of spaces, and the implications of the combined factors in the design.

The purpose of the research is to recognize the significance of acoustic design in the mosque regarding the comfort of the worshippers. From the background research, it is anticipated to increase recognition among concerned professionals, especially architects, concerning the value of acoustic design in mosques, to provide improved user comfort and enjoyment while using the mosque. It is essential to obtain an appropriate acoustic design in mosques for user comfort, but modern mosques commonly fail to achieve this. Therefore, this study conducts simulation and testing to discover how comfortable worshippers are after getting into the mosque. This study was conducted to achieve the following objectives:

- To evaluate the acoustic quality level in the mosque using ODEON 16 Basics edition.

- To recognize the factors influencing the acoustical quality level inside the selected mosques.
- To generate awareness of the application of good acoustic design in mosques by comparing two recent common mosque designs in Erbil.

II. IMPORTANCE OF ACOUSTIC DESIGN WITHIN MOSQUES

As Khabiri, et al. (2013) mentioned, mosques are a multi-function public halls hosting many worshipping activities with different acoustical requirements. Hence, every mosque has need of an acoustic design. Sü Gül and Çalıskan (2013) discussed that one of the significant features of places of worship is sound quality, and this should be considered essential in mosque design, taking into consideration speech patterns related to activities organized in those spiritual places. Ismail (2013) emphasized that the essence of speech intelligibility evolved into a bigger factor in modern-day mosque design, with the integration of further routines that include the recitation of Holy Quran, talks and speeches, as well as lectures in prayer halls becoming typical occurrences. This implies that acoustical design is important within mosques to confirm the quality of sound, to make sure that religious routines and activities are continued more efficiently.

III. RT EFFECT ON MOSQUE

In an investigation by Sü Gül and Çalıskan (2013), they discovered that RT is understood to be the time needed for the sound energy density as an average to degrade by 60 dB from steadiness stage after stopping the sound source. Sabine has researched the trend since 1900, and additionally RT is incorporated as the primary method for determining the acoustic qualities of room's environment. Acoustical simulations of Doğramacızade Ali Paşa Mosque by Sü Gül and Çalıskan (2013) were connected with RT over frequency range anticipated as an interior volume global average, modeling every single recipient position by means of distribution maps. The assessments of Sü Gül and Çalıskan (2013) indicate that perforated timber utilization on inverse triangular pendentive surface areas works equally well for populated and unpopulated circumstances of the mosque, especially in the enhancement of low to middle range of frequency. They noted that with the chosen substitute design approach, all the simulation outcomes were displayed solely for perforated wooden utilization on pendentive spots. Average mid-frequency T30 for an unpopulated mosque with acoustical treatment on pendentive surfaces is 1.94 s, with an average low-frequency T30 of 2.07 s.

Mazloomi (2010) demonstrated that the uniqueness of such pendentive constructing surfaces is that they produce a huge space in the interior of the mosque. Through proper treatment, average mid-frequency T30 for an occupied mosque is 1.34 s, and the average low frequency T30 is 1.86 s. The bass ratio (BR) is required to be higher than 1.20 for music activities, and it was established that whereas

speech is the basic activity in a mosque, the lower frequency and tone of the male imam's voice were relatively distinctive compared to normal speech, which makes it recommended to obtain a BR which is nearer to optimum for music. Moreover, Sü Gül and Çalıskan (2013) found that BR was 1.06 for the unoccupied mosque and 1.38 for the occupied mosque (regarding Doğramacızade Ali Paşa Mosque). The feature of the physical presence of worshippers increases absorption in the mid- to high-end frequency range of the mosque space that is occupied, generating a distinctive acoustical atmosphere.

Ismail (2013) found that an excessive RT will affect speech intelligibility. Furthermore, the decay time from 0 dB to -10 dB is EDT. An advanced technique, introduced by Schroeder, uses the squared reverse-integrated impulse response of an auditorium space. It is used as a rapid clue of the quantity of reflections, diffusion, or sound clarity. To sum up, this technique is beneficial for fast calculation of the EDT and can be applied for on-site uses.

IV. ROLE OF MATERIAL AND SHAPE IN MOSQUE ACOUSTIC DESIGN

Speech intelligibility is the major acoustical matter for buildings used in communication, demanding appropriate designation of volume, the geometry of the primary place, and suitable utilization of acoustically absorptive and diffusive materials, such as coating surface areas (Sü Gül and Çalıskan, 2013). It is been claimed that acoustical design ought to be incorporated into mosque design in the initial phases of conceptual building design. The biggest geometrical shapes are created during the schematic stage, along with materials to resolve considerations of esthetics and acoustics. Most contemporary mosques have sound-reflecting materials on most of their internal surfaces, apart from the horizontal surfaces, which are usually carpet-finished on the floor level (Ismail, 2013). Single-glazed material is used in large openings, and wood is used for doors. The central air conditioning units or stand-alone split units, positioned on rooftops or inside chosen spaces, increase the background noise levels inside prayer areas, and affect the acoustical calmness of space. Table I shows the sound absorption and scattering coefficients of materials used in the mosque designs.

V. METHODOLOGY

From the literature review, information was gathered regarding the application of acoustic devices inside the mosques and relevant buildings. This study undertakes a comparative assessment of acoustic quality level in two mosque case studies to identify factors influencing acoustical performance. Information was collected about the Altun Mosque and Dayk Mosque, concerning the buildings' dimensions, sizes, and internal surface materials, gathered on the sites or using computer drawings and files. The main prayer halls of both mosques were modeled using

SketchUp 2018 (a 3D modeling computer program) and were then imported to ODEON 16 Basics edition to perform the acoustic simulations (Fig. 2). The material properties of all surfaces were applied (types, absorption coefficient, and scattering affect), as shown in Fig. 3. After that, the sound sources (imam and loudspeakers) and receivers (worshippers) were allocated. General settings, such as room setup, were configured for acoustical simulation as recommended in the ODEON manual. Within Point Source Editor, natural directivity patterns (BB93_Raised_Natural.So8) were selected. The BB93_Raised_Natural source type (Education Funding Agency, 2015) corresponds to a male speaker with a raised vocal effort representing an imam's voice (Fig. 4a). Similarly, Common Loudspeaker Format (CLF), an open-source format for loudspeaker data, was selected and applied inside the Point Source Editor to the other sources to represent loudspeakers, using their sound level and directivity (Fig. 4b). Finally, the simulations were performed to investigate acoustical parameters such as SPL, RT, T30, EDT, and STI for two different situations: Fully occupied (preaching during the Friday sermon) and partially occupied (during daily prayers).

VI. THE CASE STUDY SELECTIONS

As mention previously, two different mosques were chosen as representatives of the most common contemporary mosque design typologies in Erbil, Altun Mosque and Dayk Mosque. Table II summarizes the key physical features of the two selected mosques, with data on length, width, height, volume, and overall estimated capacity at peak occupancy. Only the size of the main prayer hall is used for sound analysis, as

this is the acoustically functional area of the mosque (as described previously).

A. The Dayk Mosque

The second case study is located in Italian City II in Erbil, Iraq (Fig. 5). The main prayer hall has been selected for the investigation purpose in this mosque, located in the center of the mosque design, with a rectangular plan of 20 m by 31 m (area = 651 m²). It has an entry area of 5.2 m width and 9 m length (area = 46.8 m²), with an additional 22 m² for the front part of the hall for the imam to recite and prostrate during prayer, called the *mihrab* area, but this can be neglected as no worshippers go there (Fig. 6). As a result, the total area of the main prayer hall is about 700 m², which can be occupied with slightly more than 800 people. The height of the hall is generally around 4.6 m, but the central dome extends to a crown of 12 m, with a diameter of 9 m.

The inner surfaces have various finishing materials, with carpeting to cover the floor (Fig. 7). The wall finishing is gypsum plastering, wood, and glass, with window frames covering 7% of the total wall surfaces, covered by curtains. All walls are covered with wood of 1.20 m meter height, and the *mihrab* wall is also covered with gypsum plaster finishing. Gypsum board is used for the ceiling. Absorption coefficients of used materials are illustrated in Table III.

B. Altun Mosque

Altun Mosque is located in Bnaslawa Old Road in Erbil, Iraq (Fig. 8). The main prayer hall area is 968.2 m² with dimensions of 29 × 33.2 m, which can be occupied by slightly more than 980 persons. The ceiling height is 11 m

TABLE I
SOUND ABSORPTION AND SCATTERING COEFFICIENTS OF MATERIALS

Material	63 Hz	125 Hz	250 Hz	500 Hz	1 k Hz	2 k Hz	4 k Hz	8 k Hz	Scatte-ring factor
Sand blasted travertine	0.01	0.01	0.01	0.01	0.02	0.02	0.02	0.02	0.15
Solid timber door	0.14	0.14	0.10	0.06	0.08	0.10	0.10	0.10	0.25
Double glazing	0.10	0.10	0.07	0.05	0.03	0.02	0.02	0.02	0.10
Single glazing	0.08	0.08	0.04	0.03	0.03	0.02	0.02	0.02	0.10
Ceramic tiles	0.01	0.01	0.01	0.01	0.01	0.02	0.02	0.02	0.15
2×13 mm gyps. Board on frame	0.15	0.15	0.10	0.06	0.04	0.04	0.05	0.05	0.10
12 mm wood on studs	0.28	0.28	0.22	0.17	0.09	0.10	0.11	0.11	0.10
Perforated MDF panel (TopAkustik 5/3T)	0.20	0.30	0.80	0.95	1.00	0.80	0.60	0.60	0.10

Source: Sü Gül and and Çalıskan (2013)



Fig. 2. AutoCAD 2020, Bosch Laser Distance, SketchUp, and ODEON 16

Number	Material	Scatter	Transp.	Type	Surface name	Layer	Area -cm²>
1	3068	0.200	0.000	Normal	walls wood	walls wood	3.14
2	3068	0.200	0.000	Normal	walls wood	walls wood	3.14
3	2001	0.050	0.000	Normal	walls marble	walls marble	1.03
4	2001	0.050	0.000	Normal	walls marble	walls marble	1.08
5	2001	0.050	0.000	Normal	walls marble	walls marble	1.12
6	10003	0.030	0.000	Normal	windows	windows	35.65
7	3068	0.200	0.000	Normal	walls wood	walls wood	15.40
8	10003	0.030	0.000	Normal	windows	windows	35.65
9	3068	0.200	0.000	Normal	walls wood	walls wood	7.50
10	4036	0.020	0.000	Normal	Walls gypsum	Walls gypsum	14.97

Fig. 3. Material list in ODEON, showing material properties and area.



Fig. 4. Point source editor setup in ODEON, (a) imam source, and (b) loudspeaker source.



Fig. 5. Exterior and interior views of the Dayk Mosque.

and the dome height is 7.7 m, with a diameter of 20 m (approximately one-third of the ceiling area, as shown in Fig. 9). The mosque has different types of internal surface finishing materials (Fig. 10), with carpeting on the floor. The wall finishing is gypsum plastering, wood, and marble, with fenestration covering 20% of the total wall surfaces, covered by curtains. All walls are covered with wood of 1.20 m meter height, and the *mihrab* wall is clad in marble. Gypsum board and wood material are used for the ceiling. Absorption coefficients of the used materials are illustrated in Table III.

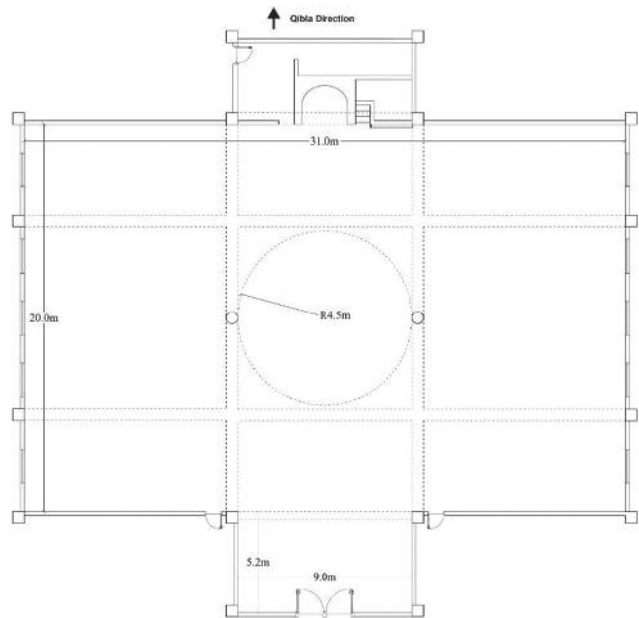


Fig. 6. Main floor plan of the main prayer hall, Dayk Mosque.

TABLE II
CASE STUDIES MEASUREMENT

No.	Mosque name	Prayer room dimension (m)			Parameters for main prayer activities room	
		Length	Width	Height	Volume (m ³)	Expected capacity
1	Dayk Mosque	20	31	4.6	3650	800
2	Altun Mosque	29	33	11	13000	980

C. Interior Materials and Noise Reduction Coefficient (NRC)

A variety of materials have typically been used in the interior of the mosques' main prayer halls, presumably to achieve best quality acoustic performance. Some materials that have been used can be categorized as reflective, and others as absorbent, according to their NRC rate. Designers, whether architects or interior designers, need to select the appropriate materials to offer balance to achieve the eligible RT. Table III illustrates the common existing materials of the interior building fabric in main prayer halls regarding their specification and absorption coefficient.

D. Computer Simulation (ODEON)

Technological developments provide new opportunities for acoustical design. The acoustical assessment of a space in the design phase used to be done with scale models, which was time-consuming and impractical. It is now possible to use computer simulations to analyze acoustical properties before the actual construction of buildings, and acoustical design can thereby become an integral part of the architectural design process from its inception. Computer simulation has proven to be a viable tool in designing music buildings, such as concert halls, opera houses, and multi-purpose auditoria, minimizing hitherto unexpected acoustic

TABLE III
THE LIST OF MATERIALS AND THEIR PROPERTIES OF DAYK AND ALTUN MOSQUES (ODEON USER'S MANUAL, 2020)

Materials	Absorption coefficient (α)							
	63 Hz	125 Hz	250 Hz	500 Hz	1000 Hz	2000 Hz	4000 Hz	8000 Hz
Plaster, gypsum, or lime, smooth finish on lath (Harris, 1991)	0.14	0.14	0.10	0.06	0.04	0.04	0.03	0.03
Gypsum board (Ref. Dalenbäck, CATT)	0.28	0.28	0.12	0.10	0.17	0.13	0.09	0.09
Plywood paneling (Harris, 1991)	0.28	0.28	0.22	0.17	0.09	0.10	0.11	0.11
Carpet heavy, on concrete (Harris, 1991)	0.02	0.02	0.06	0.14	0.37	0.06	0.65	0.65
Solid wooden door (Bobran, 1973)	0.14	0.14	0.10	0.06	0.08	0.10	0.10	0.10
Single pane of glass (Ref. Multiconsult, Norway)	0.18	0.18	0.06	0.04	0.03	0.02	0.02	0.02
Double glazing, 2-3 mm glass, 10 mm gap (Kristensen, 1984)	0.10	0.10	0.07	0.05	0.03	0.02	0.02	0.02
Single pane of glass, 3 mm (Fasold and Winkler, 1976)	0.08	0.08	0.04	0.03	0.03	0.02	0.02	0.02
Marble or glazed tile (Harris, 1991)	0.01	0.01	0.01	0.01	0.01	0.02	0.02	0.02
Audience, 1 per sq. m (Meyer, Kunstmann, and Kuttruff, 1964)	0.16	0.16	0.24	0.56	0.69	0.81	0.78	0.78

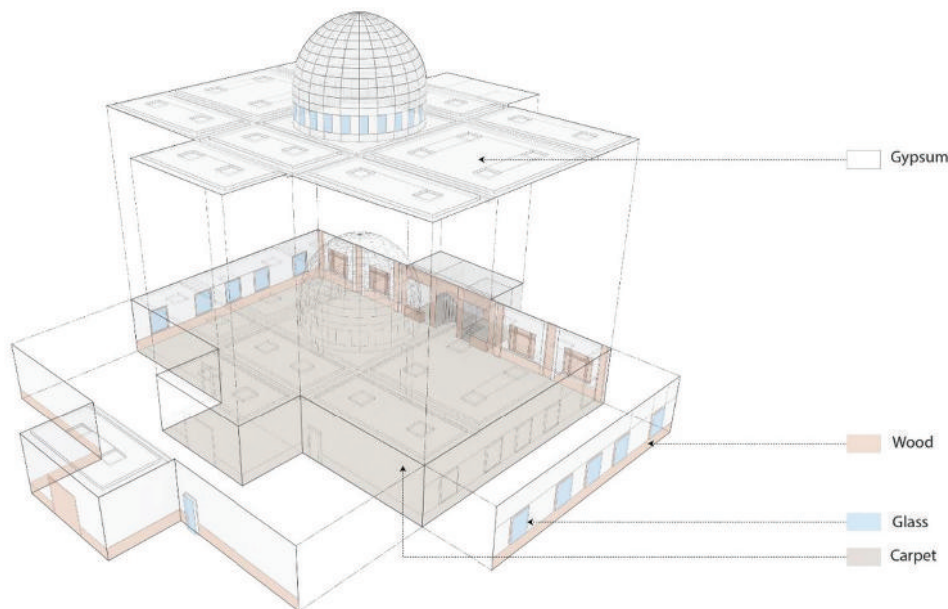


Fig. 7. Exploded diagram showing the internal surface material of the main prayer hall, Altun Mosque.



Fig. 8. Exterior and interior view of the Altun Mosque.

problems (that can now be anticipated), and allowing many alternatives to be tested in a short time span (Schmidt and Kirkegaard, 2004). Computer simulations of the studied Mosques were carried out using ODEON Room Acoustics Program 6 software, which was released by the Technical University of Denmark (Naylor, 1993) (Figs. 11 and 12). The calculation method of this software is based on prediction algorithms including the image-source method and ray tracing. The ODEON Room Acoustics Program also takes into account the statistical properties of room geometry and absorption (Rindel, 2000).

E. Sound Source and Receiver Points

Two different scenarios were examined for both mosques by the simulation. The first scenario discusses the case where worshippers are performing the prayer behind the imam. The imam recites in a standing position facing the *qibla* (the prayer direction, facing toward Mecca), and uses a raised voice, without using any electro-acoustic sound system. The worshippers are assumed to be also standing listening to the imam while performing the daily prayers. Their ear height is taken to be 1.65 m from the floor based on average human height. In the second scenario, the khatib is assumed to be delivering the Friday speech in a raised voice, with the aid of sound reinforcement system as in the case of loudspeaker usage, from the *minbars*, elevated about 1.3 and 1.0 m from the mosque floor in the Altun Mosque and Dayk Mosque, respectively. The mouth height is around 2.80 m from the floor in the Altun Mosque, and 2.50 m in the Dayk Mosque. Worshippers sit on the floor to listen to the *khatib* during the Friday sermon, with ear height of about 1.0 m from the mosque floor. Simulations were run with two assumptions: Mosques being fully or partially occupied.

Figs. 13 and 14 demonstrate the positions of sound sources and receptor points for all configurations.

F. Simulation Procedure

The main research aim is studying and exploring the acoustical performance of contemporary mosque types in Erbil. To achieve this goal, STI, EDT, RT (T30), and

SPL in the chosen mosques were simulated and measured. Simulations were carried out using ODEON Room Acoustics software. The calculation method of this software is based on prediction algorithms including the image-source method and ray tracing. “The ODEON Room Acoustics software also takes into account the statistical properties of the room’s geometry, materials, and absorption” (Rindel, 2000). As mentioned previously, a 3D model of a mosque with a dome was obtained using SketchUP Software. The model was imported to the ODEON Room Acoustics Program. In Dayk Mosque five point sources and 48 receivers are specified for each activity; the first source presents the imam and the other four sources refer to the loudspeakers. Similarly, for Altun Mosque one source as imam and five others as loudspeakers were specified, and the other 56 points were specified as receivers.

The loudspeakers in both mosques are activated or turned off according to activity in the daily prayers or Friday sermon. Whereas different materials with different sound absorption coefficients have been assigned and the calculation parameters have been selected, the receiver surfaces have been divided into grids surfaces of 6 rows for Dayk Mosque and 7 rows for Altun Mosque, having 8 points in each row, as shown in Figs. 13 and 14, illustrating the locations of the sound sources and receivers. To obtain the results of different acoustical parameters, the contour maps and graphs for calculated parameters were obtained for all scenarios and cases. This process was repeated and simulated in both mosques, which have different dome areas. SPL, RT (T30), EDT, and STI were simulated in the main prayer hall when fully and partially occupied.

It is important to mention that acoustic parameters of EDT, SPL, and T30 in ODEON are calculated for eight octave

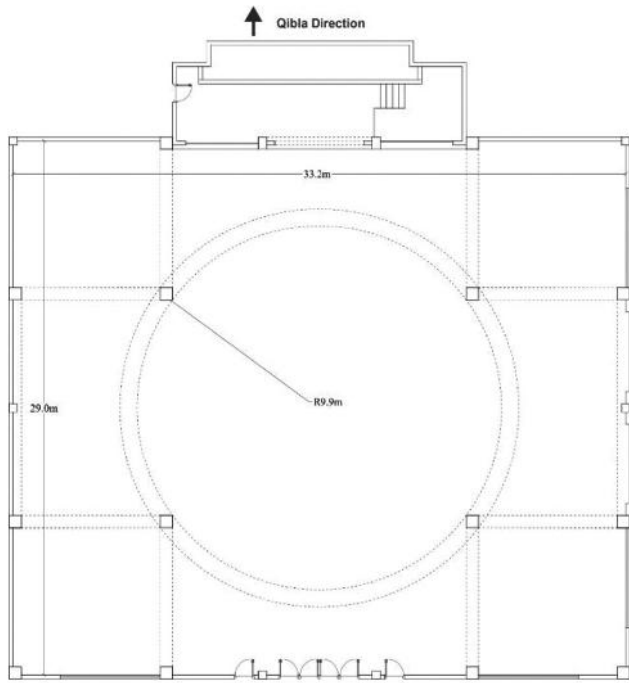


Fig. 9. Main floor plan of the prayer hall, the Altun Mosque.

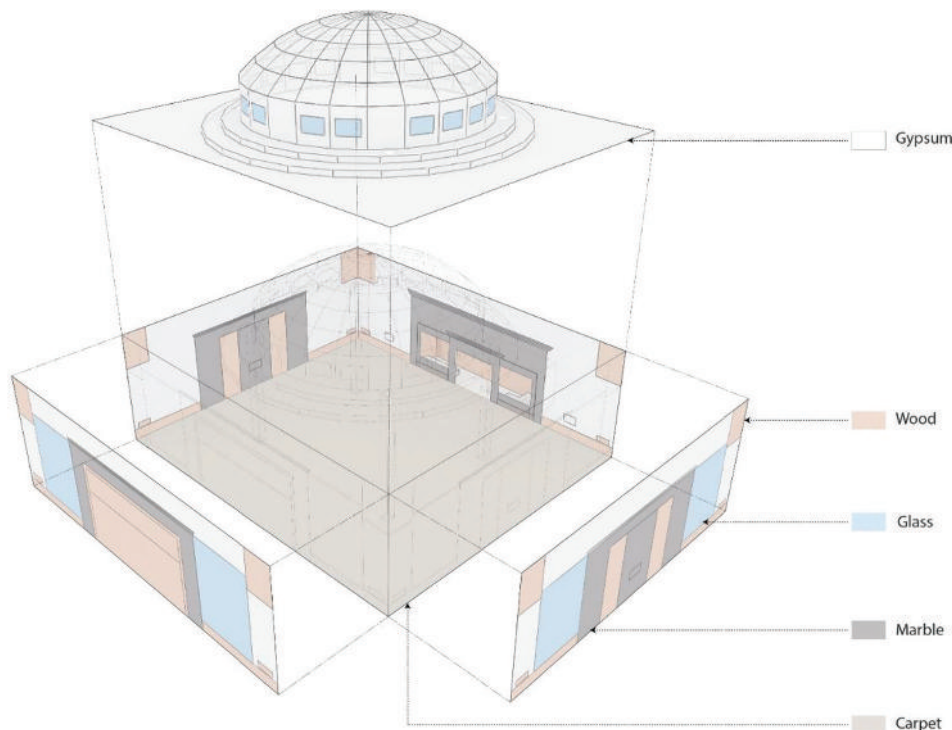


Fig. 10. Exploded diagram showing the internal surface material of the main prayer hall, Altun Mosque.

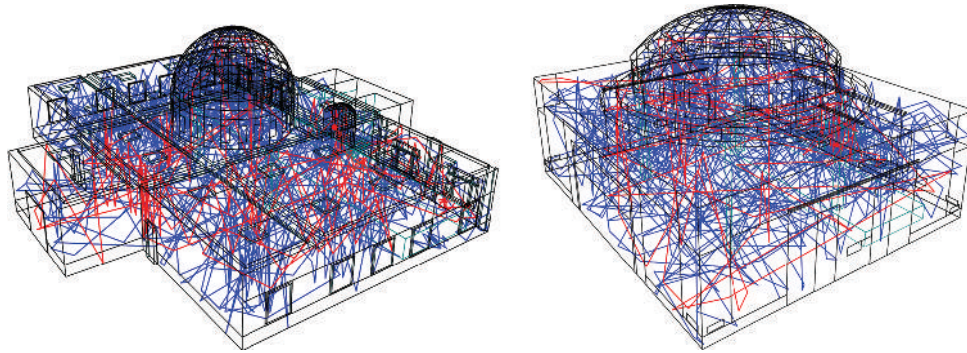


Fig. 11. 3D investigation ray tracing view in ODEON (left: Dayk Mosque, right: Altun Mosque).

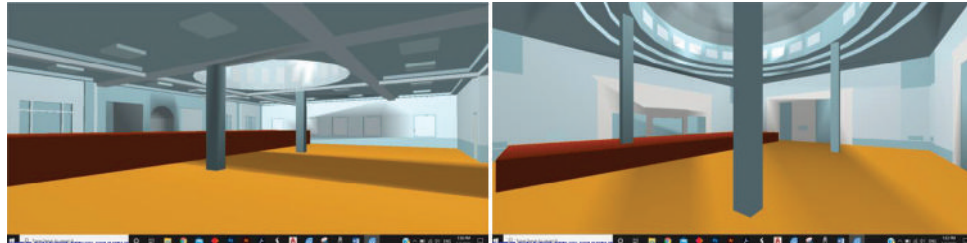


Fig. 12. Interior 3D Open-GL views of modeled mosques (left: Dayk Mosque, right: Altun Mosque).

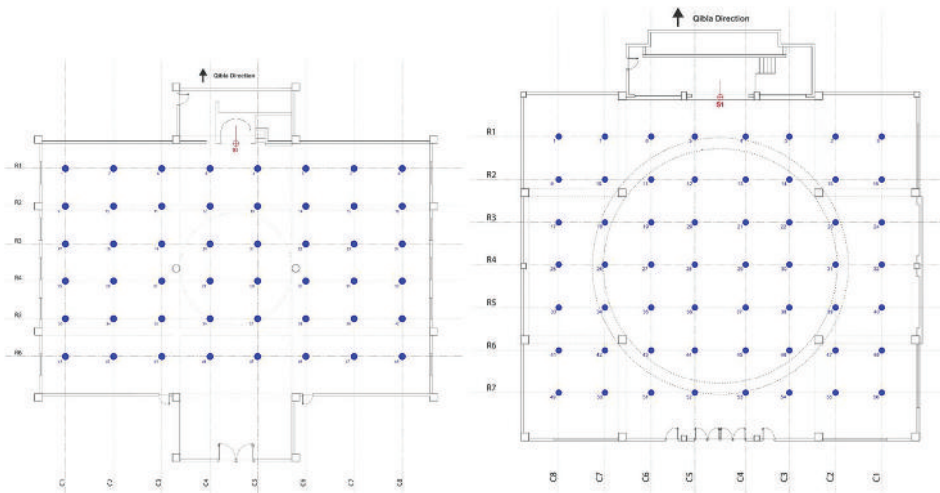


Fig. 13. Receiver points in plan view in 1st scenario with imam position source (left: Dayk Mosque, right: Altun Mosque).

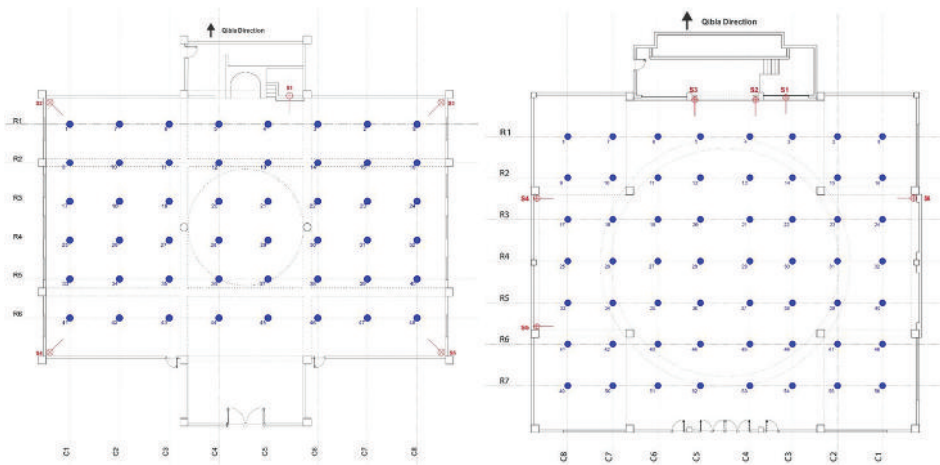


Fig. 14. Receiver points in plan view in 2nd scenario with loudspeakers and *khatib* position source (left: Dayk Mosque, right: Altun Mosque).

bands (63 Hz-8000 Hz) separately; hence, it was not possible to present all the data in this research; only the frequency of 1000 Hz is being discussed, and EDT with some other bands is presented in the Appendix. The background noise in the mosque is assumed to reach an NC rating of NC15. To include the background noise for the calculations in ODEON, NC15 was applied in the room setup. The first activity indicates the prayer mode; for this, the source is the imam in the *mihrab*, facing toward the *qibla* set at a height of 1.65 m. The *mihrab* space is highlighted in Fig. 15. The second activity is the preaching mode and the recital of the Holy Quran. The source is the *khatib* in the *minbar*, facing the worshippers, supported with four loudspeakers. The receiver height for this activity presents the seating level of approximately 1.65 m. For the two different activities, speech-related parameters are analyzed.

VII. RESULTS AND DISCUSSION

A. STI (imam and loudspeaker)

To investigate how well speech is understood for a receiver in a room, STI can be used as a quantifying method of speech transmission intelligibility. Flawless speech transmission indicates that the temporal speech envelope at the audience location replicates the speech envelope at the mouth of speaker. The intelligibility of speech can be quantified regarding the progressions achieved in the adjustment of the

speech envelope as a result of reverberation and noise in the space (Davis, Patronis and Brown, 2013). Barnett (1999) suggested that the STI subjective scale differs from 0 = bad to 1 = excellent. According to this scale, an STI of at least 0.5 is appropriate for most applications, as shown in Table IV.

1) STI measurement during daily prayer (imam position)

As presented in Fig. 16, STI ratings are indicated on the value colored scale bar in each mosque. As it can be seen in both mosques, the closer the worshippers are to the source, the better the STI score. The zones that are considered as poor and bad in STI ratings are located in the center of the rear half of the floor area, with some other poor zones near the middle-side walls, behind the column zones, and at the far front corners.

For the first activity mode, which is the most critical case when the imam is performing alone (that is, without the loudspeakers), as in the daily prayers, with one-third of the mosque occupied, the STI ranges from 0.23 to 0.65 in Dayk

TABLE IV
STI-SUBJECTIVE VALUES FOR SYLLABLE INTELLIGIBILITY (STI REFERENCE VALUES ACCORDING TO BARNETT, 1999)

No	Subjective scale	STI value
1	Bad	0.00-0.30
2	Poor	0.30-0.45
3	Fair	0.45-0.60
4	Good	0.60-0.75
5	Excellent	0.75-1.00

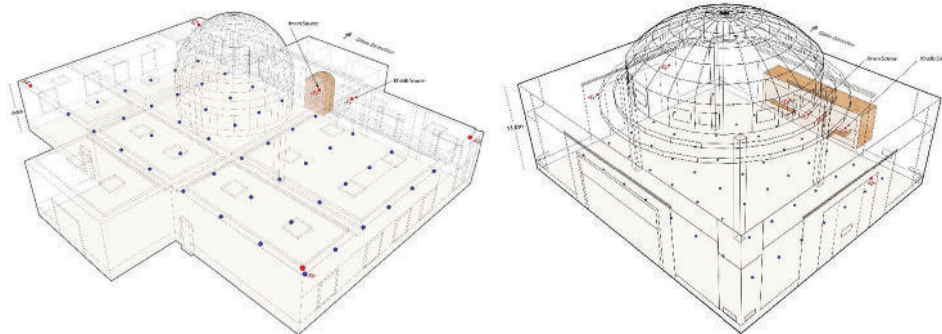


Fig. 15. All source and receiver points in 3D view in both imam and *khatib* position scenarios, highlighting the *mihrab* location (left: Dayk Mosque, right: Altun Mosque).

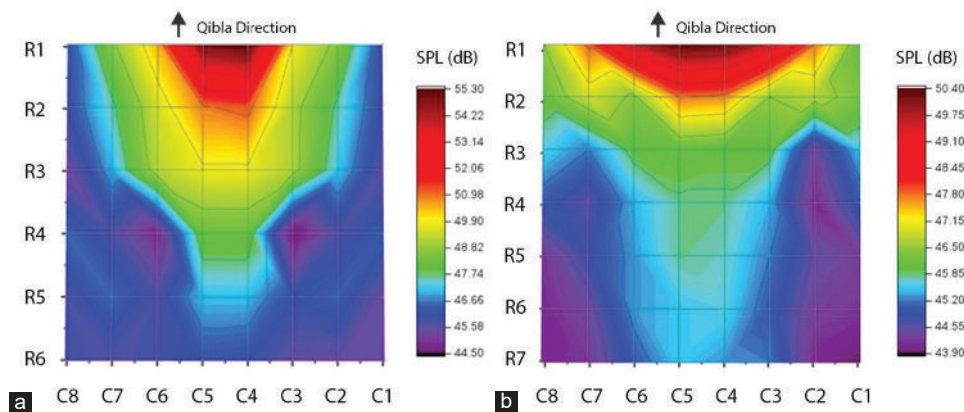


Fig. 16. Speech transmission index contour map in the case of daily prayer (imam position): (a) Dayk Mosque, (b) Altun Mosque.

Mosque, and 0.12 to 0.42 in Altun Mosque, both of which are considered poor ratings. The best values were found at locations just around the source (imam) and in the first row, where the STI is considered fair and good (respectively).

It is shown in Fig. 16a that for the imam position in Dayk Mosque, only 5% of the area has good STI values, and about 10% of the area is covered in the fair zone. The remaining area (85%) lies between the poor and bad zones. Altun Mosque generally has low STI values, as shown in Fig. 16b; only 2% of the area lies in the fair zone, whereas the remainder lies in the poor zone (8%) and the bad zone (90%).

In general, STI values are affected by the hall size, *mihrab* geometry, and the dome-to-ceiling ratio (greater dome-to-ceiling ratio provides better STI values). The size and geometry of the *mihrab* have a significant impact in the prayer mode, where the imam is facing the *mihrab*, and the proper sound reflection is essential to obtain decent speech clarity, especially with regards to the early reflections. The overall dome-to-ceiling ratio and height of the space could cause lower STI values due to the delay in reflected sound, as shown in the contour maps of Fig. 16. For instance, Dayk Mosque, which has a semicircular niche *mihrab* (Fig. 15), has a better STI value than Altun Mosque, in which no consideration has been given to the geometry and size of its *mihrab* (Fig. 15), reflected in the unnecessary scattering of sound in the case of daily prayer.

2) STI measurement in Friday sermon (*khatib* position)

Fig. 17 shows the case colored scale bar and contour map indicating STI ratings. Overall, during Friday sermon activity the support of loudspeaker drastically improved the STI values, especially in Dayk Mosque. In the Altun Mosque, only the areas near the end of the side walls, rear corners, and the far front corners were zones of poor STI rating, whereas the rest of the space had decent STI values. This is mainly because this wall side had one loudspeaker compared to the parallel side. As in the first scenario, STI values were influenced by the dome-to-ceiling ratio and the space size, in addition to loudspeaker locations and distribution.

It is shown in Fig. 17a that for the sermon case in Dayk Mosque, which is the best case, most STI values are in the

satisfactory (good) zone, covering 100% for Dayk Mosque. For Altun Mosque, as shown in Fig. 17b, the acceptable zone comprises about 70% of the area, with 55% being the fair zone, and 15% considered as a good zone. The remaining area comprises the poor zone (30%).

Dayk Mosque's STI values increased to the range of 0.6-0.69, which are considered good to excellent levels. Although using a greater number of loudspeakers greatly improved the STI levels in Altun Mosque, reaching a range of 0.4-0.6, this is not as good as the Dayk Mosque due to unusual distribution of loudspeakers, as shown in Figs. 14 and 15. The better location of loudspeakers in Dayk Mosque includes positioning all speakers in the four top corners of the main hall, each facing the audience near them in a balanced manner, which resulted in better STI scores.

B. Reverberation Time (RT) and Early Decay Time (EDT)

RT is defined as the time it takes for a sound to decay by 60 dB after the sound source has been switched off. This is noted as T60. RT is the most frequently used parameter in room acoustics. Some acousticians rely only on RT when evaluating room acoustics, but for most cases this is not sufficient in itself. RT can reveal information about the size of a room and sound absorption within it. When measuring RT in practice there is always a considerable level of background noise in the recording (for example, ambient acoustic noise, electric noise in microphone, electronics, and cables), which reduces the range of 60 dB required to derive T60. Therefore, RT is calculated based on smaller decay ranges (10 dB, 15 dB, 20 dB, and 30 dB) instead, which are well above the background noise level. However, the corresponding time it takes for each decay range is always multiplied by an appropriate factor to extrapolate the time for 60 dB decay (Davis, Patronis and Brown, 2013). Calculating RT in this way results in multiple different numbers for RT, as shown in Fig. 18. EDT is obtained from the initial 10 dB drop of the backward-integrated decay curve, by applying the best-fit linear regression line between 0 and -10 dB. Assuming that decay is linear, extrapolation of 10 dB range and 60 dB requires multiplication by 6, EDT is related to the first -10 dB. Since the early part of the decay is dominated

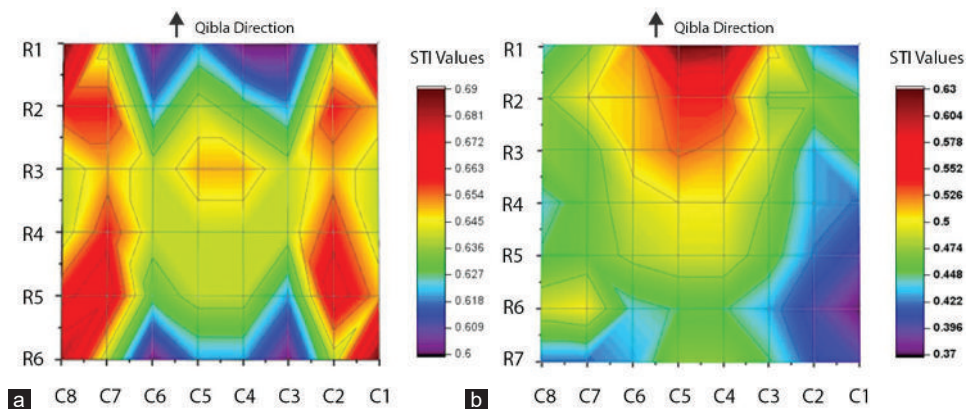


Fig. 17. Speech transmission index contour map in the case of Friday sermon (*khatib* position): (a) Dayk Mosque, (b) Altun Mosque.

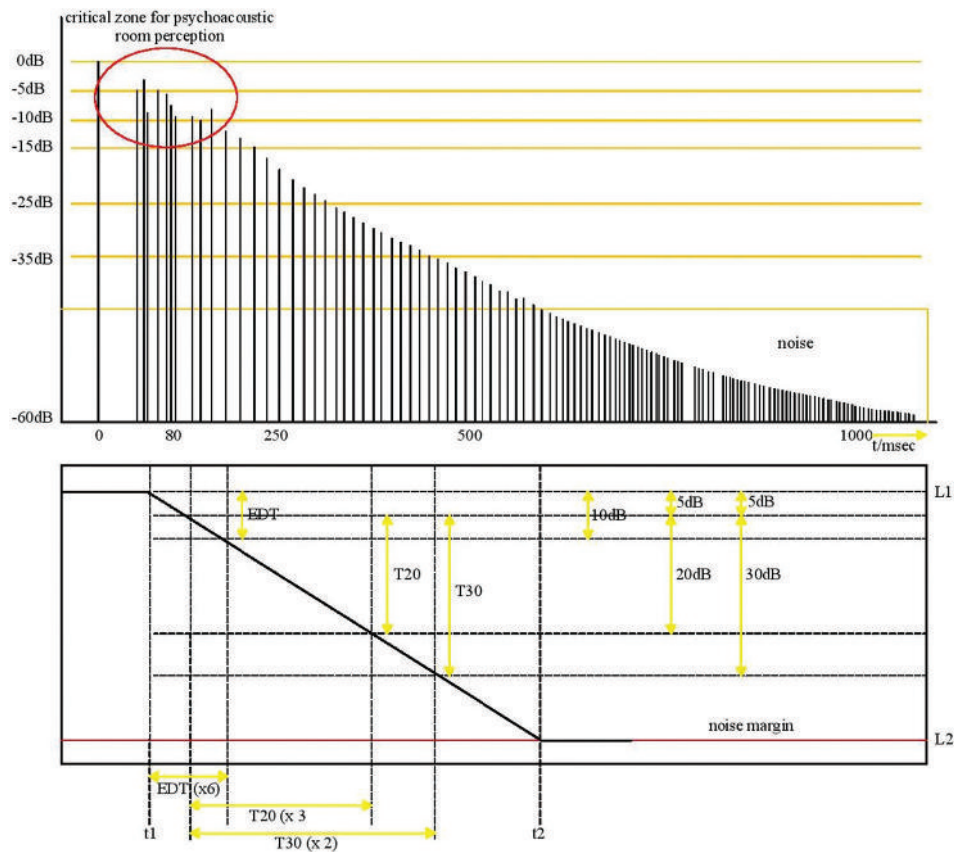


Fig. 18. The relationship among RT (T30, T20, T15) and early decay time.

by the direct sound, and it is much steeper than the rest of the decrescendo, EDT is usually shorter than the other types of RT (Barron, 2009).

In respect to RT (T30) simulation in both mosques, In general, we can compare the case in two different ways. First method is comparing the T30 of one mosque, either Dayk or Altun, according to the different activity of daily prayer of one-third occupied space, with sound emanating from the imam position; or the Friday sermon with a fully occupied hall, when the imam is preaching from the minbar (khatib position) with loudspeaker support. The difference in audience number (that is, user density) affects the overall absorption coefficient, and consequently the T30.

Second, comparison between both mosques can be undertaken, as each has a different size, geometry, materials, design, and even allocation of loudspeakers. T30 data for all octave frequency bands were attained from the simulation results. For the purpose of this discussion, the mid-frequency of 1000 Hz is considered.

The T30 of Dayk Mosque with the frequency of 1000 Hz is around 1.2 s-1.4 s during the partially occupied daily prayer of the imam position, and about 0.98 s-1.22 s with the support of all four loudspeakers in the case of fully occupied Friday preaching scenario. Similarly, the Altun Mosque T30 ranges mostly from 2.65 s to nearly 3.4 s whereas performing the daily prayer led by the imam, and 2.23 s to around 3.15 s with the loudspeakers on during the Friday sermon.

It is observed that generally T30 is longer during the daily prayer when only the imam is reciting the Quran, compared to the case of the presence of all loudspeakers for both mosques, as the imam is standing in one location facing the *mihrab*, thus sound has to be reflected on the surfaces in front of him to bounce back to the worshippers. Moreover, the greater the audience the higher the absorption coefficient, and the lower the T30.

In the Dayk Mosque, in both scenarios during the daily prayer and Friday sermon, the highest T30 value is in the center of the hall, compared to the corners and edges, as shown in Fig. 19a and Fig. 20a. This is due to the presence of the dome in the center of the ceiling, which causes a delay in the reflected sound; in other words, this area receives long-delayed reflections from the dome. Conversely, Altun Mosque has more even T30 values in each activity, as shown in Fig. 19b and Fig. 20b, whether in daily prayer or the Friday sermon, because the dome-to-ceiling ratio is greater compared to the Dayk Mosque, and the ceiling is a hard surface with reflective characteristics, hence the dome directly affects all parts of the room, causing homogenization and similar T30 values. The effect of the dome could be intensified when all the loudspeakers are used, as their allocations are not ideally distributed. However, the dome compensates for this problem by standardizing the room with similar RT values at all points, consequently resulting in similar STI. EDT has also been simulated for all the cases (Appendix M1, M2, M3, and M4).

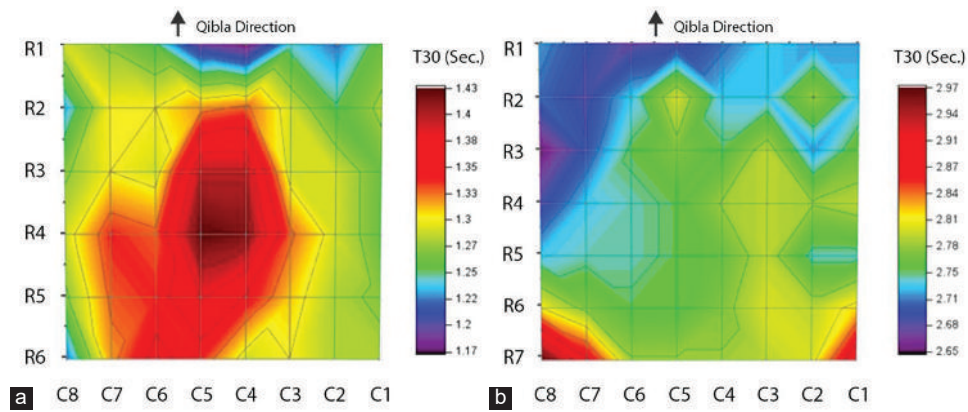


Fig. 19. T30 contour map (1000 Hz) in the case of daily prayer (imam position): (a) Dayk Mosque (b) Altun Mosque.

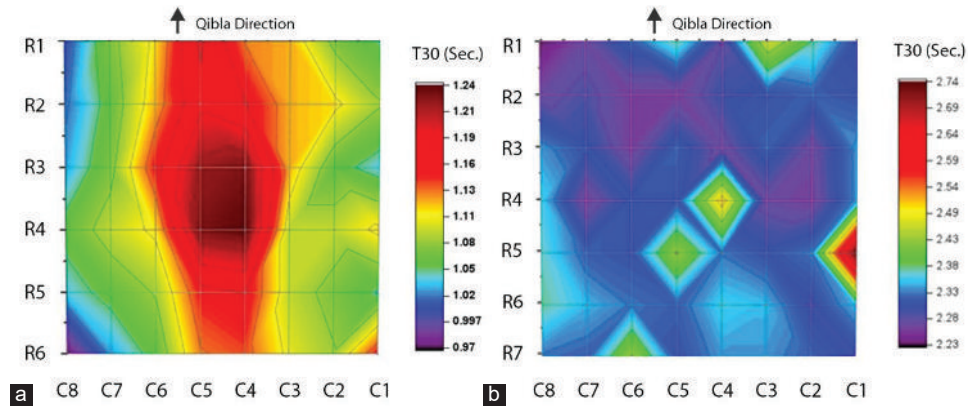


Fig. 20. T30 contour map (1000 Hz) in the case of Friday sermon (*khatib* position): (a) Dayk Mosque, (b) Altun Mosque.

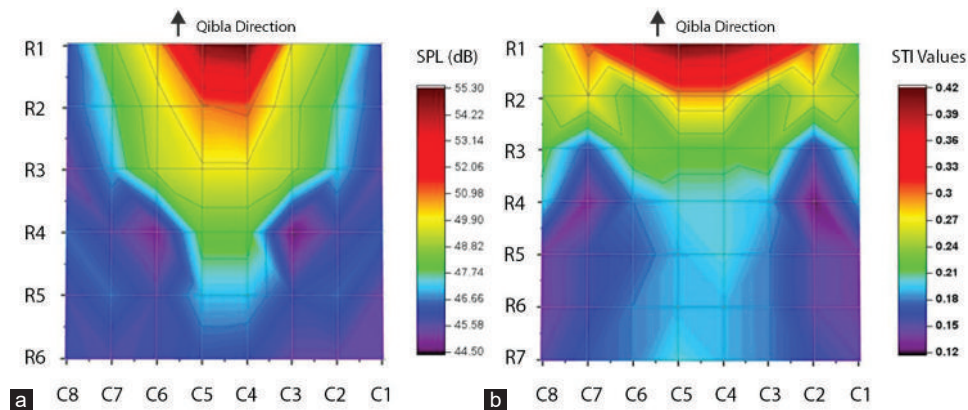


Fig. 21. Sound pressure levels contour map (1000 Hz) in the case of daily prayer (imam position): (a) Dayk Mosque, (b) Altun Mosque.

C. Sound Pressure Level (SPL)

1) SPL measurement at daily prayer (imam position)

Simulation data indicate that the values of SPL range between 45-55.30 dB in Dayk Mosque, and 44-50.40 in Altun Mosque, with a frequency of 1000 Hz for speech (imam position) (Fig. 21).

The most revealing case investigated is the first, when the imam is performing alone (that is, without the loudspeaker) in both mosques the results show that the SPL value decreases gradually as we get farther away from the

imam. According to the worshipper's location, the SPL in the front rows are in the highest level as compared to the back rows, as direct sound decays in the hall. Moreover, the irregularity of the maps for both mosques occurring close to the center of the room is because of the existing columns supporting the ceiling, which create acoustic shadows in the area just behind them, as shown in the SPL contour maps (Fig. 21). These shadows are due to the columns' positions and mass relative to the position and orientation of the imam.

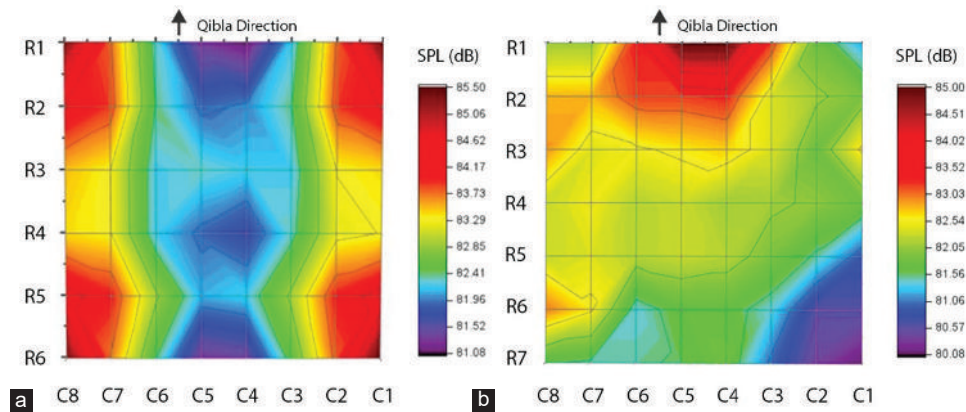


Fig. 22. Sound pressure levels contour map (1000 Hz) in the case of Friday sermon (*khatib* position): (a) Dayk Mosqu

2) SPL measurement in Friday sermon (*khatib* position)

From the SPL point of view, the situation is better for the imam with loudspeaker configuration for the Friday sermon. As expected, the introduction of the loudspeakers in the second case helps in the distribution of the sound more evenly throughout the space, minimizing the shadow area behind the columns, in addition to increasing SPL values in both mosques (Fig. 22). It is noticeable that the SPL range is increased to 80-85 and 81-85 dB in Dayk and Altun Mosque, respectively.

Comparing the SPL contour map of both mosques, another advantage is observed for Dayk Mosque over Altun in terms of the equal distribution of SPL within the space, which is due to the loudspeaker positioning in all four corners of the hall (Figs. 14 and 15). It is important to mention that if Altun Mosque did not have a significantly greater dome-to-ceiling ratio, this problem (which is fundamentally due to the unequal distribution of the loudspeakers) would not be so obvious.

VIII. CONCLUSION

Sound fields of the main prayer halls in the case studies were tested for RT and sound distribution. The main prayer halls' geometries combined with existing speakers showed the advantages of uniform spatial distribution of sound, attaining proper sound supply over the whole space. However, overcoming RT problems effectively requires a holistic understanding of the material usage and properties in the initial design stages, supported by forming suitable space geometry. Furthermore, whereas almost all of the rows have acceptable sound levels, in the case of loudspeakers being absent, the imam's position within the mosque geometry negatively affected sound fields in the middle and back rows for all receivers' positions. In that case, only the front row had appropriate levels of sound.

The research investigation conducted within this paper is anticipated to serve architects to have an enhanced understanding of the acoustical impacts of initial architectural design decisions relating to space, material, and forms of mosque architecture to incorporate necessary elements for superior quality acoustics to be enjoyed by users of structures, increasing the satisfaction of worshippers' hearing

and comfort. Considering the results in this study, aside from the mosques' physical components (especially the floor plan design and volume), various aspects affect the acoustic environment, including the area, utilized building materials, and occupant number and density. The majority of the mosque designers or architects absolutely prioritize visual esthetics and form, and some mosques merely focus on providing as much space as possible to cater for more worshippers, with no specific acoustical design consideration.

This study analyzed the acoustical characteristics of main prayer halls of two most common mosque types in Erbil during two main usage scenarios: Fully occupied during the Friday sermon, and partially occupied during daily prayers. Room simulation utilized ODEON to assess the degree of intelligibility. Good acoustic criteria were compared with the requirements of space and design guidelines.

The analysis of two mosques main prayer halls indicated that quality of sound was insufficient without using loudspeakers. In Dayk Mosque, the acoustical properties were better than in Altun Mosque, due to the even distribution of loudspeakers in the former, located in the four corners of the prayer hall for the Friday sermon. In general, areas beneath the dome had longer RT. Moreover, in Dayk Mosque in both the imam and *khatib* positions the central area had longer T30 compared to Altun Mosque, which had more even distribution of T30 for both scenarios. The more appropriate *mihrab* design for the imam's position in the Dayk Mosque had a noticeable impact on the sound distribution in daily prayer. In this scenario, the SPL and consequently the STI were clearly decreased behind the structural columns, and the closer the worshippers were to the imam, the better the SPL and STI. Due to this, the worshippers in some receiver points could not follow and understand what was said clearly in the *mihrab*. Due to the limited number of chosen mosques and limited acoustical parameters in ODEON 16 Basics to determine acoustical performance, further analyses are required on the topic of common mosque designs.

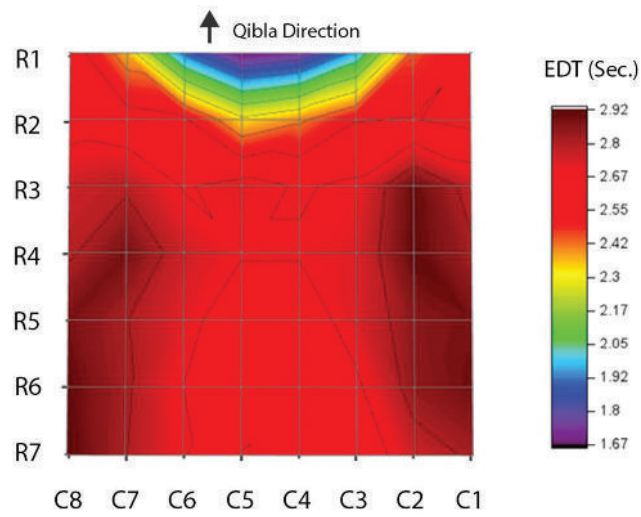
REFERENCES

Barnett, P.W., 1999. Overview of Speech Intelligibility. Vol. 21. *Proceedings IOA*, pp.1-16.

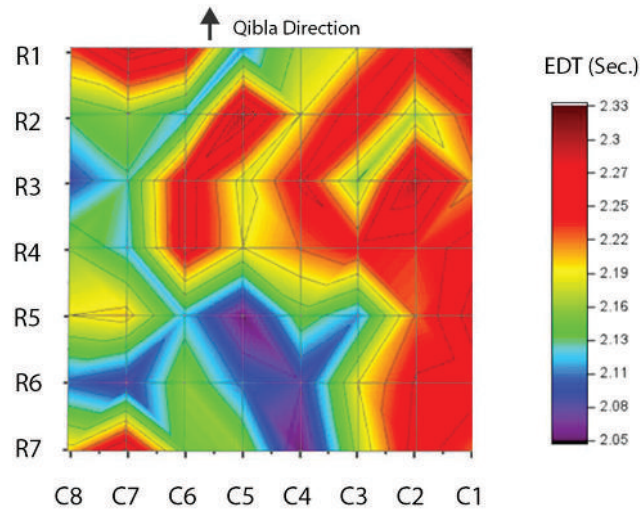
- Barron, M., 2009. *Auditorium Acoustics and Architectural Design*. 2nd ed. Taylor and Francis, Abingdon.
- Chiang, C.M. and Lai, C.M., 2008. Acoustical environment evaluation of joint classrooms for elementary schools in Taiwan. *Building and Environment*, 43(10), pp.1619-1632.
- Davis, D., Patronis, E. Jr. and Brown, P., 2013. *Sound System Engineering*. 4th ed. Routledge, London.
- Education Funding Agency, 2015. *BB93: Acoustic Design of Schools Performance Standards*. Department of Education, London. Available from: <https://www.gov.uk/government/publications/bb93-acoustic-design-of-schools-performance-standards>. [Last accessed on 2021 Jan 05].
- Ismail, M.R., 2013. A parametric investigation of the acoustical performances of contemporary mosques. *Frontiers of Architectural Research*, 2, pp.30-41.
- Khabiri, O., Ahmad, M.H. and Kandar, M.Z., 2013. Research method for computer modelling study in mosque acoustic design. *Journal of Basic and Applied Scientific Research*, 3(4), pp.227-233.
- Lamancusa, J.S., 2000. *Noise Control: Human Response to Sound*. Penn State University, University Park. Available from: https://www.mne.psu.edu/lamancusa/me458/3_human.pdf. [Last accessed on 2021 Jan 05].
- Lewers, T.H. and Anderson, J.S., 1984. Some acoustical properties of St Paul's Cathedral. *Journal of Sound and Vibration*, 92(2), pp.285-297.
- Marie, P., 2009. *Background Noise Requirements and Audience Noise in Performance Spaces*. M.Sc. Technical University of Denmark, Denmark.
- Mazloomi, A.S.H., 2010. The importance of plan unit design with reference to pedentive dome mosque architecture in early Ottoman period in Balkan Region and Anatolia. *Review of European Studies*, 2(2), pp.105-116.
- Naylor, G.M., 1993. ODEON: Another hybrid room acoustical model. *Applied Acoustics*, 38(2-4), pp.131-143.
- ODEON, 2020. *ODEON Room Acoustics Software User's Manual*. 16th ed. ODEON A/S, Lyngby.
- Othman, A.R., Harith, C.M., Ibrahim, N. and Ahmad, S.S., 2016. The importance of acoustic design in the mosques towards the worshipers' comfort. *Procedia, Social and Behavioral Science*, 234, pp.45-54.
- Rindel, J.H., 2000. The use of computer modeling in room acoustics. *Journal of Vibroengineering*, 3(4), pp.219-224.
- Schmidt, A.M.D. and Kirkegaard, P.L., 2004. On architectural acoustics design using computer simulation. In: *Eleventh International Congress on Sound and Vibration*. International Institute of Acoustics and Vibration, St Petersburg, Russia.
- Sü Gül, Z. and Çalıskan, M., 2013. Impact of design decisions on acoustical comfort parameters: Case study of Doğramacızade Ali Paşa Mosque. *Applied Acoustics*, 74(6), pp.834-844.
- Suárez, R., Sendra, J.J., Navarro, J. and León, A.L., 2004. The acoustics of the cathedral-mosque of Cordoba: proposals for architectural intervention. *Acta Acustica United with Acustica*, 90(2), pp.362-375.
- Wasim, A.O., 2007. Sound parameters in mosques. *Proceedings of Meetings on Acoustics*, 1(1), 035001.

APPENDIX

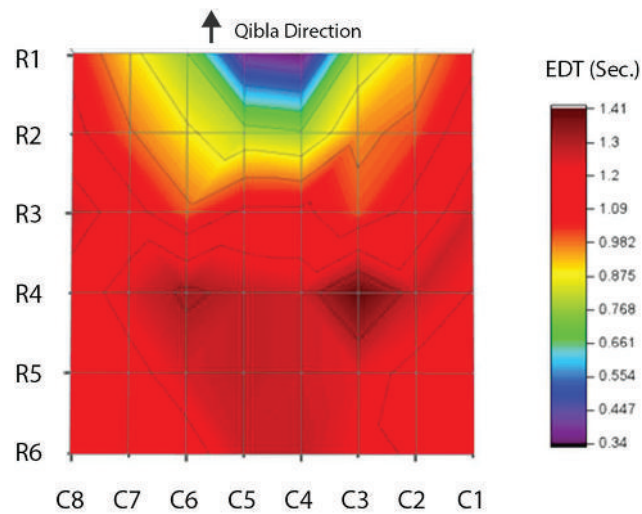
Simulated parameter heat maps for different activities:



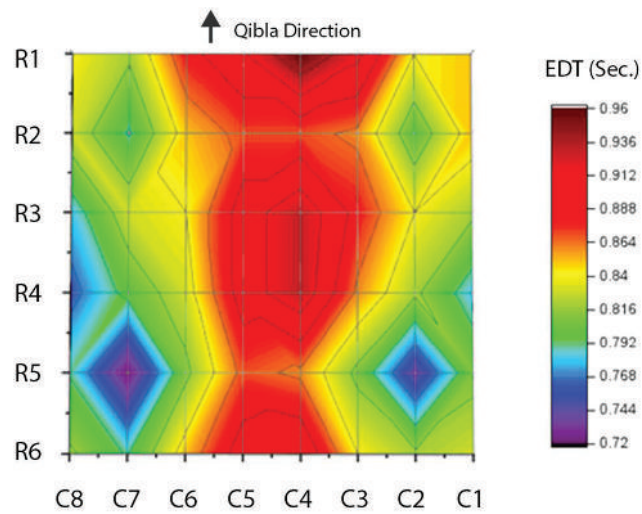
M1. Early decay time contour map (1000 Hz) in the case of daily prayer (imam position): Altun Mosque



M2: Early decay time contour map (1000 Hz) in the case of Friday sermon (*khatib* position): Altun Mosque



M3: Early decay time contour map (1000 Hz) in the case of daily prayer (imam position): Dayk Mosque



M4: Early decay time contour map (1000 Hz) in the case of Friday sermon (*khatib* position): Dayk Mosque

Design and Construction of Zana Robot for Modeling Human Player in Rock-paper-scissors Game using Multilayer Perceptron, Radial basis Functions and Markov Algorithms

Maryam Ghasemi¹, Abdolreza Roshani², Peshawa J. Muhammad Ali³, Farhad F. Nia¹,
Ehsan Nazemi⁴ and Gholam H. Roshani¹

¹Department of Electrical Engineering, Faculty of Energy, Kermanshah University of Technology, Kermanshah, Iran

²Department of Industrial Engineering, Faculty of Engineering Management, Kermanshah University of Technology, Kermanshah, Iran

³Department of Software Engineering, Faculty of Engineering, Koya University, Koya KOY45, Kurdistan Region – F.R. Iraq

⁴Imec-Vision Lab, Department of Physics, University of Antwerp, Antwerp, Belgium

Abstract—In this paper, the implementation of artificial neural networks (multilayer perceptron [MLP] and radial base functions [RBF]) and the upgraded Markov chain model have been studied and performed to identify the human behavior patterns during rock, paper, and scissors game. The main motivation of this research is the design and construction of an intelligent robot with the ability to defeat a human opponent. MATLAB software has been used to implement intelligent algorithms. After implementing the algorithms, their effectiveness in detecting human behavior pattern has been investigated. To ensure the ideal performance of the implemented model, each player played with the desired algorithms in three different stages. The results showed that the percentage of winning computer with MLP and RBF neural networks and upgraded Markov model, on average in men and women is 59%, 76.66%, and 75%, respectively. Obtained results clearly indicate a very good performance of the RBF neural network and the upgraded Markov model in the mental modeling of the human opponent in the game of rock, paper, and scissors. In the end, the designed game has been employed in both hardware and software which include the Zana intelligent robot and a digital version with a graphical user interface design on the stand. To the best knowledge of the authors, the precision of novel presented method for determining human behavior patterns was the highest precision among all of the previous studies.

Index Terms—Multilayer perceptron, Radial basis functions, upgraded Markov model, Rock, paper, Scissors game.

ARO-The Scientific Journal of Koya University
Vol. IX, No.1 (2021), Article ID: ARO.10757, 10 pages
DOI: 10.14500/aro.10757

Received: 27 November 2020; Accepted: 21 February 2021

Regular research paper: Published: 08 March 2021

Corresponding author's e-mail: hosseinroshani@kut.ac.ir

Copyright © 2021 Maryam Ghasemi, Abdolreza Roshani,
Peshawa J. Muhammad Ali, Farhad F. Nia, Ehsan Nazemi and

Gholam H. Roshani. This is an open-access article distributed under the Creative Commons Attribution License.



I. INTRODUCTION

Playing is a purposeful physical or mental activity that is performed individually or in groups with the aim of entertainment and leisure. Each game contains its own set of players, moves, or strategies as well as the principles and rules. Winning in every game is not only a function of luck but also each player during the game can move toward the victory by applying the rules of the game. Games often have well-known forms and have social, climatic, and cultural contexts (Ahmadvand, 1993). Among all games, the game of rock, paper, and scissors has a very simple environment and is considered a traditional and popular game that almost people of all ages can enjoy playing the game.

Rock, paper, and scissors are a hand game which is usually played among two players (Ali et al., 2000). This game describes a cycle between three competing species in a network (Hu et al., 2019). Each player puts his hand in one of the three allowed positions. The rock is shown with a closed fist. The scissors with closed hands whereas middle and index fingers are stretched and the paper is shown with the open palm and fingers glued together. According to Fig. 1, the general rule of the game is such a way that the rock beats the scissors, the scissors beats the paper, and the paper beats the rock.

In general, humans do not perform very well in random activities. Investigations of the behavior of the human players in this game conducted by scientists revealed that most of them have a predictable behavior pattern. Since the adaptability of the rock, paper, and scissors' game leads to a change in the player's strategy over the course of time, this game can be considered a good sample for testing the theory of behavior of human short-term memory (Ali et al., 2000). In game theory, we observe concepts that can model

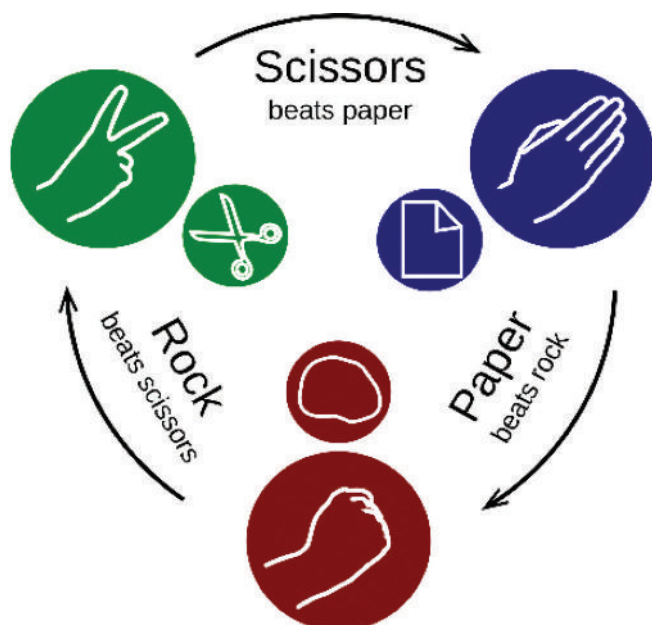


Fig. 1. The rules of rock-paper-scissors game (<https://en.wikipedia.org>).

abstract evolutionary systems very well. Among them, we can refer to the intelligent player of rock-paper-scissors who has the ability to recognize the human behavior pattern and defeat him. The development of smart players requires that their behavior to be consistent with the behavior of other players. Since creating such a player increases the excitement and difficulty of this game, special attention is paid to this problem in the gaming industry (de Souza et al., 2013). In this paper, a novel method to determine human behavior patterns during rock, paper, and scissors game was presented with high precision. To the best knowledge of the authors, the precision of novel presented method is the highest precision among all of the previous studies.

II. LITERATURE REVIEW

Game and entertainment, especially group games, have played an important role in the history of humankind. However, choosing the initial player at the beginning of group games has always been the main concern of the participants of those games. In the 18th century, a game called *Jon_Ken_Pon* was invented in Japan in an attempt to solve this problem, which is currently known as *Rock-Paper-Scissors* (Hasuda et al., 2007). Until recently, many studies have been accomplished in this field, which we will review in the following:

Ali et al. (2000) proposed a way to create an intelligent player in the game of rock-paper-scissors using genetic algorithm. In this method, a genetic string is encoded to train the intelligent player. Decent disciplines were produced in later generations, and eventually an evolved system created in which, instead of making unbiased decisions, it used the player's behavior in previous games to make concrete decisions in the current game. Another proper way to create an intelligent player of rock-paper-scissors was proposed by

de Souza et al. (2013). To achieve this goal, they used the WIZARD weightless neural network. The WIZARD device is a general system made of small units of RAM that can detect and classify different patterns. The learning operation is based on reading and writing in different locations of the memory, which makes this model effective for creating intelligent players. In this model, three training algorithms are proposed to classify input patterns over the time. It also includes a new function for encoding input data and a method to deal with incomplete information in input arrays. Cenggoro et al. (2014) proposed a technique to determine the player's future behavior in the game of rock-paper-scissors using the feed forward neural network. In a study by Salvetti et al. (2007), a new method based on entropy and LLE¹ indicators was proposed to predict the appropriate moment to use rock, paper, or scissors during the game. The right moment is when the opponent's future behavior is more predictable. The intelligent player then makes a choice to defeat the opposing player. Ghasemi et al. (2020) presented a suitable strategy for detecting human behavioral patterns in the game of rock-paper-scissors using the multilayer perceptron neural network (MLP). In the first step, the neural network learns the pattern of human behavior and in the second step; it is ready to play a real game against her or him. The results of the study for this network on 40 people showed the good performance of the MLP network in detecting human behavior patterns. Matsumoto et al. (2012) developed a program for automatic judgment in the game of rock-paper-scissors. In their work, first, using the C-Means classification method, the numbers, and the locations of the hands in the images of rock-paper-scissors are estimated, and then according to the difference between the compression of the categories, the winning, and losing judgments are made. Studies have also been carried out to diagnose hand postures (rock-paper-scissors). Chen et al. (2010) used the image processing method to investigate this. Initially, the hand image is extracted from consecutive images and then it is used to produce a binary image and filter out the interference, overall threshold, and skin color. Their main focus in this article was to identify the scissors because it involves the state of consecutive errors, whereas identifying rock and paper is rather easy. The number of zero-fingers represents rock and the number of five-fingers represents paper. If the number of fingers is 2, hence there are eight different shapes, of which only 1 is correct. To avoid the error, the distance between two fingers is used, which is the same criterion for determining the position of the scissors in some cases and to solve this problem they used the methods of division, histogram, and angle criterion. Gang et al. (2017) suggested a method to classify electromyographic (EMG) signals according to hand postures (rock-paper-scissors) by using MLP. In this method, EMGs are applied to the Hezajac-levine bilinear activation model, and then the output of the model is used as MLP inputs. Besides, cross validation method was also used to evaluate the performance of MLP classification. Hasuda et al. (2007) designed a robot that plays rock-paper-scissors in front of a human. The designed

¹ Local Lyapunov Exponent

robot includes a camera, an image processor, an evaluation system, an audio system, and also a body. In fact, the image processing system was developed to detect the shape of the human hand, and the evaluation system estimates the output of the game by comparing the shape of the player's hand with the robot. To communicate with humans effectively, this robot is able to express emotions through the sound, body gesture, and facial expressions, and also has the ability to talk to the player. In another study by Ahmadi et al. (2019), an intelligent robot named Rasa was developed to play stone-paper-scissors against humans. In the first step, the designed robot detects the movement of the player's hand using a Leap Motion sensor as well as an MLP network. In the second step, using the Markov chain model, he predicts the player's future movement. Another intelligent robot was constructed by Pozzato et al. (2013). In this robot, the Gaussian mixture model algorithm is used to predict the future movement of the player in the game of rock-paper-scissors.

In this paper, artificial neural networks (ANNs) (MLP and radial base functions [RBF]) and upgraded Markov chain model were used to build up an intelligent rock-paper-scissors player. In these algorithms, artificial intelligence learns the pattern of human behavior. Afterward, it will be able to predict the future movement of the human opponent and to defeat him by providing an appropriate answer. To ensure the ideal performance of the modeling, the effectiveness of intelligent algorithms in detecting the behavioral pattern of players was evaluated and the percentage of winner computer was calculated. In addition, another program was written to calculate the percentage of a winner computer without an intelligent algorithm for playing rock-paper-scissors against humans. In this program, all computer selections are random. Subsequently, this strategy was implemented in two physical ways. In the prototype, a robotic hand was used that performs one of the movements of rock, paper or scissors for each step of the game with the decision-making power of artificial intelligence written on the Zana robot processor. In the second phase, to make the graphical appearance of the game suitable and attractive, the possibility to play against a human opponent was added to the design of robot using the MATLAB graphical user interface (GUI) in a computer system and embedding it into a designed stand.

III. MENTAL MODELING

A. ANNs

ANNs have become the most widely used method for predicting various systems. With great negligence, these networks can be called electronic models of the neural structure of the human brain (Menhaj, 2008). According to this assumption, information processing takes place in simple elements, which are referred to as neurons. Electrical signals are transmitted between neurons and on junctions. Each connection has an associated weight that multiplies the transmitted signals in the neural network. This weight can be used to amplify or weaken the signal. Each neuron applies an activator function to its input to determine the output signal

(Fausett, 2006). In fact, the purpose of creating a software-based neural network is to create a mechanism for solving engineering problems, inspired by the behavioral pattern of biological networks rather than simulating the human brain (Menhaj, 2008). Recently, different kinds of ANNs have important role in solving different complex problems of engineering (Roshani, et al., 2014, Nazemi, et al., 2015, Roshani, et al., 2016, Roshani, et al., 2017a, Roshani, et al., 2017b, Jamshidi, et al., 2020, Roshani, et al., 2020, Roshani, et al., 2021a, Roshani, et al., 2021b, Roshani, et al., 2021c).

B. MLP Network

The MLP network is a class of ANNs. An MLP consists of at least three layers: An input layer, a hidden layer, and an output layer. The neurons in each layer connect to all the neurons in the next layer (Roshani et al., 2018). Error propagation algorithm is the most widely used method for training multilayer networks (Dehlaghi et al., 2015). The structure of the MLP network designed to detect human behavioral patterns in the game of Rock-Paper-Scissors is illustrated in Fig. 2. This structure was optimized using presented algorithm in our previous study (Roshani et al., 2018).

According to the designed MLP network structure shown in Fig. 2, the input layer has four neurons, which are the computer and player selections in two consecutive rounds. The target output of this network is player selection in the round right after two consecutive rounds. Table I shows the characteristics of the MLP network designed for detecting human behavior patterns in the game of rock-paper-scissors.

C. Radial Basis Function Network

Radial basis functions are another type of feed forward neural networks. The process of such networks depends on the radial distance from specific points. There are three types of layers in RBF networks: Input layer, hidden layer, and output layer. In the hidden layer, each node applies a radial function that has its own center and radius to the inputs. The output of this network is a linear combination of radial basis functions for input parameters and neurons. The structure of the RBF network designed to detect the pattern of human behavior in the game of rock-paper-scissors is depicted in Fig. 3. Table II shows the characteristics of the RBF network designed for detecting the pattern of human behavior in the game of rock-paper-scissors.

D. Design Algorithm of Rock-Paper-Scissors Game with ANNs

The algorithm for designing rock-paper-scissors consists of two stages. In the first stage, to train the neural network, 40 rounds of game are played between the computer and the player. In the second stage, the computer will be able to predict ten future moves of the human opponent. Flowchart of the game design of rock-paper-scissors with neural network is plotted in Fig. 4.

Step 1: Neural network training

In the game of rock-paper-scissors, the strategy of the opponents' game changes over time and also in each game.

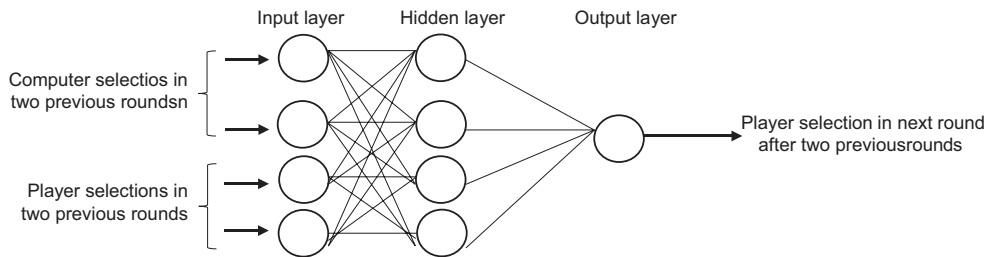


Fig. 2. Multilayer perceptron network structure designed for detecting human behavioral pattern.

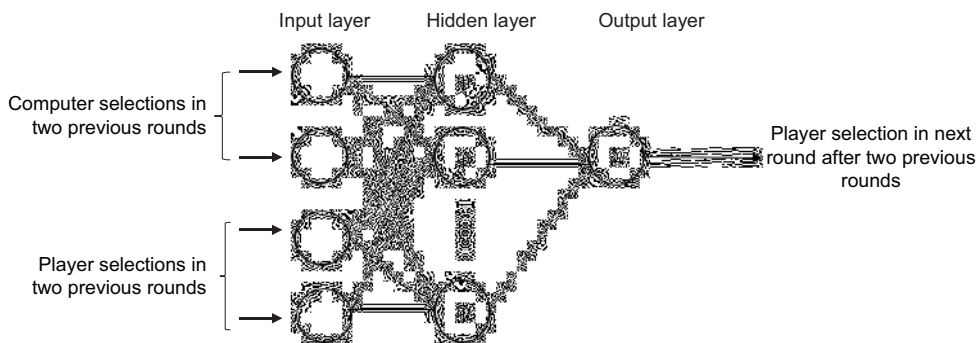


Fig. 3. Radial basis functions network structure designed for detecting human behavioral pattern.

TABLE I

MLP NETWORK SPECIFICATION WHICH WAS DESIGNED TO DETECT HUMAN BEHAVIORAL PATTERN

Applied network	MLP
The number of neurons in the input layer	4
The number of neurons in the hidden layer	4
The number of neurons in the output layer	1
The number of epochs	70
Activation function	Tansig

TABLE II

RADIAL BASIS FUNCTIONS NETWORK SPECIFICATION WHICH WAS DESIGNED TO DETECT HUMAN BEHAVIORAL PATTERN

Applied network	Radial basis functions
The number of neurons in the input layer	4
The number of maxurons	18
The number of neurons in the output layer	1
Spread	3
Goal	0

Therefore, it is necessary to adjust the network’s knowledge according to the way that each player plays. At this stage, at the same time as the computer and the player play, the input data matrix is formed for training and testing the neural network. In this regard, first 40 rounds of game are played between the computer and the player. The purpose of this stage is to enable the neural network to learn the general pattern player’s behavior. All computer selections are random. Each of the hand modes, rock, paper, and scissors is defined by the numbers 2, 1, and 3, respectively. For example, supposing that the computer and player selections are as follows then the steps of forming the input data matrix and the target output are shown in Fig. 5.

As shown in Fig. 5, first, the computer and player selections in 40 rounds are placed in a matrix with 40 rows

and two columns. The first column is the computer selection and the second column is the player selection. In the next step, the previous matrix is transformed into a matrix with 39 rows and four columns so that the first and second selections of the computer as well as the player are placed in two consecutive rounds on one row, and then the second and third selections of the computer and the player are placed on the next row. This process continues until the fortieth round. In the next step, the matrix of the previous step becomes a matrix with 38 rows and five columns. The fifth column is the target output. This column is the selection of the player in the round right after two consecutive rounds. In the last step, the matrix columns are separated. The first till the fourth columns are considered as input data and the fifth column is considered as target output. To develop the ANN model, the number of training, test, and validation data is equal to (70%) 26, (15%) 6, and (15%) 6, respectively. The low error of predicted data in testing set shows that the over fitting problem has not been occurred and the presented model is accurate and precise.

Step 2: The real game

The trained neural network has already learned the general pattern of player’s behavior base on 40 rounds of the game and now is ready for the real game against her/him. Ten rounds, that is, 41–50, are considered for this stage. In the real game, the neural network uses the player and computer selections in the previous two consecutive rounds as input data to predict the player’s future move in the round right after these two rounds, then defeats the opposing player with choosing the right selection. For example, in the 41st round, the player and computer selections in the 39th and 40th rounds, that is, two consecutive rounds before, will be given to the neural network to predict the player’s behavior. This

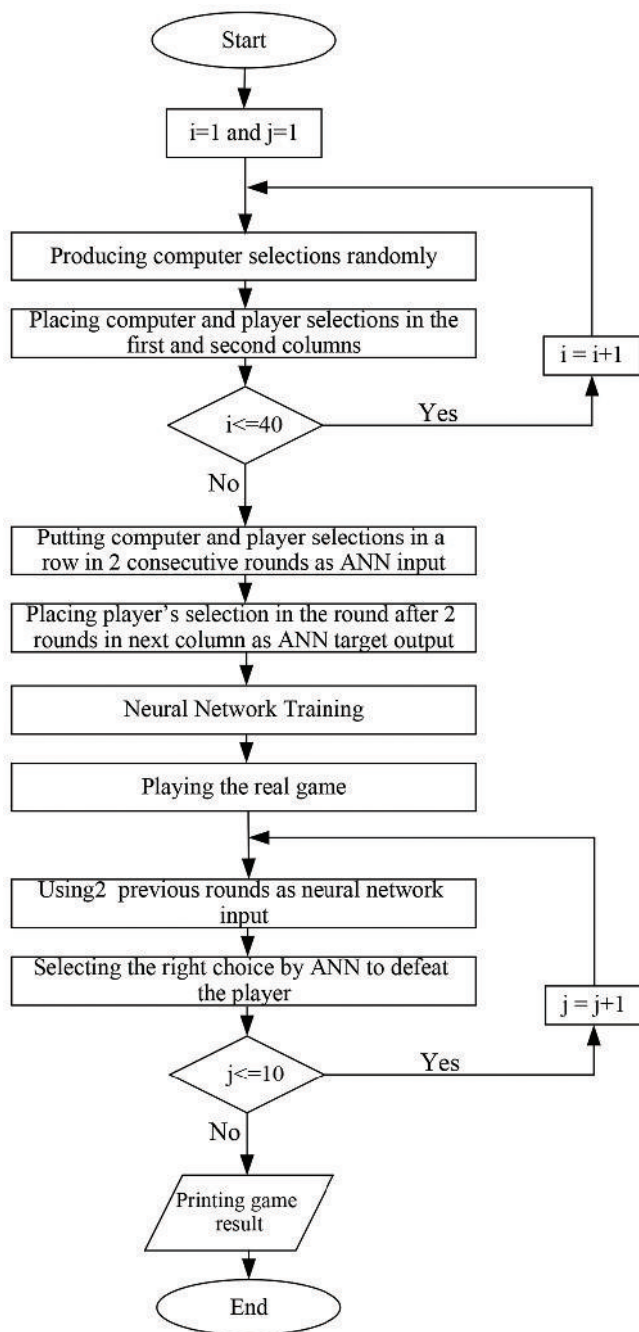


Fig. 4. Flowchart of rock-paper-scissors game designed with the neural network.

process will continue until the last round. The effectiveness of the neural network in detecting human behavior patterns and defeating players will be determined at this very stage (Real game). Finally, the winning percentage of the computer is calculated.

Then, to examine the computer winning percentage without a neural network, another program was written to play rock-paper-scissors against humans. All computer selections in this program are random. 50 rounds of game are played between the computer and the player. To create the same conditions as the neural network program, the last ten rounds, that is, 41–50, will be considered as the real game.

E. Upgraded Markov Chain Model

The random process whose future probabilities are calculated based on the recent values is called the Markov process (He, et al., 2019). The Markov chain is a statistical tool used to determine the probability of transitions between several states, which is used to model and predict the effect of future changes. If we put these probabilities inside a matrix, we get the Transition Probability Matrix (De Caro et al., 2019).

Humans always apply mental and psychological factors in their decisions. This is also the case in the game of rock-paper-scissors. In this way, the player’s movement in the next game is affected by the result of the previous game. A special feature of this intelligent algorithm is to enter the results of the game in the Markov matrix. The designed upgraded Markov model to predict the future movement of the player in the game of rock-paper-scissors is a 9×3 matrix. According to Fig. 6, this matrix contains the player’s movements (rock-paper-scissors) that have caused him to win, lose, or draw with the computer.

Forming a Markov matrix and predicting the player’s future movements

First of all, all matrix values are zero. Then, according to the number of rounds of the game, the player’s movements and the result of each round, the value of the elements increases as a unit. The player’s selections are placed in the matrix in two consecutive rounds according to the result of the previous two rounds. For example, if a player’s selections in two consecutive rounds are paper and rock, respectively, and the result of the first round (the previous two rounds) is a player’s loss, one unit is added to element of the fifth row and first column of the matrix, because the player has moved from paper (that caused him to lose) to rock. This process continues until the last round, and the Markov matrix is formed at the same time as the computer and the player keep playing.

In the first and second rounds, the computer selections are random. From the third round onwards, the computer makes its selection according to the player’s choice in the previous round and the result of this round. For example, if the player selected scissors in the previous round and the result of this round is a computer’s win, a comparison is made between the third row elements. Whichever is larger, the computer tries to defeat the player by performing the opposite move. For example, if the value of the element of the third row and the first column is more than the other two elements, it means that the player usually moves from the scissors (which caused him to win) to the rock. In the next round, the computer chooses the paper to defeat him/her. This forecasting process will continue until the last round.

IV. PHYSICAL IMPLEMENTATION

This game is implemented in two physical forms; the prototype has been designed and built robotically as the first form. Zana robot consists of two parts: Hardware

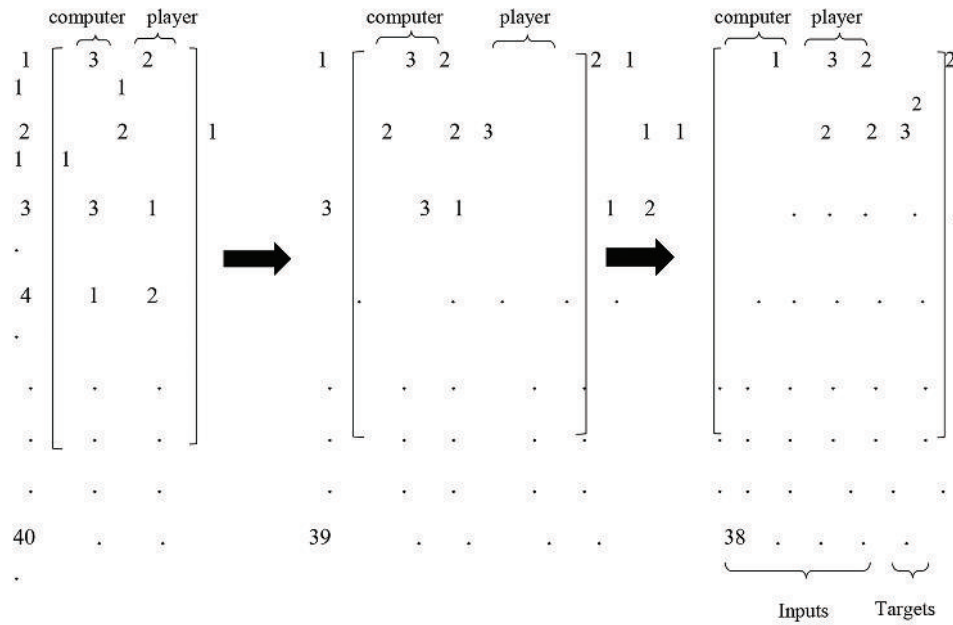


Fig. 5. The steps of forming the input data and target output matrix

		Rock	Paper	Scissor
Player win	Rock 1	P11	P12	P13
	Paper 2	P21	P22	P23
	Scissor 3	P31	P32	P33
P= Player loss	Rock 4	P41	P42	P43
	Paper 5	P51	P52	P53
	Scissor 6	P61	P62	P63
Tie	Rock 7	P71	P72	P73
	Paper 8	P81	P82	P83
	Scissor 9	P91	P92	P93

Fig. 6. The transition probability matrix of Markov upgraded

and software. The hardware part of this robot performs the movements of rock-paper-scissors through the motors installed in its structure. Zana robot's control unit has a processor (microcontroller) to control finger movement. There are also three separate keys for the user to select from one of the modes of rock-paper-scissors. Using the AVR microcontroller and its algorithm written in C, the robot is equipped with artificial intelligence, according to which the Zana robot decides at any round of the game to choose one of the rock, paper, or scissors modes. A character LCD has been also used to display the game result.

In the second form, to have a graphically appropriate and attractive appearance for the game, a stand has been designed using the GUI and coding in the App designer environment in a computer system, and then it was embedded in the designed stand such that it can be played against a human opponent. The stand uses an LCD to display the game environment and the results. A speaker is also used to produce audio effects

to make the device more attractive with a nice looking. Images of Zana intelligent robot, graphic environment, and the designed stand for playing rock-paper-scissors game are shown in Figs. 7 and 8.

V. RESULTS

A. Evaluation of the Effectiveness of ANNs in Detecting Human behavior Pattern

ANNs (MLP and RBF) designed for detecting human behavior in a game of rock-paper-scissors were tested among 20 people (ten women and ten men). Players are of from different ages and levels of education. Each player played with the desired networks in three stages. The effectiveness



Fig. 7. Robot gestures: (a) Rock, (b) Paper, (c) Scissors.

of ANNs in defeating players and the percentage of winning computer were calculated. According to the results presented in Tables III and IV, the percentage of winning computer with MLP neural network designed in 30 games played among men is equal to 55% and with the same number of games in women is equal to 63.33% and the percentage of winning computer with RBF neural network is 75% in men and 78.33% in women. Nevertheless, the percentage

of winning computer without neural network among men and women's players and with the same number of games is equal to 50% and 45%, respectively. The results show the good performance of the neural network in detecting human behavior in the game of rock-paper-scissors. It is evident that the RBF network is more effective in defeating players than the MLP network, and also the percentage of winning computer in women's players is higher than men's players. Table V shows the number of wins, losses, and ties of the computer in 30 games among men and women with the mentioned neural networks and without the neural network. According to the results presented in this table, RBF neural network has been able to win 21 games out of 30 games played with men and 22 games out of 30 games played with women. These results show the very good performance of this network in modeling the human mind in the game of rock-paper-scissors.



Fig. 8. (a) Graphic environment, (b) designed stand for playing rock-paper-scissors game.

B. Evaluation of the Effectiveness of the Upgraded Markov Model in Detecting Human behavior Pattern

The upgraded Markov model designed for detecting human behavior patterns in the game of rock-paper-scissors was tested among 20 people (ten women and ten men).

TABLE III

GAME RESULTS AND COMPUTER WINNING PERCENTAGE IN MEN WITH AND WITHOUT NEURAL NETWORKS (C, P, AND T IS COMPUTER WINS, PLAYER WINS AND TIE, RESPECTIVELY)

Men's player number	Game results									Computer winning percentage		
	With MLP neural network			With RBF neural network			Without neural network			With MLP neural network	With RBF neural network	Without neural network
	1	2	3	1	2	3	1	2	3			
1	C: 3 P: 6 T: 1	C: 3 P: 2 T: 5	C: 2 P: 1 T: 7	C: 4 P: 1 T: 5	C: 1 P: 3 T: 6	C: 2 P: 4 T: 4	C: 3 P: 5 T: 2	C: 3 P: 3 T: 4	C: 3 P: 6 T: 1	66.66%	33.33%	16.66%
2	C: 3 P: 2 T: 5	C: 2 P: 1 T: 7	C: 3 P: 3 T: 4	C: 4 P: 2 T: 4	C: 4 P: 4 T: 2	C: 5 P: 1 T: 4	C: 4 P: 2 T: 4	C: 5 P: 2 T: 3	C: 2 P: 4 T: 4	83.33%	83.33%	66.66%
3	C: 3 P: 2 T: 5	C: 2 P: 5 T: 3	C: 3 P: 3 T: 4	C: 4 P: 1 T: 5	C: 4 P: 2 T: 4	C: 6 P: 2 T: 2	C: 1 P: 4 T: 5	C: 6 P: 3 T: 1	C: 3 P: 4 T: 3	50%	100%	33.33%
4	C: 3 P: 3 T: 4	C: 9 P: 0 T: 1	C: 3 P: 2 T: 5	C: 4 P: 4 T: 2	C: 5 P: 3 T: 2	C: 4 P: 3 T: 3	C: 2 P: 6 T: 2	C: 3 P: 5 T: 2	C: 4 P: 2 T: 4	83.33%	83.33%	33.33%
5	C: 4 P: 2 T: 4	C: 2 P: 4 T: 4	C: 4 P: 4 T: 2	C: 6 P: 2 T: 2	C: 6 P: 2 T: 2	C: 3 P: 6 T: 1	C: 3 P: 5 T: 2	C: 4 P: 2 T: 4	C: 3 P: 6 T: 1	50%	66.66%	33.33%
6	C: 5 P: 4 T: 1	C: 4 P: 3 T: 3	C: 4 P: 5 T: 1	C: 4 P: 3 T: 2	C: 5 P: 2 T: 3	C: 2 P: 3 T: 5	C: 2 P: 5 T: 3	C: 4 P: 2 T: 4	C: 5 P: 3 T: 2	66.66%	50%	66.66%
7	C: 2 P: 4 T: 4	C: 4 P: 4 T: 2	C: 3 P: 5 T: 2	C: 5 P: 3 T: 2	C: 4 P: 3 T: 3	C: 2 P: 6 T: 2	C: 3 P: 5 T: 2	C: 5 P: 4 T: 1	C: 4 P: 4 T: 2	16.66%	66.66%	50%
8	C: 6 P: 1 T: 3	C: 4 P: 4 T: 2	C: 2 P: 5 T: 3	C: 4 P: 3 T: 3	C: 5 P: 3 T: 2	C: 3 P: 4 T: 3	C: 3 P: 2 T: 5	C: 3 P: 0 T: 7	C: 4 P: 4 T: 2	50%	66.66%	83.33%
9	C: 2 P: 5 T: 3	C: 2 P: 4 T: 4	C: 6 P: 3 T: 1	C: 5 P: 2 T: 3	C: 5 P: 2 T: 3	C: 8 P: 2 T: 0	C: 4 P: 1 T: 5	C: 3 P: 3 T: 4	C: 3 P: 3 T: 4	33.33%	100%	66.66%
10	C: 0 P: 6 T: 4	C: 4 P: 4 T: 2	C: 6 P: 3 T: 1	C: 6 P: 4 T: 0	C: 3 P: 1 T: 6	C: 4 P: 3 T: 3	C: 5 P: 2 T: 3	C: 2 P: 3 T: 5	C: 3 P: 3 T: 4	50%	100%	50%

TABLE IV
GAME RESULTS AND COMPUTER WINNING PERCENTAGE IN WOMEN WITH AND WITHOUT NEURAL NETWORKS (C, P, AND T IS COMPUTER WINS, PLAYER WINS AND TIE, RESPECTIVELY)

Women's player number	Game results									Computer winning percentage		
	With MLP neural network			With RBF neural network			Without neural network			With MLP neural network	With RBF neural network	Without neural network
	1	2	3	1	2	3	1	2	3			
1	C: 4 P: 3 T: 3	C: 1 P: 5 T: 4	C: 5 P: 2 T: 3	C: 7 P: 1 T: 2	C: 5 P: 1 T: 4	C: 4 P: 1 T: 5	C: 2 P: 6 T: 2	C: 6 P: 3 T: 1	C: 3 P: 4 T: 3	66.66%	100%	33.33%
2	C: 2 P: 4 T: 4	C: 3 P: 3 T: 4	C: 6 P: 3 T: 1	C: 4 P: 3 T: 3	C: 4 P: 1 T: 5	C: 3 P: 3 T: 4	C: 3 P: 6 T: 1	C: 3 P: 4 T: 3	C: 3 P: 5 T: 2	50%	83.33%	0%
3	C: 6 P: 3 T: 1	C: 1 P: 4 T: 5	C: 4 P: 2 T: 4	C: 0 P: 6 T: 4	C: 7 P: 2 T: 1	C: 9 P: 0 T: 1	C: 4 P: 4 T: 2	C: 3 P: 6 T: 1	C: 7 P: 3 T: 0	66.66%	66.66%	50%
4	C: 3 P: 1 T: 6	C: 1 P: 6 T: 3	C: 2 P: 4 T: 4	C: 4 P: 2 T: 4	C: 4 P: 2 T: 4	C: 3 P: 4 T: 3	C: 3 P: 3 T: 4	C: 1 P: 3 T: 6	C: 5 P: 1 T: 4	33.33%	66.66%	50%
5	C: 2 P: 4 T: 4	C: 0 P: 8 T: 2	C: 4 P: 2 T: 4	C: 4 P: 4 T: 2	C: 4 P: 3 T: 3	C: 5 P: 2 T: 3	C: 5 P: 4 T: 1	C: 4 P: 2 T: 4	C: 3 P: 4 T: 3	33.33%	83.33%	66.66%
6	C: 5 P: 2 T: 3	C: 3 P: 6 T: 1	C: 4 P: 2 T: 4	C: 3 P: 6 T: 1	C: 3 P: 1 T: 6	C: 2 P: 3 T: 5	C: 3 P: 3 T: 4	C: 6 P: 2 T: 2	C: 1 P: 5 T: 4	66.66%	33.33%	50%
7	C: 4 P: 3 T: 3	C: 2 P: 1 T: 7	C: 6 P: 3 T: 1	C: 3 P: 2 T: 5	C: 6 P: 1 T: 3	C: 2 P: 1 T: 7	C: 2 P: 5 T: 2	C: 3 P: 2 T: 5	C: 5 P: 2 T: 3	100%	100%	66.66%
8	C: 3 P: 1 T: 6	C: 6 P: 1 T: 3	C: 6 P: 1 T: 3	C: 2 P: 3 T: 5	C: 4 P: 2 T: 4	C: 5 P: 2 T: 3	C: 4 P: 3 T: 3	C: 2 P: 6 T: 2	C: 4 P: 2 T: 4	100%	66.66%	66.66%
9	C: 4 P: 3 T: 3	C: 4 P: 1 T: 5	C: 3 P: 3 T: 4	C: 5 P: 1 T: 4	C: 7 P: 3 T: 0	C: 5 P: 2 T: 3	C: 4 P: 1 T: 5	C: 4 P: 4 T: 2	C: 1 P: 4 T: 5	83.33%	100%	50%
10	C: 5 P: 3 T: 2	C: 4 P: 6 T: 0	C: 3 P: 4 T: 3	C: 4 P: 4 T: 2	C: 6 P: 1 T: 3	C: 8 P: 1 T: 1	C: 4 P: 4 T: 2	C: 3 P: 4 T: 3	C: 3 P: 4 T: 3	33.33%	83.33%	16.66%

TABLE V
NUMBER OF COMPUTER WINS, LOSSES AND TIES IN 30 GAMES AMONG MEN AND WOMEN WITH AND WITHOUT NEURAL NETWORKS

Sexuality	30 games played								
	With MLP neural network			With RBF neural network			Without neural network		
	Computer wins	Computer losses	Ties	Computer wins	Computer losses	Ties	Computer wins	Computer losses	Ties
Men	13 games	10 games	7 games	21 games	6 games	3 games	12 games	12 games	6 games
Women	18 games	10 games	2 games	22 games	5 games	3 games	11 games	14 games	5 games

To evaluate the performance of the modeling, each of the players played in three stages with 15 and 20 rounds with the desired intelligent algorithm. The effectiveness of the upgraded Markov model in defeating players and the percentage of winning computer were calculated. According to the results presented in Tables VI and VII, the percentage of winning computer with the 15 rounds in 30 games played with men is equal to 68.33% and with the same number of games with women is equal to 70%, whereas the percentage of winning computer with the 20 rounds with men is equal to 73.33% and with women is equal to 76.66%. Table VIII shows the number of wins, losses, and ties of the computer in 30 games among men and women. The results show the very good performance of the improved Markov model in detecting human behavior in the game of rock-paper-scissors.

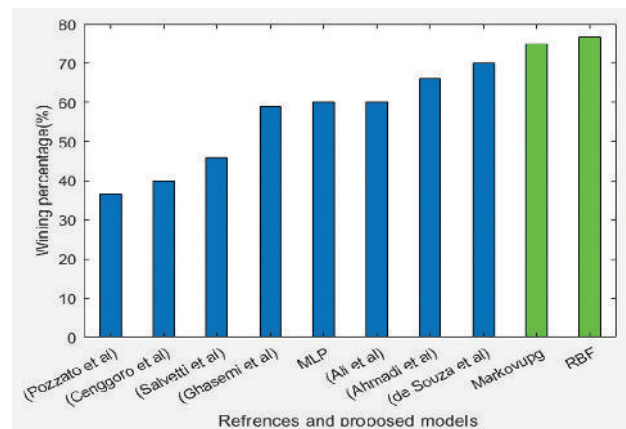


Fig. 9. Winning percentage of the proposed models in comparison with the previous reported literature.

TABLE VI

GAME RESULTS AND COMPUTER WINNING PERCENTAGE IN MEN WITH MARKOV UPGRADED MODEL (C, P, AND T IS COMPUTER WINS, PLAYER WINS AND TIE, RESPECTIVELY)

Men' player number	Game results						Computer winning percentage	
	With 15 rounds			With 20 rounds			With 15 rounds	With 20 rounds
	1	2	3	1	2	3		
1	C: 6 P: 5 T: 4	C: 4 P: 5 T: 6	C: 6 P: 0 T: 9	C: 7 P: 4 T: 9	C: 9 P: 4 T: 7	C: 5 P: 4 T: 11	66.66%	100%
2	C: 4 P: 3 T: 8	C: 5 P: 4 T: 6	C: 2 P: 7 T: 6	C: 5 P: 5 T: 10	C: 6 P: 5 T: 9	C: 10 P: 3 T: 7	66.66%	83.33%
3	C: 8 P: 2 T: 5	C: 3 P: 5 T: 7	C: 5 P: 4 T: 6	C: 8 P: 8 T: 4	C: 10 P: 6 T: 4	C: 5 P: 6 T: 9	66.66%	50%
4	C: 7 P: 5 T: 3	C: 2 P: 8 T: 5	C: 4 P: 4 T: 7	C: 6 P: 8 T: 6	C: 9 P: 7 T: 4	C: 8 P: 8 T: 4	50%	50%
5	C: 3 P: 5 T: 7	C: 7 P: 5 T: 3	C: 12 P: 2 T: 1	C: 9 P: 4 T: 7	C: 11 P: 7 T: 2	C: 5 P: 4 T: 11	66.66%	100%
6	C: 5 P: 4 T: 6	C: 5 P: 8 T: 2	C: 7 P: 4 T: 4	C: 6 P: 9 T: 5	C: 10 P: 4 T: 6	C: 5 P: 7 T: 8	66.66%	33.33%
7	C: 6 P: 5 T: 4	C: 10 P: 3 T: 2	C: 9 P: 6 T: 0	C: 9 P: 4 T: 7	C: 12 P: 4 T: 4	C: 8 P: 4 T: 8	100%	100%
8	C: 7 P: 4 T: 4	C: 5 P: 5 T: 5	C: 7 P: 4 T: 4	C: 3 P: 6 T: 11	C: 8 P: 5 T: 7	C: 9 P: 7 T: 4	83.33%	66.66%
9	C: 8 P: 5 T: 2	C: 5 P: 4 T: 6	C: 4 P: 5 T: 6	C: 11 P: 5 T: 4	C: 10 P: 4 T: 6	C: 5 P: 8 T: 7	66.66%	66.66%
10	C: 6 P: 3 T: 6	C: 6 P: 6 T: 3	C: 2 P: 3 T: 10	C: 8 P: 6 T: 6	C: 7 P: 7 T: 6	C: 7 P: 4 T: 9	50%	83.33%

TABLE VII

GAME RESULTS AND COMPUTER WINNING PERCENTAGE IN WOMEN WITH MARKOV UPGRADED MODEL (C, P, AND T IS COMPUTER WINS, PLAYER WINS AND TIE, RESPECTIVELY)

Women's player number	Game results						Computer winning percentage	
	With 15 rounds			With 20 rounds			With 15 rounds	With 20 rounds
	1	2	3	1	2	3		
1	C: 4 P: 3 T: 8	C: 8 P: 3 T: 4	C: 6 P: 3 T: 6	C: 9 P: 4 T: 7	C: 5 P: 7 T: 8	C: 11 P: 5 T: 4	100%	66.66%
2	C: 10 P: 4 T: 1	C: 5 P: 8 T: 2	C: 4 P: 6 T: 5	C: 5 P: 11 T: 4	C: 9 P: 6 T: 5	C: 11 P: 2 T: 7	33.33%	66.66%
3	C: 4 P: 3 T: 8	C: 6 P: 4 T: 5	C: 9 P: 2 T: 4	C: 8 P: 6 T: 6	C: 15 P: 3 T: 2	C: 6 P: 4 T: 10	100%	100%
4	C: 5 P: 4 T: 6	C: 7 P: 4 T: 4	C: 5 P: 7 T: 3	C: 15 P: 4 T: 1	C: 18 P: 1 T: 1	C: 3 P: 10 T: 7	66.66%	66.66%
5	C: 6 P: 4 T: 5	C: 6 P: 3 T: 6	C: 4 P: 5 T: 6	C: 9 P: 6 T: 6	C: 4 P: 8 T: 8	C: 8 P: 7 T: 5	66.66%	66.66%
6	C: 8 P: 3 T: 4	C: 5 P: 10 T: 0	C: 7 P: 2 T: 6	C: 7 P: 5 T: 8	C: 9 P: 8 T: 2	C: 9 P: 4 T: 7	66.66%	100%
7	C: 8 P: 4 T: 3	C: 7 P: 4 T: 4	C: 9 P: 2 T: 4	C: 10 P: 6 T: 4	C: 13 P: 4 T: 3	C: 4 P: 6 T: 10	100%	66.66%
8	C: 5 P: 7 T: 3	C: 6 P: 5 T: 4	C: 7 P: 4 T: 4	C: 9 P: 6 T: 5	C: 7 P: 6 T: 7	C: 11 P: 5 T: 4	66.66%	100%
9	C: 3 P: 5 T: 7	C: 6 P: 4 T: 5	C: 8 P: 3 T: 4	C: 6 P: 8 T: 6	C: 8 P: 3 T: 9	C: 11 P: 7 T: 2	66.66%	66.66%
10	C: 4 P: 6 T: 5	C: 6 P: 8 T: 1	C: 8 P: 2 T: 5	C: 11 P: 2 T: 7	C: 5 P: 7 T: 8	C: 13 P: 3 T: 4	33.33%	66.66%

According to the comparison in Table IX and Fig. 9, it is clear that the average winning computer percentage in men and women with a RBF neural network and the upgraded Markov model presented in this paper is higher than previous studies. These results show a very good performance of these two intelligent algorithms in modeling the human mind in the game of rock-paper-scissors. It should be noted that the upgraded Markov model has a better performance in recognizing the human behavior pattern in the game of rock-paper-scissors with 20 rounds and fewer games than the RBF neural network with 50 rounds of the game, clearly, as the number of game rounds increases this model works more powerfully since its database becomes richer.

VI.CONCLUSION

Computer games in their present form are the result of the efforts and creative ideas of their inventors and creators. These kinds of games are an important phenomenon in today's world as an effective educational solution, a popular media, a tool for entertainment, and a fruitful economy. The main purpose of this study is to create an intelligent player in the game of rock-paper-scissors who can recognize the pattern

TABLE VIII

NUMBER OF COMPUTER WINS, LOSSES, AND TIES IN 30 GAMES AMONG MEN AND WOMEN WITH MARKOV UPGRADED MODEL

Sexuality	30 games played					
	With 15 rounds			With 20 rounds		
	Computer wins	Computer losses	Ties	Computer wins	Computer losses	Ties
Men	19 games	8 games	3 games	20 games	6 games	4 games
Women	21 games	9 games	0 games	23 games	7 games	0 games

TABLE IX

COMPARISON OF WINNING PERCENTAGE OF THE PROPOSED MODELS AND PREVIOUS STUDIES

Pervious studies	Winning percentage
Ali et al., 2000	60%
de Souza et al., 2013	70%
Cenggoro et al., 2014	40%
Salvetti et al., 2007	46%
Ghasemi et al., 2020	59%
Ahmadi et al., 2019	66%
Pozzato et al., 2013	36.65%
In this study with MLP neural network	60%
With RBF neural network	76.66%
Markov upgraded with 20 rounds	75%

of human behavior and defeat her/him. To achieve this, ANNs (MLP and RBF) and upgraded Markov model were used. The results showed that the percentage of winning computer with RBF neural network and upgraded Markov model, on average in men and women is 76.66% and 75%. These results indicate the excellent performance of these two intelligent algorithms in detecting human behavior in the game of rock-paper-scissors. It is worth to mention that the percentage of winning computer with the mentioned algorithms is higher than the percentage of computer wins without intelligent algorithms. Moreover, this game can be played against a human opponent by implementing it in the form of Zana intelligent robot together with MATLAB GUI graphical environment.

REFERENCES

- Ahmadi, E., Pour, A.G., Siamy, A., Taheri, A. and Meghdari, A., 2019. Playing rock-paper-scissors with RASA: A case study on intention prediction in human-robot interactive games. In: *International Conference on Social Robotics*. Springer, Cham, pp.347-357.
- Ahmadvand, M.A., 1993. *Game Psychology*. 1st ed. Payame Noor University, Iran.
- Ali, F.F., Nakao, Z. and Chen, Y.W., 2000. Playing the rock-paper-scissors game with a genetic algorithm. In: *Proceedings of the 2000 Congress on Evolutionary Computation, CEC00 (Cat. No. 00TH8512)*. Vol. 1. IEEE, United States, pp.741-745.
- Ahmadi, E., Pour, A.G., Siamy, A., Taheri, A., Meghdari, A., 2019. Playing rock-paper-scissors with RASA: A case study on intention prediction in human-robot interactive games. In: Salichs, M.A., Ge, S.S., Barakova, E.I., Cabibihan, J.J., Wagner, A.R., Castro-González, Á., He, H., (Eds.), *Social Robotics, Lecture Notes in Computer Science, ICSR 2019*. Vol. 11876. Springer, Cham.
- Cenggoro, T.W., Kridalaksana, A.H., Arriyanti, E. and Ukkas, M.I., 2014. Recognition of a human behavior pattern in paper rock scissor game using back propagation artificial neural network method. In: *2014 2nd International Conference on Information and Communication Technology (ICICT)*. IEEE, United States, pp.238-243.
- Chen, W.Y., Chung, C.H., Heish, S.Y. and Ku, C.C., 2010. Rock, paper and scissors image identification scheme. In: *4th International Conference on New Trends in Information Science and Service Science*. IEEE, United States, pp.748-753.
- De Caro, F., Vaccaro, A. and Villacci, D., 2019. A Markov chain-based model for wind power prediction in congested electrical grids. *The Journal of Engineering*, 2019(18), pp.4961-4964.
- de Souza, D.F., Carneiro, H.C., França, F.M. and Lima, P.M., 2013. Rock-paper-scissors WiSARD. In: *2013 BRICS Congress on Computational Intelligence and 11th Brazilian Congress on Computational Intelligence*. IEEE, United States, pp.178-182.
- Dehlaghi, V., Taghipour, M., Haghparast, A., Roshani, G.H., Rezaei, A., Shayesteh, S.P., Adineh-Vand, A. and Karimi, G.R., 2015. Prediction of the thickness of the compensator filter in radiation therapy using computational intelligence. *Medical Dosimetry*, 40(1), pp.53-57.
- Fausett, L.V., 2006. *Fundamentals of Neural Networks: Architectures, Algorithms and Applications*. Pearson Education, India.
- Gang, T., Cho, Y. and Choi, Y., 2017. Classification of rock-paper-scissors using electromyography and multi-layer perceptron. In: *2017 14th International Conference on Ubiquitous Robots and Ambient Intelligence (URAI)*. IEEE, United States, pp.406-407.
- Ghasemi, M., Roshani, G.H. and Roshani, A., 2020. Detecting of human behavioral pattern in rock, paper, scissors game using artificial intelligence. *Computational Engineering and Physical Modeling*, 3(1), pp.21-30.
- Hasuda, Y., Ishibashi, S., Kozuka, H., Okano, H. and Ishikawa, J., 2007. A robot designed to play the game Rock, Paper, Scissors. In: *2007 IEEE International Symposium on Industrial Electronics*. IEEE, United States, pp.2065-2070.
- He, J., La Croix, A.D., Wang, J., Ding, W. and Underschultz, J.R., 2019. Using neural networks and the Markov Chain approach for facies analysis and prediction from well logs in the Precipice Sandstone and Evergreen Formation, Surat Basin, Australia. *Marine and Petroleum Geology*, 101, pp.410-427.
- Hu, W., Zhang, G., Tian, H. and Wang, Z., 2019. Chaotic dynamics in asymmetric rock-paper-scissors games. *IEEE Access*, 7, pp.175614-175621.
- Jamshidi, M., Lalbakhsh, A., Talla, J., Peroutka, Z., Hadjilooei, F., Lalbakhsh, P., Jamshidi, M., Spada, L.L., Mirmozafari, M., Dehghani, M., Sabet, A., Roshani, S., Roshani, S., Bayat-Makou, N., Mohamadzade, B., Malek, Z., Jamshidi, A., Kiani, S., Hashemi-Dezaki, H. and Mohyuddin, W., 2020. Artificial intelligence and COVID-19: Deep learning approaches for diagnosis and treatment. *IEEE Access*, 8, pp.109581-109595.
- Matsumoto, Y., Yamamoto, T., Honda, K., Notsu, A. and Ichihashi, H., 2012. Application of cluster validity criteria to Rock-Paper-Scissors game judgment. In: *2012 IEEE International Conference on Fuzzy Systems*. IEEE, United States, pp.1-5.
- Menhaj, M.B., 2008. *Fundamentals of Neural Networks (Computational Intelligence)*. Vol. 1. Center Published of Professor Hesabi, Iran, p.715.
- Nazemi, E., Roshani, G.H., Fegghi, S.A.H., Setayeshi, S. and Peyvandi, R.G., 2015. A radiation-based hydrocarbon two-phase flow meter for estimating of phase fraction independent of liquid phase density in stratified regime. *Flow Measurement and Instrumentation*, 46, pp.25-32.
- Pozzato, G., Michieletto, S. and Menegatti, E., 2013. Towards smart robots: Rock-Paper-Scissors gaming versus human players. In: *PAI@AI*IA*, pp.89-95.
- Roshani, G.H., Fegghi, S.A.H., Mahmoudi-Aznavah, A., Nazemi, E. and Adineh-Vand, A., 2014. Precise volume fraction prediction in oil-water-gas multiphase flows by means of gamma-ray attenuation and artificial neural networks using one detector. *Measurement*, 51, pp.34-41.
- Roshani, G.H., Nazemi, E. and Fegghi, S.A.H., 2016. Investigation of using ⁶⁰Co source and one detector for determining the flow regime and void fraction in gas-liquid two-phase flows. *Flow Measurement and Instrumentation*, 50, pp.73-79.
- Roshani, G.H., Nazemi, E. and Roshani, M.M., 2017. Intelligent recognition of gas-oil-water three-phase flow regime and determination of volume fraction using Radial basis function. *Flow Measurement and Instrumentation*, 54, pp.39-45.
- Roshani, G.H., Nazemi, E. and Roshani, M.M., 2017. Usage of two transmitted detectors with optimized orientation in order to three phase flow metering. *Measurement*, 100, pp.122-130.
- Roshani, G.H., Roshani, S., Nazemi, E. and Roshani, S., 2018. Online measuring density of oil products in annular regime of gas-liquid two phase flows. *Measurement*, 129, pp.296-301.
- Roshani, M., Phan, G., Faraj, R.H., Phan, N.H., Roshani, G.H., Nazemi, B., Corniani, E. and Nazemi, E., 2021. Proposing a gamma radiation based intelligent system for simultaneous analyzing and detecting type and amount of petroleum by-products. *Nuclear Engineering and Technology*, 2020, pp.1-7.
- Roshani, M., Phan, G., Roshani, G.H., Hanus, R., Nazemi, B., Corniani, E. and Nazemi, E., 2021. Combination of X-ray tube and GMDH neural network as a nondestructive and potential technique for measuring characteristics of gas-oil-water three phase flows. *Measurement*, 168, p.108427.
- Roshani, M., Phan, G.T., Ali, P.J.M., Roshani, G.H., Hanus, R., Duong, T., Corniani, E., Nazemi, E. and Kalmoun, E.M., 2021. Evaluation of flow pattern recognition and void fraction measurement in two phase flow independent of oil pipeline's scale layer thickness. *Alexandria Engineering Journal*, 60(1), pp.1955-1966.
- Roshani, M., Sattari, M.A., Ali, P.J.M., Roshani, G.H., Nazemi, B., Corniani, E. and Nazemi, E., 2020. Application of GMDH neural network technique to improve measuring precision of a simplified photon attenuation based two-phase flow meter. *Flow Measurement and Instrumentation*, 75, p.101804.
- Salveti, F., Patelli, P. and Nicolo, S., 2007. Chaotic time series prediction for the game, Rock-Paper-Scissors. *Applied Soft Computing*, 7(4), pp.1188-1196.

Evaluation of Flying Ad Hoc Network Topologies, Mobility Models, and IEEE Standards for Different Video Applications

Ghassan A. QasMarrogy

Department of Communication and Computer Engineering, College of Engineering, Cihan University-Erbil, Kurdistan Region, Iraq

Abstract—Nowadays, drones became very popular with the enhancement of the technological progress of moving devices with a connection to each other, known as Flying Ad Hoc Network (FANET). It is used in most worldwide necessary life scenarios such as video recording, search and rescue, military missions, moving items between different areas, and many more. This leads to the necessity to evaluate different network strategies between these flying drones, which are essential to improve their quality of performance in the field. Several challenges must be addressed to effectively use FANET, to provide stable and reliable transmission for different types of data during vast changing topologies, such as different video sizes, different types of mobility models, recent Wireless Fidelity standards, types of routing protocols used, security problems, and many more. In this paper, a fully comprehensive analysis of FANET will be done to evaluate and enhance these challenges that concern different video types, mobility models, and IEEE 802.11n standards for best performance, by measuring throughput, retransmission attempt, and delay metrics. The result shows that Gauss–Markov mobility model gives the highest result using Ad Hoc On-Demand Vector and lowest delay, whereas for retransmission attempts, 2.4 GHz frequency has the lowest as it can reach more coverage area than 5 GHz.

Index Terms—Video transmission; flying ad hoc network; mobility model; 2.4–5 GHz standards; routing protocols

I. INTRODUCTION

Recently, mobile networks became very popular with the advance in the technology sector, as they can move and fly at different speeds, equipped with multitools to offer different types of application services such as video recording, item carrying, search and rescue, military operations, and many more. There are different types of these mobile networks, namely, ad hoc network, mobile ad hoc network (MANET),

vehicular ad hoc networks, and flying ad hoc network (FANET) (Kaur and Singh, 2018), all of them use different types of routing protocols to communicate as they change their topology frequently. FANET is a set of moving drones that change its topology consistently without any fixed infrastructure while communicating with a base station from different heights, as shown in Fig. 1 (Marrogy, 2020).

One of the main requirements of FANET is video recording, it is used to capture high-quality videos while flying at different speeds across the area. The formats of the recorded video play a key role in data transmission between the drones, as it needs more time and higher bandwidth B.W to transfer high-quality videos during movement, this also requires better converging between the routing protocols to route the big size packets from node to node (Zheng, Sangaiah and Wang, 2018). Therefore, due to the fast movement of FANET causing the topology to be changed rapidly, it is difficult to capture and transmit high-quality videos between the nodes while movement, which gives FANET limited capability in transmitting. Furthermore, different other challenges and constraints are fronting FANET such as drone’s scalability, limited B.W, different types of data transmission, different types of routing protocols, and the time required to finish tasks (Khan, Safi, Qureshi and Khan, 2017).

To communicate between drones, an IEEE 802.11 wireless adapter is needed to transmit with different frequencies such as 2.4 GHz, 5 GHz, and 6 GHz frequency bands. A numbering scheme was used by the Wireless Fidelity (WiFi) Alliance as a WIFI generation 802.11b, 802.11a, 802.11g, 802.11n, 802.11ac, and 802.11ax protocols, respectively (Deng, et al., 2020), whereas some of these generations can support a dual band of 2.4 GHz and 5 GHz together (Karmakar, Chattopadhyay and Chakraborty, 2017). Table I shows the list of WIFI 802.11n standards.

Due to the mentioned challenges, an analysis is needed to test and simulate different types of realistic scenarios for FANET, to determine the best results and parameters for video data transmission.

In this paper, different types of realistic scenarios will be evaluated and analyzed for FANET, to simulate and find the best results for the mentioned challenges, concerning

ARO-The Scientific Journal of Koya University
Vol. IX, No.1 (2021), Article ID: ARO.10764, 82 pages
DOI:10.14500/aro.10764

Received: 07 December 2020; Accepted: 14 February 2021
Regular research paper: Published: 08 May 2021

Corresponding author’s e-mail: ghassan.qasmarrogy@cihanuniversity.edu.iq

Copyright © 2021 Ghassan A. QasMarrogy. This is an open-access article distributed under the Creative Commons Attribution License.



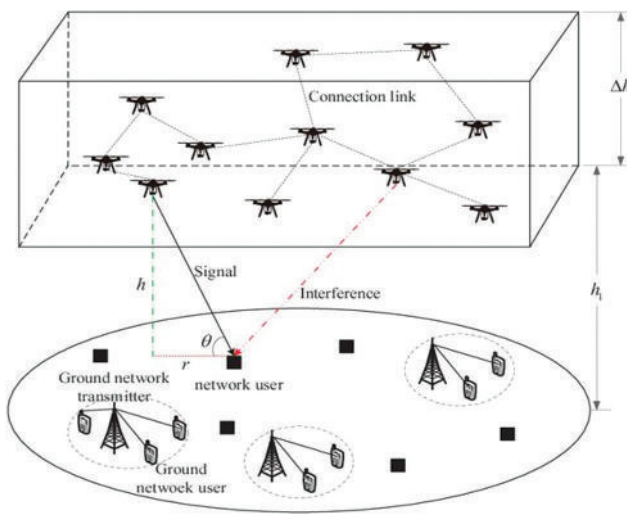


Fig. 1. Flying ad hoc networks [2].

TABLE I
LIST OF WIFI 802.11N STANDARDS (KARMAKAR, CHATTOPADHYAY AND
CHAKRABORTY, 2017)

IEEE standard	Frequency/medium	Speed	Transmission range
802.11	2.4 GHz RF	1–2 Mbps	20 feet
802.11a	5 GHz	Up to 54 Mbps	25–75 feet; range can be affected by building materials
802.11b	2.4 GHz	Up to 11 Mbps	Up to 150 feet; range can be affected by building materials
802.11g	2.4 GHz	Up to 54 Mbps	Up to 150 feet; range can be affected by building materials.
802.11n	2.4 GHz/5 GHz	Up to 600 Mbps	175+feet; range can be affected by building materials
802.11ac	5 GHz	Up to 600 Mbps	175+feet; range can be affected by building materials

WIFI: Wireless Fidelity

different video sizes, different type of mobility model, and transmitting with dual bands of IEEE standards by measuring the throughput, retransmission attempts, and delay metrics.

This paper gives extra importance to FANET, as it analyzes different transmission challenges using infrastructure-less FANET flying drones, which is useful for video recording, surveillance, tactical and wireless sensor networks, firefighters, search and rescue teams, and thermal detection which is very important for detecting COVID-19 patients.

The following is the structure of the paper, part two explains the recent related work that analyzed FANET with different scenarios, part three shows and explains the full parameters used for the different scenarios of the paper simulations, part four shows the results and the performance analysis, and finally, part five will conclude the paper with a given future work.

II. RELATED WORK

Different researches were published that analyzed and optimized FANET challenges, using several techniques and methods to enhance the performance of data transmission.

In Mahmud and Cho, 2019, a new technique was proposed for low-energy hello interval adaptive signals by choosing the best route to the receiver and minimizing the number of FANET drones used to establish routes. The new technique decreases up to 25% less from the used energy. In He, Tang, Zhang, Du, Zhou and Guizani, 2019, a new protocol for FANET was proposed course-aware opportunistic routing estimate the best position of the next drone to transmit the data with lower delay and higher throughput, the result shows lower delay with highly performance improvement and better throughput. In Srivastava and Prakash, 2021, a comprehensive survey is presented regarding FANET and discussion about its main critical problems, such as FANET's characteristics, many mobility models, types of possible communication, architecture, categorization, routing protocol, and topologies, also a discussion about FANET's related problems and challenges was analyzed to determine the probabilistic listed points of the research and methods for better results. The researcher in QasMarrogy, 2020, shows an attempt to enhance the video transmission in 5 GHz frequency in IEEE Wifi standard by changing wireless LAN parameters of MANET nodes, the result shows better performance and throughput with lower delay using specific parameters. Finally, AlKhatieb, Felemban and Naseer, 2020, presented an evaluation and comparison about different types of mobility models such as Pursue Mobility Model, Semi-Random Circular Movement (SCRM), Manhattan Grid Mobility Model (MGM), and Random Waypoint Mobility (RWPM), the paper concludes MGM model effect highly on the packet dropping ratio and delay.

III. FANET'S PARAMETER

In this part, a full explanation will be presented and analyzed regarding the calculated FANET parameters in this paper.

A. Routing Protocols

Routing protocols are a set of rules that connect drones to guide the transmitted packets from the source node to the destination. There are different types of routing protocols used to connect the flying drones or moving nodes (QasMarrogy, Alqaysi and Almashhadani, 2017), and they can be classified into three types, namely, reactive, proactive, and hybrid routing protocols, as shown in Fig. 2.

In this paper, two types of routing protocols were selected and simulated as they give the highest result for FANET, namely, Ad Hoc On-Demand Vector (AODV) and Optimized Link State Routing (OLSR) Protocol.

Due to the reactive nature of AODV, it broadcast discovery messages tagged with sequence numbers to select a recently updated route to the destination. When the sender sends a packet to the destination the discovery mechanism started, and the sender will record all the fresh recent routes in its routing table to the time that the sender finishes the transmission, and the stored routes will be deleted, then when a new packet will be transmitted another discovery message will be broadcast and the same circle will be repeated, which

can give more delay to the packets and higher overhead at the beginning of the transmission (QasMarrogy, 2021).

Furthermore, due to the proactive nature of OLSR, it exchanges the final recent information regarding all the latest routes between a group of selected devices or drones called Multipoint Relays, resulting in lower delays during the process of route discovery. After finishing transmission, all the used routes will be stored and used again for the next transmission while collecting more information about more effective routes all the time, this can cause lower delay during transmission but gives higher load as there is too much information broadcasted all the time to prepare available routes continuously (QasMarrogy, 2021).

B. Mobility Models of FANET

Mobility models show the movement of drones from one location to another location with varying velocity and direction over a specific amount of time. The main challenge in FANET is the varying speed and height of flying drones, which causes the packets to be delayed, failed to be received, or dropped (Chriki, Touati, Snoussi and Kamoun, 2019). Therefore, to break this challenge, the performance of FANET must be evaluated using different mobility models with realistic scenarios that are used in real-life missions. Many researchers use the RWPM to simulate real-life scenarios for FANET, where the drones in this model flies to random directions with random speeds, which lowest the performance as they cause multiple route link breakage between the drones.

In this paper, three different mobility models were simulated, namely, Gauss Markov Mobility (GMM) Model, RWPM, and SRCM Model, as shown in Fig. 3.

The first type of mobility model used in this paper is the RWPM, it uses random times for movements and pauses, and random values for speeds and directions. This model starts when the simulation begins and finishes when the simulation is finished. This randomness in movement and speed will be repeated during simulation time. This model is very important for real-life scenarios such as wireless sensor networks, scanning areas, and search and rescue missions (Sharma and Kim, 2019).

The second type is the SRCM, which uses a route shaped like a hexagon or a circle with a fixed speed to the destination drone, both hexagon area and directions are specified at the beginning of the simulation, and it is used for patrolling surveys and target monitoring (Adya and Sharma, 2020).

The third type is the GMM, it updated the direction and speed of the drone according to their past values during

earlier time intervals. Direction and speed calculations are done with a specific degree of randomness that depends on FANET parameters. Finally, each drone movement is independent of all other drones in the same FANET (Korneev, Leonov and Litvinov, 2018).

C. IEEE WIFI Standards

In the wireless world, WIFI is a standard means of wireless access transmission, by sending the packet without any cable using radio frequencies, which is a trademark owned by the WIFI Alliance that sets the IEEE of 802.11 wireless standards (Deniau, Gransart, Romero, Simon and Farah, 2017).

One of the standards of WIFI is the IEEE 802.11n that uses dual B.W frequencies of 2.4 GHz and 5 GHz, which considered an essential upgrade to the WIFI standards, by increasing data transmission speed while decreasing the delay and interference (Dolińska, Jakubowski and Masiukiewicz, 2017), Fig. 4 shows a comparison between both 2.4 GHz and 5 GHz in terms of speed, delay, interference, and range.

Data transmission in WIFI can affect the performance of FANET greatly, using 5 GHz frequency can increase the speed of transmission, as it has less network congestion, much reliable WIFI connection, more solid, and lower interference, as it uses more than 20 channel to operate than the 2.4 GHz which uses 13 channels with three non-overlapping channels (1, 6, and 11), as shown in Fig. 5 (Qaddus, 2019). Still, as a disadvantage, it has less coverage range as it has shorter radio waves. Nonetheless, WIFI coverage can be extended using high gain directional antennas (Aziz, Abd Razak and Ghani, 2017).

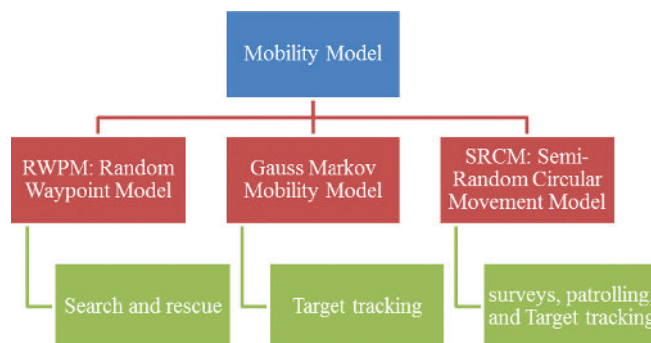


Fig. 3. Real-life mobility model scenarios (Chriki, Touati, Snoussi and Kamoun, 2019).

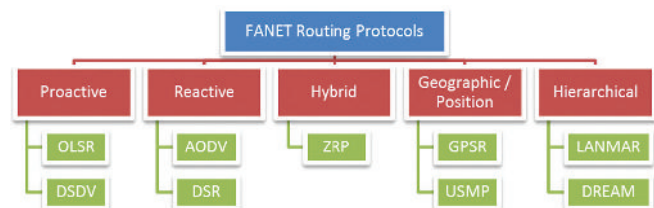


Fig. 2. Flying ad hoc network routing protocols (QasMarrogy, Alqaysi and Almashhadani, 2017).

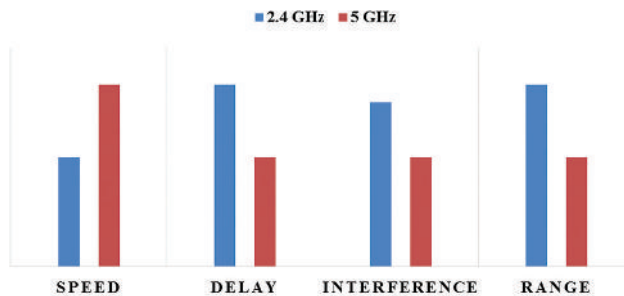


Fig. 4. 2.4 GHz versus 5 GHz comparison (Deniau, Gransart, Romero, Simon and Farah, 2017).

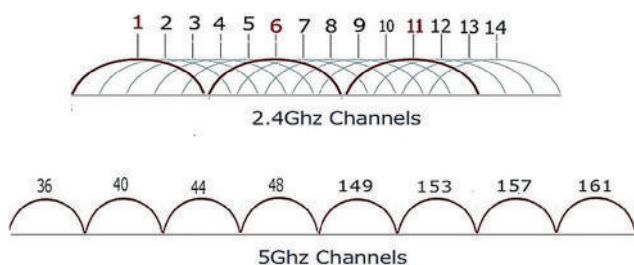


Fig. 5. 2.4 GHz and 5 GHz channel band (Aziz, Abd Razak and Ghani, 2017).

For high-quality video transmission, IEEE 802.11n 5 GHz frequency will be more required as it can support a higher transfer rate of data as possible (Qaddus, 2019).

IV. RESULTS AND ANALYSIS

In this paper, a comprehensive analysis of realistic FANET scenarios will be done, to evaluate different aspects of challenges and parameters that facing FANET, to enhance its performance by comparing the results of the simulations together. A 1500×1500 square meter area was simulated with 30 drones flying at a height of 20 m, with a varying speed from 1.4 m/s (human walking speed) to 20 m/s (drone speed), recording two types of video quality, HD and 2k, moving with three different types of mobility models, namely, RWPM, SRCM, and GMM. These flying drones stream and send the recorded videos from one to one until they reach the destination drone using two types of WIFI IEEE 802.11n standards, 2 GHz and 5 GHz, with the support of two types of routing protocols AODV, and OLSR. All simulations were repeated 10 times with average calculations to get the optimal values by calculating the end-to-end delay, throughput, and retransmission attempt of the transmitted packets metrics. Finally, the NS3 simulator was used to simulate FANET as it is one of the best network simulation tools.

To calculate the required B.W for video quality formats, the following equation will be used Equation (1) (Li, Salehi, Bayoumi and Buyya, 2016).

$$\text{Size of Video} = \text{Color Depth} \times \text{frame Rate} \\ \times \text{Streaming Duration} \times (\text{Frame } w \times h)$$

To calculate the two sizes of videos chosen in this paper using Equation (1), with size of 1280×720 pixel for the HD video and 2048×1080 pixel for the 2K video, with a depth color of 240 bits, 30 frame rate, and 60 s streaming duration. The audio size will be neglected as it does not affect the B.W, the final size will be as follows:

$$\text{Size of HD Video} = 240 \times 30 \times 60s \times (1280 \times 720) \approx 47,460 \text{ MB}$$

$$\text{Size of 2K Video} = 240 \times 30 \times 60s \times (2048 \times 1080) \approx 113,906 \text{ MB}$$

The full parameters used in the simulations are shown in Table II.

The results in Fig. 6 demonstrate the streaming of HD video throughput for IEEE 802.11n, routing protocols, and mobility models of FANET. It shows that AODV gives a high

TABLE II
SIMULATION PARAMETERS

Parameters	Values
Video formats	HD (1280×720) pixels, 2K (2048×1080) pixels
Area size	1500×1500 m ²
FANET routing protocols	AODV, OLSR
FANET number	30 Drone
Mobility models	RWPM, SRCM, GMM
Simulation time	1 min
Node speed, height	Varying 1.4–20 m/s, 20 m
WIFI IEEE 802.11n	2.4 GHz, 5 GHz

FANET: Flying ad hoc network

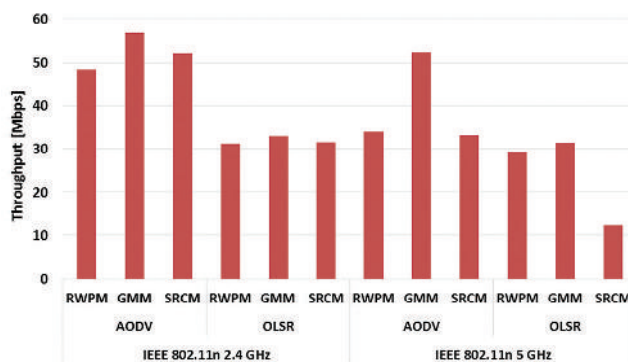


Fig. 6. HD video throughput for IEEE 802.11n, routing protocols, and mobility models.

result in GMM for the 5 GHz and 2.4 GHz whereas OLSR shows less result. As a reactive protocol AODV requires less B.W to discover a recent fresh route to destination, still it overhead high message at the beginning of the transmission to find recent routes, after that the packets transmitted until the simulation ends. Whereas OLSR keeps transmitting advertising messages to find routes continuously, but due to FANET movement, the topology is changing all the time which is difficult to keep consistent routes for transmission.

GMM in mobility models shows higher throughput as it keeps the distance and speed from one point to another, this keeps the route fresher for a long time for transmission. RWPM gives the lowest results, as its routes keep changing due to high random mobility direction and speed.

Fig. 7 demonstrates the streaming of 2K video throughput for IEEE 802.11n, routing protocols, and mobility models of FANET. It shows that AODV has also higher results as its search for a new route in the beginning of the transmission, therefore, it can keep the route for a longer time. OLSR also shows less result with the RWPM mobility model.

The result in Fig. 8 demonstrates the streaming of HD video delay for IEEE 802.11n, routing protocols, and mobility models of FANET. It shows that the mobility model GMM for AODV gives less delay for both 2.4 and 5 GHz, respectively, as AODV uses a fresh route for more time than OLSR, which keeps the route alive for a long time for transmission, therefore, it lowers the delay to find other routes on request.

SRCM and RWPM in mobility models show higher delay as their movement and speed change all the time, which causes the route to be broken.

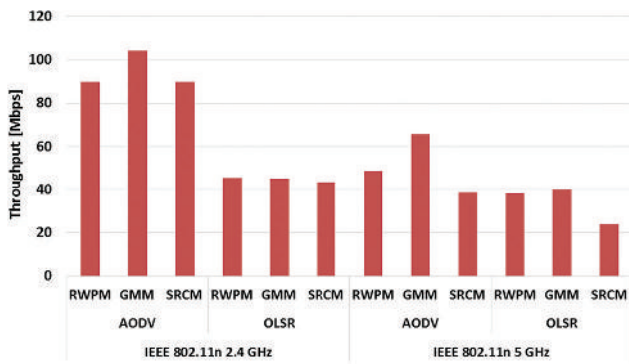


Fig. 7. 2K video throughput for IEEE 802.11n, routing protocols, and mobility models.

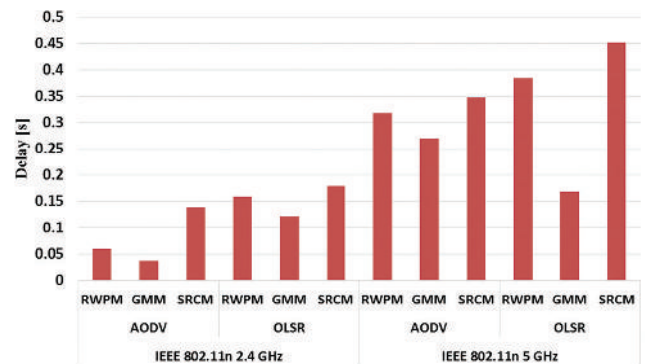


Fig. 9. 2K video delay for IEEE 802.11n, routing protocols, and mobility models.

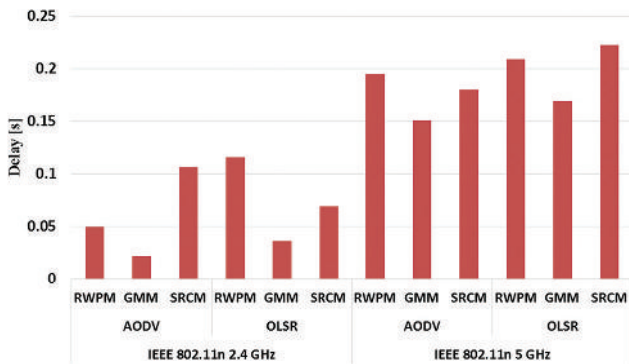


Fig. 8. HD video delay for IEEE 802.11n, routing protocols, and mobility models.

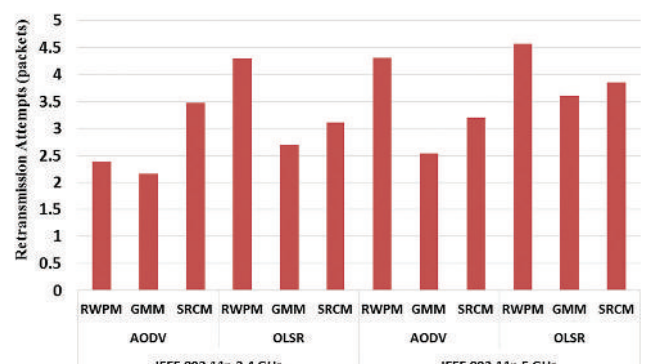


Fig. 10. HD video retransmission attempts for IEEE 802.11n, routing protocols, and mobility models.

Fig. 9 demonstrates the streaming of 2K video delay for IEEE 802.11n, routing protocols, and mobility models of FANET. It shows that 2.4 GHz gives less delay for all mobility models as the distance between the nodes get higher, which is not convenient for 5 GHz as it has small coverage distance, thus causing a higher delay.

The result in Fig. 10 demonstrates the streaming of HD video retransmission attempts for IEEE 802.11n, routing protocols, and mobility models of FANET. It shows that the mobility model GMM for AODV also gives less retransmission attempt for both 2.4 and 5 GHz, as the route remains longer than OLSR which support the packet delivery, thus decreasing the retransmission attempts from the drone.

RWPM always shows higher retransmission attempts as the drone movement and speed changes all the time, which causes the route to be broken, and the packet to be dropped and retransmit again.

Fig. 11 demonstrates the streaming of 2K video retransmission attempts for IEEE 802.11n, routing protocols, and mobility models of FANET. It shows that 2.4 GHz gives less retransmission attempts for all mobility models as the distance between the nodes get higher, which is not convenient for 5 GHz as it has small coverage distance, thus causing higher route breakage, and more retransmission attempts from the drones.

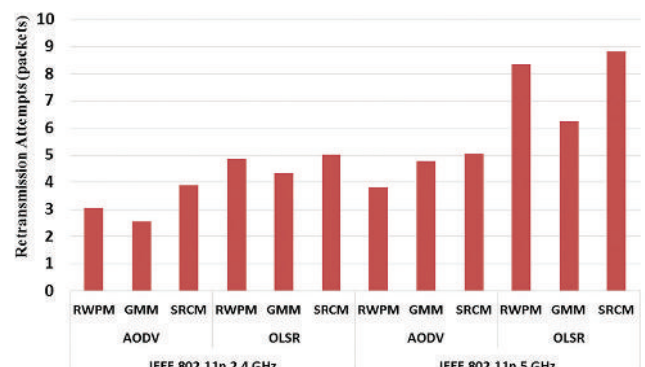


Fig. 11. 2K video retransmission attempts for IEEE 802.11n, routing protocols, and mobility models.

V. CONCLUSION

Recently, FANET is considered one of the most important future technologies to be used, as it can achieve more realistic missions without any physical guidance such as thermal detection for COVID-19, search and rescue, military missions, moving objects between different areas, and many more. Still, FANET is facing different types of challenges to achieve better performance for heavy duty missions such as battery life, transmission rate, and coverage, mobility

models, and more. Thus, it is very important to analyze these challenges of FANET.

In this paper, a comprehensive analysis for FANET was done for 30 drones, flying with varying speed of 1.4, to 20 m/s, using two types of routing protocol, AODV, and OLSR, with three types of mobility models, RWPM, GMM, and SRCM, while transmitting two types of video format HD and 2K, using IEEE 802.11n standards 2.4 GHz and 5 GHz frequencies.

The result shows that the mobility model GMM gives higher throughput and lower delay for both 2.4 and 5 GHz frequencies using the AODV routing protocol, as it keeps the same routes available for a longer time than OLSR, which gives more time for the packets to be transmitted with lower delay, as OLSR keeps changing its routes during topology changes. IEEE 802.11n 2.4 GHz gives a better result as it supports more coverage area from 5 GHz, therefore. When the node changing its speed and direction randomly, their distance becomes larger, which will be out of the area of coverage for 5 GHz frequency. For mobility models, GMM is better for drones as it keeps its speed and direction with the group, therefore, no route breakage or packet dropping happens.

As FANET is upgrading all the time, future work is needed, to test and simulate more frequencies and more mobility models, with different types of applications and metrics, also different sizes of drones are needed to be analyzed.

REFERENCES

- Adya, A. and Sharma, K.P., 2020. Energy Aware Clustering Based Mobility Model for FANETs. In: *Proceedings of ICETIT 2019*. Springer, Cham, pp.36-47.
- AlKhatieb, A., Felemban, E. and Naseer, A., 2020. Performance evaluation of Ad-Hoc routing protocols in (FANETs). In: *2020 IEEE Wireless Communications and Networking Conference Workshops (WCNCW)*. IEEE, United States, pp.1-6.
- Aziz, T.A.T., Abd Razak, M.R. and Ghani, N.E.A., 2017. The performance of different IEEE802. 11 security protocol standard on 2.4 GHz and 5GHz WLAN networks. In: *2017 International Conference on Engineering Technology and Technopreneurship (ICE2T)*. IEEE, United States, pp.1-7.
- Chriki, A., Touati, H., Snoussi, H. and Kamoun, F., 2019. FANET: Communication, mobility models and security issues. *Computer Networks*, 163, p.106877.
- Deng, C., Fang, X., Han, X., Wang, X., Yan, L., He, R., Long, Y. and Guo, Y., 2020. IEEE 802.11 be Wi-Fi 7: New challenges and opportunities. *IEEE Communications Surveys and Tutorials*, 22(4), pp.2136-2166.
- Deniau, V., Gransart, C., Romero, G.L., Simon, E.P. and Farah, J., 2017. IEEE 802.11 n communications in the presence of frequency-sweeping interference signals. *IEEE Transactions on Electromagnetic Compatibility*, 59(5), pp.1625-1633.
- Dolińska, I., Jakubowski, M. and Masiukiewicz, A., 2017. Interference comparison in Wi-Fi 2.4 GHz and 5 GHz bands. In: *2017 International Conference on Information and Digital Technologies (IDT)*. IEEE, United States, pp.106-112.
- He, Y., Tang, X., Zhang, R., Du, X., Zhou, D. and Guizani, M., 2019. A course-aware opportunistic routing protocol for FANETs. *IEEE Access*, 7, pp.144303-144312.
- Karmakar, R., Chattopadhyay, S. and Chakraborty, S., 2017. Impact of IEEE 802.11 n/ac PHY/MAC high throughput enhancements on transport and application protocols-a survey. *IEEE Communications Surveys and Tutorials*, 19(4), pp.2050-2091.
- Kaur, P. and Singh, A., 2018. Nature-inspired optimization techniques in VANETs and FANETs: A survey. In: *Advanced Computational and Communication Paradigms*. Springer, Singapore, pp.651-663.
- Khan, M.A., Safi, A., Qureshi, I.M. and Khan, I.U., 2017. Flying ad-hoc networks (FANETs): A review of communication architectures, and routing protocols. In: *2017 First International Conference on Latest trends in Electrical Engineering and Computing Technologies (INTELLECT)*. IEEE, United States, pp.1-9.
- Korneev, D.A., Leonov, A.V. and Litvinov, G.A., 2018. Estimation of mini-UAVs network parameters for search and rescue operation scenario with Gauss-Markov mobility model. In: *2018 Systems of Signal Synchronization, Generating and Processing in Telecommunications (SYNCHROINFO)*. IEEE, United States, pp.1-7.
- Li, X., Salehi, M.A., Bayoumi, M. and Buyya, R., 2016. CVSS: A cost-efficient and QoS-aware video streaming using cloud services. In: *2016 16th IEEE/ACM International Symposium on Cluster, Cloud and Grid Computing (CCGrid)*. IEEE, United States, pp.106-115.
- Mahmud, I. and Cho, Y.Z., 2019. Adaptive hello interval in FANET routing protocols for green UAVs. *IEEE Access*, 7, pp.63004-63015.
- Marrogy, G.A.Q., 2020. Enhancing video streaming transmission in 5 GHz fanet drones parameters. *Telecommunications and Radio Engineering*, 79(11), pp.997-1007.
- Qaddus, A., 2019. An Evaluation of 2.4 GHz and 5 GHz ISM radio bands utilization in backhaul IP microwave wireless networks. In: *2019 International Conference on Information Science and Communications Technologies (ICISCT)*. IEEE, United States, pp.1-5.
- QasMarrogy, G.A., 2020. Optimizing video transmission performance in 5GHz MANET. *Journal of Duhok University*, 23(2), pp.402-411.
- QasMarrogy, G.A., 2021. Improving VoIP transmission for IEEE 802.11 n 5GHz MANET. *Zanco Journal of Pure and Applied Sciences*, 33(1), pp.157-162.
- QasMarrogy, G.A., Alqaysi, H.J. and Almashhadani, Y.S., 2017. Comprehensive study of hierarchical routing protocols in MANET using simple clustering. In: *Conference of Cihan University-Erbil on Communication Engineering and Computer Science*, p.62.
- Sharma, P.K. and Kim, D.I., 2019. Random 3D mobile UAV networks: Mobility modeling and coverage probability. *IEEE Transactions on Wireless Communications*, 18(5), pp.2527-2538.
- Srivastava, A. and Prakash, J., 2021. Future FANET with application and enabling techniques: Anatomization and sustainability issues. *Computer Science Review*, 39, p.100359.
- Zheng, Z., Sangaiah, A.K. and Wang, T., 2018. Adaptive communication protocols in flying ad hoc network. *IEEE Communications Magazine*, 56(1), pp.136-142.

A Comparative Study of Electrical Characterization of *P*-Doped Distributed Bragg Reflectors Mirrors for 1300 nm Vertical Cavity Semiconductor Optical Amplifiers

Faten A. Chaqmaqchee

Department of Physics, Faculty of Science and Health, Koya University, Koya KOY45, Kurdistan Region - F.R. Iraq

Abstract—This paper presents an electrical analysis of various diameters of two *p*-types of GaAs/Al_{0.3}Ga_{0.7}As and two *p*-types of GaAs/Al_{0.3}Ga_{0.7}As/Al_{0.9}Ga_{0.1}As distributed Bragg reflectors (DBRs) mirrors structure grown on undoped and on *p*-doped GaAs, which affects the characteristics of 1300 nm vertical cavity surface emitting lasers (VCSELs) and vertical cavity semiconductor optical amplifiers (VCSOAs). Electrical characterizations and Hall measurements of current–voltage (*I*/*V*) for GaAs/Al_{0.3}Ga_{0.7}As linear DBRs and GaAs/Al_{0.3}Ga_{0.7}As/Al_{0.9}Ga_{0.1}As graded DBRs were also performed at temperatures between 13 and 300 K. Consequently, *p*-type DBRs are designed with graded composition interfaces technique. The smaller mesa diameters are used to reduce vertical and longitudinal resistances and to limit the heating effect and improve the characteristics of VCSEL/VCSOA devices.

Index Terms—AlGaAs/GaAs, Current-voltage, Distributed Bragg reflectors, Mobility.

I. INTRODUCTION

A distributed Bragg reflector (DBRs) are called Bragg mirror or quarter wavelength stacks of alternating materials with varied refractive index (Garmire, 2003; Marciniak, et al., 2020; Chaqmaqchee and Lott, 2020). DBRs represent an essential layer of an optical cavity of vertical-cavity surface-emitting lasers (VCSELs) (Croquette and Hou, 1997; Chaqmaqchee, 2019) and vertical cavity semiconductor optical amplifiers (VCSOAs) (Wang et al., 2019; Chaqmaqchee, Abubekr Salh, and Sabri, 2020) for a target wavelength of 1300 nm. The optically active layers of such optoelectronic devices can be grown between two DBR mirrors. Epitaxial growth of III-V semiconductor compounds of AlGaAs/GaAs DBRs was demonstrated in 1983 by molecular-beam epitaxy (MBE)

(Ogura et al., 1983), which is in use today. The alloy AlGaAs/GaAs is of great interest for many high speed electronics and optoelectronic applications because the lattice parameter difference between these two compounds is very small. The serious problem with VCSELs and VCSOAs is abnormally high resistance in the upper of quarter wavelength stacks (Zhang, ElAfandy and Han, 2019; Chaqmaqchee, et al. 2012). The DBRs are requiring low resistance to allow current injection and reduce the carrier heating in quantum wells (QWs). When the level doping of the DBR is high, it causes a reduction in Fermi level and thus a decrease in potential barrier height (Pickrella et al., 2005) as well efficient in increasing the tunneling current. However, it is also related to higher internal optical losses due to the free carrier absorption. Therefore, *p*-type DBRs are regularly designed using graded composition interfaces and eventually, high doping concentration to reduce the series resistance (Pohl, et al. 2018).

In this paper, a comprehensive study of two *p*-types of GaAs/Al_{0.3}Ga_{0.7}As plus two *p*-types of GaAs/Al_{0.3}Ga_{0.7}As/Al_{0.9}Ga_{0.1}As on undoped and *p*-doped GaAs substrates using different diameters is presented. Current-voltage characteristics of *p*-type DBRs at temperatures between 13 K and 300 K are experimentally demonstrated. This includes comparison between various mesa diameters structure and Hall measurements. High performance DBRs are confirmed with graded layers, which simultaneously reduce electrical resistivity, enabling current to inject directly into QWs of VCSEL and VCSOA devices.

II. MATERIAL AND METHODS

DBR samples (two with linear and two with graded interface) were grown by MBE in the National Epitaxy Facility at the *University of Sheffield, United Kingdom*. The growth rate for AlGaAs/GaAs components (DBR on an undoped GaAs and on a doped *p*-type GaAs substrate) is about 1.0 ml/s (0.28 nm/s). During the sample growth, the beryllium cell's temperature is kept constant at 620°C. The growth rate is about 1.0 ml/s for the Al_{0.3}Ga_{0.7}As but it sets on 0.33 ml/s (0.94 nm/s) for the Al_{0.9}Ga_{0.1}As part because they cannot grow it with independent sources. The temperature

ARO-The Scientific Journal of Koya University
Vol. IX, No.1 (2021), Article ID: ARO.10741, 06 pages
DOI: 10.14500/aro.10741

Received 24 October 2020; Accepted: 29 April 2021

Regular research paper: Published: 03 June 2021

Corresponding author's e-mail: Email: faten.chaqmaqchee@koyauniversity.org

Copyright © 2021 Faten A. Chaqmaqchee. This is an open-access article distributed under the Creative Commons Attribution License.



is kept between 600 and 610°C throughout the growth process. The growth rate for the graded samples might be slightly variable, but all the time it is kept at around 1.0 ml/s. With these conditions, the nominal doping concentration is not constant across the DBRs but changes according to Fig. 1. Therefore, in conclusion the graded DBRs use two gallium cells and one aluminum cell. To have two different Al compositions, the Ga cell has been changed and uses the same Al flux: The growth rates for the three DBR layers are 1.1 ml/sec for the GaAs (Ga+Ga2 cells), 1.5 ml/sec for the

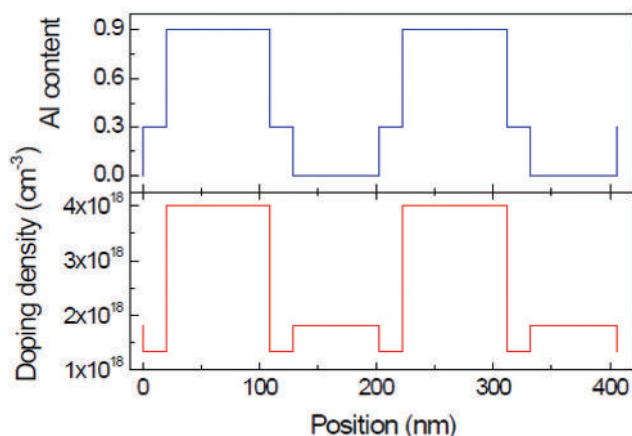


Fig. 1. Nominal doping profile changes across the semiconductor mirror distributed Bragg reflector period with two Al compositions of 90% and 30%.

Al (30%), GaAs (Al+Ga2 cells), and only 0.5 ml/s for the Al (90%), GaAs (Al+Ga1 cells) to give some very good results in terms of resistivity.

Two DBRs samples were fabricated into mesa-rings to investigate the vertical transport properties of the DBRs. The other two samples are fabricated into Hall bar shaped samples to study longitudinal transport along the layers. In the linear case, the DBR samples consist of 14 periods of GaAs/Al_{0.9}Ga_{0.1}As and are grown on undoped and *p*-doped GaAs substrates. In graded samples, 14 periods of GaAs/Al_{0.3}Ga_{0.7}As/Al_{0.9}Ga_{0.1}As, have been grown on an undoped and a *p*-doped substrate. The thickness and composition of the DBR layers have been designed to be suitable for VCSELs and VCISOAs operating at 1300 nm. To analyse the reflectance of the layers at an interface, the transmission matrix approach is used (Macleod, 1986), which includes the individual properties of the various layers.

The surface roughness for the two samples of AlGaAs/GaAs DBR on undoped GaAs substrate (coded VN1734) and AlGaAs/GaAs DBR on *p*-type doped GaAs substrate (coded VN1743) has been checked by atomic force microscope. In Fig. 2a, the surface root mean square (RMS) roughness is very low ~ 0.2 nm and roughly the same for all the structure, independently of the substrate type as in Fig. 2b. In Fig. 2c and d, the stopband center wavelength variation across the wafer of graded DBRs (coded VN1800 and VN1802) is <3.5 nm, which shows good flux homogeneity in the system. The stopband center wavelength is longer than the targeted value but the samples are ideal for current-voltage characterization.

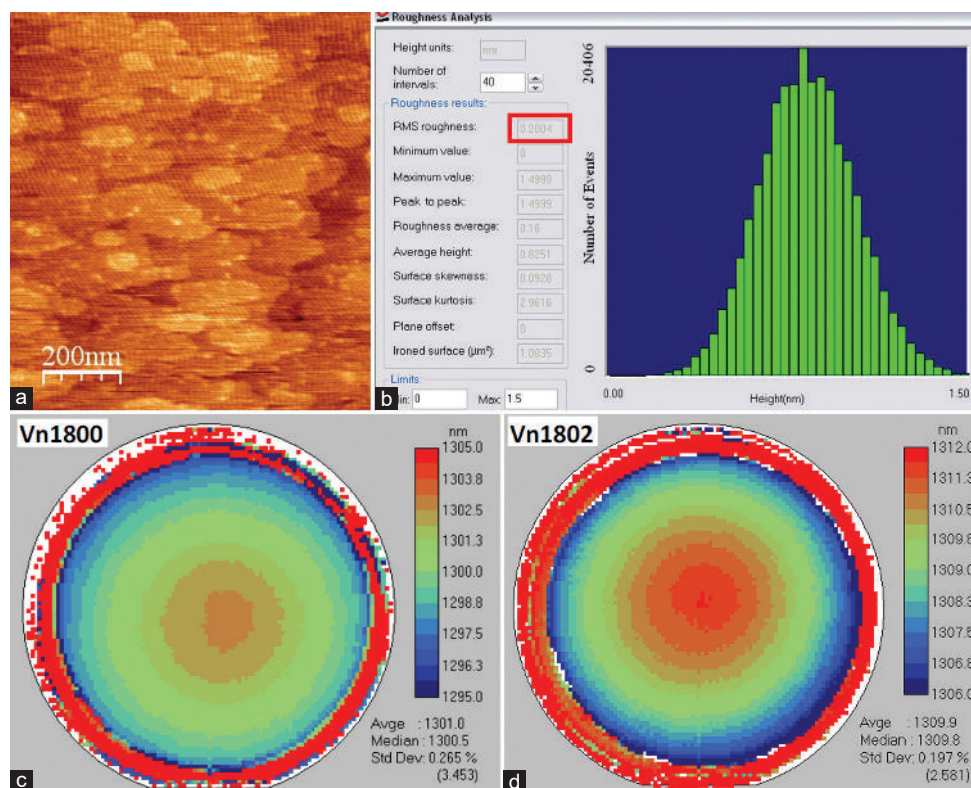


Fig. 2. (a) Atomic force micrographs for surface characterization of the distributed Bragg reflector (DBR) on *p*-type GaAs substrate, where (b) the root mean square roughness at around 0.2 nm, and (c and d) variation across the wafer- stopband center wavelength for graded DBRs grown on an undoped (VN1800) and a *p*-doped (VN1802) substrate.

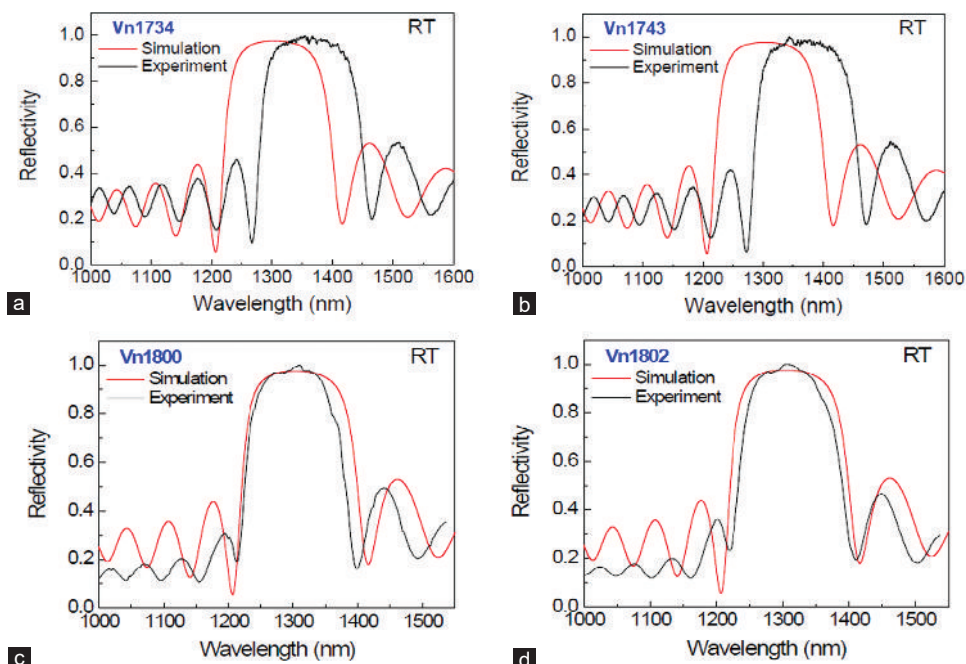


Fig. 3: Room temperature reflectivity's of 14 Bragg pairs confirming the agreement between measurements and simulations of AlGaAs/GaAs distributed Bragg reflector on (a) undoped GaAs substrate (coded VN1734), (b) p-type GaAs substrate (coded VN1743), (c) undoped GaAs substrate (coded VN1800), and (d) p-type GaAs substrate (coded VN1802).

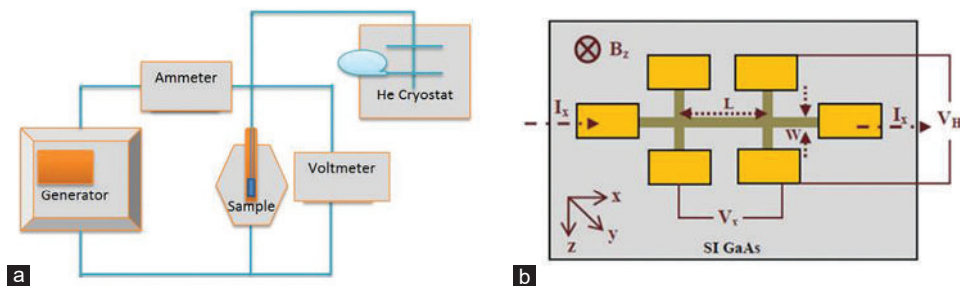


Fig. 4. Schematic diagram illustrates (a) the operation of the oxford closed cycle cooler system for current-voltage (IV) measurements, and (b) the Hall Effect on a semiconductor sample.

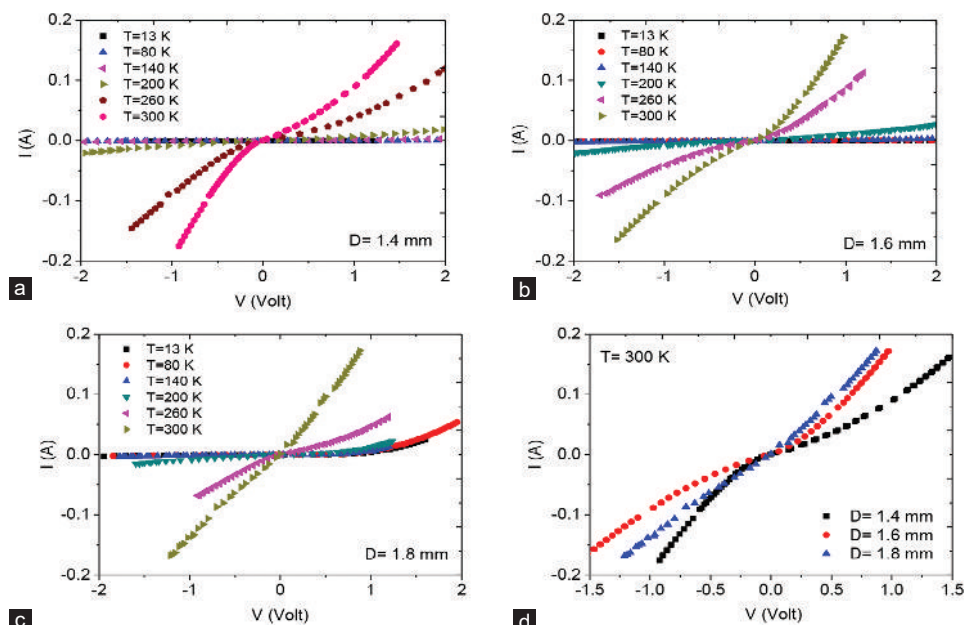


Fig. 5. Electrical characterizations (IV) for linear samples of distributed Bragg reflector (DBRs) with diameters of (a) 1.4 mm, (b) 1.6 mm, and (c) 1.8 mm at $T=13$ to 300 K, (d) IV for diameters of 1.4, 1.6, and 1.8 mm DBRs at 300 K.

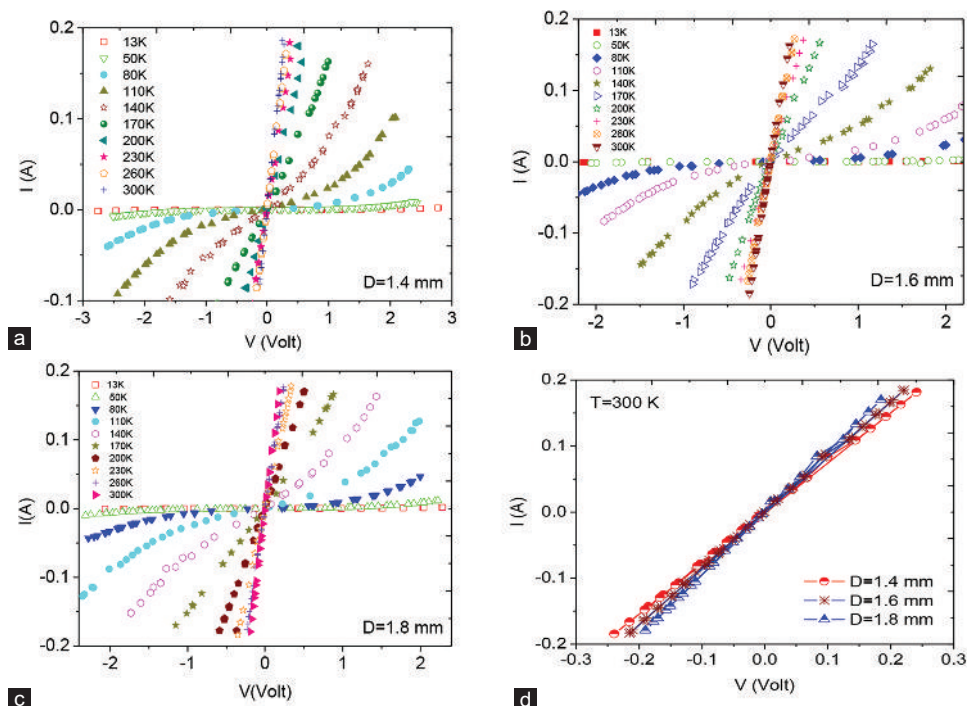


Fig. 6. Electrical characterizations (I) for the graded samples of distributed Bragg reflector (DBRs) coded (VN1802) with diameters of (a) 1.4 mm, (b) 1.6 mm and (c) 1.8 mm at $T=13$ to 300 K, and (d) for various DBRs diameters at 300 K.

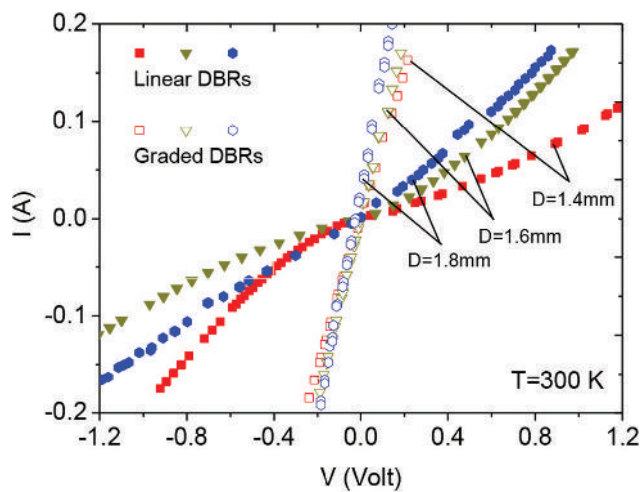


Fig. 7. Comparative current versus voltage measurements between linear distributed Bragg reflectors (DBRs) coded (VN1734) and graded DBRs coded (VN 1802) samples.

In Fig. 3a and b, room temperature reflectivity spectra for both samples coded VN1734 and VN1743 are nearly the same with only a 6 nm shift (thickness difference lower than 0.5%) between the two samples. In Fig. 3c and d, the reflectivity spectra for samples coded VN1800 and VN1802 are in agreement with the simulation results.

III. EXPERIMENTAL DETAILS

Electrical resistivity and Hall Effect measurements are the most commonly used techniques for semiconductor characterization. Several electrical characterizations of DBR

mirrors have been achieved including longitudinal and vertical carrier transport and hence device applications. The current-voltage (I) characteristics are recorded at various temperatures from 13 to 300 K. As shown in Fig. 4a, a 40 MHz Arbitrary waveform (TGA1421) generator is used to supply a positive ramp waveform of about 10 s duration with amplitude up to 20 V_{pp} (peak to peak). This experiment was performed with a closed-cycle Helium cryostat system, and the temperature controller in the Cryodrive compressor unit. The cold head is connected to the base of the sample by a copper link which is fitted with a temperature sensor and a heater to allow variable temperature operation. During the running of the system, if the sample rod is removed from the fitted holder, a slight over pressure of Helium exchange gas should be preserved. The outer vacuum should be evacuated to a pressure of $<10^{-5}$ mbar using a suitable rotary/turbomolecular pumping system. Once the sample rod is inserted in place, the sample space should be evacuated to $\sim 10^{-1}$ mbar using a rotary pump. Once the cryostat temperature has reached 220 K, Helium exchange gas must be added to the sample space. The Helium gas is added using a football bladder which is already connected to the sample space valve. Then with the heater in MAN mode, it can set to the low temperature at around 10 K.

In addition, electrical characterizations of DBR mirrors have been achieved using longitudinal carrier transport. The Hall bar shaped sample is effectively recommended for quantitative measurements over a wide range of temperatures and can be tested to provide information about material impurities, uniformity and mobility limiting scattering mechanisms. The simple Hall bar has side arms, in which the current flows from left to right under an applied electric

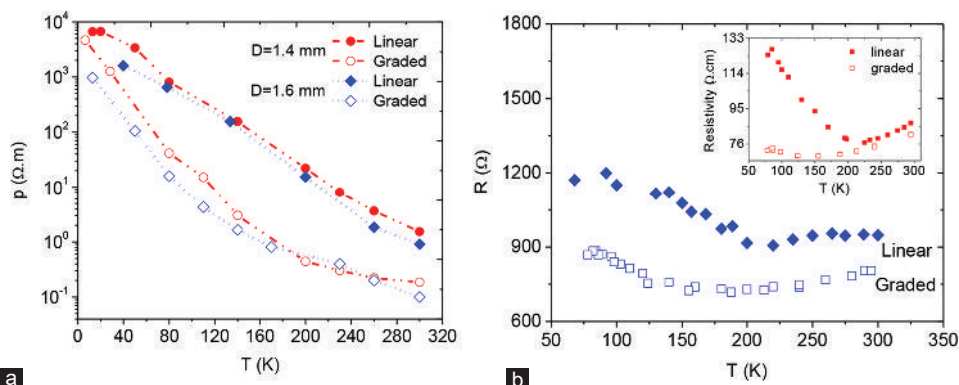


Fig. 8. Temperature dependence of the (a) vertical resistivity in logarithmic scale with linear and graded DBRs diameters of 1.4 and 1.6 mm, (b) Hall resistance under the current flow of 480 μ A. The inset shows the resistivity against temperature.

field E_y as depicted in Fig. 4b. The magnetic induction B_z is applied normal to the sample surface and to the direction of current flow I_x . However, in vertical transport measurements, the current-voltage (IV) characteristics of DBR samples are used to assess the quality of sample contacts.

IV. RESULTS AND DISCUSSION

To determine the series resistances of vertical DBRs with different diameters, electrical measurements were performed on samples coded VN1743 at a temperature between 13 and 300 K. Fig. 5a-c shows the current-voltage (IV) for 14 periods of GaAs/ $Al_{0.9}Ga_{0.1}As$ on p -doped GaAs substrates (linear DBRs) diameters of 1.4, 1.6, and 1.8 mm, respectively. The results of current-voltage (IV) of DBRs measurements show that the resistance slope for GaAs/ $Al_{0.9}Ga_{0.1}As$ based Bragg reflectors are often non-linear and caused by the impurity of the sample. The sample is biased with applied voltages between 1.5 and 2 V. The current for each linear DBRs diameters increases with increasing temperatures from 13 to 300 K. In addition, the current increases with increasing the linear DBRs diameters from 1.4 into 1.8 mm at 300 K as indicated in Fig. 5d.

Furthermore, electrical characterization of vertical DBRs of 14 periods of GaAs/ $Al_{0.3}Ga_{0.7}As/Al_{0.9}Ga_{0.1}As$ on the p -doped substrate (coded VN1802) with diameters of 1.4, 1.6, and 1.8 mm as a function of temperatures is depicted in Fig. 6a-c. The graded reflectors have a linear IV reaction between 200 and 300 K because the tunneling distance is affected less by the small bias. The resistance is increased usually with decreasing temperatures due to the thermionic emission method (Nabiev and Chang-Hasnain, 1995). The graded layer drastically reduces the potential barrier of p -type DBR (Winston and Hayes, 1998). In addition, the IV measurements of graded DBRs with diameters of 1.4, 1.6, and 1.8 mm at 300 K are shown in Fig. 6d. It clearly shows that the current spreading is strongly dependent on the size of mesa sample, which is high in the smallest DBR diameter.

Fig. 7 shows a typical current-voltage (IV) plot for 14 period's GaAs/ $Al_{0.9}Ga_{0.1}As$ DBRs (linear) and GaAs/ $Al_{0.3}Ga_{0.7}As/Al_{0.9}Ga_{0.1}As$ DBR (graded) on p -doped substrate

with three different mesa diameters. It is obvious that current increases by increasing mesa diameters in both linear and graded DBR samples, and leading to reduce the resistance, especially in the graded region.

The fabrication Ohmic contacts were formed with channel main bar length of 1.75 mm and width of 0.4 mm. A magnetic field of around 0.35 T is applied perpendicular to the sample. The current flowing through the sample kept relatively low ($< 480 \mu$ A) to ensure ohmic conditions. Resistivity as a function of temperature for both linear and graded DBRs (coded VN1743 and VN1802) with diameters of 1.4 and 1.6 mm is shown in Fig. 8a. Hall Effect measurements of GaAs/AlGaAs heterostructures (coded VN1734 and VN1800) were carried out as a function of temperature between 77 and 300 K. Fig. 8b shows the temperature dependence for two types of DBRs, and the inset shows their longitudinal resistivity. The graded sample has lower resistance than the linear sample in the studied temperature range. The inset shows the resistivity as a function of temperature, which exhibit low resistivity compared to the linear DBR sample (Chaqmaqchee, et al., 2012).

V. CONCLUSION

This paper presents an extensive electrical characterization of four types p -doped design based linear and graded DBRs using various mesa diameters. DBRs are improved with reduction in the resistance attributed to grading of the layers and smaller mesa diameters. Reducing the resistivity of the quarter wavelength thick is required for the reducing of the heating generation combined with improved thermal conductivity. Thus for optoelectronic devices structure, low series resistance to limit heating effect and sufficient heat dissipation are important to achieve high output power operation. This increases the VCSEL/VCSOA performance, which have great interest in optical fiber communication systems including metro and access networks.

VI. DISCLOSURE

The authors report no conflicts of interest in this work.

VII. ACKNOWLEDGMENT

This research was financially supported by the ministry of higher education and scientific research of IRAQ. FC highly appreciates the support of the University of Essex team during this work. FC also acknowledges Koya University, Department of Physics for allowing this study.

REFERENCES

- Chaqmaqchee, F., Abubekr Salh, S. and Sabri, M.M., 2020. Optical analysis of 1300 nm GaInNAsSb/GaAs vertical cavity semiconductor optical amplifier, *Zanco Journal of Pure and Applied Sciences*, 32(2), pp.87-92.
- Chaqmaqchee, F.A.I. and Lott, J.A., 2020. Impact of oxide aperture diameter on optical output power, spectral emission, and bandwidth for 980 nm VCSELs. *OSA Continuum*, 3(9), pp.2602-2613.
- Chaqmaqchee, F.A.I., 2019. Performance characteristics of conventional vertical cavity surface emitting lasers VCSELs at 1300 nm. *ZANCO Journal of Pure and Applied Sciences*, 31(2), pp.14-18.
- Chaqmaqchee, F.A.I., Mazzucato, S., Sun, Y., Balkan, N., Tiras, E., Hugues, M. and Hopkinson, M., 2012. Electrical characterisation of p-doped distributed Bragg reflectors in electrically pumped GaInNAs VCISOAs for 1.3 μ m operation. *Materials Science and Engineering B*, 177(10), pp.739-743.
- Croquette, K.D. and Hou, H.Q., 1997. Vertical-cavity surface emitting lasers: Moving from research to manufacturing, *Proceedings of the IEEE*, 85(11), pp.1730-1739.
- Garmire, E., 2003. Theory of quarter-wave-stack dielectric mirrors used in a thin Fabry-Perot filter. *Applied Optics*, 42, pp.5442-5449.
- Macleod, H.A., 2018. *Thin-film Optical Filters*, CRC Press, Taylor and Francis, Arizona, USA.
- Marciniak, M., Gebiski, M., Broda, A., Muszalski, J., Czyszanowski, T. and Lott, J.A., 2020. *Impact of Top Mirror Power Reflectance on 980-nm VCSEL Performance*. Vol. 11300. Proceedings SPIE.
- Nabiev, R.F. and Chang-Hasnain, C.J., 1995. Voltage drop in n- and p-type Bragg reflectors for vertical-cavity surface-emitting lasers. *IEEE Photonics Technology Letters*, 7(7), pp.733-735.
- Ogura, M., Hata, T., Kawai, N.J. and Yao, T., 1983. GaAs/Al_xGa_{1-x}As multilayer reflector for surface emitting laser diode. *Japanese Journal of Applied Physics*, 22(2A), pp.L112-L114.
- Pickrella, G.W., Louderbacka, D.A., Fisha, M.A., Hindia, J.J., Lina, H.C., Simpsona, M.C., Guilfoylea, P.S. and Lear, K.L., 2005. Compositional grading in distributed Bragg reflectors, using discrete alloys, in vertical-cavity surface-emitting lasers. *Journal of Crystal Growth*, 280(1-2), pp.54-59.
- Pohl, J., Cole, G.D., Zeimer, U., Aspelmeyer, M. and Weyers, M., 2018. Reduction of absorption losses in MOVPE-grown AlGaAs Bragg mirrors. *Optics Letters*, 43(15), pp.3522-3525.
- Wang, G., Li, K., Chen, S. and Yang, H., 2019. Analysis of pulse amplification characteristics in vertical cavity semiconductor optical amplifiers. *Journal Integrated Ferroelectrics*, 198(1), pp.39-54.
- Winston, D.W. and Hayes, R.E., 1998. Optoelectronic device simulation of Bragg reflectors and their influence on surface-emitting laser characteristics, *IEEE Journal of Electronics*, 34(4), pp.711.
- Zhang, C., ElAfandy, R. and Han, J., 2019. Distributed Bragg reflectors for GaN-based vertical-cavity surface-emitting lasers, *Applied Sciences*, 9(8), pp.1-20.

Assessment the Natural Radioactivity of Radionuclides (^{226}Ra , ^{232}Th , ^{40}K , and ^{137}Cs) in Wheat Grain

Zakariya A. Hussein, Najeba F. Salih and Shalaw Z. Sedeeq

Department of Physics, Faculty of Science and Health, Koya University, Koya KOY45, Kurdistan Region - F.R. Iraq

Abstract—This paper investigates the activity concentration of radionuclides (^{226}Ra , ^{232}Th , ^{40}K , and ^{137}Cs) in the wheat grain samples using a high-purity germanium detector. Thirty-six wheat grain samples were collected from different locations of Koya City, Iraqi Kurdistan region. Average activity concentrations of ^{226}Ra , ^{232}Th , and ^{40}K in wheat grain are found to be $0.407 \pm 0.097 \text{ Bq.kg}^{-1}$, $0.36 \pm 0.14 \text{ Bq.kg}^{-1}$, and $109.25 \pm 2.214 \text{ Bq.kg}^{-1}$ for ^{226}Ra , ^{232}Th , and ^{40}K , respectively. The measured activity concentrations for the radionuclides are compared with the reported data from other countries. In addition, the fallout radionuclide of ^{137}Cs has no detection of in the wheat grain samples. The radium equivalent activity Ra_{eq} , internal and external hazard indices H_{in} and H_{ex} , and annual gonadal dose equivalent are calculated for the measured samples. The total ingestion dose is $113.19 \mu\text{Sv.y}^{-1}$, which is below the world average value of $290 \mu\text{Sv.y}^{-1}$.

Index Terms—Natural Radioactivity, Wheat Grain, Radionuclides, ^{226}Ra , ^{137}Cs .

I. INTRODUCTION

Natural sources of ionizing radiation have continual property of emission of nuclear particles or Gamma-rays, therefore, the exposure to human beings by those sources of radiation is inescapable. The primordial radionuclides comprise the natural series such as ^{238}U , ^{232}Th , and non-series ^{40}K which are ordinarily long lived and with a half-life more than one hundred million years (Al-Hamzawi, 2017a, UNSCEAR, 2000). The radionuclide radiation could be a serious problem to the living tissues, because can cause damage them just when the radiation energy is absorbed in that tissues, and food ingestion is the most common pathway to transfer radionuclides to people, therefore, the detection of radioactive materials is absolutely important in the process of people and environment protection (Harb, et al., 2014).

Uranium and its isotopes are considered most serious pollution due to its radiological and toxicological activity which is a threat to the human and the environment, the ingestion of food is considered the main pathways of uranium entrance into the human body (Zakariya, 2019). Human beings are exposed to both external and internal radiation. The internal exposure comes from the intake of terrestrial radionuclides through inhalation or ingestion pathway. The inhalation exposure is related to the existence of dust particles in the air which comprise the radionuclides from the decay series of ^{238}U and ^{232}Th and non-series ^{40}K as well. Plants acquire the main source of natural background radiation (terrestrial radionuclides) through the roots and leaves whereas humans and animals acquire radionuclides through consumption of these plants, there are two different mechanisms for the transferring of radionuclides to plants, either through root uptake or directly through aerial deposition (Khan, et al., 2011).

The levels of radionuclides in plants vary typically from a few tens of Becquerel (Bq) to several hundred of Becquerel per kilogram (Wang, et al., 1997). The radionuclides that exist in the fertilizers are uranium and thorium decay series as well as potassium. Besides, the concentration of radionuclides in fertilizers differs from different countries and depending on the origin of the components. Measurement and assessment of natural radioactivity is necessary because of its immediate effect on the human beings safety. In the most countries of the world, the study of naturally occurring radiation and environmental radioactivity was carried out (UNSCEAR, 2000). During the past decades, the agricultural activities in Iraqi Kurdistan region widely grew up, especially wheat planting due to the application of different types of fertilizers, pesticides, and some other chemicals to improve soil properties, enhance the quality of the crop products and to get more gain in terms of crop quantity as well. In other words, their concentration could be increased as contaminants over the time (Brigden, et al., 2002). From many countries, to establish a baseline data to the natural radioactivity levels, measurement of natural radionuclides in environmental elements has been carried out (Zakariya, 2019).

Therefore, this research was carried out to investigate the levels of radioactivity due to the natural radionuclides of ^{226}Ra , ^{232}Th , ^{40}K , and ^{137}Cs in wheat grain of Koya City,

ARO-The Scientific Journal of Koya University
Vol. IX, No.1 (2021), Article ID: ARO.10736, 8 pages
DOI: 10.14500/aro.10736

Received 04 October 2020; Accepted: 30 April 2021
Regular research paper: Published: 28 June 2021

Corresponding author's e-mail: zakariya.hussein@koyauniversity.org
Copyright © 2021 Zakariya A. Hussein, Najeba F. Salih and Shalaw Z. Sedeeq. This is an open-access article distributed under the Creative Commons Attribution License.



Iraqi Kurdistan, and also to estimate the radiological hazard parameters of wheat grain samples.

II. RESEARCH METHODOLOGY

A. Study Area

This study was conducted at Koya (Koysinjaq) in Erbil governorate from the south part of Iraqi Kurdistan region, as shown in Fig. 1. Koya district is about 582 m high from sea level, and its geographical coordinates are 36.0751° N and 44.6199° E. Furthermore, Koya is a mountainous area, and it is surrounded by many villages which have affected the lifestyle of the people that living there. In general, it is considered as a good agricultural region. The intensive farming of wheat is distributed at the plain of Erbil, south of Koysinjaq district (Zakaria, et al., 2013, Hussein, 2015). The proper location and weather of this district (rainy winter and hot summer) are two helpful parameters in growing up the agricultural activities there. Especially, wheat planting has attracted a lot of attention of the farmers due to the facility in planting and its well growing in that region (Salih, et al., 2020a). So that, wheat production can be considered as a dominant agricultural activity in that district and the largest area of agricultural lands is devoted for wheat planting (86.4%, 171,750 donums). As well as, it is estimated that wheat covers the most portion of farmlands in the world (Servitzoglou, et al., 2018). Therefore, this study was done to estimate the concentration levels of natural radionuclides and the radiological hazards in wheat grains resulting from consumption of wheat flour in Koya district.

B. Radioactivity in Wheat Plant

One of the most important food crops in the world is wheat. Annually, the largest agricultural area is devoted to wheat plantation. Wheat is a stable daily food in many different forms. In Kurdistan region, an ample amount of wheat is consumed in the form of flat bread which is locally called Nan. It is known that the major fraction of the radioactivity is retained by root part of the wheat plant. Some fraction of the radioactivity is up taken by the grain part of the wheat from the soil (Chen, et al., 2005). A part of the radionuclides which present in the fertilized soils could be taken by the plants through root uptake. Then, they can be transferred to the human body by food ingestion. The radiation dose rate taken by the human body through the different organisms



Fig. 1. Map of Iraq with Erbil governorate from north of Iraq and location under the study (Koysinjaq) (Google Maps).

depends on several factors; the rate of food consumption, the soil characteristics which the particular crop has grown on it, the health and how old is the user (Tsukada, et al., 2002). Depending on their requirement, the plants may take up the nutritious ions then they are transferred to particular tissues according to the function of the element in plant metabolic process. The primordial radionuclides could also be transported along with nutrients and may have the same chemical behavior as the indispensable nutrient. The distribution of ^{238}U and ^{232}Th in various parts of the wheat plant there is a decreasing trend as; root > shoot > husk > grains, radionuclides have the lowest concentration in the wheat grains and about 50% of Ra is observed to pile up in the roots and nearly 22% in the shoots and husk. From the figure, it is also could be seen that the higher concentration of ^{40}K is in the shoots and it follows a decreasing trend as shoot > root > husk > grain (Pulhani, et al., 2005).

C. Wheat Grain Sampling

A total of 36 samples of mature wheat grains obtained from the wheat plants grown were collected at harvesting time during, among the center of Koya district and its five subdistricts (Ashti sub-district, Taq taq sub-district, Segirdkan sub-district, Shorsh sub-district, and Siktan sub-district) within 36 villages where the local growers use a great area of land for the cultivation of wheat plant. The sample locations are shown in Fig. 2. To make a representative sample from each location, 6 points were selected across each wheat plantation field, and the area of each point was 2 m × 2 m (IAEA, 1989). The wheat grain samples were labeled and transferred into a polythene bag. Thereafter, the samples were transported into the laboratory of research at Koya University. After then, the samples were carefully cleaned from wheat roots, wheat leaves, and any kind of debris. Then, the samples were crushed using a powder grinder machine (Silver Crest, model No.: SL-8859) and passed through a 1 mm mesh to get homogenized samples. To remove moisture and for adequate drying, the samples were placed in an electrical oven at 100°C for 10 h (Alshahri, 2016). A very sensitive balance was used to measure the mass of the dried samples, each sample about 1 ± 0.02 Kg of dry weight. For measurements, the samples were packed into standard size containers (Marinelli beakers) and tightly sealed then stored for a month to reach secular equilibrium (Zakariya, 2015). Finally, after ensuring that the radioactive equilibrium of the decay products of ^{226}Ra and ^{232}Th series reached by storage for 30 days (Cevik, et al., 2007). The stored samples were transported into the counting room (Nuclear Physics Laboratory – Koya University) for measurement and analysis.

D. EFFICIENCY CALIBRATION

The efficiency of a detector is ratio of the number of pulses recorded by the detector to the number of gamma-ray photons emitted by the source. Efficiency is the most important characteristic of the detectors, so that, a precise efficiency calibration of a gamma-ray spectrometry system

is necessary for the analysis of radionuclides available in a sample (Mostajaboddavati, et al., 2006). The calibrations of efficiency calibration for the system were performed using standard sources from the International Energy Agency (IAEA) as a function of gamma-ray energies. The detector has a relative efficiency of 73.8% at 1.33 MeV for ⁶⁰Co, and its resolution (FWHM) was 1.18 keV at 122 keV for ⁵⁷Co, and at 1332 keV of ⁶⁰Co was 1.97 keV, the radioactivity measurements were carried out for 36,000 s (Essiett, et al., 2015, Salih, et al., 2020). The efficiency calibration of the gamma-ray spectrometry study was performed using ²²⁶Ra (186.1, 295, 351.9, 609, 665, 1120, and 1764 keV), ⁶⁰Co (1175.2 and 1332.5 keV), and ¹³⁷Cs (661.7 keV). The relative efficiency curve of the detector was made of the different energy values covering the energy range from 186 keV to 1332.5 keV. The efficiency calibration curve of high-purity germanium detector is shown in Fig. 3.

E. Calculation of the Activity Concentration of Radionuclide and Hazard Indices

After storing the samples for a month and under the assumption that secular equilibrium was achieved between ²²⁶Ra and ²³²Th and their decay products, the activity concentration of ²²⁶Ra was calculated from the average concentrations of the ²¹⁴Pb and ²¹⁴Bi decay products and that for ²³²Th was calculated from the average concentrations of ²⁰⁸Tl and ²²⁸Ac decay products in the sample that is agree with AL-harbiI and El-Taher, 2013.

Activity concentration of radionuclides

The activity concentration of the interested radionuclides ²²⁶Ra, ²³²Th, ⁴⁰K, and ¹³⁷Cs in a unit of Bq.kg⁻¹ has been calculated using the relation (Murtadha, et al., 2017, Salih, et al., 2020).

$$Activity\ concentration \left(\frac{Bq}{kg} \right) = \frac{Net\ count}{\epsilon \times I_{\gamma} \times t \times m} \quad (1)$$

Where, I_{γ} is the emission probability per decay of the specific peak, ϵ is the absolute gamma peak efficiency for the detector at a particular photopeak, t is the counting time in seconds, and m is the mass of the sample in kilogram.

Hazard indices

The exposure to radiation arising from the primordial radionuclides of ²²⁶Ra, ²³²Th, and ⁴⁰K in the wheat grains can be determined in terms of some parameters, as given below; Radium equivalent activity (Ra_{eq})

The radium equivalent activity (Ra_{eq}), which is a single index, used to describe the gamma output from different mixtures of ²²⁶Ra, ²³²Th, and ⁴⁰K in the material. It was calculated from this equation (Nisar, 2015; Al-Hamed, et al., 2017).

$$Ra_{eq} = A_{Ra} + 1.43A_{Th} + 0.077A_K \quad (2)$$

Where, A_{Ra} , A_{Th} , and A_K are activity concentrations of ²²⁶Ra, ²³²Th, and ⁴⁰K, respectively.

Internal hazard indices (H_{in})

Internal hazard index of the gamma-ray specific activity concentrations of ²²⁶Ra, ²³²Th, and ⁴⁰K is calculated using Equation (3) given by (Ismail et al, 2020, Mehra, et al., 2007).

$$H_{in} = \frac{A_{Ra}}{185} + \frac{A_{Th}}{259} + \frac{A_K}{4810} \leq 1 \quad (3)$$

External hazard indices (H_{ex})

The external hazard index is a description that quantifies the exposure factor and is an estimation of the hazard of the

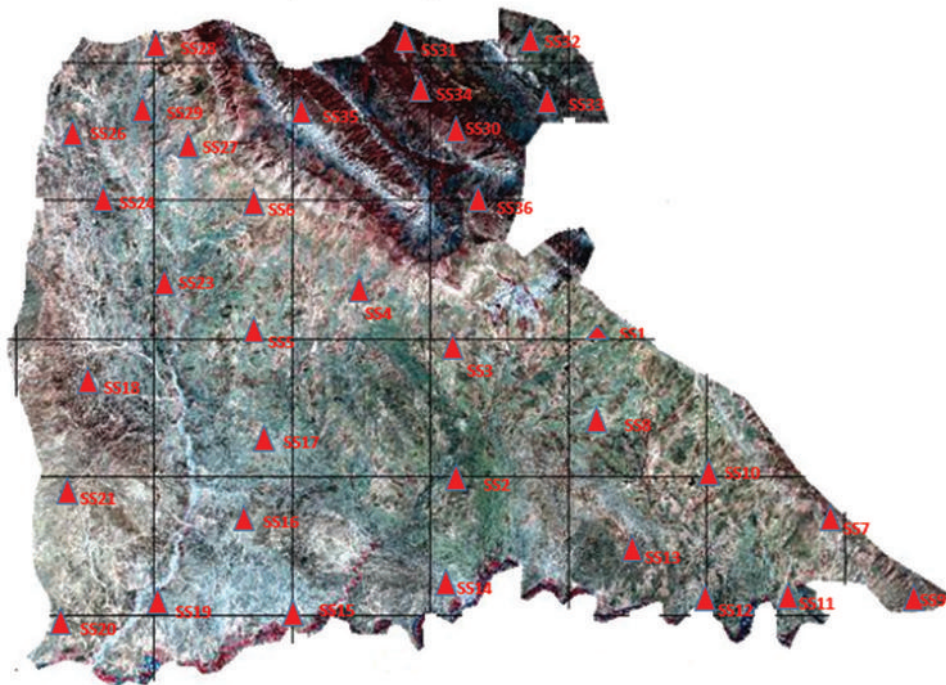


Fig. 2. Sampling locations of wheat grain samples on the map of the Koysinjq district (Google Maps).

natural gamma radiation due to the terrestrial radionuclides of ^{226}Ra , ^{232}Th , and ^{40}K . It can be calculated using Equation (4) (Taiwo, et al., 2014).

$$H_{ex} = \frac{A_{Ra}}{370} + \frac{A_{Th}}{259} + \frac{A_K}{4810} \leq 1 \quad (4)$$

Ingestion dose (E_{ING})

Annual ingestion dose: The annual ingestion dose (E_{ING}) for human was coming from consumption of grain, due to the ingestion of radionuclides. The concentration of naturally occurring radionuclides of ^{226}Ra , ^{232}Th , and ^{40}K in foodstuffs and the consumption rate of food and water by human beings affect the annual ingestion dose rates (UNSCEAR, 2000). The annual ingestion dose for Koya inhabitants (E_{ING}) coming from the consumption of wheat was calculated using the following equation given by (Canbazoglu and Dogru, 2013, Salih, 2018).

$$IAED = \sum i(Li \times Ai, r) \times FDC_r \quad (5)$$

Where, i represents a food category (grain, vegetable, fruits, etc.); Li and Ai, r represent the annual consumption rate of plant crops per capita (kg/year) and the activity concentration of radioactive nuclide r in food category i (Bq/kg), respectively, and FDC_r is the dose conversion factor for the ingestion of radionuclide r (Sv/Bq). The committed DCFs for the radioactive nuclides in adults were obtained from the ICRP 2012 reported as 0.28, 0.23, and 0.006 $\mu\text{Sv/Bq}$ for calculations of the effective dose due to ^{226}Ra , ^{232}Th , and ^{40}K , respectively (Murtadha, et al., 2017).

Annual gonadal dose equivalent (AGDE)

Gamma radiation affects various organs of the human body depending on the type of the organs and the duration of exposure. The most sensitive organs interested by UNSCEAR, 2010, are the bone surface, bone marrow, lungs, thyroids, female's breast, and the gonads. Therefore, the AGDE due to the natural radionuclides of ^{226}Ra , ^{232}Th , and ^{40}K in the collected samples is calculated using the following formula (Mamont-Ciesla, et al., 1982).

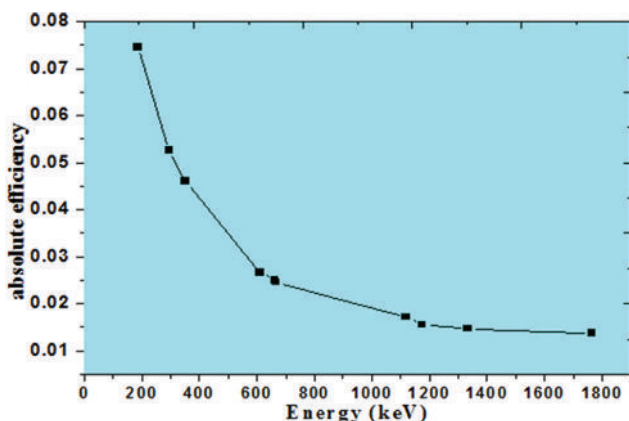


Fig. 3. Efficiency calibration curve for the high-purity germanium detector.

$$AGDE (\mu\text{Sv.y}^{-1}) = 3.09A_{Ra} + 4.18A_{Th} + 0.314A_K \quad (6)$$

III. RESULTS AND DISCUSSION

Fig. 4 shows the activity concentrations in (Bq.kg⁻¹) of the radionuclide ^{137}Cs and ^{226}Ra , ^{232}Th , and ^{40}K for 36 investigated wheat grain samples. The radionuclide ^{137}Cs was not detected in the all measured wheat grain samples. The activity concentration of ^{226}Ra varies from 0.245 ± 0.116 Bq.kg⁻¹ (WS₁₀- Ella Allah village) to 0.746 ± 0.086 Bq.kg⁻¹ (WS₁₅- Kani lala village) with an average value of 0.407 ± 0.097 Bq.kg⁻¹. The activity concentration of ^{232}Th was below minimum detectable activity in the samples of WS₃, WS₅, WS₈, WS₂₂, WS₂₇, WS₂₉, WS₃₂, and WS₃₅ and it was not detected of two samples (WS₁₃ and WS₃₄). This activity ranged from below minimum detectable activity BMDA to 0.814 ± 0.367 Bq.kg⁻¹ (WS₁₆ - Talabani gawra) with an average value of 0.36 ± 0.14 Bq.kg⁻¹. Furthermore, the activity concentration of ^{40}K was found in all samples with the minimum value of 72.04 ± 1.561 Bq.kg⁻¹ (WS₂ - Pebazok) and the maximum value of 136.1 ± 2.659 Bq.kg⁻¹ (WS₃₁ - Sinawa), with average value of 109.25 ± 2.214 Bq.kg⁻¹. The activity concentration of ^{40}K has been high because it is naturally high abundance in environmental samples. Moreover, ^{226}Ra detection in wheat grain samples was expected, because it is a daughter product in the decay series of ^{238}U which is typically found in environmental samples. Moreover, the activity concentration of ^{232}Th was not detected or BMDA below minimum detectable activity in some wheat grain samples, but it does not imply absolutely that the absence of ^{232}Th in these samples. In fact, many researchers in their studies have reported BMDA or non-detection for ^{232}Th in wheat grains (Changizi et al., 2013, Abojassim et al., 2015, Hosseini et al., 2006). The obtained results showed the activity concentrations of the radionuclides ($^{226}\text{Ra} < ^{232}\text{Th} < ^{40}\text{K}$) which is in accordance with the information presented by (Changizi et al., 2013). The soil-to-wheat grain transfer factors of ^{40}K are considerably higher than those for ^{226}Ra and ^{232}Th because of the high solubility of ^{40}K in water and its high mobility in soil (Kumar, et al., 2008). The noticeably high recorded values of ^{40}K in the wheat grain samples within the present study are similar findings recorded by Akhtar and Tufail, 2006, Alshahri, 2016. The average values of activity concentrations of ^{226}Ra , ^{232}Th , and ^{40}K for the wheat grain samples in this study were too lower than the worldwide average values recommended by the United Nations Scientific Committee on the Effects of Atomic Radiation Sources as 32 Bq/kg for ^{226}Ra , 45 Bq/kg for ^{232}Th , and 412 Bq/kg for ^{40}K (UNSCEAR, 2000).

Furthermore, Fig. 4 shows the variations of concentration levels of ^{226}Ra , ^{232}Th , and ^{40}K according to the different wheat grain samples. These variations may be due to the different concentration of the radionuclides ^{226}Ra , ^{232}Th , and ^{40}K in the soils of wheat plantation fields which could be absorbed by wheat plants (El-Taher and Makhluf, 2010). Overall, the obtained results indicated that radioactivity levels in the

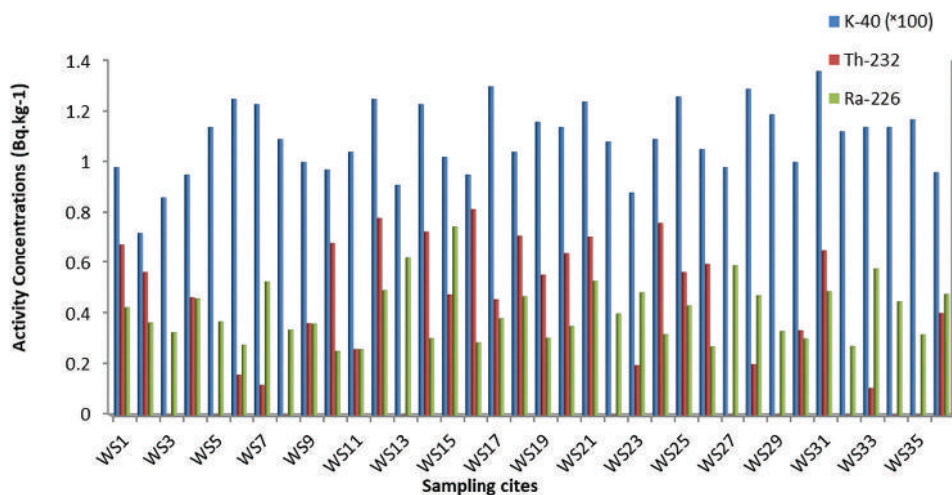


Fig. 4. A activity concentration levels of ²²⁶Ra, ²³²Th, and ⁴⁰K of the related wheat grain samples.

wheat grain samples collected from the wheat plantation fields of Koya district are not at the range of health risk.

Furthermore, there is study in Iraq, aiming at clarifying the radiation hazard indices and ingestion effective dose in wheat flour samples collected from Iraqi markets was conducted by (Abojassim et al., 2015), by used NaI (TI) detector was used to radiometric analysis for 12 different types of flours those were available in Iraqi markets. The specific activities were varied from 1.086 ± 0.0866 to 12.532 ± 2.026 for ²³⁸U, from 0.126 ± 0.066 to 4.298 ± 0.388 for ²³²Th, and from 41.842 ± 5.875 to 264.729 ± 3.843 for ⁴⁰K. The average values of radium equivalent and internal hazard index in wheat flour samples were found to be $19.6347 \text{ Bq.kg}^{-1}$ and 0.0708 , respectively.

Comparisons between the natural radioactivity levels in wheat grain samples of the present study with some other studies among worldwide listed in Table I.

Table II shows the values of radium equivalent activity Ra_{eq} of the wheat grain samples. The results of Ra_{eq} for the measured wheat grain samples were ranged from 6.71 to 11.9 Bq.kg^{-1} with average value of 9.33 Bq.kg^{-1} that is less than the permissible limit (370 Bq.kg^{-1}) (UNSCEAR, 2000), this result indicates that the collected wheat grain samples among the wheat farming lands of Koya district have no radiation hazards. The values of other parameters such as internal and external hazard indices H_{in} and H_{ex} and AGDE due to the specific activities of ²²⁶Ra, ²³²Th, and ⁴⁰K are presented in Table II, the values of H_{in} , H_{ex} , and AGDE were ranged from 0.019 to 0.03 with average value of 0.026, from 0.018 to 0.032 with average value of 0.025, and from $26.1 \mu\text{Sv.y}^{-1}$ to $46.97 \mu\text{Sv.y}^{-1}$ with average value of $37.06 \mu\text{Sv.y}^{-1}$, respectively, the lowest values of H_{in} , H_{ex} , and AGDE of the wheat grain sample were found in Pebazok village. Whereas, the highest values of the wheat grain sample were found in Siktan village. The obtained results were compared to the recommended permissible limits. This study indicated that the average values of H_{in} and H_{ex} of wheat grain samples were found to be lower than unity (<1), this reveals that the radiation hazards due to the wheat grain samples among the

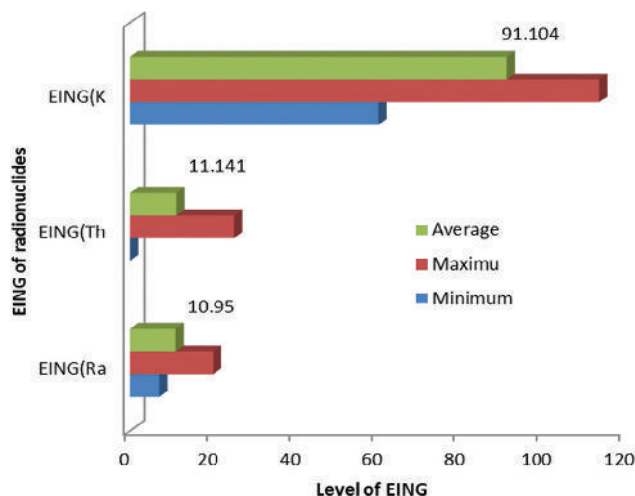


Fig. 5. The average $E_{ING(Ra-226)}$, $E_{ING(Th-232)}$, $E_{ING(K-40)}$, and $E_{ING(Total)}$ in $\mu\text{Sv.y}^{-1}$ of the wheat grain samples.

TABLE I
COMPARISON BETWEEN THE NATURAL RADIOACTIVITY LEVELS IN WHEAT GRAIN SAMPLES UNDER STUDY AND SOME OTHER STUDIES AMONG THE WORLDWIDE KURDISTAN

Country	Activity concentrations of ²²⁶ Ra, ²³² Th, and ⁴⁰ K (Bq.kg ⁻¹)			Reference
	²²⁶ Ra (Bq.kg ⁻¹)	²³² Th (Bq.kg ⁻¹)	⁴⁰ K (Bq.kg ⁻¹)	
Egypt	1.352	1.142	111.98	(AL-harbil and El-Taher, 2013)
Iran	1.67	0.5	91.73	(Changizi, et al., 2013a)
Saudi Arabia	22.7±3.2	22.4 ± 2.5	242±19	(Alshahri, 2016)
India	0.7±0.09	0.7 ± 0.01	88.7±7.8	(Pulhani et al., 2005)
Kazakhstan	1.1±0.176	0	99.4±2	(Akhtar et al., 2005)
Macedonia	0.6±0.173	0.316±0.165	240±.1	(Aleksandra et al., 2017)
France	0.57±0.057	<0.035	146.3±7.3	(Akhtar et al., 2005)
Belgium	0.1±0.05	0.15±0.05	115±22	(Lindahl et al., 2011)
Iraq, Kurdistan region	0.407±0.097	0.36±0.14	109.25± 2.214	The present study

TABLE II

THE RADIUM EQUIVALENT ACTIVITY Ra_{eq} , INTERNAL HAZARD INDEX (H_{in}), EXTERNAL HAZARD INDEX (H_{ex}), AND ANNUAL GONADAL DOSE EQUIVALENT OF THE WHEAT GRAIN SAMPLES

Sample code	Ra_{eq} (Bq.kg ⁻¹)	Hazard indices		AGDE (μ Sv.y ⁻¹)
		H_{in}	H_{ex}	
WS ₁	8.968	0.0253	0.0242	35.038
WS ₂	6.719	0.0191	0.0181	26.109
WS ₃	6.968	0.0197	0.0188	28.092
WS ₄	8.477	0.0241	0.0228	33.348
WS ₅	9.217	0.0258	0.0248	37.221
WS ₆	10.147	0.0281	0.0273	40.840
WS ₇	10.228	0.0290	0.0276	40.994
WS ₈	8.777	0.0246	0.0236	35.458
WS ₉	8.633	0.0242	0.0233	34.252
WS ₁₀	8.702	0.0241	0.0234	34.114
WS ₁₁	8.703	0.0242	0.0235	34.804
WS ₁₂	11.231	0.0316	0.0303	44.029
WS ₁₃	7.6559	0.0223	0.0206	30.605
WS ₁₄	10.813	0.0300	0.0291	42.596
WS ₁₅	9.334	0.0272	0.0252	36.542
WS ₁₆	8.813	0.0245	0.0237	34.310
WS ₁₇	11.045	0.0308	0.0298	43.910
WS ₁₈	9.544	0.0270	0.0257	37.288
WS ₁₉	10.068	0.0280	0.0271	39.842
WS ₂₀	10.092	0.0282	0.0272	39.751
WS ₂₁	11.087	0.0313	0.0299	43.524
WS ₂₂	8.786	0.0248	0.0237	35.433
WS ₂₃	7.610	0.0218	0.0205	30.228
WS ₂₄	9.830	0.0274	0.0265	38.517
WS ₂₅	11.010	0.0309	0.0297	43.542
WS ₂₆	9.215	0.0256	0.0248	36.330
WS ₂₇	8.179	0.0236	0.0220	32.770
WS ₂₈	10.702	0.0301	0.0288	42.843
WS ₂₉	9.549	0.0266	0.0257	38.614
WS ₃₀	8.497	0.0237	0.0229	33.799
WS ₃₁	11.901	0.0334	0.0321	46.971
WS ₃₂	8.950	0.0249	0.0241	36.231
WS ₃₃	9.561	0.0273	0.0258	38.244
WS ₃₄	9.227	0.0261	0.0249	37.183
WS ₃₅	9.328	0.0260	0.0251	37.723
WS ₃₆	8.457	0.0241	0.0228	33.349
Minimum values	6.719	0.0191	0.0181	26.109
Maximum values	11.901	0.0334	0.0321	46.971
Average values	9.334	0.0263	0.0252	37.068

TABLE III

THE ANNUAL EFFECTIVE INGESTION DOSE E_{ING} DUE TO THE INTAKE OF ²²⁶Ra, ²³²Th, AND ⁴⁰K BY THE CONSUMPTION OF WHEAT GRAINS

Sample code	Annual Ingestion Dose E_{ING} (μ Sv. y ⁻¹)			
	$E_{ING(Ra-226)}$	$E_{ING(Th-232)}$	$E_{ING(K-40)}$	$E_{ING(Total)}$
WS ₁	11.459	20.881	82.064	114.404
WS ₂	9.845	17.447	60.074	87.366
WS ₃	8.823	0.000	71.915	80.738
WS ₄	12.400	14.384	79.620	106.406
WS ₅	9.953	0.000	95.815	105.768
WS ₆	7.478	4.949	104.404	116.832
WS ₇	14.176	3.650	103.236	121.063
WS ₈	9.092	0.000	91.395	100.487
WS ₉	9.710	11.229	83.973	104.914
WS ₁₀	6.832	21.066	80.955	108.854
WS ₁₁	7.020	8.074	87.392	102.487
WS ₁₂	13.261	24.098	104.237	141.597
WS ₁₃	16.731	0.000	76.176	92.908
WS ₁₄	8.177	22.458	102.569	133.206
WS ₁₅	20.067	14.725	85.641	120.434
WS ₁₆	7.747	25.181	79.720	112.649
WS ₁₇	10.275	14.137	108.407	132.820
WS ₁₈	12.616	21.932	87.309	121.858
WS ₁₉	8.231	17.137	97.149	122.518
WS ₂₀	9.468	19.829	95.564	124.863
WS ₂₁	14.257	21.840	103.403	139.500
WS ₂₂	10.786	0.000	90.811	101.598
WS ₂₃	13.046	6.125	74.100	93.2719
WS ₂₄	8.608	23.510	91.228	123.347
WS ₂₅	11.647	17.447	105.821	134.917
WS ₂₆	7.289	18.437	87.642	113.370
WS ₂₇	15.897	0.000	82.180	98.0787
WS ₂₈	12.723	6.248	107.656	126.629
WS ₂₉	8.957	0.000	99.817	108.775
WS ₃₀	8.150	10.363	83.556	102.070
WS ₃₁	13.154	20.169	113.493	146.817
WS ₃₂	7.343	0.000	93.980	101.324
WS ₃₃	15.548	3.279	95.648	114.475
WS ₃₄	12.078	0.000	95.064	107.142
WS ₃₅	8.581	0.000	97.566	106.147
WS ₃₆	12.858	12.466	80.171	105.496
Minimum	7.020	0.000	60.074	80.738
Maximum	20.067	25.181	113.493	141.597
Average	10.952	11.141	91.104	113.198

studied area are insignificant. Moreover, the average value of AGDE was lower than the permitted limit of 300 μ Sv.y⁻¹ as given by UNSCEAR, 2000.

The annual effective ingestion dose due to the consumption of wheat grains was calculated based on annual intake of 134.5 kg.y⁻¹(dry weight) of wheat grains by adults in Iraq, Kurdistan region, as given by Azeez, et al., 2019. The ingestion dose due to the intake of each of natural radionuclides ²²⁶Ra, ²³²Th, and ⁴⁰K is presented in Table III. The calculated values were ranged from 7.02 to 20.06 μ Sv.y⁻¹ with the average value of 10.95 μ Sv.y⁻¹ of E_{ING} (²²⁶Ra), from 0 to 25.18 μ Sv.y⁻¹ with average value of 11.14 μ Sv.y⁻¹ of E_{ING} (²³²Th), and from 60.07 to 113.49 μ Sv.y⁻¹ with a mean value of 91.1 μ Sv.y⁻¹ of E_{ING} (⁴⁰K). The total ingestion dose E_{ING} (total) due to the summation of E_{ING} (²²⁶Ra), E_{ING} (²³²Th), and E_{ING} (⁴⁰K) ranges from 80.7 to 141.59 μ Sv.y⁻¹ with

average value of 113.19 μ Sv.y⁻¹ which is twice smaller than the worldwide average value of 260 μ Sv.y⁻¹ as recommended by UNSCEAR, 2000. Radionuclide absorption from soil by plants depends on the soil characteristics which include pH content, clay content, soil texture, cation exchange capacity, dominant clay minerals, exchangeable cations, and organic matter content. In addition, the uptake of radionuclides is affected by the plant type and type of radionuclides – the radionuclide is heavy or light element (Konoplev, et al., 1993). Thus, this study revealed that the radiation hazard due to the total internal dose by the intake of ²²⁶Ra, ²³²Th, and ⁴⁰K of the consumption of wheat grains is insignificant. In Fig. 5, the results show that the average ingestion dose due to the intake of ⁴⁰K (91.1 μ Sv.y⁻¹) is more than average ingestion dose for both ²²⁶Ra (11.14 μ Sv.y⁻¹) and ²³²Th (10.95 μ Sv.y⁻¹),

but the results value of average ingestion dose ingestion dose for ^{226}Ra and ^{232}Th is so near together because the half-life for both have patents is very long.

IV. CONCLUSIONS

This research aimed to measure the natural radioactivity levels wheat grain samples from the wheat plantation fields of Koya district, the average of concentration of radionuclides of ^{226}Ra , ^{232}Th , and ^{40}K in the wheat grain samples was found to be lower than the worldwide average values recommended by UNSCEAR, but no detection of ^{137}Cs in the wheat grain samples. The total annual ingestion dose due to the intake of natural radionuclides of ^{226}Ra , ^{232}Th , and ^{40}K by the consumption of wheat grains was equal half of the world average value of $260 \mu\text{Sv.y}^{-1}$ as given by UNSCEAR, therefore, the accumulation of primordial radionuclides in the wheat grains was produced from the wheat plantation fields of Koya district does not have a significant health risk. The obtained results of the this study would be a useful data for making a baseline of artificial and natural radioactivity and heavy metal concentration levels in soils of the studied area. These baseline data will help us to assess any variations in the radioactivity levels due to any unexpected events such as nuclear reactor accidents and/or nuclear weapon tests or due to the anthropogenic activities within the study area.

REFERENCES

- Abojassim, A.A., AL-Alasadi, L.A., Shitake, A.R., AL-Tememie, F.A. and Husain, A.A., 2015. Assessment of annual effective dose for natural radioactivity of gamma emitters in biscuit samples in Iraq. *Journal of Food Protection*, 78(9), pp.1766-1769.
- Akhtar, N. and Tufail, M., 2006. Natural radioactivity intake into wheat grown on fertilized farms in two districts of Pakistan. *Radiation Protection Dosimetry*, 123(1), pp.103-112.
- Alesandra, A.A., Elizebeta, D.S., Radmila, C.N., Hajurlei, M.Z., Biljana, D., Riste, U. and Dean, J., 2017. Evaluation of doses of radiation due to natural radioactivity in wheat as animal feed in the surrounding of the city of Skopje (Macedonia). *IOSR Journal of Pharmacy*, 7(6), pp.20-23.
- AL-Hamzawi, A.A., 2017a. Natural radioactivity measurements in vegetables at Al-Diwaniyah Governorate, Iraq and evaluation of radiological hazard. *Journal of Al-Nahrain University*, 20(4), pp.51-55.
- AL-harbil, A. and EL-Taher, A., 2013. A study on transfer factors of radionuclides from soil to plant. *Life Science Journal*, 10(2), pp.532-539.
- Alshahri, F., 2016. Evaluation of radionuclides contamination in wheat flour and bread using gamma-ray spectrometry. *Life Science Journal*, 13(3), pp.34-42.
- Azeez, H.H., Mansour, H.H. and Ahmad, S.T., 2019. Transfer of natural radioactive nuclides from soil to plant crops. *Applied Radiation and Isotopes*, 147, pp.152-158.
- Brigden, S. and Santill, O., 2002. *Heavy Metal and Radionuclide Contamination of Fertilizer Products and Phosphogypsum Waste Produced by the Lebanese Chemical Company*. Greenpeace Research Laboratories, Department of Biological Sciences, University of Exeter, Exeter EX4 4PS, UK.
- Canbazoglu, C. and Dogru, M., 2013. A preliminary study on ^{226}Ra , ^{232}Th , ^{40}K and ^{137}Cs activity concentrations in vegetables and fruits frequently consumed by inhabitants of Elazığ Region, Turkey. *Journal of Radioanalytical and Nuclear Chemistry*, 295(2), pp.1245-1249.
- Cevik, U., Damla, N. and Nezar, S., 2007. Radiological characterization of Cayrhan coal-fired power plant in Turkey. *Fuel Journal*, 86(16), pp.2509-2513.
- Changizi, V., Shafiei, E. and Zareh, M.R., 2013. Measurement of ^{226}Ra , ^{232}Th , ^{137}Cs and ^{40}K activities of wheat and corn products in ilam province-Iran and resultant annual ingestion radiation dose. *Iranian Journal of Public Health*, 42(8), pp.903-914.
- Chen, S.B., Zhu, Y.G. and Hu, Q.H., 2005. Soil to plant transfer of ^{238}U , ^{226}Ra and ^{232}Th on a uranium mining-impacted soil from Southeastern China. *Journal of Environmental Radioactivity*, 82(2), pp.223-236.
- EL-Taher, A. and Makhluif, S., 2010. Natural radioactivity levels in phosphate fertilizer and its environmental implications in Assuit governorate, Upper Egypt. *Indian Journal of Pure and Applied Physics*, 48, pp.697-702.
- Essiett, A.A., Essien, I.E. and Bede, M.C., 2015. Measurement of surface dose rate of nuclear radiation in coastal areas of Akwa Ibom state Nigeria. *International Journal of Physics*, 3, pp.224-229.
- Harb, S., EL-Kamel, A.H., EL-Mageed, A.I.A., Abbady, A. and Rashed, W., 2014. Radioactivity levels and soil-to-plant transfer factor of natural radionuclides from protectorate area in Aswan, Egypt. *World Journal of Nuclear Science and Technology*, 4, pp.7-15.
- Hosseini, T., Fathivand, A., Abbasisar, F., Karimi, M. and Barati, H., 2006. Assessment of annual effective dose from ^{238}U and ^{226}Ra due to consumption of foodstuffs by inhabitants of Tehran city, Iran. *Radiation Protection Dosimetry*, 121(3), pp.330-332.
- Hussein, Z.A., 2015. Measurement of indoor radon concentration in dwellings of koya using nuclear track detectors. *International Journal of Science and Research*, 4(1), pp.2465-2467.
- Hussein, Z.A., 2015. Measurement of indoor radon concentration in dwellings of Koya using nuclear track detectors. *International Journal of Science and Research*, 4(1), pp.2465-2467.
- Hussein, Z.A., 2019. Assessment of natural radioactivity levels and radiation hazards of soils from Erbil governorate, Iraqi Kurdistan. *ARO-The Scientific Journal of Koya University*, 7(1), pp.34-39.
- Hussein, Z.A., 2019. Assessment of natural radioactivity levels and radiation hazards of soils from Erbil Governorate, Iraqi Kurdistan. *The Scientific Journal of Koya University*, 7(1), pp.34-39.
- IAEA., 1989. *A Guidebook: Measurement of Radionuclides in Food and the Environment*. IAEA, Vienna, Austria.
- Ismail, H.A., Hussein, Z.A. and Yaba, S.P., 2020. Investigation a relation between radioactivity concentrations of 40 Potassium (40K) in tooth and the various ethnic groups and its impacts on the rate of tooth damage. *Environmental Nanotechnology, Monitoring and Management*, 14, p.100385.
- Khan, H.M., Ismail, M., Khan, K. and Akhter, P., 2011. Measurement of radionuclides and gamma-ray dose rate in soil and transfer of radionuclides from soil to vegetation, vegetable of some Northern area of Pakistan using γ -ray spectrometry. *Water, Air and Soil Pollution*, 219, pp.129-142.
- Konoplev, A., Viktorova, N., Virchenko, E., Popov, V., Bulgakov, A. and Desmet, G., 1993. Influence of agricultural countermeasures on the ratio of different chemical forms of radionuclides in soil and soil solution. *Science of the Total Environment*, 137, pp. 147-162.
- Kumar, A., Singhal, R., Preetha, J., Rupali, K., Narayanan, U., Suresh, S., Mishra, M.K. and Ranade, A., 2008. Impact of tropical ecosystem on the migrational behavior of K-40, Cs-137, Th-232 U-238 in perennial plants. *Water, Air, and Soil Pollution*, 192(4), pp.293-302.
- Lindahl, P., Maquet, A., Hult, M., Gasparro, J., Marissens, G. and de Orduna, R.G., 2011. Natural radioactivity in winter wheat from organic and conventional agricultural systems. *Journal of Environmental Radioactivity*, 102(2), pp.163-169.
- Mamont, C.A.K., Gwiazdowski, B., Biernacka, M. and Zak, A., 1982. Radioactivity of building materials in Poland. In: Vohra, G., Pillai, K.C. and Sadavisan, S., Eds. *Natural Radiation Environment*. Halsted Press, New York,

p.551.

Mehra, R., Singh, S., Singh, K. and Sonkawade, R., 2007. ^{226}Ra , ^{232}Th and ^{40}K analysis in soil samples from some areas of Malwa region, Punjab, India using gamma ray spectrometry. *Environmental Monitoring and Assessment*, 134(3), pp.333-342.

Mostajaboddavati, M., Hassanzadeh, S. and Faghihian, H., 2006. Efficiency calibration and measurement of self-absorption correction for environmental gamma-spectroscopy of soil samples using Marinelli beaker. *Journal of Radioanalytical and Nuclear Chemistry*, 268(3), pp.539-544.

Murtadha, S.H.A., Mohamad, S.J. and Salih F.N., 2017. Estimation of annual effective dose due to natural radioactivity in ingestion of vegetables from Cameron Highlands, Malaysia. *Environmental Technology and Innovation*, 8(5), pp.96-102.

Nisar, A., Mohamad, S.J., Muhammad, B. and Muhammad, R., 2015. An overview on measurements of natural radioactivity in Malaysia. *Journal of Radiation Research and Applied Sciences*, 8, pp.136-141.

Pulhani, V.A., Dafauti, S., Hegde, A.G., Sharma, R.M. and Mishra, U.C., 2005. Uptake and distribution of natural radioactivity in wheat plants from soil. *Journal of Environmental Radioactivity*, 79(3), pp.331-346.

Salih, F.N., Zakariya, A.H. and Shalaw, Z.S., 2020. Environmental radioactivity levels in agricultural soil and wheat grains collected from wheat of farming lands of Koya district, Kurdistan region Iraq. *Radiation Protection and Environment*, 24(4), pp.1-11.

Salih, F.N., 2018. Determination of ^{226}Ra , ^{232}Th and ^{40}K in teeth by use of gamma spectroscopy. In: *Isotopes in Environmental and Health Studies*. Taylor and Francis, United Kingdom, pp.1-13.

Servitzoglou, N., Stoulos, S., Katsantonis, D., Papageorgiou, M. and Siountas, A., 2018. Natural radioactivity studies of phosphate fertilizers applied on greek farm soils used for wheat cultivation. *Radiation Protection Dosimetry*, 181(3), pp.190-198.

Taiwo, A.O., Adeyemo, D.J., Sadiq, U. and Bappah, I.A., 2014. Determination of external and internal hazard indices from natural occurring radionuclide around a superphosphate fertilizer factory in Nigeria. *Archives of Applied Science Research*, 6(1), pp.23-27.

Tsukada, H., Hasegawa, H. and Hisamatsu, S., 2002. Distributions of alkali and alkaline earth metals in several agricultural plants. *Radioprotection Colloques*, 37, pp.535-540.

UNSCEAR., 2000. *United Nations Scientific Committee on the Effects of Atomic Radiation Sources, Effects and Risks of Ionizing Radiation*. Report to the General Assembly with Scientific Annexes, United Nations, New York.

Wang, C.J., Lai, S.Y., Wang, J.J. and Lin, Y.M., 1997. Transfer of radionuclides from soil to grass in Northern Taiwan. *Applied Radiation and Isotopes*, 48(2), pp.301-303.

Zakaria, S., AL-Ansari, N., Mustafa, Y., Knutsson, S., Ahmed, P. and Ghafour, B., 2013. Rainwater Harvesting at Koysinjaq (Koya), Kurdistan Region, Iraq. *Journal of Earth Sciences and Geotechnical Engineering*, 3(4), pp.25-46.

Design and Fabrication of a Novel Ultra Compact Microstrip Diplexer Using Interdigital and Spiral Cells

Salah I. Yahya^{1,2}, Abbas Rezaei³

¹Department of Communication and Computer Engineering, Cihan University-Erbil, Erbil, Iraq

²Department of Software Engineering, Faculty of Engineering, Koya University, Koya KOY45, Iraq

³Department of Electrical Engineering, Kermanshah University of Technology, Kermanshah, Iran

Abstract—A dual-band bandpass-bandpass microstrip diplexer with very small size and good performance is designed in this work. The proposed diplexer has a novel structure which is introduced for the 1st time in this paper. In comparison with the previously reported diplexers, it occupies the most compact size of $0.002 \lambda_g^2$ (226.7 mm^2), fabricated on 0.787 mm dielectric substrate height. The resonance frequencies of the presented diplexer are located at 0.76 GHz and 1.79 GHz making it suitable for the global system for mobile communications applications. It has a wide flat channels with two fractional bandwidths (FBWs) of 41.1% and 50%. Another feature of the proposed diplexer is its ability to suppress the harmonics. It can attenuate the 1st–7th harmonics. Moreover, it has low insertion losses and low group delays at both channels, whereas the isolation and return losses are acceptable. Finally, the proposed diplexer is fabricated and measured to verify the simulation results, where a good agreement between the simulation and measurement results is obtained.

Index Terms—Compact size, Diplexer, Low loss, Microstrip, Harmonics, Group delay.

I. INTRODUCTION

Dual-band microstrip diplexers are three-port passive components. They can be used for separating desired radiofrequency (RF) signals and delivering them through two channels (Yahya, Rezaei and Noori, 2020). The structure, performance, and designing method of several microstrip dual-band bandpass-bandpass diplexers have been reviewed in Yahya, Rezaei and Noori, 2020. Several types of microstrip structures have been utilized to design of dual-band bandpass-bandpass diplexers for modern

communication systems (Guan, Yang, Liu and Zhu, 2014; Bukuru and Song, 2015; Chen, Zhu, Bu and Cheng, 2015; Peng and Chiang, 2015; Xiao, Zhu, Li, Tian and Ma, et al., 2015; Huang, Wang, Zhu and Wu, 2016; Jun-Mei, Zhou and Cao, 2016; Salehi, Keyvan, Abiri and Noori, 2016; Bui, Vuong, Allard, Verdier and Benech, 2017; Feng, Zhang and Che, 2017; Noori and Rezaei, 2017a; Noori and Rezaei, 2017b; Rezaei, Noori and Mohamadi, 2017; Rezaei and Noori, 2018a; Rezaei and Noori, 2018b; Rezaei and Noori, 2018c; Danaeian, 2019; Kumar and Upadhyay, 2019; Rezaei, Yahya and Jamaluddin, 2019; Rezaei and Mohammadi, 2019; Rezaei, Noori and Mohammadi, 2019; Yahya, Rezaei and Noori, 2020; Yahya, Rezaei and Nouri, 2020; Rezaei, Yahya and Jamaluddin, 2020). However, occupying very large implementation areas are the common disadvantage of these diplexers. On the other hand, all of these diplexers have narrow channels, which make some of them suitable for only narrowband applications. Another common disadvantage of the above reported diplexers is their undesired harmonics. The coupling structures have been used in majority of these diplexers. Coupled meandrous cells in Rezaei, Yahya, Noori, and Jamaluddin, 2019a, coupled open-loop in Xiao, Zhu, Li, Tian and Ma, 2015, coupled step impedance and low impedance sections in Noori and Rezaei, 2017a, coupled spirals in Bukuru and Song, 2015, and coupled E-shape cells in Guan, Yang, Liu and Zhu, 2014 have been utilized. Similar to Rezaei, Yahya, Noori, and Jamaluddin, 2019a, the coupled meandrous cell has been used in Rezaei, Noori and Mohammadi, 2017. The proposed diplexers in Rezaei, Yahya, Noori, and Jamaluddin, 2019a; Xiao, Zhu, Li, Tian and Ma, 2015; Noori and Rezaei, 2017; Bukuru and Song, 2015; Guan, Yang, Liu and Zhu, 2014; Rezaei, Noori and Mohamadi, 2017, could not attenuate harmonics, where for the best case, they could only suppress the 3rd harmonic. The other problems of the previous diplexers are poor selectivity in Rezaei, Yahya, Noori, and Jamaluddin, 2019a, high insertion losses in Xiao, Zhu, Li, Tian and Ma, 2015; Noori and Rezaei, 2017; Bukuru and Song, 2015; Guan, Yang, Liu and

ARO-The Scientific Journal of Koya University
Vol. IX, No.1 (2021), Article ID: ARO.10819, 06 pages
DOI:10.14500/aro.10819

Received 20 April 2021; Accepted: 22 June 2021

Regular research paper: Published: 30 June 2021

Corresponding author's e-mail: salah.ismael@koyauniversity.org

Copyright © 2021 Salah I. Yahya and Abbas Rezaei. This is an open-access article distributed under the Creative Commons Attribution License.



Zhu, 2014, undesired isolation between channels in Noori and Rezaei, 2017, and non-flat channels in Rezaei, Noori and Mohamadi, 2017. Despite this fact that the passband flatness and group delay are two important factors for filters and diplexers, majority of the previously reported diplexers did not pay attention to these problems. Meanwhile, there is some information about the flatness in Noori and Rezaei, 2017, which show that it has two non-flat channels with high group delays. In Noori and Rezaei, 2017b, an approximated equivalent LC circuit of coupled lines has been analyzed to design of a microstrip diplexer for wireless applications. This diplexer has poor frequency selectivity at the upper channel. The interdigital cells in Bui, Vuong, Allard, Verdier and Benech, 2017, coupled triangular open-loop resonators in Salehi, Keyvan, Abiri and Noori, 2016, and engraved semi-patch cells in Rezaei and Noori, 2018a have been used to obtain three microstrip diplexers with low insertion losses for RF energy harvesting. Meanwhile, the introduced diplexer in Salehi, Keyvan, Abiri and Noori, 2016, could suppress harmonics from 1st up to 4th harmonics. In Chen, Zhu, Bu and Cheng, 2015, slot line-loaded microstrip ring resonator, in Rezaei and Noori, 2018b, the spiral and engraved cells, in Rezaei, Noori and Mohammadi, 2019, coupled meandrous structure, similar to Rezaei, Yahya and Jamaluddin, 2019; Rezaei, Noori and Mohammedi, 2017, and in Huang, Wang, Zhu and Wu, 2016, coupled stub-loaded U-shape cell have been used. The reported diplexer in Chen, Zhu, Bu and Cheng, 2015, has high insertion loss problem where the passbands in Rezaei and Noori, 2018b, are very narrow. The achievements of the proposed diplexer in Rezaei, Yahya, Noori and Jamaluddin, 2019b, are low insertion losses at both channels and relatively wider fractional bandwidths (FBWs), whereas it is designed based on coupled step impedance cells. A diplexer using microstrip half- and quarter-wavelength resonators has been proposed in Jun-Mei, Zhou and Cao, 2016. In Peng and Chiang, 2015, new types of dual-mode ring filters have been used to design of two diplexers. These two diplexers have very high insertion losses at their channels. A novel diplexer based on a new form of coupled triangular microstrip structure has been proposed in Rezaei and Noori, 2018c, for L-band applications. This diplexer has low loss, narrow channels, and 3rd attenuated harmonic. In Feng, Zhang and Che, 2017, the folded open-loop ring resonators have been utilized to obtain a microstrip diplexer with high isolation. In Yahya, Rezaei and Nouri, 2020, an artificial neural network (ANN) has been used to design of a compact microstrip diplexer. In Roshani and Roshani, 2019, a compact and sharp diplexer with bended lines has been introduced for the global system for mobile communications and long-term evolution (LTE) applications. In Kumar and Upadhyay, 2019, a via-free composite right/left-handed transmission line-based diplexer has been introduced for WiMAX and WLAN applications. In Xu, Yu and Chen, 2021, a tunable microstrip diplexer with multiple transmission zeroes has been presented using common element-loaded uniform impedance resonator (UIR). In Chen, et al., 2021, a novel circuit model has been presented to design of microstrip multifunction integrated

diplexers with frequency selection, frequency division, and power division functions.

This work presents the design of a microstrip diplexer, which has the most compact size, the widest FBWs, low insertion losses, and the best stopband rejection, whereas the other diplexer parameters are acceptable. The proposed diplexer has a novel microstrip structure, which is presented for the 1st time in this work. It is composed of the interdigital and spiral cells.

II. DESIGN AND ANALYSIS

To create a passband channel, we used the spiral and interdigital cells with the inductance and capacitance features, respectively. The advantage of using the spiral cells is saving the size significantly. Meanwhile, by optimizing the structure, the interdigital cell can be used as a compact capacitor. Accordingly, we proposed a microstrip resonator as depicted in Fig. 1a. It includes two spiral cells with different dimensions, which are integrated by an interdigital structure. Thus, this structure can create a passband channel. Fig. 1b shows an approximated equivalent LC circuit of the proposed resonator, where L_1 and L_2 are related to the spiral cells 1 and 2, respectively. As mentioned above, the middle interdigital cell is a capacitor which is shown by C . By removing the insignificant inductors and capacitors related to the bent and steps in widths, our LC circuit can be simplified.

The ABCD matrix of the proposed resonator is calculated as follows:

$$T = \begin{bmatrix} A & B \\ C & D \end{bmatrix} = \begin{bmatrix} 1 & j\omega(L_1 + L_2) + \frac{1}{j\omega C} \\ 0 & 1 \end{bmatrix} \quad (1)$$

where, ω is an angular frequency. As presented in the following equation, the reflection coefficient can be obtained:

$$\begin{aligned} \Gamma &= \frac{A+B-C-D}{A+B+C+D} = \frac{j\omega(L_1 + L_2) + \frac{1}{j\omega C}}{2 + j\omega(L_1 + L_2) + \frac{1}{j\omega C}} \\ &= \frac{1 - \omega^2 C(L_1 + L_2)}{2j\omega C - \omega^2 C(L_1 + L_2) + 1} \end{aligned} \quad (2)$$

For $\Gamma = 0$, we can obtain a perfect matching.

$$\Gamma = 0 \Rightarrow \omega_m = \frac{1}{\sqrt{C(L_1 + L_2)}} \quad (3)$$

Where, ω_m is the angular frequency with perfect matching. On the other hand, we can calculate the input impedance (Z_{in}) from its equivalent LC circuit of the proposed resonator:

$$Z_{in} = (L_1 + L_2)j\omega + \frac{1}{j\omega C} \quad (4)$$

The resonance frequency can be obtained from (4) by setting $Z_{in} = 0$. Therefore, the angular resonance frequency (ω_r) is:

$$\omega_r = \frac{1}{\sqrt{C(L_1 + L_2)}} \quad (5)$$

It is clear that $\omega_r = \omega_m$ which proves we have a perfect matching at the resonance frequency. Consequently, our resonator has a low loss inherently. To miniaturize the resonator size, we can optimize its dimensions by changing the widths of microstrip lines. Since we have only a resonance frequency, our resonator is a single mode without harmonics. We can see harmonics in the frequency response of the resonators with several resonance frequencies. Some of the calculated resonance frequencies may represent

unwanted harmonics (Salehi and Noori, 2015), therefore, our resonator is able to suppress the harmonics inherently. By knowing this information about resonator behavior, we can optimize the dimensions and find the physical dimensions of our proposed structures. Based on the proposed resonator, two bandpass filters (BPFs) are designed and presented in Fig. 2a and b, which we named them BPF1 and BPF2, respectively. The dimensions of both BPFs are in mm. As depicted in Fig. 2a and b, the spiral and interdigital structures are used similar to the designed resonator. The proposed filters are simulated by ADS software on a RT/duroid 5880 substrate with $\epsilon_r=2.2$, $h=31$ mil, and 0.0009 loss tangent. The frequency responses of BPF1 and BPF2 are shown in Fig. 2c and d, respectively. As shown in these figures, BPF1 creates a channel from 590 MHz to 900 MHz with an operational frequency at $f_{o1}=740$ MHz. It attenuates the harmonics up to $3.37 f_{o1}$ (2.5 GHz), whereas the maximum harmonic level is 20 dB. Moreover, it has 0.1 dB low insertion loss. The frequency response of BPF2 shows that it operates at $f_{o2} = 1.85$ GHz with 0.049 dB insertion loss and 22.5 dB return loss. This very low insertion loss verifies the perfect matching at the resonance frequency. The -3 dB cutoff frequencies of BPF2 are 1.41 GHz and 2.3 GHz so that it has a wide flat channel. Using BPF1 and BPF2, we designed a compact microstrip diplexer. The layout configuration of the proposed diplexer is shown in Fig. 3. The proposed diplexer is formed by integrating BPF1 and BPF2 so that the other dimensions are exactly similar to Fig. 2a and b.

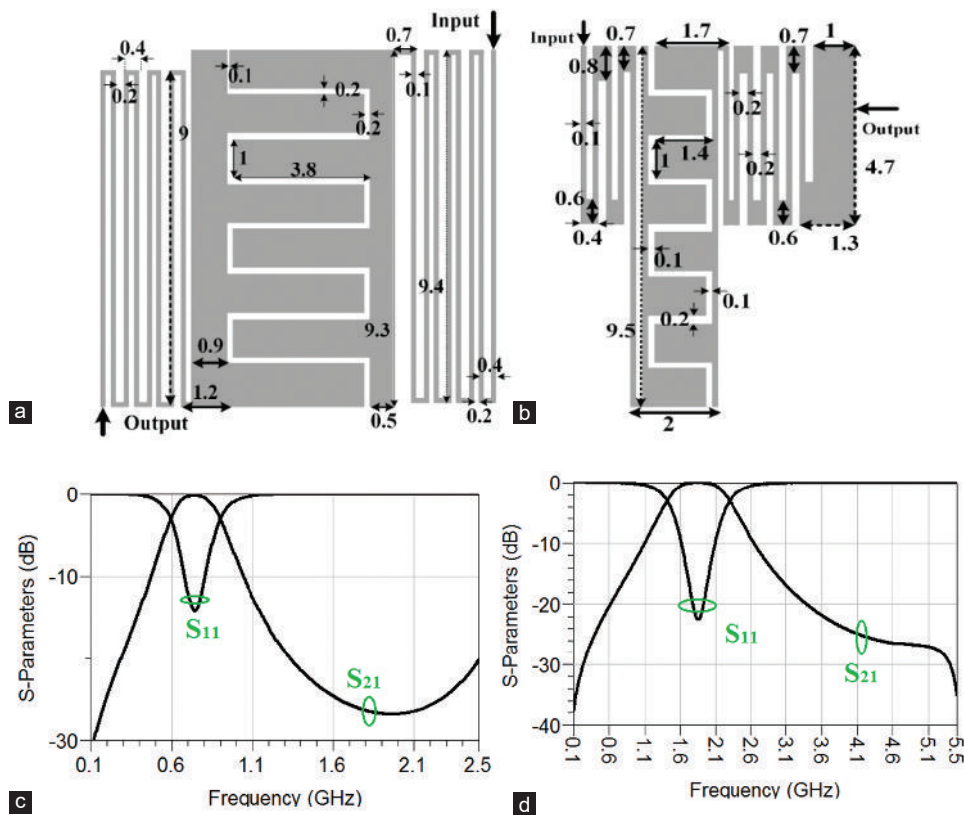
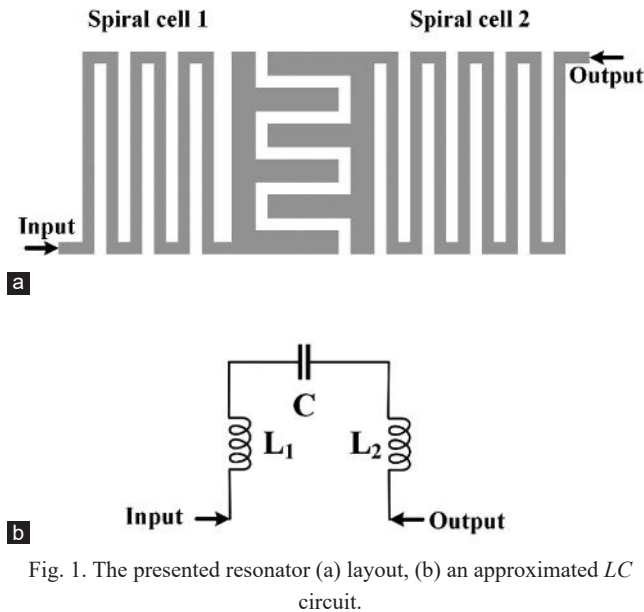


Fig. 2. (a) BPF1, (b) BPF2, (c) frequency response of BPF1, (d) frequency response of BPF2.

III. RESULTS, DISCUSSION, AND COMPARISON

The designed diplexer is simulated by the full-wave EM simulator of Advanced Design System (ADS) software. It is designed, simulated, and fabricated on a RT/Duroid 5880 substrate with $\epsilon_r=2.2$, $h=31$ mil, and 0.0009 loss tangent. The fabricated structure is measured by Agilent network analyzer N5230A. The simulated and measured S_{21} and S_{31} of the proposed diplexer are depicted in Fig. 4a, whereas Fig. 4b shows the simulated and measured common port return loss and isolation between the channels. The first channel is from 615 MHz to 925 MHz with 41.1% FBW%. The resonance frequency of this channel is located at $f_{r1} = 755$ MHz, where it has 0.169 dB and 15.7 dB simulated insertion and return losses, respectively. The resonance frequency of the upper channel is $f_{r2} = 1.79$ GHz, whereas it has two -3 dB cutoff frequencies at 1.4 GHz and 2.3 GHz. Similar to the lower channel, the upper channel is wide and flat with 50% FBW%.

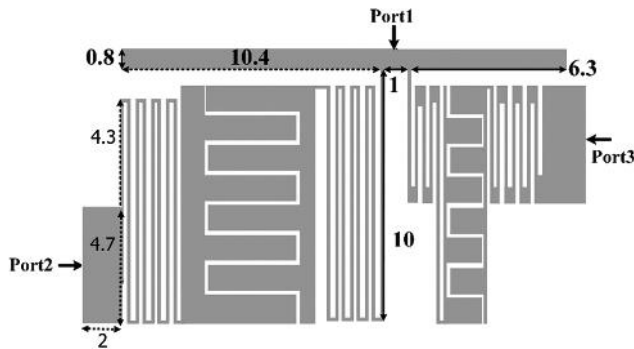


Fig. 3. The proposed diplexer layout.

The simulated insertion and return losses of this channel are better than 0.08 dB and 24.8 dB, respectively. Due to the copper and junction losses in the fabricated diplexer, the measured losses are a little higher than the simulation results. As presented in Fig. 4a, the harmonics are attenuated up to 5.5 GHz ($7.28 f_{r1}$). It means that the proposed diplexer can suppress 1st up to 7th harmonics with the maximum harmonic level 14.92 dB. The isolation between the channels is better than 19.98 dB from DC to 5.5 GHz, which is an acceptable value. The overall size of our compact diplexer is only $10.9 \text{ mm} \times 20.8 \text{ mm}$ ($0.002 \lambda_g^2$), where λ_g is the guided wavelength calculated at the first resonance frequency. Due to having SubMiniature Version A connectors and junction losses, the measured losses are a little higher than the simulated losses. A photograph of the fabricated diplexer is presented in Fig. 4b. To show the features of this work, we compared it with the previously reported diplexers. The comparison results are presented in Table I, where f_r , IL, and FBW are the resonance frequency, insertion loss, and FBWs, respectively. Furthermore, the indexes 1 and 2 are related to the 1st and 2nd channels, respectively. As shown in the comparison table, our diplexer is the most compact diplexer and it is very smaller than the other previously reported diplexers. Moreover, it has the widest FBWs, low simulated insertion losses at both channels, and the best harmonic attenuation.

Fig. 5a and b shows the group delays of the lower and upper channels, respectively. As depicted in Fig. 5, the group delays at the first and second channels are lower than 1.73 ns and 0.79 ns, respectively. Despite the importance of

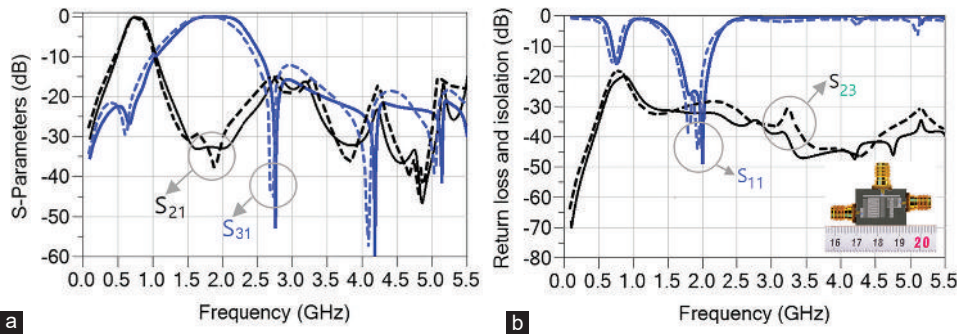


Fig. 4. (a) Simulated (solid line) and measured (dotted line) S_{21} and S_{31} , (b) simulated and measured common port return loss and isolation between the channels and the fabricated diplexer.

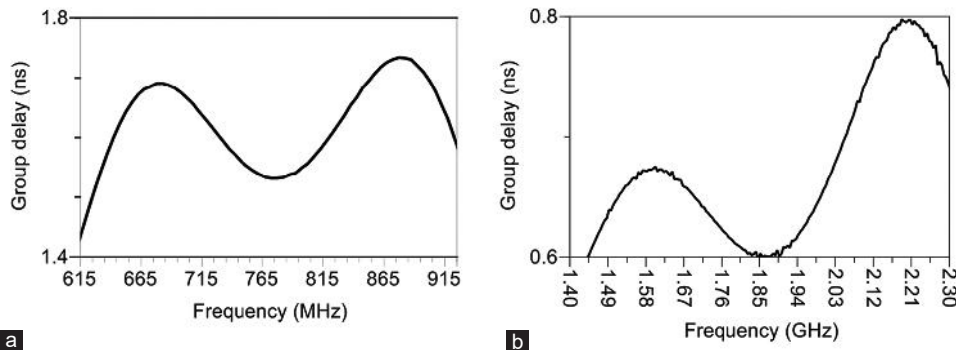


Fig. 5. Group delays at the (a) first channel, (b) second channel.

TABLE I
COMPARISON BETWEEN THIS DIPLEXER AND THE PREVIOUSLY REPORTED DIPLEXERS

Reference	IL ₁ , IL ₂ (dB)	f _{r1} , f _{r2} (GHz)	FBW ₁ , FBW ₂	Size (λg ²)	N th attenuated harmonic	LFWH (GHz)
Our diplexer	0.17, 0.08	0.76, 1.79	41.1%, 50%	0.002	7 th (7.2 f _{r1})	5.5
Rezaei, Yahya and Jamaluddin, 2020	0.17, 0.30	19, 21	12.5%, 4.2%	0.026	---	---
Yahya, Rezaei and Nouri, 2020	0.06, 0.07	28.6, 20	47%, 45%	0.004	---	---
Danaeian, 2019	1.65, 1.75	13, 30	---	0.029	---	---
Roshani and Roshani, 2019	0.9, 2.6	19.6, 22	---	0.017	---	---
Rezaei, Yahya, Noori, and Jamaluddin, 2019a	0.25, 0.26	2.1, 3.9	---	0.038	2 nd (2.1 f _{r1})	4.5
Rezaei, Yahya, Noori, and Jamaluddin, 2019b	0.10, 0.16	1.6, 2.1	16.8%, 11%	0.054	2 nd (2.2 f _{r1})	3.5
Rezaei, Noori and Mohammadi, 2019	0.36, 0.44	2.88, 3.29	---	0.028	1 st (1.8 f _{r1})	5
Kumar and Upadhyay, 2019	0.87, 1.25	17, 15.5	21.2%, 13.2%	0.12	---	---
Rezaei and Noori, 2018a	0.14, 0.16	1.8, 2.4	11%, 7.1%	0.022	3 rd (3.6 f _{r1})	6.5
Rezaei and Noori, 2018c	0.28, 0.29	0.8, 0.9	3.2%, 3.2%	0.01	2 nd (2.7 f _{r1})	2.2
Rezaei and Noori, 2018b	0.21, 0.21	1, 1.3	4.6%, 4.6%	0.018	3 rd (3.3 f _{r1})	3.3
Bui, Vuong, Allard, Verdier and Benech, 2017	0.4, 0.4	1.8, 2.45	---	0.095	1 st (1.6 f _{r1})	3
Feng, Zhang and Che, 2017	1.4, 3.4	1.05, 1.87	6.1%, 4%	0.089	3 rd (3.8 f _{r1})	4
Noori and Rezaei, 2017a	0.6, 0.9	2.6, 6	---	0.076*	2 nd (2.7 f _{r1})	7*
Noori and Rezaei, 2017b	0.2, 0.4	2.3, 4	---	0.09*	3 rd (3.4 f _{r1})	8
Rezaei, Noori and Mohammedi, 2017	0.18, 0.39	2.4, 2.7	---	0.075	2 nd (2.5 f _{r1})	6
Huang, Wang, Zhu and Wu, 2016	1, 0.9	2.3, 2.7	6.1%, 5.8%	0.127	1 st (1.7 f _{r1})	4
Jun-Mei, Zhou and Cao, 2016	2.2, 2.1	1.8, 2.4	2.8%, 1.9%	0.064	2 nd (2.8 f _{r1})	5
Salehi, Keyvan, Abiri and Noori, 2016	0.5, 0.4	2.3, 2.5	3.6%, 3.4%	0.088*	4 th (4.3 f _{r1})	10
Bukuru and Song, 2015	1.35, 1.31	3.6, 5.2	8.2%, 7.6%	0.05	3 rd (3.6 f _{r1})	13*
Chen, Zhu, Bu and Cheng, 2015	1.83, 1.52	1.1, 1.3	8%, 9.2%	0.705	1 st (1.4 f _{r1})	1.6
Peng and Chiang, 2015	2.1, 2.1	1.7, 1.8	5%, 5%	0.07	1 st (1.4 f _{r1})	2.4
Xiao, Zhu, Li, Tian and Ma, 2015	1.43, 1.59	2.4, 3.5	---	0.282	2 nd (2.1 f _{r1})	5
Guan, Yang, Liu and Zhu, 2014	1.2, 1.5	1.9, 2.1	3.5%, 3.2%	0.136	1 st (1.3 f _{r1})	2.5

LFWH: Last frequency without harmonics; *: Approximated values

TABLE II
THE MAXIMUM GROUP DELAYS COMPARISON

References	Maximum group delay at first channel	Maximum group delay at the second channel
This work	1.73 ns	0.79 ns
Rezei, et al., 2019a	4 ns	1.8 ns*
Noori and Rezaei, 2017a	3.15 ns	2.98 ns
Rezaei and Noori, 2018a	3 ns	3.14 ns
Rezaei, Yahya, Noori, and Jamaluddin, 2019b	2.2 ns	2.6 ns
Rezaei and Noori, 2018b	4.5 ns	4.25 ns

*: Approximated value

group delay, it is not included in many reported diplexers. However, some of the previous works mentioned the group delay that we compared them with our work in Table II. As depicted in Table II, the lowest group delays at both channels are obtained in this work.

IV. CONCLUSION

This paper presents a novel microstrip resonator with several features for the 1st time in this work. The proposed microstrip resonator includes a step impedance interdigital cell connected to the spiral structures. We used the presented resonator to design of two compact BPFs. By integrating the proposed BPFs using a simple matching circuit, a high-performance microstrip diplexer was presented. This diplexer has the most compact size in comparison with the previous works. It has two flat channels with the lowest group delays

better than 1.73 ns. Furthermore, our diplexer has the widest FBW and the best harmonic suppression.

REFERENCES

Bui, D.H.N., Vuong T.P., Allard B., Verdier J. and Benech P., 2017. Compact low-loss microstrip diplexer for RF energy harvesting. *Electronics Letters*, 53(8), pp.552-554.

Bukuru, D. and Song, K., 2015. Compact wide-stopband planar diplexer based on rectangular dual spiral resonator. *Microwave and Optical Technology Letters*, 57(1), pp.174-178.

Chen, C.F., Zhou, K.W., Chen, R.Y., Tseng, H.Y., He, Y.H., Li, W.J. and Weng, J.H., 2021. Design of Microstrip multifunction integrated diplexers with frequency division, frequency selection, and power division functions. *IEEE Access*, 9, pp.53232-53242.

Chen, D., Zhu, L., Bu, H. and Cheng, C.H., 2015. A novel planar diplexer using slot line-loaded microstrip ring resonator. *IEEE Microwave and Wireless Components Letters*, 25(11), pp.706-708.

Danaeian, M., 2019. Miniaturized half-mode substrate integrated waveguide diplexer based on SIR-CSRR unit-cell. *Analog Integrated Circuits and Signal Processing*, 102, pp.555-561.

Feng, W., Zhang, Y. and Che, W., 2017. Tunable dual-band filter and diplexer based on folded open loop ring resonators. *IEEE Transactions on Circuits and Systems*, 64(9), pp.1047-1051.

Guan, X., Yang, F., Liu, H. and Zhu, L., 2014. Compact and high-isolation diplexer using dual-mode stub-loaded resonators. *IEEE Microwave and Wireless Components Letters*, 24(6), pp.385-387.

Huang, F., Wang, J., Zhu, L. and Wu, W., 2016. Compact microstrip balun diplexer using stub-loaded dual-mode resonators. *IET Electronic Letters*, 52, pp.1994-1996.

- Jun-Mei, Y., Zhou, H.Y. and Cao, L.Z., 2016. Compact diplexer using microstrip half- and quarter wavelength resonators. *Electronics Letters*, 52(19), pp.1613-1615.
- Kumar, A. and Upadhyay, D., 2019. A compact planar diplexer based on via-free CRLH TL for WiMAX and WLAN applications. *International Journal of Microwave and Wireless Technologies*, 11, pp.130-138.
- Noori, L. and Rezaei A., 2017a. Design of a microstrip dual-frequency diplexer using microstrip cells analysis and coupled lines components. *International Journal of Microwave and Wireless Technologies*, 9(7), pp.1467-1471.
- Noori, L. and Rezaei, A., 2017b. Design of a microstrip diplexer with a novel structure for WiMAX and wireless applications. *AEU-International Journal of Electronics and Communications*, 77, pp.18-22.
- Peng, H. and Chiang, Y., 2014. Microstrip diplexer constructed with new types of dual-mode ring filters. *IEEE Microwave and Wireless Components Letters*, 25(1), pp.7-9.
- Rezaei, A. and Noori, L., 2018a. Compact low-loss microstrip diplexer using novel engraved semi-patch cells for GSM and WLAN applications. *AEU-International Journal of Electronics and Communications*, 87, pp.158-163.
- Rezaei, A. and Noori, L., 2018b. Miniaturized microstrip diplexer with high performance using a novel structure for wireless L-band applications. *Wireless Networks*, 26, pp.1795-1802.
- Rezaei, A. and Noori, L., 2018c. Novel compact microstrip diplexer for GSM applications. *International Journal of Microwave and Wireless Technologies*, 10(3), pp.313-317.
- Rezaei, A., Noori, L. and Mohamadi, H., 2017. Design of a novel compact microstrip diplexer with low insertion loss. *Microwave and Optical Technology Letters*, 59(7), pp.1672-1676.
- Rezaei, A., Noori, L. and Mohammadi, H., 2019. Design of a miniaturized microstrip diplexer using coupled lines and spiral structures for wireless and WiMAX applications. *Analog Integrated Circuits and Signal Processing*, 98, pp.409-415.
- Rezaei, A., Yahya S.I., Noori, L. and Jamaluddin, M.H., 2019a. Design and fabrication of a novel compact low-loss microstrip diplexer for WCDMA and WiMAX applications. *Journal of Microwaves, Optoelectronics and Electromagnetic Applications*, 18(4), pp.482-491.
- Rezaei, A., Yahya, S.I. and Jamaluddin M.H., 2020. A novel microstrip diplexer with compact size and high isolation for GSM applications. *AEU-International Journal of Electronics and Communications*, 114, p.153018.
- Rezaei, A., Yahya, S.I., Noori L. and Jamaluddin, M.H., 2019b. Design of a novel wideband microstrip diplexer using artificial neural network. *Analog Integrated Circuits and Signal Processing*, 101(1), pp.57-66.
- Roshani, S. and Roshani S., 2019. Design of a very compact and sharp bandpass diplexer with bended lines for GSM and LTE applications. *AEU-International Journal of Electronics and Communications*, 99, pp.354-360.
- Salehi, M and Noori, L., 2015. Miniaturized microstrip bandpass filters using novel stub loaded resonator. *ACES Journal*, 30(6), pp.692-697.
- Salehi, M.R., Keyvan, S., Abiri E. and Noori L., 2016. Compact microstrip diplexer using new design of triangular open loop resonator for 4G wireless communication systems, *AEU-International Journal of Electronics and Communications*, 70(7), pp.961-969.
- Xiao, J. K., Zhu M., Li Y., Tian L. and Ma J.G., 2015. High selective microstrip bandpass filter and diplexer with mixed electromagnetic coupling, *IEEE Microwave and Wireless Components Letters*, 25(12), pp.781-783.
- Xu L., Yu W. and Chen J.X., 2021. Unbalanced-/balanced-to-unbalanced diplexer based on dual-mode dielectric resonator. *Access IEEE*, 9, pp.53326-53332.
- Yahya, S.I., Rezaei, A. and Noori, L., 2020. Design and performance of microstrip diplexers: A review. *ARO-The Scientific Journal Koya University*, 8(1), pp.38-49.
- Yahya, S.I., Rezaei, A. and Nouri, L., 2020. The use of artificial neural network to design and fabricate one of the most compact microstrip diplexers for broadband L-band and S-band wireless applications. *Wireless Networks*, 27, pp.663-676.

Chemical Characterization and Antidiabetic Activity of Essential Oils from *Pelargonium graveolens* Leaves

Javed Ahamad¹ and Subasini Uthirapathy²

¹Department of Pharmacognosy, Faculty of Pharmacy, Tishk International University, Kurdistan Region, Erbil, Iraq

²Department of Pharmacology, Faculty of Pharmacy, Tishk International University, Kurdistan Region, Erbil, Iraq

Abstract—*Pelargonium graveolens* (Geranium) is a source of finest quality of fragrance and its essential oils (EOs) are used as antibacterial and antifungal agent. The aim of the current research is to determine chemical constituents in EO of *P. graveolens* by gas chromatography–mass spectrometry (GC–MS) and evaluate its antidiabetic activity through α -glucosidase inhibition assay. The chemical composition of *P. graveolens* EO was determined by GC/MS and its antidiabetic activity was assessed through inhibition of α -glucosidase enzyme in *in vitro* models. GC–MS analysis determines 36 chemical components in the EO of *P. graveolens* leaves, and citronellyl isovalerate (10.41%), menthol (9.61%), linalool (8.63%), *p*-menthone (6.31%), and geranyl tiglate (4.99%) were recorded as major constituents. The EO of *P. graveolens* leaves showed concentration-dependent inhibition of α -glucosidase enzyme ranging from 28.13 ± 1.41 to $74.24 \pm 2.53\%$ for concentration ranging from 31.25 to 1000 $\mu\text{g/mL}$, respectively. The IC_{50} values for of *P. graveolens* and acarbose were found as 93.72 ± 4.76 and 80.4 ± 2.17 $\mu\text{g/mL}$, respectively, against the α -glucosidase enzyme. The study finding explores the chemical components of *P. graveolens* growing in Iraqi Kurdistan region and scientifically supported its possible use in diabetic patients for controlling postprandial hyperglycemia.

Index Terms—*Pelargonium graveolens*, Geranium, Geraniaceae, Diabetes, Gas chromatography–mass spectrometry, α -Glucosidase enzyme.

I. INTRODUCTION

Medicinal plants have emerged as major source drugs for the treatment of chronic diseases such as cancer, diabetes, and cardiovascular complications. Natural products derived from medicinal plants are considered safe and effective compared

to synthetic modern drugs based on the long history of use by humans as food and medicine (Ahmad, et al., 2019). Diabetes is a chronic disorder of metabolism caused by an absolute or relative lack of insulin and characterized by hyperglycemia, glycosuria, and hyperlipidemia (Gin and Rigalleau, 2000). The number of people in the world with diabetes has increased dramatically over recent years. Postprandial hyperglycemia (PPHG) is one of the key risk factors associated with diabetes. PPHG results due to the fast uptake of glucose in the intestine under the influence of hydrolyzing enzymes α -amylase and α -glucosidase that change polysaccharides through oligosaccharides to monosaccharides (Subramanian, Asmawi and Sadikun, 2008). Inhibition of α -amylase and α -glucosidase enzymes leads to a reduction in their hydrolysis and thereby controlled blood glucose levels (Dong, Li, Zhu, Liu and Huang, 2012). Therefore, an important strategy for managing PPHG is to inhibit α -amylase and α -glucosidase enzymes (Scheen, 2003). The α -amylase and α -glucosidase enzyme inhibitors as therapeutic agents are being increasingly pursued. These enzymes are preferred targets for the management of PPHG particularly in pre-diabetics or those with impaired glucose tolerance (Ahmad, Naquvi, Mir and Ali, 2011). Natural products as α -amylase and α -glucosidase inhibitors have attracted considerable interest in the drug discovery endeavors (Ahmad, Hasan, Amin and Mir, et al., 2016; Ahmad, Alkefai, Amin and Mir, 2020; Alkefai, Ahmad, Amin and Mir, et al., 2018; Alkefai, Ahmad, Amin and Mir, 2018). The clinically used inhibitors of carbohydrate metabolizing enzymes such as acarbose, voglibose, and miglitol are non-specific in their action. This results in side effects such as flatulence and distension caused due to bacterial fermentation of undigested carbohydrates. Thus, the search for selective inhibitors of these enzymes is still on and more and more medicinal plants are being screened continuously. Screening of traditionally used plants for the drug discovery process is often advocated as the chances of success using this approach are more (Fabricant and Farnsworth, 2001).

Pelargonium genus belonging to the family Geraniaceae and contains about 250 species (such as *Pelargonium*

ARO-The Scientific Journal of Koya University
Volume. IX, No.1 (2021), Article ID: ARO.10791, 5 pages
DOI:10.14500/aro.10791

Received: 24 February 2021; Accepted: 22 June 2021

Regular research paper: Published: 30 June 2021

Corresponding author's e-mail: javed.ahamad@tiu.edu.iq

Copyright © 2021 Javed Ahamad, Subasini Uthirapathy. This is an open-access article distributed under the Creative Commons Attribution License.



graveolens, *Pelargonium capitatum*, *Pelargonium zonale*, *Pelargonium roseum*, and *Pelargonium odoratissimum*). *Pelargonium* is distributed throughout Mediterranean region but most profoundly present in South Africa (Miller, 2002). *P. graveolens* is a source of high-quality essential oil (EO) that is rich in citronellol and geraniol. *P. graveolens* EO is commonly known as geranium oil and is extensively used as perfumes and in skin care products. *P. graveolens* EO is also used in aromatherapy, and pharmacologically, it acts as antibacterial, antifungal, insect repellent, and has skin cleansing properties (Pattnaik, Subramanyam and Kole, 1996; Pattnaik, Subramanyam, Bapaji and Kole, 1997; Rao Rajeswara, Kaul, Mallavarapu and Ramesh, 1996; Lis-Balchin, Buchbauer, Ribisch and Wenger, 1998; Lis-Balchin, Steyrl and Krenn, 2003). In the present research work, an attempt has been made to determine the chemical composition of EO from leaves of *P. graveolens* by gas chromatography–mass spectrometry (GC–MS). The present study was also designed to evaluate its antidiabetic activity through inhibition of α -glucosidase enzyme.

II. MATERIALS AND METHODS

A. Plant Materials and Chemicals

The fresh leaves of *P. graveolens* (500 g) were collected in the month of March 2020 from local market of Erbil, Kurdistan Region, Iraq. The authenticity of all the accession was ascertained by Taxonomist. The plant sample was kept in the Faculty of Pharmacy, Tishk International University, Erbil, Iraq. For future reference (voucher number: PRL/2020/07), *p*-Nitrophenyl- α -D-glucopyranoside (PNPG), 3,5-dinitrosalicylic acid (DNS), acarbose, and α -glucosidase enzyme were brought from Subra Scientific Company, Chennai, India. All other solvents and chemicals used in the study were of analytical grade.

B. Isolation of EO from Leaves of *P. graveolens*

The fresh *P. graveolens* leaves (500 g) were hydrodistilled for 6 h in Clevenger apparatus. After isolation of EO, the volatile oil was collected in the graduated tube and dried over anhydrous sodium sulfate and stored at 4°C in a refrigerator for further use.

C. GC–MS Analysis and Identification of Chemical Constituents

The chemical composition of *P. graveolens* EO was determined by the GC–MS method. Agilent Bench Top GC–MS (Agilent Technologies, Wilmington, DE, USA) equipment with a capillary column of DB-5 glass (specifications 30 m \times 2.5 mm i.d.; film thickness of 0.25 μ m) was applied for test sample analysis. Helium was used as carrier gas at flow rate of 1 mL/min. The oven temperature was set at 50°C for 1 min and then holds isothermally for 2 min at 320°C. The temperature of injector port was maintained at 250°C, and ion source temperature was kept at 200°C, and interface temperature was maintained at

300°C. The EO (1 μ L) was injected and the split ratio was kept at 1:5. Data capture took place at 70 eV using scanning times of 1.5 s in the mass range of 50–1000 amu and run time was kept up to 38 min. The chromatography and mass spectra were handled with ChemStation software (Agilent Technologies, Wilmington, DE, USA).

The individual peaks/constituents were identified by comparison of their Kovats index (K.I.) with those of literature in close agreement to K.I. Further identification of EO constituents was made by comparison of the fragmentation pattern of mass spectra obtained by GC/MS analysis with those stored in the spectrometer database of NIST, NBS 54 K.L, WILEY8 libraries, and published literature (Adams, 2007; Ali, 2001; Rana, et al., 2002; Bhattacharya, Kaul, Rao, Ramesh and Mallavarapu, 1993; Abd El-Kareem, Rabbih, Elansary and Al-Mana, 2020). The percent composition of the EO compounds was calculated. The qualitative analysis was based on the percent area of each peak of the sample compounds.

D. In vitro α -Glucosidase Inhibitory Activity

Antidiabetic activity of EO of *P. graveolens* was assessed through α -glucosidase inhibition assay. The assay method briefly summarized as 60 μ L of EO of *P. graveolens* in DMSO with concentrations ranging from 31.25 to 1000 μ g/mL and 0.1 M phosphate buffer (50 mL; pH 6.8) containing α -glucosidase solution (0.2 U/mL) was incubated at 37°C for 20 min in 96-well plates. PNPG (50 mL; 5 mM) solution in a 0.1 M phosphate buffer (pH 6.8) was applied to each well after pre-incubation and further incubated for 20 min at 37°C. Then, the reaction was stopped by adding 160 mL of 0.2 M NaCO₃ into each well. Absorbance (A) was reported at 405 nm with microplate reader and compared to a control which had 60 μ L of buffer solution in place of the test sample. Acarbose was used as a standard drug and evaluated same way as the test sample (Ahamad, Alkefai, Amin and Mir, 2020). The % inhibition of α -glucosidase enzyme was calculated using the following formula:

$$\% \text{Inhibition} = \frac{\text{Abs control} - \text{Abs test}}{\text{Abs control}} \times 100$$

where, Abs is absorbance of the control and absorbance of the sample

III. RESULTS AND DISCUSSION

A. GC–MS Analysis of EO of *P. graveolens*

The EO from leaves of *P. graveolens* was isolated by the hydrodistillation method. The hydrodistillation yielded 0.45% of EO from leaves of *P. graveolens*. The chemical composition of EO of *P. graveolens* was determined by the GC–MS method and results are presented in Table I and Fig. 1. Thirty-six components representing 99.17% of the total detected constituent were identified. The major constituents in the EO of *P. graveolens* include

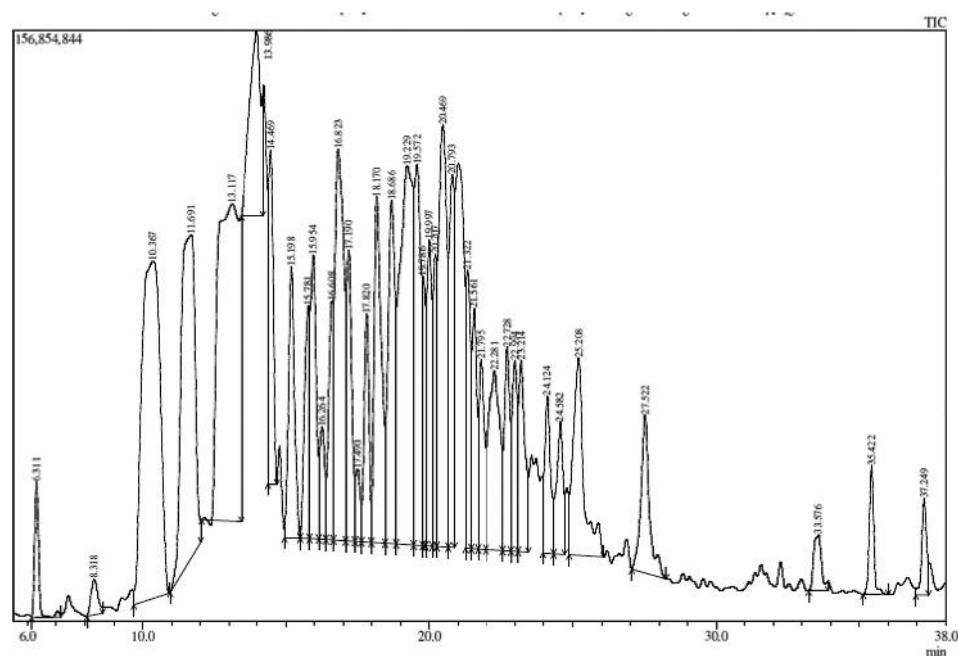


Fig. 1. Gas chromatography–mass spectrometry chromatogram of essential oil of *Pelargonium graveolens*.

citronellyl isovalerate (10.41%), menthol (9.61%), linalool (8.63%), *p*-menthone (6.31%), geranyl tiglate (4.99%), neryl propionate (4.79%), isocaryophyllene (3.77%), and caryophyllene epoxide (3.63%). The other components of *P. graveolens* EOs are geranyl butyrate (3.50%), neryl hexanoate (2.98%), geranyl heptanoate (2.93%), heptaminol (2.92%), citronellyl hexanoate (2.64%), neryl acetate (2.32%), myrtanol (2.23%), citronellol (2.22%), and nerolidyl acetate (2.18%). Other minor chemical components (<2%) of EO of *P. graveolens* are also presented in Table I. Rana, et al. studied the EO composition of *P. graveolens* leaves from Uttarakhand, India. The results show that citronellol (33.6%), geraniol (26.8%), linalool (10.5%), citronellyl formate (9.7%), and *p*-menthone (6.0%) were major chemical components in EO (Rana, et al., 2002). Bhattacharya, et al. (1993) studied volatile oil components of rose-scented *Geranium* and found that citronellol (25.44%), geraniol (21.87%), and linalool (7.87%) as major chemical compounds. In another study, EO components of *P. graveolens* from Egypt were studied by GC–MS. The study also shows citronellol (27.67%), *cis*-Menthone (10.23%), linalool (10.05%), eudesmol (9.40%), geraniol formate 6.87%, and rose oxide (5.77%) as major constituents (Abd El-Kareem, Rabbih, Elansary and Al-Mana, 2020). The present research is the first study on EO composition of *Geranium* growing in Iraqi Kurdistan. The study shows the presence of derivatives of citronellyl and geraniol, the major components already reported by other researchers such as citronellyl isovalerate (10.41%) and geranyl tiglate (4.99%). The present study finding is also comparable with the previous findings as study shows the presence of menthol (9.61%), linalool (8.63%), and *p*-menthone

(6.31%) as other major components. The variation in the chemical composition of *Geranium* is maybe due to variations in geographical location, temperature, rainfall, soil, etc. (Ahmad, Uthirapathy, Ameen and Anwer, 2019).

B. α -Glucosidase Inhibition Activity of EO of *P. graveolens*

The EO of *P. graveolens* showed concentration-dependent α -glucosidase enzyme inhibition that varies from 28.13 ± 1.41 to $74.24 \pm 2.53\%$ for concentration ranging from 31.25 to 1000 $\mu\text{g/mL}$ (Table II and Fig. 2). Acarbose was used as positive standard and it also showed concentration-dependent inhibition of α -glucosidase enzyme inhibition ranging from 31.94 ± 2.45 to $81.26 \pm 3.21\%$ for the same concentration as test sample above. The IC_{50} values for *P. graveolens* and acarbose were found as 93.72 ± 4.76 and 80.4 ± 2.17 $\mu\text{g/mL}$, respectively, against α -glucosidase enzyme.

The results of enzyme inhibition assay indicate that the EO of *P. graveolens* inhibits α -glucosidase enzyme in *in vitro* study. The results also show that the EO of *P. graveolens* was found comparable with standard acarbose in inhibition of α -glucosidase enzyme. α -Amylase and α -glucosidase enzymes are present in brush border of gastrointestinal tract and responsible for breakdown of polysaccharides and disaccharides, respectively. Inhibition of these enzymes leads reduction of monosaccharides available for absorption in blood and ultimately it controls sudden rise of blood glucose level after meals. The increased blood sugar level after a meal is known as PPHG and controlling it by inhibiting α -glucosidase enzyme is a new strategy in management of type 2 diabetes. The inhibitors of α -amylase and α -glucosidase enzymes such as acarbose and miglitol are non-specific in their action, the strong inhibition of both enzymes leads decreased metabolism of polysaccharides which causes

TABLE I
CHEMICAL COMPOSITION OF ESSENTIAL OIL OF *P. GRAVEOLENS*

Chemical constituents	RT	KI	Concentration (%)
<i>p</i> -Cymene	6.311	1026	0.78
Limonene	8.318	1031	0.34
Linalool	10.367	1097	8.63
<i>p</i> -Menthone	11.691	1153	6.31
Menthol	13.117	1173	9.61
Heptaminol	13.986	1188	2.92
Citronellol	14.469	1226	2.22
Myrtanol	15.198	1259	2.23
Citronellyl acetate	15.781	1353	1.57
Neryl acetate	15.954	1365	2.32
α -Copaene	16.264	1376	0.79
Isocaryophyllene	16.608	1413	3.77
Neryl propionate	17.190	1428	4.79
Epoxy cholesterol	17.490	-	0.48
α -Himachalene	17.820	1447	1.57
Geranyl butyrate	18.170	1562	3.50
Citronellyl isovalerate	19.229	1563	10.41
Caryophyllene epoxide	19.572	1581	3.63
Epicubenol	19.786	1613	0.99
Nerolidyl acetate	19.997	1632	2.18
Cubenol	20.207	1641	1.44
Geranyl tiglate	20.469	1700	4.99
Citronellyl hexanoate	20.793	1702	2.64
Citronellyl cinnamate	21.322	-	1.78
Geranyl hexanoate	21.561	1725	1.65
Kauren-19-yl-acetate	21.795	-	1.43
Geranyl heptanoate	22.281	1824	2.93
1-Hexadecanol	22.728	1868	1.58
3,7-Dimethyloct-6-en-1-yl heptanoate	22.994	-	1.40
2,6-Octadien-1-ol, 3,7-dimethyl-, propanoate	23.214	1831	1.68
Citronellyl valerate	24.124	1880	1.31
Hexadecanoic acid	24.582	1972	1.18
Neryl hexanoate	25.208	2031	2.98
Methyl linolenate	27.522	2098	1.87
2-Methylhexacosane	33.576	2663	0.61
Tetrapentacontane	35.422	-	0.66

Where, RT: Retention time, and KI: Kovats index

TABLE II
A-GLUCOSIDASE ENZYME INHIBITORY ACTIVITY OF EO FROM LEAF OF
P. GRAVEOLENS

Conc. (μ g/mL)	Acarbose	<i>P. graveolens</i>
31.25	31.94 \pm 2.45	28.13 \pm 1.41
62.5	45.44 \pm 2.63	41.72 \pm 0.93
125	57.23 \pm 3.31	55.17 \pm 3.46
250	63.82 \pm 2.47	59.03 \pm 2.45
500	76.81 \pm 2.96	63.28 \pm 2.45
1000	81.26 \pm 3.21	74.24 \pm 2.53
IC ₅₀ values	80.4 \pm 2.17	93.72 \pm 4.76

Data were presented as mean of % inhibition in triplicate determinations \pm SD

flatulence and distension as side effects due to bacterial fermentation from undigested carbohydrates (Subramanian, Asmawi and Sadikun, 2008; Dong, Li, Zhu, Liu and Huang, 2012). The present study finding supports the potential antidiabetic effects of *P. graveolens* EO in controlling PPHG through inhibition of α -glucosidase enzyme.

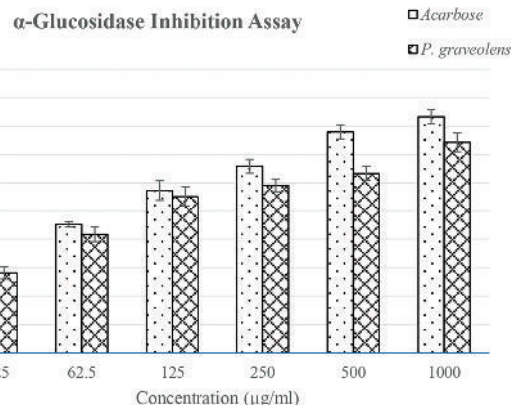


Fig. 2. α -Glucosidase enzyme inhibitory activity of essential oils from the leaf of *Pelargonium graveolens*.

IV. CONCLUSION

GC-MS analysis of Kurdish *P. graveolens* EO yielded citronellyl isovalerate, menthol, linalool, *p*-menthone, and geranyl tiglate as major constituents. *P. graveolens* EO also found potent inhibitors of α -glucosidase enzyme. The current research is first reports on the chemical composition of *P. graveolens* growing in Iraqi Kurdistan region. The findings of the present study also provide a scientific basis for its use in diabetic patients for controlling PPHG.

V. ACKNOWLEDGMENT

We gratefully acknowledge the Tishk International University, Erbil, Iraq, for providing research facilities. We also acknowledge Trichy Research Institute of Biotechnology Pvt. Ltd., Trichy, Tamil Nadu, India, for providing the research facilities.

REFERENCES

- Abd El-Kareem, M.S.M., Rabbih, M.A., Elansary, H.O. and Al-Mana, F.A., 2020. Mass spectral fragmentation of *Pelargonium graveolens* essential oil using GC-MS semi-empirical calculations and biological potential. *Processes*, 8, p.128.
- Adams, R.P., 2007. *Identification of Essential Oil Components by Gas Chromatography/Mass Spectrometry*. 4th ed. Allured Publishing, Carol Stream, IL, USA.
- Ahamad, J., Alkefai, N.H.A., Amin, S. and Mir, S.R., 2020. Standardized extract from *Enicostemma littorale* ameliorates post-prandial hyperglycaemia in normal and diabetic rats. *Journal of Biologically Active Products from Nature*, 10(1), pp.34-43.
- Ahamad, J., Hasan, N., Amin, S. and Mir, S.R., 2016. Swertiamarin contributes to glucose homeostasis via inhibition of carbohydrate metabolizing enzymes. *Journal of Natural Remedies*, 16(4), pp.125-130.
- Ahamad, J., Naquvi, K.J., Mir, S.R. and Ali, M., 2011. Review on role of natural α -glucosidase inhibitors for management of diabetes mellitus. *International Journal of Biomedical Research*, 6, pp.374-380.
- Ahamad, J., Toufeeq, I., Khan, M.A., Ameen, M.S.M., Anwer, E.T., Uthirapathy, S., Mir, S.R. and Ahmad, J., 2019. Oleuropein: A natural antioxidant molecule in the treatment of metabolic syndrome. *Phytotherapy Research*, 33(12), pp.3112-3128.
- Ahamad, J., Uthirapathy, S., Ameen, M.S.M. and Anwer, E.T., 2019. Essential

- oil composition and antidiabetic, anticancer activity of *Rosmarinus officinalis* L. leaves from Erbil (Iraq). *Journal of Essential Oil Bearing Plants*, 22(6), pp.1544-1553.
- Ali, M., 2001. *Techniques in Terpenoid Identification*. Birla Publication, New Delhi, India, pp.4-51.
- Alkefai, N.H., Ahamad, J., Amin, S. and Mir, S.R., 2018. Arylated gymnemic acids from *Gymnema sylvestre* R.Br. as potential α -glucosidase inhibitors. *Phytochemistry Letters*, 25, pp.196-202.
- Alkefai, N.H., Sharma, M., Ahamad, J., Amin, S. and Mir, S.R., 2019. New olean-15-ene type gymnemic acids from *Gymnema sylvestre* (Retz.) R.Br. and their antihyperglycemic activity through α -glucosidase inhibition. *Phytochemistry Letters*, 32, pp.83-89.
- Bhattacharya, A.K., Kaul, P.N., Rajeswara, B.R.R., Ramesh, S.I. and Mallavarapu, G.R., 1993. Composition of the oil of rose-scented Geranium (*Pelargonium* sp.) grown under the semiarid tropical climate of South India. *Journal of Essential Oil Research*, 5(2), pp.229-231.
- Dong, H.Q., Li, M., Zhu, F., Liu, F.L. and Huang, J.B., 2012. Inhibitory potential of trilobatin from *Lithocarpus polystachyus* rehd against α -glucosidase and α -amylase linked to Type 2 diabetes. *Food Chemistry*, 130, pp.1261-66.
- Fabricant, D.S. and Farnsworth, N.R., 2001. The value of plants used in traditional medicine for drug discovery. *Environmental Health Perspectives*, 109(1), pp.69-75.
- Gin, H., and Rigalleau, V., 2000. Post-prandial hyperglycemia and diabetes. *Diabetes and Metabolism*, 26, pp.265-272.
- Lis-Balchin, M., Buchbauer, G., Ribisch, K. and Wenger, M.T., 1998. Comparative antibacterial effects of novel *Pelargonium* essential oils and solvent extracts. *Letters in Applied Microbiology*, 27(3), pp.135-141.
- Lis-Balchin, M., Steyrl, H. and Krenn, E., 2003. The comparative effect of novel *Pelargonium* essential oils and their corresponding hydrosols as antimicrobial agents in a model food system. *Phytother. Phytotherapy Research*, 17(1), pp.60-65.
- Miller D.M., 2002. Geranium and *Pelargonium*. In: Lis-Balchin, M., Ed. *Medicinal and Aromatic Plants-Industrial Profiles*. Taylor and Francis, London, UK, p.49.
- Pattnaik, S., Subramanyam, V.R. and Kole, C.R., 1996. Antibacterial and antifungal activity of ten essential oils *in vitro*. *Microbios*, 86, p.237.
- Pattnaik, S., Subramanyam, V.R., Bapaji, M. and Kole, C.R., 1997. Antibacterial and antifungal activity of aromatic constituents of essential oils. *Microbios*, 89(358), pp.39-46.
- Rajeswara, B.R.R., Kaul, P.N., Mallavarapu, G.R. and Ramesh, S., 1996. Effect of seasonal climatic changes on biomass yield and terpenoid composition of rose-scented geranium (*Pelargonium* species). *Biochemical Systematics and Ecology*, 24(7-8), pp.627-635.
- Rana, V.S., Juyal, J.P. and Blazquez, M.A., 2002. Chemical constituents of essential oil of *Pelargonium graveolens* leaves. *International Journal of Aromatherapy*, 12(4), pp.216-218.
- Scheen, A.J. 2003. Is there a role for α -glucosidase inhibitors in the prevention of Type 2 diabetes mellitus? *Drugs*, 63, pp.933-951.
- Subramanian, R., Asmawi, M.Z. and Sadikun, A., 2008. *In-vitro* α -glucosidase and α -amylase enzyme inhibitory effects of *Andrographis paniculata* extract and andrographolide. *Acta Biochimica Polonica*, 55(2), pp.391-398.

A Study on the Prevalence and Source of Staphylococci and Methicillin-resistant *Staphylococcus aureus* Causing Superficial Incisional Surgical Site Infection

Kameran M. Ali¹ and Bahrouz M. A. Al-Jaff²

¹Department of Medical Lab Technology, Kalar Technical College, Sulaimani Polytechnic University, Kalar, Kurdistan Region – F.R. Iraq

²Department of Biology, College of Education, University of Sulaimani, Sulaimani, Kurdistan Region – F.R. Iraq

Abstract—*Staphylococcus aureus* and coagulase-negative staphylococci (CoNS) are common causatives of superficial incisional surgical site infection (SSI). The source of the pathogens is still not fully diagnosed whether it is endogenous or exogenous particularly with regard to the extent of its resistance to antibiotics. Therefore, this study is designed to determine the rate of infection, the source of pathogens, and the extent of their resistance to antibiotics. For this purpose, pre-, intra- and post-operative swabs from the nasal and skin of patients undergoing surgeries and samples from the hospital environment have been collected and processed for isolation and identification of staphylococci. Bacterial analysis and antibiotic susceptibility profiles of the isolates are assessed by unweighted pair group method with arithmetic mean (UPGMA) analysis based on random amplified polymorphic DNA-polymerase chain reaction (RAPD-PCR) and disc diffusion test for antibiotics susceptibility profile. The microbiological and PCR results indicate that SSIs are found in 113/512 (22.07%), *Staphylococcus* spp. rated 67/512 (13.09%) of infections. Further analysis indicates that *S. aureus*, CoNS, and both of them were causes SSI with different rates 41/67 (61.2%), 23/67 (34.3%), and 3/67 (4.5%), respectively. Results of RAPD-PCR for 70 isolates reveal that 52/70 (74.28%) of SSIs are from endogenous source, followed by 10/70 (14.29%) and 8/70 (11.43%) from hospitals acquired and undetermined sources, respectively. Moreover, results of antibiotic susceptibility test reveal that 24/44 (54.5%) of isolates belong to methicillin-resistant *Staphylococcus aureus*; from both endogenous and exogenous sources with 13/24 (54.17%) and 11/24 (45.83%), respectively.

Index Terms—Methicillin-resistant *Staphylococcus aureus*, Source of Infections, *Staphylococcus* spp., Surgical site infection.

I. INTRODUCTION

Surgical site infection (SSI) is a common postsurgical nosocomial infection that occurs at the operation site. It increases the occurrence of morbidity and mortality, leading to increased health-care costs through extended hospitalization times and the emergence of antimicrobial resistance in pathogens (Mangram et al., 1999). The Center for Disease Control and Prevention has classified SSIs as either incisional or organ/space infections. SSIs are further categorized into superficial (affecting skin and subcutaneous tissues, or deep (attacking deeper soft tissues) (Horan et al., 1992).

There are several risk factors related to SSI, including age, nutritional status, smoking, obesity, preexisting infection, diabetes and other chronic diseases, blood transfusion, prolonged hospitalization (either pre- or post-operative), poor surgical technique, prolonged duration of surgery, and inadequate sterilization of surgical instruments (Cheadle, 2006; Owens and Stoessel, 2008). Aside from the inoculum of contaminant bacteria introduced into the incision either during or after the operation, the microenvironment and the immunological integrity of the host have importance in determining the severity of infection (Medeiros et al., 2005).

Bacteriological studies have shown that SSIs are usually caused by endogenous and/or exogenous bacteria that enter the operative wound either during or after surgery (Owens and Stoessel, 2008; Dancer et al., 2012; Berrios-Torres et al., 2017). The most commonly isolated bacteria in SSIs are *Staphylococcus aureus* and coagulase-negative staphylococci (CoNS) (Anderson and Kaye, 2009; Pal et al., 2019; Dohmen, 2006), which frequently colonize the skin and nares in the healthy population, and in pre-operative patients are associated with an elevated risk of SSI (Dohmen, 2006). In general, patients who are nasal and skin carriers of staphylococci are 2–9 times more likely to develop an SSI, and it has been shown that 85% of SSIs can be traced to endogenous colonization of the patients (Skråmm et al., 2014). Although the isolated bacteria from SSI depending on

ARO-The Scientific Journal of Koya University
Volume IX, No.1 (2021), Article ID: ARO.10752, 08 pages
DOI:10.14500/aro.10752

Received: 16 November 2020; Accepted: 22 June 2021
Regular research paper: Published: 30 June 2021

Corresponding author's e-mail: kameran.m.ali@spu.edu.iq
Copyright © 2021 Kameran M. Ali, Bahrouz M. A. Al-Jaff. This is an open-access article distributed under the Creative Commons Attribution License.



the surgical procedures, whereas the problem is that some of them are resistant to antibiotics, particularly methicillin-resistant *Staphylococcus aureus* (MRSA), which increase the incidence of SSIs (Bhattacharya et al., 2016). The widespread use of broad-spectrum antibiotics leads to emergence of antimicrobial resistant strains in hospitals. The problem is more complicated in developing countries as a result of poor infection control practices, overcrowded hospitals, and inappropriate use of antimicrobials (Negi et al., 2015).

In spite of the comprehensive techniques and careful surgical procedures used to control infections, the rate of staphylococcal SSI remains a real threat in surgical settings (Mawalla et al., 2011). Therefore, it is important to identify whether the source of bacterial pathogens (*Staphylococcus* spp.) isolated from patients with post-operative SSI is the patients' skin or contaminated items existent in the hospital environment (Reichman and Greenberg, 2009).

Determining the sources of SSI is a crucial avenue of research in remedying these problems and finding solutions to minimize the threat of SSI. However, there is to date no standardized diagnostic method for SSI infection and often no post-discharge surveillance system in place (WHO, 2016). The incidence rate of SSI has not yet been established in Kurdistan Region of Iraq. Therefore, this study aims to use various diagnostic methods to determine the rate and the source of bacterial SSIs, and to assess the risk of these causative agents through testing their antibiotic susceptibility profiles.

II. MATERIALS AND METHODS

A. Sampling and Data Collection

A hospital-based cross-sectional study was conducted from August 2018 to July 2019 in three surgical centers of hospitals (Kalar General Hospital, Life Private Hospital and Sheray Naqib Hospital) in the Kalar city, Kurdistan, Iraq. A total of 512 patients (233 males, 279 females, and ages 9–67 years) who had undergone surgeries were followed up for staphylococcal superficial incisional SSIs until they had fully recovered or were discharged from the hospital. Nasal and skin swabs were taken aseptically from patients on admission to the hospital and after operation completion from subcutaneous wounds. Swabs were also taken from elements within the hospital environment, including the instruments and disinfectants used for each patient. Clinical data were obtained from the patients' files and by physical examination using structured and pretested questionnaires.

The patients who underwent surgery were continuously monitored for signs and symptoms of SSI during hospital admission and after discharge (follow-up on an outpatient basis) for 30 days of surveillance. Sterile cotton swabs were collected aseptically from superficial surgical wounds of each patient suspected of having SSI before the injury was cleaned with antiseptic. Swabs were obtained from the surgical sites while avoiding contamination by skin commensals and transported immediately to the molecular biology lab of Garmian University for processing by standard laboratory procedures (Elmer et al., 1997).

B. Isolation and Identification of Causative Agents

For isolation and preliminary identification, specimens were streaked on 5% sheep blood agar and mannitol salt agar, and then incubated for 24 h at 37°C. In case no bacterial growth, the plates were further incubated for 24 h more. Then, after 48 h the specimens with no growth, they were reported as negative. Identification at the species level depended on colony morphology, Gram's staining, and conventional biochemical tests including catalase test, coagulase test, and detection of hemolysin activity (Forbes et al., 2007).

C. Molecular Identification by PCR

Identifications were confirmed by PCR using specific primers for each *Staphylococcus* species. The target genes have been selected for each species. Then, species-specific primers were designed using Primer-BLAST on NCBI. Finally, all primers were BLAST analyzed before they were synthesized by Macrogen Inc. (Seoul, Korea).

DNA extraction

Extraction of DNA from clinical isolates was performed according to the kit manufacturer's instructions (Geneaid Biotech Ltd., New Taipei City, Taiwan). Concentration and purity (260/280 ratio) of the extracted DNA was checked by NanoDrop (Thermo Scientific, Waltham, MA, USA).

Multiplex PCR

S. aureus was detected using single PCR. However, CoNS detection was carried out in two sets of multiplex PCR as previously described by Kim et al., 2018. For this purpose, a pair of universal primers was added to each set of multiplex assays for the identification of CoNS species. 16S rRNA sequencing was used for the identification of isolates that were not detected by the PCR sets that mentioned in Table I.

PCR amplification reactions were carried out with 10 µl of MasterMix and 2.5 µl of template DNA for a final volume of 20 µl in a single pathogen tube, using a Gradient Thermocycler (Eppendorf, Germany). The protocol used included an initial denaturation at 95°C for 5 min, followed by 35 cycles of denaturation at 95°C for 30 s, primer annealing for 30 s, primer extension at 72°C for 45 s, and the final extension at 72°C for 5 min. The primer sequences, multiplex sets, concentrations, annealing temperature, and calculated lengths of the corresponding amplicons are listed in Table I.

D. Determination the Source of Causative Staphylococci Using Random Amplified Polymorphic DNA-polymerase Chain Reaction (RAPD-PCR) and UPGMA Analysis

Randomly amplified polymorphic DNA analysis by PCR (RAPD-PCR) was performed for genotyping of *S. aureus* and CoNS, and to ascertain the source of infection by comparing them with each other. The RAPD-PCR reaction was performed using 10-mer primers 5'-AGCGTCACTG-3' (Casey et al., 2006), 5'-GCGATCCCCA-3', 5'-AGCGTCACTG-3', and 5'-TGACCCGCC-3' (Pereira et al., 2002). The reaction was carried out in a 20 µl reaction volume containing 10 µl

TABLE I
LIST OF PRIMERS USED IN THIS STUDY

PCR name	Targeted bacteria/ gene	Primer name	Primer sequences (5'-3')	Amplicon size by (bp)	Annealing temperature	Primer conc. for each of F & R (pmol/mL)	Reference
PCRSA1	<i>S. aureus</i>	Sa442-F Sa442-R	AATCTTTGTGCGGTACACGATATTCTTCACG CGTAATGAGATTTTCAGTAGATAATACAACA	108	55°C	0.5	(Martineau et al., 1998)
PCRSA2	<i>S. aureus</i> (rpoB) gene	SA2-F SA2-R	TTCAGCAGCTGATTCTGGT TCAAGAACGATACCGCCAGC	673	56°C	0.5	This study
MultPCR1 CoNS	<i>S. xylosum</i> (sodA) gene	SX297-F SX297-R	GCAAATCTAGACAGTGTTCAGAAAAT CTTCTGAGTTTGGAGTTAAT	297	55°C	0.2	(Kim et al., 2018)
	<i>S. pasteurii</i> (sodA) gene	PA237-F PA237-R	GCTAATTTAGACAGTGTACCTTCTG GCCCGTTATTACTACTAACCA	237		0.2	(Kim et al., 2018)
1/2CONS	<i>S. warneri</i> (sodA) gene	SW110-F SW110-R	GTAACAAAATTAATGACAGCTG TCTTACTGCAGTTTGAATATCAGA	110		0.2	(Kim et al., 2018)
	<i>S. haemolyticus</i> (sodA) gene	HA54-F HA54-R	AAACAAACTATGAAAATCCATCATG ATTTGGTAAACATACGTGTTGTG	54		0.3	(Kim et al., 2018)
MultPCR2 CoNS	CONS staphylococci (sodA) gene	CONS-F CONS-R	TTGACGCATTAGAACCACACATC CTGCAGCTTTGTACGCGAAT	330	54°C	0.3	This study
	<i>S. caprae</i> (sodA) gene	CR252-F CR252-R	AATTTAGATAGCGIACCTTTG AGTTACGATTTCTAATTGACCGTT	252	53°C	0.2	(Kim et al., 2018)
PCR16S	<i>S. epidermidis</i> (gse) gene	Epi-F Epi-R	GGCAAATTTGTGGGTCAAGA TGGCTAATGGTTTGTACCA	194		0.2	(Byrne et al., 2007)
	<i>S. capitis</i> (sodA) gene	CT103-F CT103-R	TCAGATATTCAAACTGCAGTACG CTACTTCACCTTTTTCTTCAGA	103		0.3	(Kim et al., 2018)
PCR16S	<i>S. saprophyticus</i> (sodA) gene	SA52-F SA52-R	TGGACACTTAAACCACTACTA CTTCTGATTTGGAGTTAAT	52		0.2	(Kim et al., 2018)
	16srRNA	27F 1492R	AGAGTTTGATCMTGGCTCAG GGTTACCTTGTACGACTT	1500	60°C	0.5	(Lane, 1991)

MasterMix, 1.2 µl primers, 2.5 µl DNA template, and 6.3 µl sterile deionized water. The negative control for each primer contained all the components except template DNA. The amplification procedure was comprised of one cycle for 5 min at 94°C, followed by 5 low-stringency cycles of 30 sec at 94°C, 2 min at 20°C, and 2 min at 72°C, and 30 high-stringency cycles of 30 sec at 94°C, 1 min at 32°C, and 2 min at 72°C. The amplification was concluded within 5 min at 72°C. Then, 10 µl of each product and 5 µl of a 100 bp DNA molecular mass ladder (TransGen Biotech Co., Ltd., Beijing, China) were loaded into separate wells in a 2% agarose gel containing 5 µl of safe dye and electrophoresed at 100 V for 1 h in 1% TBE buffer. The clearest and most reproducible bands were chosen for the determination of their presence or absence in each strain. Faint bands that could not be systematically visualized were not taken into account.

Typing of bacteria was used for monitoring pathogens and revealing the source of infection. The RAPD patterns were considered to be different when the profiles differed by at least one band (Burnie et al., 1997; Marsou et al., 2001). Here, we used RAPD-PCR followed by agarose gel electrophoresis for typing of isolates that were collected from pre-, during, and post-operative nasal, skin, and subcutaneous wound specimens of patients with SSI, as well as the hospital environment. The relationships among *S. aureus* and CoNS RAPD profiles were determined by unweighted pair group method with arithmetic mean (UPGMA) dendrogram cluster analysis (Addinsoft, 2020).

E. Antibacterial Susceptibility Testing by Disc Diffusion Method (Kirby-Bauer Test)

Antibacterial susceptibility testing of *Staphylococci* spp. was performed using the disc diffusion method on Müller-Hinton agar medium (Oxoid, UK). The antibiotic discs with respective concentrations prescribed in the study area included the known six antibiotic classes (Oxoid, UK) and were selected as they used in testing resistance for nosocomial bacteria in addition to that mentioned in inpatients prescriptions in local hospitals and Clinical Laboratory Institute Standards (CLSI) guidelines (Wayne, 2017). The used antibiotics were penicillin G (10 IU), ampicillin (10 µg), amoxicillin/clavulanic acid (20/10 µg), cephalothin (30 µg), clindamycin (15 µg), azithromycin (15 µg), tetracycline (30 µg), rifampicin (5 µg), erythromycin (15 µg), vancomycin (30 µg), ceftriaxone (30 µg), ciprofloxacin (5 µg), levofloxacin (5 µg), gentamycin (10 µg), trimethoprim/sulfamethoxazole (25 µg), amikacin (30 µg), nitrofurantoin (100 µg), imipenem (10 µg), and meropenem (10 µg). MRSA was identified using cefoxitin (30 µg) and oxacillin (1 µg) and interpreted according to CLSI guidelines (2017).

One to three colonies were picked up from a new pure culture and mixed aseptically in a test tube containing 3 ml sterile saline to form a homogenous suspension. Turbidity of the suspension was adjusted to a 0.5 McFarland standard using a photometric device (Densimat, BioMérieux). Within 15 min, a sterile cotton swab was dipped into the bacterial suspension, excess fluid was removed, and the swab used to evenly streak the surface of Müller-Hinton agar in three different planes, rotating the plates approximately 60° each

time. The rim of the plate was then swabbed once. After 5 min, the selected antibiotic discs were placed aseptically on the surface of the inoculated media using sterile forceps. The plates were inverted and incubated aerobically at 35–37°C for 18–24 h, after which the mean radii diameters of the inhibition zone were measured in millimeters using calipers and interpreted using CLSI guidelines (Wayne, 2017). The standard reference strain *S. aureus* ATCC 25923 was used to assess the disc's quality. Multidrug resistance (MDR) was considered as resistance to at least one antibiotic in three or more antibacterial categories (Magiorakos et al., 2012).

F. Ethics Statement

The study was approved by the Ethical Committee of the Department of Medical Lab. Technology, Kalar Technical Institute, Sulaimani Polytechnic University, the Declaration of Helsinki regarding the ethical principles for medical research involving human subjects was considered. Patients' consent was acquired; for minors, guardians' consent was acquired.

G. Statistical Analysis

Statistical analysis was performed using the Statistical Package for the Social Sciences version 16.0 software program (IBM Corporation, Armonk, NY, USA) to determine associations of SSI incidence in patients. $P < 0.05$ was considered as statistically significant. The incidence rate was expressed as the percentage of patients who acquired SSI among those admitted to surgical centers. Antibiotic resistance was expressed as the ratio between the numbers of isolates confirmed as resistant over the total number of isolates subjected to the antibiotic.

III. RESULTS

A. Rate and Etiology

Obtained results of molecular identification were exhibited that the SSI rate of those included in the study was 113/512 (22.07%). The rate of staphylococcal SSI was 67/512 (13.09%); infection by *S. aureus* occurred in 41/67 patients (61.2%), infection by CoNS occurred in 23/67 (34.3%), and infection by both *S. aureus* and CoNS occurred in 3/67 (4.5%), Table II. Most staphylococcal infections (95.5%) were caused by a single species, with the remaining 4.5% caused by multiple species. *Staphylococcus* spp. were isolated from 29/67 male patients (43.3%) and 38/67 from female patients (56.7%).

Among the 70 isolated staphylococci, 26 of them were CoNS species and they distributed as 17 (65.38%) *S. epidermidis*, 4 (15.38%) *S. haemolyticus*, 3 (11.54%) *S. capitis*, and 1 (3.85%) of each *S. warneri* and *S. hominis*.

B. Determination the Source of Causative Agents Using RAPD-PCR and UPGMA Analysis

RAPD typing for both 44 *S. aureus* and 26 CoNS SSI isolates produced amplicons with a range of profiles. UPGMA analysis for *S. aureus* revealed three clusters, with 10 SSI

TABLE II
STAPHYLOCOCCUS SPP. ISOLATED IN THE SURGICAL SITE INFECTIONS

Bacterial species	Number of SSI (%)	Total bacterial no. (%)
SSI patients with <i>S. aureus</i>	41 (61.19%)	44 (62.86%)
SSI patients with CoNS	23 (34.33)	26 (37.14%)
SSI patients with both <i>S. aureus</i> and CoNS	3 (4.48%)	
Total	67 (100%)	70 (100%)

isolates showing similarities in banding patterns to those of exogenous surgical ward isolates; the other isolates were determined to show non-similar patterns. The typing profile revealed that 29 infections were caused by endogenous *S. aureus* not related to surgical centers, Fig. 1. UPGMA analysis revealed that out of 26 CoNS isolates, 23 of them were similar to nasal and skin isolates of the same patients, revealing the endogenous source of the causative pathogens, all *S. haemolyticus*, *S. warneri*, and *S. hominis* isolates were sourced from the endogenous source, whereas two isolates of *S. epidermidis* and single isolate of *S. capitis* were appeared to be from the exogenous source, Fig. 2.

Regarding the source of *Staphylococcus* spp. causing SSI, UPGMA analysis revealed that 52/70 (74.28%) were sourced from patients themselves (endogenous source), whereas 10 (14.29%) were sourced from the hospital environment (exogenous source) and 8 (11.43%) were from an undetermined exogenous source, Fig. 3a.

C. Antibiotic Resistance Profile

All staphylococci isolated from SSIs were resistant to at least one class of the antibiotics used; 68.6% of them were multiple drug resistant (MDR). Most of *S. aureus* and CoNS were resistant to penicillin G (95.5% and 88.5%, respectively), with moderate resistance to gentamicin, tetracycline, erythromycin, and trimethoprim/sulfamethoxazole. *S. aureus* showed higher resistance than CoNS to those drugs that mentioned above. MRSA was recorded in 54.5% of the isolated staphylococci; the majority of MRSA sources (13/24, 54.17%) were the patients themselves, whereas the remainder (11/24, 45.83%) were exogenous or undetermined. About 20.5% of isolated MRSA were resistant to vancomycin. Out of 26 CoNS isolates, 5 (19.2%) were resistant to methicillin: *S. epidermidis* (3), *S. haemolyticus* (1), and *S. capitis* (1). The resistance to the other antibiotics was variable. *S. aureus* and CoNS were highly susceptible to rifampicin, showing resistances to only 13.6% and 11.5%, respectively. The susceptibility to nitrofurantoin was also high (8.2% and 15.4% resistance, respectively), Table III.

Out of 44 *S. aureus* SSI isolates, 10 had an antibiotic resistance profile with a high degree of similarity to that of a surgery environment isolate. Of the other 34 isolates, 29 of them showed profiles identical to those of the same patients' pre-surgical isolates, whereas the remaining 5 showed no similarity in profile to pre-surgical or environmental isolates. The antibiotic profile of 26 CoNS isolates revealed that 22 of them were identical to the same patients' pre-surgical isolates, whereas the other 4 showed no similarity in profile to pre-surgical and environmental isolates.

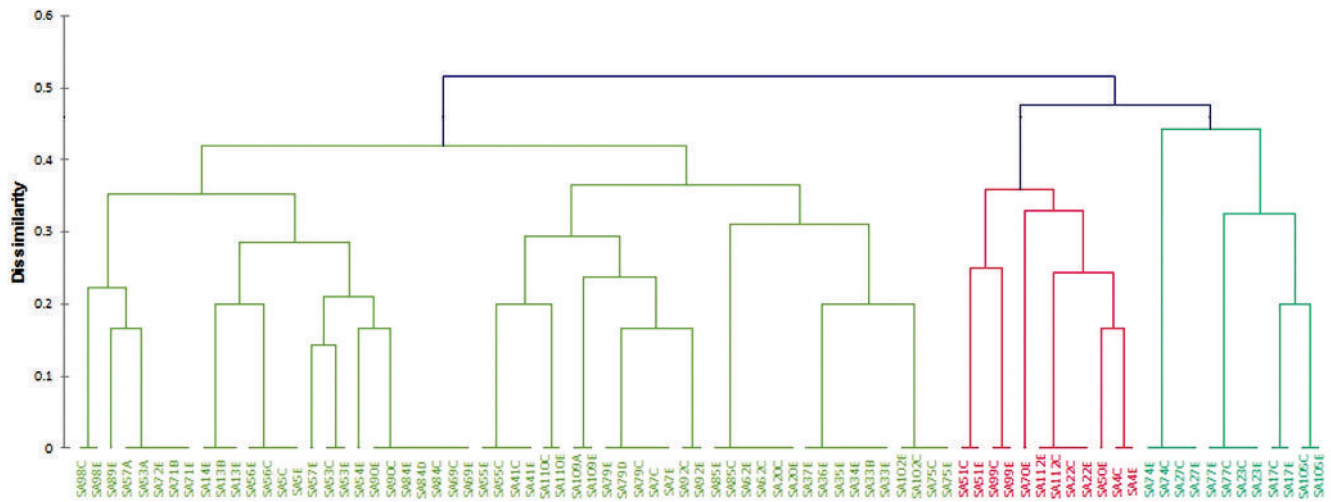


Fig. 1. UPGMA dendrogram analysis of RAPD profiles from SA isolates. SA: *Staphylococcus aureus*.

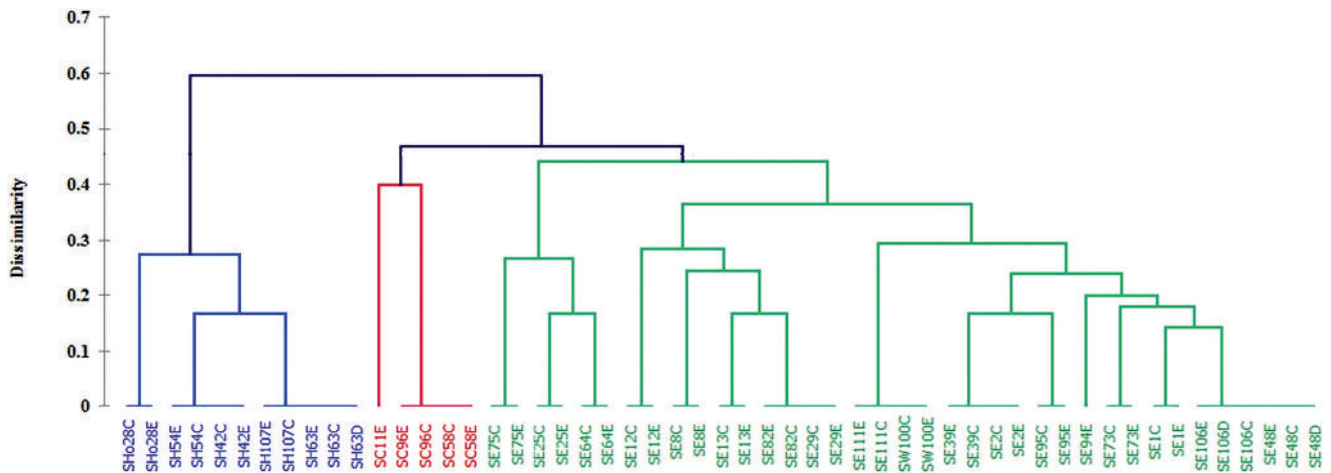


Fig. 2. UPGMA dendrogram analysis of RAPD profiles from CoNS isolates. SE: *Staphylococcus epidermidis*, SH: *Staphylococcus haemolyticus*, SC: *Staphylococcus capitis*, SHo: *Staphylococcus hominis*, SW: *Staphylococcus warneri*.

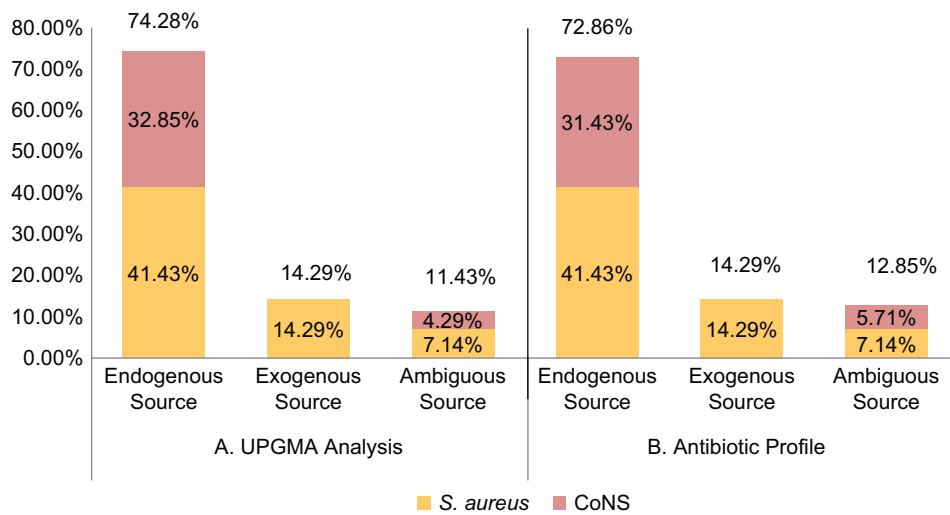


Fig. 3. The percentage of Staphylococcal Surgical Site Infections Source: (a) The source of staphylococcal SSI according UPGMA analysis; (b) the source of staphylococcal SSI according to antibiotic profile.

TABLE III
ANTIBACTERIAL RESISTANCE PATTERN AMONG SSI *STAPHYLOCOCCUS* SPP. ISOLATES

No. Antibiotic	Resistant <i>Staphylococcus aureus</i> (n=44)		Resistant coagulase-negative staphylococci (n=26)	
	n	%	n	%
1 Penicillin G (10 IU)	42	95.5	23	88.5
2 Ampicillin (10 µg)	39	88.6	18	69.2
3 Amoxicillin/clavulanate (30 µg)	26	59.1	14	53.8
4 Cephalothin (30 µg)	19	43.2	11	42.3
5 Imipenem (10 µg)	21	47.7	5	19.2
6 Meropenem (10 µg)	19	43.2	3	11.5
7 Oxacillin (1 µg)	24	54.5	5	19.2
8 Cefoxitin (30 µg)	23	52.3	5	19.2
9 Cefepime (30 µg)	15	34.1	6	23.1
10 Levofloxacin (5 µg)	15	34.1	2	7.7
11 Ciprofloxacin (5 µg)	25	56.8	15	57.7
12 Erythromycin (15 µg)	29	65.9	15	57.7
13 Clindamycin (10 µg)	26	59.1	14	53.8
14 Azithromycin (15 µg)	15	34.1	12	46.2
15 Tetracycline (30 µg)	31	70.5	17	65.4
16 Rifampicin (5 µg)	6	13.6	3	11.5
17 Vancomycin (30 µg)	9	20.5	2	7.7
18 Gentamicin (10 µg)	38	86.4	15	57.7
19 Amikacin (30 µg)	32	72.7	14	53.8
20 Nitrofurantoin (100 µg)	8	18.2	4	15.4
21 Trimethoprim/sulfamethoxazole (25 µg)	28	63.6	19	73.1

Results of antibiotic resistance profiling show that 51/70 (72.86%) of *Staphylococcus* caused SSIs were of an endogenous source, 10 (14.29%) were sourced from the hospital environment, and 9 (12.86%) were of an undetermined source, Fig. 3b.

IV. DISCUSSION

Despite advances in surgical technique and improved understanding of the pathogenesis of wound infections, management of SSIs represents a significant challenge to any surgical health-care facility procedure (Medeiros et al., 2005, Sattar et al., 2019). Globally, SSI rates have ranged from 2.5% to 41.9% (Mawalla et al., 2011). The rate reported in this study (22.07%) is similar to those reported in related studies of some developing countries (Giri et al., 2013; Mezemir et al., 2020), but higher than those recorded for developed countries (Fan et al., 2014; Roumelaki et al., 2008). In fact, the literature has mentioned that incidence rates of SSIs in developing countries may be up to 3–4 times higher than those of developed countries (Danzmann et al., 2013; Curcio et al., 2019; Mezemir et al., 2020), the difference may be due to reasons linked to patient-related and procedure-related factors including poor hospital infrastructure, poor hygiene, failure to follow-up on the patient’s treatment, overwhelmed health-care services due to population burden, and contamination from the external environment (Mukagendaneza et al., 2019; Assawapalangool et al., 2016).

The rate of staphylococcal SSI reported in this study is in agreement with a study that revealed the predominance of

Staphylococci spp. (Rolston et al., 2014) in SSIs; however, other studies including studies conducted in Baghdad and Duhok cities have reported a lower proportion of *Staphylococci* spp. (Mohammed et al., 2020; Merdaw, 2011; Dessie et al., 2016). In this study, *S. aureus* was found to be the causative agent of more than one-third of infections and it has been found to be the single greatest cause of SSIs in the current study, as well as in the previous studies worldwide (Bhattacharya et al., 2016; Negi et al., 2015). Indeed, *S. aureus* is a widespread member of skin and nasal microbiota, with high proximity to potential surgical points of entry. During surgery, the integrity of the skin may be breached, leading to skin and soft-tissue infection by *Staphylococcus* spp. already inhabited on the skin of patients or found in the environment, on surgical instruments, or on the hands of health care workers (David and Daum, 2010; Reichman and Greenberg, 2009). The difference in the distribution of SSI bacteria may be due to variations in common pathogens inhabiting surgery centers, aseptic techniques, infection control and prevention policies, geographical distribution, resistance patterns of the bacterial isolates, surgical procedures performed, contamination due to poor personal hygiene or post-procedural contamination, and outbreaks (Mukagendaneza et al., 2019; Rao et al., 2013).

Most staphylococcal isolates from this study were found to be multidrug resistant. They were generally susceptible to carbapenems, rifampicin, and nitrofurantoin, but resistant to penicillinase-sensitive penicillins, tetracycline, gentamicin, and trimethoprim/sulfamethoxazole. In consistent to this finding, similar results were reported by Dessie et al., 2016. The high rate of resistance to these drugs may be attributed to the fact that these antibiotics are widely prescribed by physicians for both inpatients and outpatients to treat various bacterial infections, in addition to their relatively cheap price (Rao et al., 2013). The prophylactic use of antibiotics before and/or after surgery may induce new resistance bacteria through the transmission of resistance genes from other established bacterial species in the hospital environment and it became difficult to control (Schentag et al., 1998). The development and spread of resistant bacterial strains have emerged as a global problem. The appearance of MDR bacterial strains over the past decades has been regarded as an inevitable genetic response to the strong selective pressure imposed by antimicrobial chemotherapy (Negi et al., 2015).

More than half of *S. aureus* isolates were MRSA that were resistant to the penicillinase-resistant penicillins, oxacillin, and cefoxitin, which are similar to results reported by the previous studies on SSI isolated *S. aureus* (Bhattacharya et al., 2016; Khairy et al., 2011). However, it appears that this proportion cannot be generalized for SSI infections globally. For example, a study has revealed that 15.7% MRSA among SSI isolates in India (Negi et al., 2015). Surgical patients with MRSA carriage can increase the risk of SSI development; the previous study by Safdar and Bradley (2008) illustrated that patients colonized with MRSA were 4 times more likely to develop an infection than patients colonized with MSSA. It has been mentioned that the variation in the prevalence of MRSA may depend on pre- and post-operative antibiotic

use, as well as patient surveillance programs (Bhattacharya et al., 2016). However, results of the current study were revealed that the highest proportion (88.57%) belongs to pre-operative patients' skin, nasal, and hospital environment. This was confirmed through isolation of same bacterial types from post-operative SSIs which indicates that the most significant source of MRSA is from the patients themselves.

The RAPD-PCR and UPGMA analyses revealed that the incidence rate of endogenous-sourced SSIs (including *S. aureus*, MRSA, and CoNS) was 3 times higher than that of exogenous sourced SSIs. Most SSIs were reported to be caused by patients' body microbiota, whereas infections caused by exogenous bacteria following surgery were less common (Skråmm et al., 2014; Leaper et al., 2008; Perl et al., 2002). *S. aureus* colonizes the skin and nose of human beings, and several studies have identified patients' nasal and skin *S. aureus* as a major risk factor for SSIs (Munoz et al., 2008; Liu et al., 2017; Wertheim et al., 2005). MRSA can spread from the anterior nares to other areas on the skin surface and then contaminate the surgical site (Leaper et al., 2008; Women's and Health, 2011). It has been reported that most of *S. aureus* strains are causing SSIs and they have the same identity as isolates from the nares of the patients themselves, these results were confirmed by Perl et al., 2002. In this study, the identification of the causative identities for both *S. aureus* and CoNS, including MRSA, and their endogenous or exogenous sources, was performed through RAPD-PCR genotyping, and involved actual matching of isolates with pre-, inter-, and post-operative isolates.

V. CONCLUSION

Isolation of *S. aureus* and CoNS with MDR was strongly associated with post-operative SSIs. The incidence rate of staphylococcal SSIs is high, and these SSIs including infections caused by MRSA were sourced mostly from the skin and nares of the patients themselves, rather than the surgery ward or hospital environment.

REFERENCES

- Addinsoft., 2020. *XLSTAT Statistical and Data Analysis Solution*. Addinsoft, Boston, USA. Available from: <https://www.xlstat.com>.
- Anderson, D.J. and Kaye, K.S., 2009. Staphylococcal surgical site infections. *Infectious Disease Clinics of North America*, 23, pp.53-72.
- Assawapalangool, S., Kasatpibal, N., Sirichotiyakul, S., Arora, R. and Suntornlinsiri, W., 2016. Risk factors for cesarean surgical site infections at a Thai-Myanmar border hospital. *American Journal of Infection Control*, 44, pp.990-995.
- Berrios-Torres, S.I., Umscheid, C.A., Bratzler, D.W., Leas, B., Stone, E.C., Kelz, R.R., Reinke, C.E., Morgan, S., Solomkin, J.S. and Mazuski, J.E. 2017. Centers for disease control and prevention guideline for the prevention of surgical site infection, 2017. *JAMA Surgery*, 152, pp.784-791.
- Bhattacharya, S., Pal, K., Jain, S., Chatterjee, S.S. and Konar, J., 2016. Surgical site infection by methicillin resistant *Staphylococcus aureus*-On decline? *Journal of Clinical and Diagnostic Research*, 10, p.DC32.
- Burnie, J., Naderi-Nasab, M., Loudon, K. and Matthews, R., 1997. An epidemiological study of blood culture isolates of coagulase-negative staphylococci demonstrating hospital-acquired infection. *Journal of Clinical Microbiology*, 35, pp.1746-1750.
- Byrne, F.J., Waters, S.M., Waters, P.S., Curtin, W. and Kerin, M., 2007. Development of a molecular methodology to quantify *Staphylococcus epidermidis* in surgical washout samples from prosthetic joint replacement surgery. *European Journal of Orthopaedic Surgery and Traumatology*, 17, pp.449-456.
- Casey, A., Worthington, T., Caddick, J., Hilton, A., Lambert, P. and Elliott, T., 2006. RAPD for the typing of coagulase-negative staphylococci implicated in catheter-related bloodstream infection. *Journal of Infection*, 52, pp.282-289.
- Cheadle, W.G., 2006. Risk factors for surgical site infection. *Surgical Infections*, 7, pp.s7-s11.
- Curcio, D., Cane, A., Fernández, F. and Correa, J., 2019. Surgical site infection in elective clean and clean-contaminated surgeries in developing countries. *International Journal of Infectious Diseases*, 80, pp.34-45.
- Dancer, S. J., Stewart, M., Coulombe, C., Gregori, A. and Viridi, M., 2012. Surgical site infections linked to contaminated surgical instruments. *Journal of Hospital Infection*, 81, pp.231-238.
- Danzmann, L., Gastmeier, P., Schwab, F. and Vonberg, R.P., 2013. Health care workers causing large nosocomial outbreaks: A systematic review. *BMC Infectious Diseases*, 13, p.98.
- David, M.Z., & Daum, R.S., 2010. Community-associated methicillin-resistant *Staphylococcus aureus*: Epidemiology and clinical consequences of an emerging epidemic. *Clinical Microbiology Reviews*, 23, pp.616-687.
- Dessie, W., Mulugeta, G., Fentaw, S., Mihret, A., Hassen, M. and Abebe, E., 2016. Pattern of bacterial pathogens and their susceptibility isolated from surgical site infections at selected referral hospitals, Addis Ababa, Ethiopia. *International Journal of Microbiology*, 2016, 2418902.
- Dohmen, P.M., 2006. Influence of skin flora and preventive measures on surgical site infection during cardiac surgery. *Surgical Infections*, 7, pp.s13-s17.
- Elmer, W., Stephen, D., William, M., Paul, C. and Washington, C., 1997. *Color Atlas and Textbook of Diagnostic Microbiology*. Lippincott, Philadelphia, PA.
- Fan, Y., Wei, Z., Wang, W., Tan, L., Jiang, H., Tian, L., Cao, Y. and Nie, S., 2014. The incidence and distribution of surgical site infection in mainland China: A meta-analysis of 84 prospective observational studies. *Scientific Reports*, 4, p.6783.
- Forbes, B.A., Sahm, D.F. and Weissfeld, A.S., 2007. *Diagnostic Microbiology*. Mosby, St Louis.
- Giri, S., Kandel, B.P., Pant, S., Lakhey, P.J., Singh, Y.P. and Vaidya, P., 2013. Risk factors for surgical site infections in abdominal surgery: A study in nepal. *Surgical Infections*, 14, pp.313-318.
- Horan, T.C., Gaynes, R.P., Martone, W.J., Jarvis, W.R. and Emori, T.G., 1992. CDC definitions of nosocomial surgical site infections, 1992: A modification of CDC definitions of surgical wound infections. *Infection Control and Hospital Epidemiology*, 13, pp.606-608.
- Khairy, G.A., Kambal, A.M., Al-Dohayan, A.A., Al-Shehri, M.Y., Zubaidi, A.M., Al-Naami, M.Y., Alsaif, F.A., Al-Obaid, O.A., Al-Saif, A.A. and El-Farouk, O.Y., 2011. Surgical site infection in a teaching hospital: A prospective study. *Journal of Taibah University Medical Sciences*, 6, pp.114-120.
- Kim, J., Hong, J., Lim, J.A., Heu, S. and Roh, E., 2018. Improved multiplex PCR primers for rapid identification of coagulase-negative staphylococci. *Archives of Microbiology*, 200, pp.73-83.
- Lane, D., 1991. 16S/23S rRNA sequencing. In: *Nucleic Acid Techniques in Bacterial Systematics*. John Wiley and Sons, New York, pp.115-175.
- Leaper, D., Burman-Roy, S., Palanca, A., Cullen, K., Worster, D., Gautam-Aitken, E. and Whittle, M., 2008. Prevention and treatment of surgical site infection: Summary of NICE guidance. *BMJ*, 337, p.a1924.
- Liu, Z., Norman, G., Iheozor-Ejirofor, Z., Wong, J. K., Crosbie, E.J. and

- Wilson, P., 2017. Nasal decontamination for the prevention of surgical site infection in *Staphylococcus aureus* carriers. *Cochrane Database of Systematic Reviews*, 5(5), p.CD012462.
- Magiorakos, A.P., Srinivasan, A., Carey, R., Carmeli, Y., Falagas, M., Giske, C., Harbarth, S., Hindler, J., Kahlmeter, G. and Olsson-Liljequist, B., 2012. Multidrug-resistant, extensively drug-resistant and pandrug-resistant bacteria: An international expert proposal for interim standard definitions for acquired resistance. *Clinical Microbiology and Infection*, 18, pp.268-281.
- Mangram, A.J., Horan, T.C., Pearson, M.L., Silver, L.C. and Jarvis, W.R. 1999. Guideline for prevention of surgical site infection, 1999. *Infection Control and Hospital Epidemiology*, 20, pp.247-280.
- Marsou, R., Bes, M., Brun, Y., Boudouma, M., Idrissi, L., Meugnier, H., Freney, J. and Etienne, J., 2001. Molecular techniques open up new vistas for typing of coagulase-negative staphylococci. *Pathologie Biologie*, 49, pp.205-215.
- Martineau, F., Picard, F.J., Roy, P.H., Ouellette, M. and Bergeron, M.G., 1998. Species-specific and ubiquitous-DNA-based assays for rapid identification of *Staphylococcus aureus*. *Journal of Clinical Microbiology*, 36, pp.618-623.
- Mawalla, B., Mshana, S.E., Chalya, P.L., Imirzalioglu, C. and Mahalu, W., 2011. Predictors of surgical site infections among patients undergoing major surgery at Bugando Medical Centre in Northwestern Tanzania. *BMC Surgery*, 11, p.21.
- Medeiros, A.C., Aires-Neto, T., Azevedo, G.D., Vilar, M.J.P., Pinheiro, L.A.M. and Brandão-Neto, J., 2005. Surgical site infection in a university hospital in Northeast Brazil. *Brazilian Journal of Infectious Diseases*, 9, pp.310-314.
- Merdaw, M.A., 2011. postoperative wound infections and the antimicrobial susceptibility in Baghdad Hospitals. *Iraqi Journal of Pharmaceutical Sciences*, 20, pp.59-65.
- Mezemir, R., Seid, A., Gishu, T., Demas, T. and Gize, A., 2020. Prevalence and root causes of surgical site infections at an academic trauma and burn center in Ethiopia: A cross-sectional study. *Patient Safety in Surgery*, 14, p.3.
- Mohammed, A.A., Hussein, N.R., Arif, S.H. and Daniel, S., 2020. Surgical site infection among patients with *Staphylococcus aureus* nasal carriage. *International Journal of Surgery Open*, 24, pp.1-7.
- Mukagendaneza, M.J., Munyaneza, E., Muhawenayo, E., Nyirasebura, D., Abahuje, E., Nyirigira, J., Harelimana, J.D.D., Muvunyi, T.Z., Masaisa, F. and Byiringiro, J.C., 2019. Incidence, root causes, and outcomes of surgical site infections in a tertiary care hospital in Rwanda: A prospective observational cohort study. *Patient Safety in Surgery*, 13, p.10.
- Munoz, P., Hortal, J., Giannella, M., Barrio, J., Rodríguez-Créixems, M., Pérez, M., Rincón, C. and Bouza, E., 2008. Nasal carriage of *S. aureus* increases the risk of surgical site infection after major heart surgery. *Journal of Hospital Infection*, 68, pp.25-31.
- Negi, V., Pal, S., Juyal, D., Sharma, M.K. and Sharma, N., 2015. Bacteriological profile of surgical site infections and their antibiogram: A study from resource constrained rural setting of Uttarakhand state, India. *Journal of Clinical and Diagnostic Research*, 9, p.DC17.
- Owens, C. and Stoessel, K., 2008. Surgical site infections: Epidemiology, microbiology and prevention. *Journal of Hospital Infection*, 70, pp.3-10.
- Pal, S., Sayana, A., Joshi, A. and Juyal, D., 2019. *Staphylococcus aureus*: A predominant cause of surgical site infections in a rural healthcare setup of Uttarakhand. *Journal of Family Medicine and Primary Care*, 8, p.3600.
- Pereira, M., Leal, N.C., Leal, T., Sobreira, M., de Almeida, A., Siqueira Júnior, J. and Campos Takaki, G., 2002. Typing of human and bovine *Staphylococcus aureus* by RAPD-PCR and ribotyping-PCR. *Letters in Applied Microbiology*, 35, pp.32-36.
- Perl, T.M., Cullen, J.J., Wenzel, R.P., Zimmerman, M.B., Pfaller, M.A., Sheppard, D., Twombly, J., French, P.P., Herwaldt, L.A. and Mupirocin And The Risk Of *Staphylococcus aureus* Study Team. 2002. Intranasal mupirocin to prevent postoperative *Staphylococcus aureus* infections. *New England Journal of Medicine*, 346, pp.1871-1877.
- Rao, R., Sumathi, S., Anuradha, K., Venkatesh, D. and Krishna, S., 2013. Bacteriology of postoperative wound infections. *International Journal of Pharmacy and Biomedical Research*, 4, pp.72-76.
- Reichman, D.E. and Greenberg, J.A., 2009. Reducing surgical site infections: A review. *Reviews in Obstetrics and Gynecology*, 2, p.212.
- Rolston, K.V., Neshler, L. and Tarrand, J.T., 2014. Current microbiology of surgical site infections in patients with cancer: A retrospective review. *Infectious Diseases and Therapy*, 3, pp.245-256.
- Roumelaki, M., Kritsotakis, E.I., Tsioutis, C., Tzilepi, P. and Gikas, A., 2008. Surveillance of surgical site infections at a tertiary care hospital in Greece: Incidence, risk factors, microbiology, and impact. *American Journal of Infection Control*, 36, pp.732-738.
- Safdar, N. and Bradley, E.A., 2008. The risk of infection after nasal colonization with *Staphylococcus aureus*. *The American Journal of Medicine*, 121, pp.310-315.
- Sattar, F., Sattar, Z. and Zaman, S.A.M., 2019. Frequency of post-operative surgical site infections in a Tertiary care hospital in Abbottabad, Pakistan. *Cureus*, 11, e4243.
- Schentag, J.J., Hyatt, J.M., Carr, J.R., Paladino, J.A., Birmingham, M.C., Zimmer, G.S. and Cumbo, T.J., 1998. Genesis of methicillin-resistant *Staphylococcus aureus* (MRSA), how treatment of MRSA infections has selected for vancomycin-resistant *Enterococcus faecium*, and the importance of antibiotic management and infection control. *Reviews of Infectious Diseases*, 26, pp.1204-1214.
- Skråmm, I., Moen, A.E.F., Årøen, A. and Bukholm, G., 2014. Surgical site infections in orthopaedic surgery demonstrate clones similar to those in orthopaedic *Staphylococcus aureus* nasal carriers. *JBJS*, 96, pp.882-888.
- Wayne., 2017. *M100-S27: Performance Standards for Antimicrobial Susceptibility Testing*. Clinical and Laboratory Standards Institute, Wayne, PA.
- Welsh, A., National Collaborating Centre for Women's and Children's Health (Great Britain), 2011. *Surgical Site Infection: Prevention and Treatment of Surgical Site Infection*. RCOG Press.
- Wertheim, H.F., Melles, D.C., Vos, M.C., Van Leeuwen, W., Van Belkum, A., Verbrugh, H.A. and Nouwen, J.L., 2005. The role of nasal carriage in *Staphylococcus aureus* infections. *The Lancet Infectious Diseases*, 5, pp.751-762.
- WHO., 2016. *Global Guidelines for the Prevention of Surgical Site Infection*. World Health Organization, Geneva.

General Information

ARO's Mission: ARO seeks to publish those papers that are most influential in their fields or across fields and that will significantly advance scientific understanding. Selected papers should present novel and broadly important data, syntheses, or concepts. They should merit the recognition by the scientific community and general public provided by publication in ARO, beyond that provided by specialty journals.

We welcome submissions from all fields of natural science and technology, and from any source. We are committed to the prompt evaluation and publication of submitted papers. ARO is published biannually; selected papers are published online ahead of print.

Submission

Manuscripts should be submitted by the correspondent authors of the manuscript via the on-line submission page. Regardless of the source of the word-processing tool, only electronic Word (.doc, .docx, .rtf) files can be submitted on-line. There is no page limit. Only online submissions are accepted to facilitate rapid publication and minimize administrative costs. Submissions by any other one but the authors will not be accepted. The submitting author takes responsibility for the paper during submission and peer review. If for some technical reason submission through the email is not possible, the author can contact aro.journal@koyauniversity.org for support. Before submitting please check ARO's guide to authors thoroughly to avoid any delay in the review and publication process.

Authors are explicitly responsible for the language of their texts. Paper should be submitted in a well written in understandable English. Authors should not expect the editor or editorial board to rewrite their paper. Prior to submission, authors should have their paper proofread by a possible academic native speaker of English.

- Submit the Article with contact Information
- File name should be your article title
- Don't submit your article in multiple journal, we are taking only minimum time for review process. please don't waste our time
- Once the paper is accepted, it can't be withdrawn
- Please follow publication ethics and regulation
- Avoid plagiarism and copied material
- Strictly Follow ARO's Template

Terms of Submission

Papers must be submitted on the understanding that they have not been published elsewhere and are not currently under consideration by another journal or any other publisher. ARO accepts original articles with novel impacts only. Post conference papers are not accepted "as is", however, regular papers on the same topic but with a different title can be submitted. The new paper should contain significant improvements in terms of extended content, analysis, comparisons with popular methods, results, figures, comments, etc. Please do not forget that the publication of the same or similar material in ARO constitutes the grounds for filing of an (auto) plagiarism case.

The submitting author is responsible for ensuring that the article's publication has been approved by all the other co-authors. It is also the authors' responsibility to ensure that the articles emanating from a particular institution are submitted with the approval of the necessary institution. Only an acknowledgement from the editorial office officially establishes the date of receipt. Further correspondence and proofs will be sent to the author(s) before publication unless otherwise indicated. It is a condition of submission of a paper that the authors permit editing of the paper for readability. All enquiries concerning the publication of accepted papers should be addressed to aro.journal@koyauniversity.org.

Peer Review

All manuscripts are subject to peer review and are expected to meet standards of academic excellence. Submissions will be considered by an editor and “if not rejected right away” by peer-reviewers, whose identities will remain anonymous to the authors.

Guide to Author

We welcome submissions from all fields of science and from any source. We are committed to the prompt evaluation and publication of submitted papers. Selected papers are published online ahead of print. Authors are encouraged to read the instructions below before submitting their manuscripts. This section arranged into an overview speedy guidelines below and more detailed at the bottom section of this page

Manuscript Preparation

Submitting your manuscript will be in two stages namely before final acceptance and after.

Stage one:

At the first stage manuscript needs to be prepared electronically and submitted online via the online submission page in a Word (.doc, .docx, .rtf) format of one column double-spaced page, Times New Roman font type, and 12 p font size. A pdf version of the submitted manuscript should be submitted too. All authors' names, affiliations, e-mail addresses, and mobile phone numbers should be typed on a cover page, indicating the correspondent author.

Stage two:

- File type: MS-Word version 2003 or later.
- Format: The preferred format of the manuscript two-column template with figures and captions included in the text. This template can be downloaded via the following link. Please follow instructions given in the template; <http://aro.koyauniversity.org/about/submissions#onlineSubmissions>
- Text: All text is in Times New Roman font. The main text is 10-point, abstract is 9-point font and tables, references and captions are 8-point font.
- Figures: Figures should be easily viewed on a computer screen.

Units of Measurement

Units of measurement should be presented simply and concisely using System International (SI) units.

Title and Authorship Information

The following information should be included;

- Paper title.
- Full author names.
- Affiliation.
- Email addresses.

Abstract

The manuscript should contain an abstract. The abstract should be self-contained and citation-free and should not exceed 200 words.

Introduction

This section should be succinct, with no subheadings.

Materials and Methods

This part should contain sufficient detail so that all procedures can be repeated. It can be divided into subsections if several methods are described.

Results and Discussion

This section may each be divided by subheadings or may be combined.

Conclusions

This should clearly explain the main conclusions of the work highlighting its importance and relevance.

Acknowledgements

All acknowledgements (if any) should be included at the very end of the paper before the references and may include supporting grants, presentations, and so forth.

References

References must be included in the manuscript and authors are responsible for the accuracy of references. Manuscripts without them will be returned. ARO is following Harvard System of Referencing. (Learn how to import and use Harvard Styling in your Microsoft Office by following this link:

<http://bibword.codeplex.com/releases/view/15852>)

Preparation of Figures

Upon submission of an article, authors are supposed to include all figures and tables in the PDF file of the manuscript. Figures and tables should be embedded in the manuscript. Figures should be supplied in either vector art formats (Illustrator, EPS, WMF, FreeHand, CorelDraw, PowerPoint, Excel, etc.) or bitmap formats (Photoshop, TIFF, GIF, JPEG, etc.). Bitmap images should be of 300 dpi resolution at least unless the resolution is intentionally set to a lower level for scientific reasons. If a bitmap image has labels, the image and labels should be embedded in separate layers.

Preparation of Tables

Tables should be cited consecutively in the text. Every table must have a descriptive title and if numerical measurements are given, the units should be included in the column heading. Vertical rules should not be used.

Copyright

Open Access authors retain the copyrights of their papers, and all open access articles are distributed under the terms of the Creative Commons Attribution License, which permits unrestricted use, distribution and reproduction in any medium, provided that the original work is properly cited.

The use of general descriptive names, trade names, trademarks, and so forth in this publication, even if not specifically identified, does not imply that these names are not protected by the relevant laws and regulations.

While the advice and information in this journal are believed to be true and accurate on the date of its going to press, neither the authors, the editors, nor the publisher can accept any legal responsibility for any errors or omissions that may be made. The publisher makes no warranty, express or implied, with respect to the material contained herein.

ARO Reviewer/Associate Editor Application Form

ARO is a scientific journal of Koya University (p-ISSN: 2410-9355, e-ISSN: 2307-549X) which aims to offer a novel contribution to the study of Science. The purpose of ARO is twofold: first, it will aim to become an ongoing forum for debate and discussion across the sciences and Engineering. We hope to advance our problem solving capacity and deepen our knowledge regarding a comprehensive range of collective actions. Second, ARO accepts the challenges brought about by multidisciplinary scientific areas and aspires to expand the community of academics who are able to learn from and help to produce advances in a variety of different disciplines.

The Journal is seeking reviewers who can provide constructive analysis of papers thus enhancing overall reputation of the Journal. If any expert is interested in participating of the review process, we highly encourage you to sign up as a reviewer for our Journal and help us improve our presence in domain of your expertise. Appropriate selection of reviewers who have expertise and interest in the domain relevant to each manuscript are essential elements that ensure a timely, productive peer review process. We require proficiency in English.

How to apply

To apply for becoming a reviewer of ARO, please submit the application form by following the link:

<http://aro.koyauniversity.org/user/register>

To apply for becoming a member of the Editorial Board of ARO, please submit the application form by following the link: <http://aro.koyauniversity.org/pages/view/AEB>

Both Associate Editor and Reviewers should specify their areas of research and expertise. Applicants must have a doctorate (or an equivalent degree), and if Master degree they need to have significant publishing experience. Please note that;

- You will need to write your full official name.
- Please provide an email which reflects your official name, such as nameOne.NameTwo@... , or your institute's official email.
- All data need to be written in English.

Note: For more information, kindly visit the following websites:

1. aro.koyauniversity.org.
2. <http://libweb.anglia.ac.uk/referencing/harvard.htm>.
3. <http://bibword.codeplex.com/releases/view/15852>.

INDEXING



KOYA UNIVERSITY

Koya University is a young University established in 2003 and it is located in the city of Koya (Koysinjaq), short distance to the East of regional capital city of Erbil (Arbil, Hewlêr) in Kurdistan Region of Iraq. It is on the foothills of beautiful High Mountain. Its campus has been carefully laid out to embrace the beautiful mountainous nature. The Koya University has a Faculty system which enhances the interactions between similar academic fields. Today, Koya University has four Faculties: Engineering, Science and Health, Humanities and Social Sciences and Education in addition to the School of Medicine, which all consist of twenty-five scientific departments in different fields, such as Petroleum Engineering, Geotechnical Engineering, Software Engineering, Physics, Chemistry, Clinical Psychology, Social Science, Medical Microbiology and Sport Education.

ARO-The Scientific Journal of Koya University is a biannual journal of original scientific research, global news, and commentary in the areas of Science and Technology. ARO is a Peer-reviewed Open Access journal with CC BY-NC-SA 4.0 license. It provides immediate, worldwide and barrier-free access to the full text of research articles without requiring a subscription to the journal, and has no article processing charge (APC). ARO Journal seeks to publish those papers that are most influential in their fields or across fields and that will significantly advance scientific understanding. ARO Journal is a member of ROAD and Crossref agencies and has got ESCI, DOAJ seal, SHERPA/RoMEO deposit policy, and LOCKSS archiving policy.

ARO

The Scientific Journal of Koya University

Koya University (KOU)
University Park

Danielle Mitterrand Boulevard
Koya KOY45, Kurdistan Region - Iraq